The Characteristics of Instantaneous Angular Speed of Diesel Engines for Fault Diagnosis

Misan Madamedon

A thesis submitted to the University of Huddersfield in partial fulfilment of the requirements for the degree of
Doctor of Philosophy

Department of Mechanical Engineering
School of Computing and Engineering
University of Huddersfield

September 2017

ABSTRACT

Early fault detection and diagnosis of diesel engines are paramount now, especially with countries like the UK and France, in-line with the 2015 Paris agreement on climate change, making plans to ban the use of an automobile with diesel and petrol engines before the year 2040. This ban could affect other sectors where diesel engines are the prime mover and result in more stringent exhaust emission regulations. The instantaneous angular speed (IAS) model based fault diagnosis has shown more prospects of fault detection and location. However, there are serious gaps in available knowledge regarding IAS model based fault diagnosis which takes into account the effect of the system's modal properties. Hence, this research focuses on the online modal properties identification of a typical engine-load system for an improved performance of IAS based fault diagnosis.

Having acknowledged the essentials of IAS based fault diagnosis techniques through a comprehensive literature study, this research firstly investigates the impact of modal properties on the IAS of a four-cylinder engine. This is achieved through a three degree of freedom (DOF) torsional vibration model of the engine-load system, which allows for the modal properties of the system to be calculated and analysed. The calculated modal properties of the system showed one rigid and two flexible modes which had a low (<13Hz) and high (<92Hz) frequencies. The mode shape of the low frequency resonance shows more amplitude on the flywheel-load reference point of the system while that of the high frequency resonance shows more amplitude on the engine-flywheel reference point of the system. It then simulated the IAS which represents the torsional vibration signature with altered modal properties. The simulated result demonstrated that the low frequency resonance is more sensitive to the peak and trough values of the IAS waveform.

After identifying the deployment merits of operational modal analysis (OMA) techniques through a comprehensive literature study, this research then explore the prospect of an IAS based output-only modal properties identification of a typical engine-load system. This was done through both experimental and simulation evaluations, which allowed simulated and experimental IAS to be used for implementing covariance-driven reference based stochastic subspace identification (SSI). The simulated result using pseudo-random input shows that the identified resonance frequencies

and mode shapes are 80% correlated with the calculated ones. The simulation results also demonstrated that the accuracy of the identified modal properties is dependent on the number of IAS responses used for implementing the covariance-driven reference based SSI technique. The experimental result using estimated IAS during engine shutdown operation showed that both high and low frequency vibration mode can be identified. The identified resonance frequencies with their mode shapes are 80% correlated with the predicted ones.

Having identified the modal properties of the engine-load system online through the implementation of an IAS based covariance-driven SSI, this research then investigates the impact of misfire on the system's modal properties especially the mode shape of the low frequency resonance. This was achieved experimentally by inducing a complete misfire in respective cylinders (1^{st}, 3^{rd} and 4^{th}) and the IAS estimated during engine's transient shutdown operation was used for implementing a covariance-driven reference based stochastic subspace modal properties identification. While the mode shape of the identified high frequency resonance (<80Hz) showed no characteristics for cylinder misfire detection, that of the low frequency resonance (<13Hz) did.

Faults in the engine's injection system and an abnormal clearance valve train conditions significantly affects its combustion process. The cylinder by cylinder pressure torque obtained from measured IAS through order domain deconvolution technique can be used to detect and diagnose injection faults. In the interim, this research has also recognised that the closer the low-resonance frequency of the model used for the order domain deconvolution gets to its real time value the more accurate the pressure torque becomes. The reconstructed pressure torque which takes into consideration the real time low frequency resonance can be used to detect faulty injection system with different severities and abnormal clearance valve conditions of several severities. Furthermore, the importance of an accurate modal properties utilisation in IAS model based fault diagnosis of a four-cylinder diesel engine is shown.

Declaration

No portion of this work referred to in this thesis has been submitted in support of an application for another degree or qualification of this or any other university or another institute of learning.

Misan Madamedon

Acknowledgement

I would give all the praise and glory to the almighty God who has given me good health and strength to the complete this work all through my study period.

My unreserved gratitude goes to my supervisory team which comprises of the director of studies University of Huddersfield **Prof. Andrew David Ball** and **Dr Fengshou Gu** for the continuous support, motivation, encouragement, advice, guidance and supervision which they expressed towards me all through my years of study. Their constant direction and doors open for discussions anytime were of great help to me all through my years of study. I really appreciate their effort and contribution towards this research and couldn't have asked for any other team than them both.

To the team leader of the automotive lab **Martin Gargett,** I want to say without you the experiment conducted in this research would not have come to a realization. I cannot thank you enough for the help you rendered all through the experimental stage of this research. My special thanks to the **Nigerian government** represented by the **Office of the Special Adviser on Niger Delta Affairs (OSPNDA)** for proving me with the required funding for this research. I would like to appreciate my parents Mr and Mrs **Louis Madamedon** for their encouragement all through the period of my research.

Most of all I would like to appreciate my adorable and beautiful wife **Abiola Madamedon** for her patience, love and care all through the years of my research. And I cannot forget my two lions **Jeremiah** and Isaiah **Madamedon** who are priceless jewels of joy to me.

To all my friends at **the Centre for Efficiency and Performance Engineering (CEPE)** research group **Ugo, Osama, Naima, Zainab, Yuandong** and others I want to say a big thank you for their input one way or the other in this research.

List of Contents

List of Figures

List of Tables

List of Abbreviations

ADC	Analogue to Digital Converter
AR	Auto Regressive
BDC	Bottom Dead Centre
CAGR	Compound Annual Growth Rate
CMFD	Condition Monitoring and Fault Diagnosis
Cyl	Cylinder
DAQ	Data Acquisition
DC	Direct Current
DOF	Degree of freedom
EFDD	Enhanced Frequency Domain Decomposition
EGR	Exhaust Gas Recirculation
EMA	Experimental Modal Analysis
EPC	Exhaust Valve Closed
EPO	Exhaust Valve Open
ERA	Eigensystem Realization Algorithm
ET	Elapsed Time
FD	Frequency Domain

FDD	Frequency Domain Decomposition
FEA	Finite Element Analysis
FFT	Fast Fourier Transform
FM	Frequency-Modulation
FRF	Frequency Response Function
FSDD	Frequency-Spatial Decomposition
HT	Hilbert Transform
HTL	High Threshold Logic
IAS	Instantaneous Angular Speed
IC	Internal Combustion
IF	Instantaneous Frequency
IFFT	Inverse Fast Fourier Transform
IMEP	Indicated Mean Effective Pressure
IPC	Intake Valve Closed
IPO	Inlet Valve Open
IRF	Impulse Response Function
ITD	Ibrahim time domain
LSCF	Least-Square Complex Frequency
MA	Moving Average
MAC	Modal Assurance Criterion

MIF	Modal Indication Function
MISO	Multi-Input Single-Output
ML	Maximum Likelihood
MPUs	Magnetic Pickup Sensor
NExT	Natural Excitation Technique
OBD	On-board Diagnostic System
OHC	Overhead Camshaft
OHV	Overhead Valves
OMA	Operational Modal Analysis
PDF	Probability Density Function
PM	Particulate Matter
PP	Pick peaking
PPR	Pulse per Revolution
PSD	Power Spectrum Density
PSD	Power spectrum density
RFP	Rational Fraction Polynomial
Rpm	Revolution per Minute
S-DOF	Single Degree of Freedom
SISO	Single-Input Single-Output
SNR	Signal to Noise Ratio

SSI	Stochastic Subspace Identification
SVD	Singular Value Decomposition
TC	Time Count
TDC	Top Dead Centre
TTL	Transistor-Transistor Level
VGT	Variable Geometry Turbochargers
ZOH	Zero-Order-Hold

List of Publications

Madamedon Misan, Gu Fengshou, Aburass Ali and Ball, Andrew (2016) Online Estimation of Engine Driveline Dynamic Properties. In: International Conference for Student on Applied engineering, 20-21st October 2016, Newcastle

E.Muo Ugonnaya, Madamedon Misan, Ball Andrew and Gu Fengshou (2017) Wavelet Packet Analysis and Empirical Mode Decomposition for the Fault Diagnosis In: 23rd International Conference on Automation & Computing, 7-8 September 2017 Huddersfield

List of Notations

$[s(t)]$	A sinusoidal signal
ca	Absolute damping
A_{en}	Amplitude of encoder signal
$\ddot{\theta}$	Angular acceleration vector
θ	Angular displacement
ω_c	Angular frequency
ω	Angular speed
$\dot{\theta}$	Angular speed vector
$P\ Q$	Auxiliary matrix for the derivation of state space model
f_c	Carrier frequency
Ψ	Complex eigenvectors
B_c	Continuous time input influence matrix
A_c	Continuous time state matrix
r	Crank radius
C_t	Damping matrix
$y_k\ u_k$	Discrete input and output
C	Discrete output matrix

A	Discrete state matrix
D	Discrete transmission matrix
x_p	Downward displacement of piston
Λ_c	Eigenvalues matrix
Θ	Eigenvalues of original second order system
Λ	Eigenvector of original second order system
N_p	Encoder resolution
f_o	Firing frequency
ω_0	Fixed part of angular speed
H^{ref}	Hankel Matrix
f	Highest frequency component
$H\left[s(t)\right]$	Hilbert transform of a signal
i	Indices of sampled data
J	Inertia matrix
J_i	Inertia of each DOF
$\varnothing_c$	Initial phase of waveform
B	Input influence matrix
u	Input vector

$\varnothing_s$	Instantaneous phase of waveform
l	Length of connecting rod
$a\ b$	Modal matrices
C_a	Output location matrix for angular acceleration
C_d	Output location matrix for angular displacement
C_V	Output location matrix for angular velocity
T_c	Period of waveform
θ_e	Phase angle of carrier frequency
a_p	Piston acceleration
f_p	Piston force
v_p	Piston velocity
G_{xx}	Power spectrum density of output
G_{yy}	Power spectrum density of output
Pr	Probability of an event
n_o	Random noise
S_n	Random noise power
λ	Ratio of crank radius to the length of connecting rod
m	Reciprocating inertia

C	Relative damping
m_r	Ripples per revolution of a modulating signal
f_r	Rotational frequency
F_s	Sampling frequency
Gs	Shear modulus
K	Stiffness matrix
f_{conrod}	Tangential force acting on connecting rod
F_t	Tangential force acting on crankshaft
F_{tg}	Tangential force produced by gas pressure
F_{tr}	Tangential force produced by reciprocating inertia
t	Time
T_{tg}	Torque due to gas pressure
T_{tr}	Torque due to reciprocating inertia
k	Torsional stiffness
T	Total engine torque
$\delta\omega$	Varying part of angular speed

CHAPTER ONE

1 INTRODUCTION

This chapter gives an introduction to the work presented in this thesis. Firstly, the fields of condition monitoring and diagnostic system implementation procedures are introduced. Secondly, the project in this thesis is introduced; the research work aims and objectives are outlined and the thesis structure is presented.

1.1 Introduction to Condition Monitoring

In recent decades, the need for early fault detection and diagnosis in machines has become increasingly important. This importance is due to the ever growing demands for machines to perform to their designed specification and installed capacity. As a result of these growing demands, machines are expected to run without any major downtime and should be in proper conditions(Bauer. H, 2004). The maintenance department is there to ensure that they (machines) are running in appropriate conditions to avoid any significant failure. Maintenance of machines is traditionally carried out based on the number cycles they (machines) have completed(Mahon, 1992). Individual components of the machines are maintained or replaced on a schedule. Although these schedules were followed, it came to the point where instead of replacing a part, they were inspected and not replaced if they are deemed to be good enough. This method of maintenance is based heavily on risk and is prone to human error, which can lead to catastrophic failures, unplanned and prolonged downtime and potential high repair cost. Another approach which allows maintenance to be carried out when it is actually required for a specific component is condition monitoring. Condition monitoring is an aspect of preventive maintenance which is based on the use of past and present conditions of the machine(Dalpiaz & Rivola, 1997). In order to know these conditions, suitable sensors are installed on the machine to collect and analyse pertinent information. This information will then guide the operator or technician in making decisions regarding the appropriate maintenance. In the course of operation, every machine gives out information or signals which can be in the form of noise, vibration, temperature, lubricating oil condition, quality and quantity of the motor current drawn, etc. These signals can be acquired by installing transducers to measure the mechanical parameters of machines. The signals obtained exist at all times and are usually analogue. So as to extract meaningful information from these signals, they are converted into a digital domain by analogue-to-digital converters(Rao, 1996). The obtained discrete data which conforms to the analogue signal is analysed using signal processing techniques and can be used to develop algorithms for fault diagnosis. Developments are continually being made for the relevant features of condition monitoring such as transducers, instrumentation, signal analysis and decision making. Fault diagnosis in machines using condition monitoring technologies can be classified into four levels:

- Level 1- detection: Is there a fault or not in the machine?

- Level 2- localization: where is the fault located?
- Level 3- quantification: what is the extent of the fault?
- Level 4- prediction: what is the remaining service life of the machine?

Although, this work is mainly relative to level 1 to 3, more emphasis is on level two and three.
Although torsional vibration-based condition monitoring is applicable to a large range of machines, this thesis focuses on its application on diesel engines, due to its versatile usage in different industries that are vital to the world economy.

1.2 Research Background and Motivation

Over the years condition monitoring of diesel engines has attracted a lot of interest from both researchers and maintenance experts. This is due to the high level of success achieved in the development of heavy-duty diesel engines with numerous engine components which have the potential to fail during operation. Perhaps, the potential advantages of reduced maintenance cost, improved reliability, increased engine availability and reduction in the risk of engine failure, which is obtainable from an efficient implementation of engine condition monitoring technology is an appealing factor. This has led to the advent of some primitive condition monitoring methods like data recording of parameters ,for example load, speed, pressures and temperatures, manual tests such as measurement of peak cylinder pressure and visual inspection. The cylinder pressure characteristics such as the peak pressure and the indicated mean effective pressure contains relevant information which can be used for efficient engine's health condition monitoring. These pressure characteristics not only provide information which can be used to differentiate combustion grades, but they also enable the calculation of gear forces. More precisely, as the engine goes through different cycles with different cylinder pressure and temperature, its total power output results from a direct relationship between the working fluid and its mechanical component. Hence, it is viable to distinguish the grade of combustion of each cylinder from the movement of the crankshaft since it is directly connected to the cylinders.
Whilst, there are pressure transducers which can be used to measure the cylinder combustion pressure of an engine accurately, its applicability tends to be intrusive in nature as such it is mainly limited to engines for research and development purpose. Hence, the alternative of using the crankshaft's torsional vibration signature. This method involves the use of an encoder signal often used for shaft speed measurement to construct the instantaneous angular speed (IAS) waveform

which mimics the crankshaft torsional vibration signature. IAS extraction is achieved from an encoder pulse train by measuring the time intervals between pulses and then IAS is calculated. Current IAS based fault diagnostic can be classified into signal and model based methods. The IAS signal based fault diagnostic method uses the properties of the estimated IAS signal for fault detection. The IAS model based diagnostics estimates parameters such as pressure torque and cylinder pressure from the IAS signal using some developed analytic model of the engine-load system. The aim of IAS model based diagnostic is to use the measured IAS, to gain insight of the characteristics of the input torque generated by respective cylinders. Therefore, to gain insight into the individual cylinder pressure torque from the measured IAS signal, it is essential to determine the torsional modal properties of the engine-load system in real time. So, the torsional modal properties (resonance frequency, damping and modal vectors) are essential for efficient implementation of IAS model based diagnostics.

1.2.1 Focus of this Thesis

It is undeniable from the previous section that a lot of work on IAS based condition monitoring of diesel engines has already been carried out. Nevertheless, IAS based condition monitoring and fault detection of diesel engines which account for the influence of torsional modal properties (frequency, damping and modal vectors) has been less studied over the years. Thus, this work presents an investigation into an IAS based diagnostics which accounts for the influence of torsional modal properties to enhance its fault detection capability. The project has been split into three parts: IAS extraction and measurement implication: modal analysis of a typical engine-load system where the load, in this case, is a dynamometer and IAS based fault diagnosis, with each part having both simulation and experimental studies.

1.2.2 Research Aims and Objectives

The thesis uses IAS as a condition monitoring technique to study the predictive maintenance of a direct injection diesel engine. The purpose of this study is to show the influence of torsional modal properties on IAS model based fault diagnosis, so as to enhance its accuracy and sensitivity for early fault detection in diesel engines. Each part of the research has been subdivided into distinctive objectives presented below:

IAS Extraction and Measurement Implication

- **Objective -01:** To study, develop and implement a non-intrusive IAS measurement strategy for data collection from the engine.
- **Objective -02:** To investigate and implement IAS extraction algorithms for transient and steady engine operating conditions.

Modal Analysis of Engine Driveline

- **Objective -03**: To develop a torsional vibration model for typical engine driveline, so as to simulate IAS data from the engine under steady and random excitation.
- **Objective -04**: To investigate which of engine's transient operations can be considered as random excitation and to implement output only modal analysis using data from engine's transient operation.
- **Objective -05**: To develop and implement output only modal analysis using IAS response from random excitation and transient engine operation.

IAS Based Diagnosis

- **Objective -06**: To study IAS signal and model based diagnosis.
- **Objective -07**: To implement IAS signal and model based fault diagnosis by introducing specific quantified fault into the engine.
- **Objective 08**: To investigate the effect of accurate modal properties in model based diagnosis

1.3 Thesis Structure and Organization

A brief introduction of the content to each chapter is provided in this section with the relative emphasis of the chapter as regards to the research objectives.

Chapter One: This chapter gives an introduction to the work presented in this thesis. Firstly, the fields of condition monitoring and diagnostic system implementation procedure are introduced. Secondly, the project in this thesis is introduced; the research work aims and objectives are outlined, and the thesis structure is presented.

Chapter Two: This chapter provides a general introduction to the diesel engine condition monitoring. Firstly, engine fundamentals are discussed, and then an overview of diesel engine condition monitoring is provided. The principal faults occurring within the engines are presented,

and relevant measurement procedures for condition monitoring are briefly discussed. The chapter then present a review on IAS based engine diagnostic.

Chapter Three: This chapter presents an overview of the techniques used for IAS measurement and estimation. Firstly, every component of the IAS generation process is discussed. Then the theoretical basis for the IAS time and frequency domain estimation techniques is discussed. Both methods were then compared using simulated square wave signal.

Chapter Four: This chapter contains detailed descriptions of the experimental test facilities used for this thesis. Firstly, the specifications and performance characteristics of the test engine is discussed. Then the specification of instrumentation used is presented. Lastly, the simulated faults and test procedure is presented.

Chapter Five: This chapter presents a numerical and state space model of the engine-dynamometer structure as a three degree of freedom system with the engine, flywheel and dynamometer as individual inertias.

Chapter Six: This chapter present results from the models described in chapter five. It shows the results from the numerical model and the state space model. While the numerical model is used to validate the model, the state space model is used to show the effect of altered resonance frequency on simulated system response.

Chapter Seven: This chapter presents a brief overview of modal analysis and a review of output-only modal analysis techniques. It provided detailed mathematical derivation of how to use the measured responses of a system for estimating system matrices, as well as their modal properties, using the stochastic subspace identification (SSI) technique.

Chapter Eight: This chapter presents both simulated and experimental evaluation results from the identification method discussed in chapter six above.

Chapter Nine: This chapter present results of IAS based signal and model based diagnostics. It shows IAS time and frequency domain representation of three faults (complete cylinder misfire, abnormal valve clearance and injector fault) seeded on the test engine.

Chapter Ten: This chapter presents the conclusions and achievements of the work done in this thesis. It also presents recommendations for further research works.

CHAPTER TWO

2 DIESEL ENGINES AND CONDITION MONITORING

This chapter provides a general introduction to the diesel engine condition monitoring. Firstly, engine fundamentals such as the basic engine cycle, engine valve operation and fuel injection system are discussed. Then the main faults which occur within engines are reviewed. This is then followed by a brief review of the strength and weaknesses of relevant condition monitoring and fault diagnosis techniques used for diesel engines. A detailed review of the IAS signal and model based diagnosis is presented in the last section.

2.1 Introduction

Today, the diesel engine, due to its reliability and efficiency, is still one of the most commonly used engines globally. It has become a popular component in sectors such as plant machinery, vans, shipping, trucks and commercial vehicles(David John Moore, 2013; Global Diesel Engine Market, 2016; Trimby, 2016). It is also commonly used for backup power generation in industrial and business settings (Mahon, 1992). For example, it is used as emergency generation system in the banking sector, live TV broadcasting and is used to monitor and maintain cooling system in nuclear power stations. The most appealing feature of the diesel engine is its exceptional fuel efficiency. This feature can exceed 40% in vehicular applications and even 50% in large, two-stroke units of marine propulsion or electrical generation(Rakopoulos & Giakoumis, 2006) . Thus, a vehicle fitted with diesel engines can attain much lower specific fuel consumption and carbon dioxide emissions when compared with similarly rated spark ignition counterparts over the entire range(Bauer. H, 2004). This results in the substantial amount of money being saved over the lifetime of the vehicle. Moreover, characteristics of diesel engines such as the absence of throttling, low sensitivity in terms of air-fuel ratio disparities, high torque and high tolerability in maximum combustion pressure and temperatures, supports the application of numerous turbocharging schemes(Rakopoulos & Giakoumis, 2010). Over some years now the vast majority of diesel engines are typically turbocharged and aftercooled.

The advent of turbocharging application in diesel engines has led to improvements in the combustion process and fuel quality, which allowed for a massive increase in engine power output without any substantial increase in displacement volume and an only modest growth in engine speed as shown in Table 2-1. More benefits of turbocharging the diesel engine includes better fuel economy and reduced carbon dioxide emissions, increased mechanical efficiency and active pump work(Mollenhauer & Tschöke, 2010).

Despite the global economic recession and highly competitive automotive market in recent years, last year (2016), the diesel vehicles still maintain a market share of 45-50% in Western Europe(Global Diesel Engine Market, 2016). Although this is a small decrease than the market share value of 53% in 2010, the prospects and benefit of diesel engines are still underlying. It is expected that the diesel engine market will grow at a CAGR (Compound Annual Growth Rate) of 8.65% during the period of 2016-2020.

Table 2-1 Diesel engine characteristics for heavy trucks (Rakopoulos & Giakoumis, 2010)

Year	Displacement Volume (L)	Maximum Torque (Nm)	Maximum Power (kW)
1930s	8.5-16.6	520-1010	70-110
1955/6	8.3–11.6	620–1050	107–132
1960	9.7–12.7	680–760	140–154
Ca.1985	11.5–18.3	1285–1300	283–304
1996 (Euro II)	12.1–18.3	1850–2700	309–441

In recent decades, the automotive industry has been continuously dominated with stringent exhaust emission regulations, which has forced manufacturers to source new developments(Kiencke & Nielsen, 2005). As regards to diesel engines, the regulations emphasis is on the reduction of nitrogen oxide (NO_x) and particulate matter (PM) emission. This is due to the harmfulness of inhaling the nanoparticles and the fact that these pollutants are typically higher when compared with those from corresponding rated, port-injected petrol engines fitted with a three-way catalyst (Li, 2000; Oskam, 2014; Rakopoulos & Giakoumis, 2010; Roger, 2000). Because of the trade-off between the reduction of PM and NO_x, a complicated control strategy that requires a complex after-treatment system is needed. Hence, features such as complex exhaust gas recirculation (EGR), twin turbocharging systems, variable geometry turbochargers (VGT), electric superchargers, multi-valve configurations with variable valve timing and ultra-high injection pressure, have been applied so as to reduce pollutant emissions and still offer consumers desired pulling power and excellent fuel economy(Rakopoulos & Giakoumis, 2010). Moreover, carbon dioxide emissions, which have a connection with global warming are becoming increasingly important. Excellent fuel economy and the use of biofuels is a primary way of limiting carbon dioxide production. The present day diesel engine has not only been able to achieve an emission level which is 50% lower than those of a few years ago, but has also demonstrated greater fuel efficiency than ever before. The application of these technological advances mentioned above, resulted to a significant increase in the complexity of the engine and its control system(Kiencke & Nielsen, 2005). It became essential for manufacturers to develop a more efficient condition monitoring and early fault detection method as shown in the Figure 2-1 below.

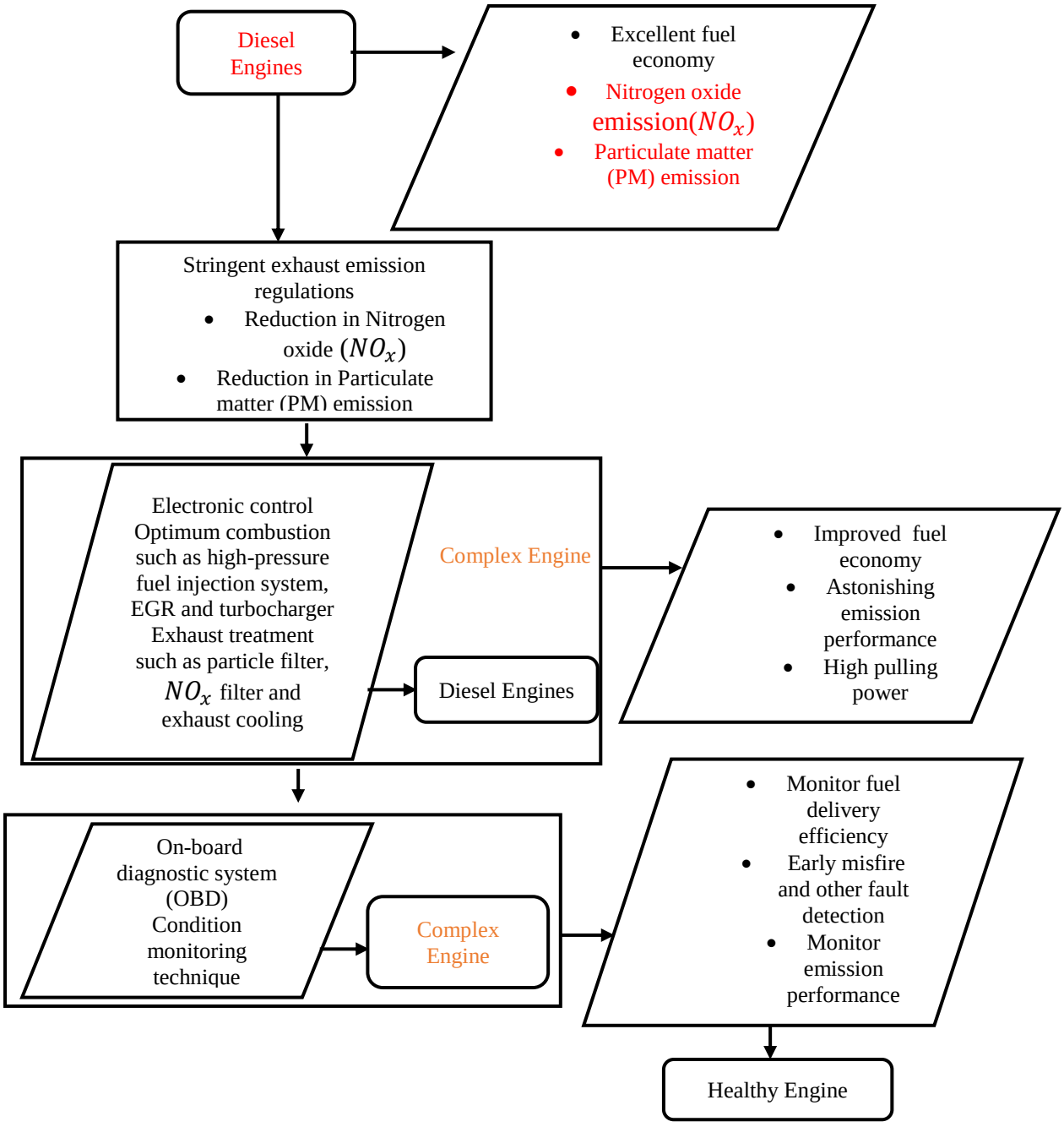

Figure 2-1 flow chart for diesel engine new technologies trend

Hence, a computerized, onboard diagnostic system (OBD), with the capacity to monitor and detect faults was developed. Some of the related components which OBD can monitor are exhaust gas recirculation (EGR) system, fuel delivery system, engine misfire, etc.

However, to date, a condition monitoring technique integrated into OBD system of diesel engines, that can accurately detect and localize early combustion and mechanical related faults in engines

is still in demand. Thus, this research presents an investigation which enhances the diagnostics capability of a condition monitoring technique which is already integrated into OBD systems of diesel engines.

2.2 Engine Valve and Injection System

Generally, internal combustion (IC) engines are a type of reciprocating machinery which can be classified into compression-ignition (diesel engines) and spark-ignition engines (petrol). Although the parts of both engines are similar, the way they individually mix and ignite fuel differs(Heywood, 1988). For a comprehensive read on basic principles of diesel engine see Heywood, 1988. Because the fault simulated in this thesis is relative to valve and injection system, their operation is described in following sections.

2.2.1 Diesel Engine Valve Operation System

In internal combustion engines, the operation of the valves is controlled by a mechanical system called the valve train. For direct injection diesel engine, as described in the previous section, the engine uses the valve to control the intake of air and outflow of residual gas out of the cylinder before and after combustion(Roger, 2000). The system consists of poppet valves, pushrods, rocker arms and a camshaft. Although the configuration of the valve operating system or valve train varies, they all still perform the same task of opening and closing the valves at the needed times for proper engine operations. They can be classified as systems with camshaft or the cam-less systems(Blair, 1999; Rakopoulos & Giakoumis, 2010). For systems with the camshaft, it can be mounted in the cylinder block (overhead valves (OHV)) valves or in the cylinder head with an overhead camshaft (OHC). Figure 2-2 below depicts an OHV system in which the camshaft drives the valve through the camshaft followers, push rods, and rocker arms. This is a very cost effective arrangement because a simple belt or chain is used to drive to the camshaft, the only machining is in done in the cylinder block(Roger, 2000). The gap between the cam and the top of the valve is called the valve clearance. For the OHV with a rocker arm, the valve clearance is the distance between the cam and the rocker arm pad. This can be adjusted by turning a set-screw, which is located at the end of the rocker arm(Roger, 2000). While turning the screw clockwise moves the rocker arm towards the cam (less clearance), turning the screw counter clockwise moves the rocker arm away from the cam (more clearance).

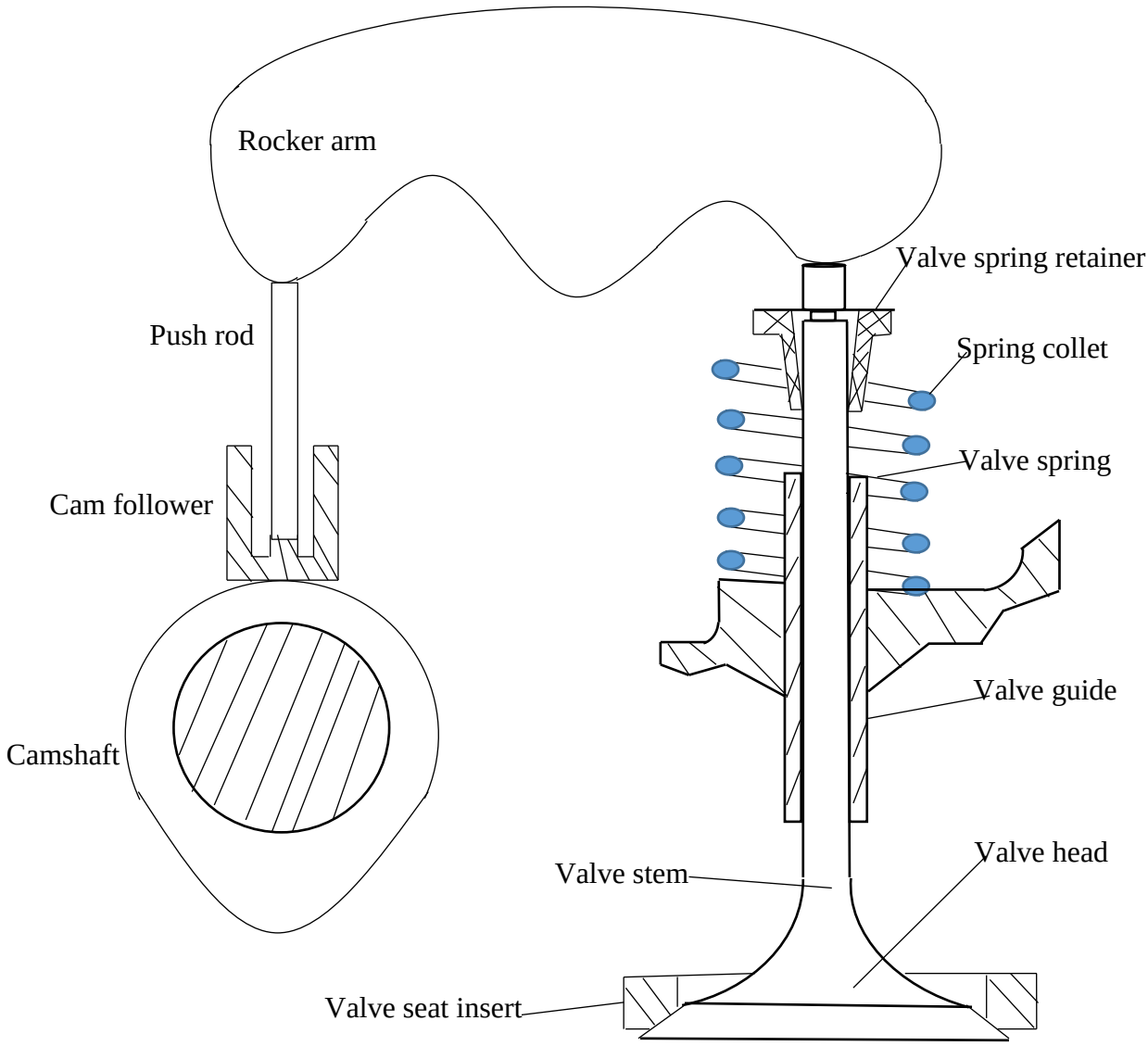

Figure 2-2 overhead valve drive

Figure 2-3 below depicts an OHC system where the camshaft is on a follower. A shim is used to adjust the valve clearance. This makes the valve clearance harder to adjust compared to the system that uses rockers, however for the OHC drive; the clearance is less likely to change. The importance of valve clearance in healthy engine operations cannot be over emphasized. When they are too big, the valves cannot fully open, restricting the flow of clean air and exhaust gases out of the cylinder hence the engine is not breathing properly(Heywood, 1988). On the other hand, when

they are too small, the valves would not close properly resulting in loss of compression and burnt valve seats.

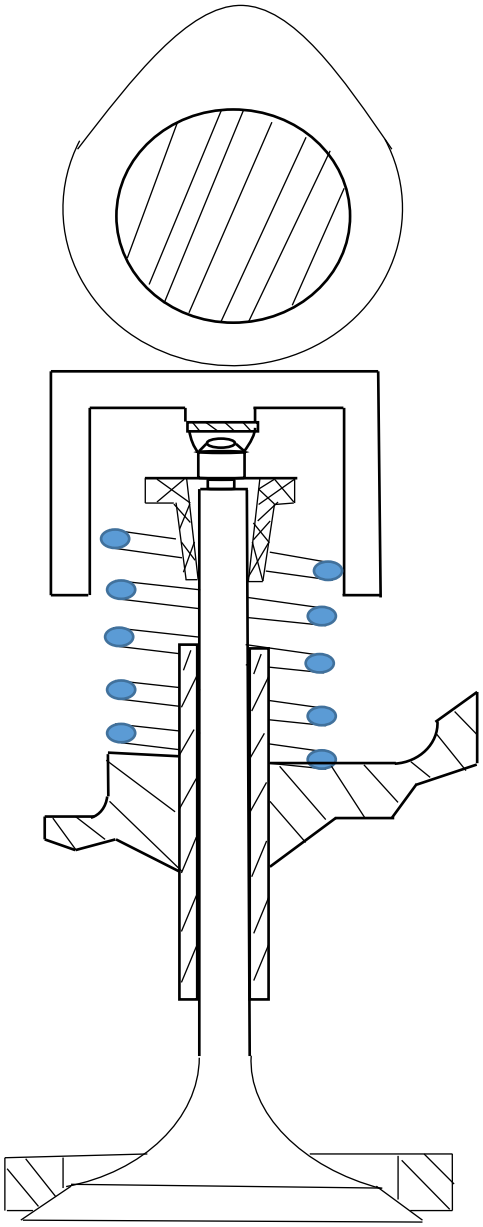

Figure 2-3 overhead camshaft drive

2.2.2 **Diesel Engine Fuel Injection System**

Although the supply of fuel into the cylinders of an engine, is the primary purpose of the fuel injection system, other things need to be considered, in order to ensure that the engine makes

efficient use of the fuel (Basshuysen & Schaefer, 2016). The fuel supplied to the cylinder must be injected at the proper time i.e. controlled injection timing, and the actual quantity of fuel must be provided to meet the power requirement. So as to achieve good combustion, the fuel supply system also ensures fuel atomization, bulk mixing and air utilization (Basshuysen & Schaefer, 2016; Mollenhauer & Tschöke, 2010; Rakopoulos & Giakoumis, 2010). The fuel system consists of lift pump, fuel filters, injection pump and fuel injectors. For a holistic overview see Basshuysen and Schäfer, 2016. The entire fuel system can be divided into low and high-pressure subsystems. While, the low-pressure subsystem ensures that the fuel is supplied to the high-pressure injection pump, the high-pressure subsystem ensure that the fuel is injected at high pressure into the cylinders through the injectors. This is usually done by either a plunger or a piston pump. In order to deliver the fuel to the engine at the right moment, there is the need for a timing system. Generally, two basic timing systems are available: electrical or mechanical (Mahon, 1992; Rakopoulos & Giakoumis, 2010).

The fuel injector is the component of the fuel supply system that acts as a fuel valve that allows the controlled introduction of fuel into the cylinder (Mahon, 1992). Its main purpose is to inject the actual quantity of atomized fuel and also distribute the fuel in the combustion chamber. The injector design depends on the engine's combustion system geometry of the combustion chamber, spray shape, injection rate and the number of injector holes. Figure 2-4 below details the construction of a typical hole-type direct injection diesel fuel injector.

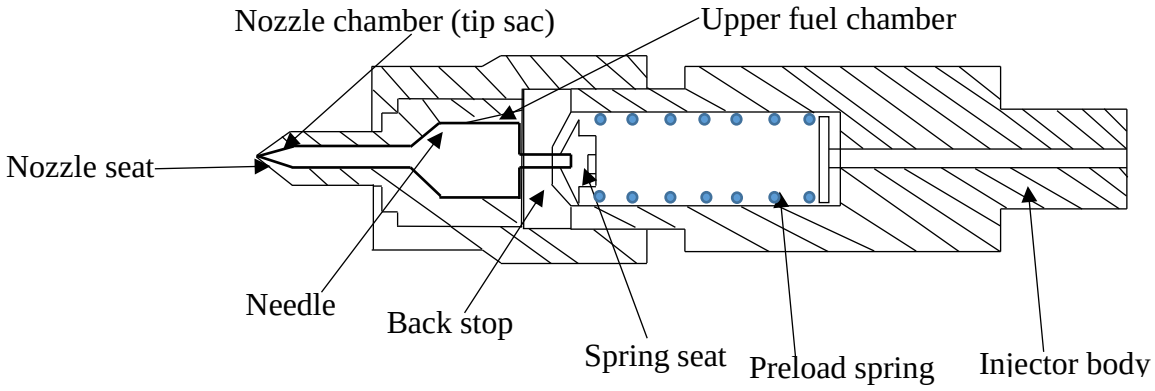

Figure 2-4 Schematic of fuel injector of diesel engine

The needle of the injector is held in contact with its seat by the preload spring, before injection starts, thereby blocking the fuel outlets hole. When the high-pressure fuel injection pump supplies

fuel to the injector, the fuel flows into the upper chamber of the injector first before moving to the lower chamber (Lakshminarayanan & Aghav, 2010; Merker, 2006). When the lifting force exerted by the fuel in the upper chamber exceeds the force which holds the needle in contacts with its seat, the needle lifts off its seat, unblocking the outlet holes and fuel injection starts (Fengshou Gu & Ball, 1996). As the injection period comes to an end, the fuel line pressure falls due to the opening of a spill port in the fuel pump, thereby causing the pressure in the upper chamber to drop below the value to keep the needle retracted. As such, the needle moves back in contact with its seat, stopping the injection of fuel. The diesel engine fuel injection system is fundamentally responsible for providing the engine with tolerable emission quality, low fuel consumption and smooth running with low noise. Hence, any fault to the fuel injection system will not only affect its efficient usage but can cause hazardous environmental pollution.

2.3 Review of Principal Faults in Diesel Engines

Faults are generally considered as any unacceptable change of state in engine's component that may lead to its malfunction and failure. Faults in a diesel engine can be classified according to their effect on the engine's component such as mechanical and combustion related faults or according to their location in the engine's system such as fuel system related faults, cooling system related faults and lubrication system related faults (Mahon, 1992; Mollenhauer & Tschöke, 2010; Charles, 2009). The damage of stationary or moving parts of the engine such as crank or camshaft, piston rings valves, fuel pipes and bearings are classified as mechanical related faults. These faults will not only cause physical damage to the part involved but will also affect the efficiency of the engine's performance. Faults which have a direct and significant impact on the quality of combustion are classified as combustion related faults. Combustion related faults can occur as a result of a malfunction in the components of any engine system such as fuel injection system (component such as fuel injector, fuel pump and fuel filter, etc.), or intake system (component such as air filter, inlet manifold and turbocharger). Combustion related faults have adverse effect on the engine emission and fuel consumption.

According to the findings of Mahon the fuel supply and injection system have the highest likelihood (26%) to produce faults, followed by the water system and cooling system (17%), valve drive system and seating (16%), bearings (11%), and the lubrication system, piston assemblies, gearing, turbocharger and drives each (6%)(1992). Although the statistics provided is old, recent

studies (Albarbar, A.S., 2006) suggest the most common causes for diesel engine failures are related to the fuel supply and injection system and valve drive system and seating. These faults if not detected early enough and allowed to develop fully, can directly affect the power output of the engine and other engine performance parameters. Hence it is invaluable to study condition monitoring techniques that can efficiently diagnose faults associated with the fuel supply and injection system and the valve train system.

Table 2-2 summary of engine faults

Engine system	Fault likelihood
Fuel supply and injection system	26%
Water system and cooling system	17%
Valve drive system and seating	16%
Bearings	11%
Lubrication system, piston assemblies, gearing, turbocharger and drives each	6% each

2.4 Condition Monitoring and Fault Diagnosis (CMFD) for Diesel Engines: An Overview

Due to the negative impact of the faults discussed in the previous section, there is the need for condition monitoring for the early and accurate fault detection in diesel engines (Jones & Li, 2000; Rao, 1996). Over the years, valuable sets of practices have been designed and developed to ensure proper and efficient engine operations. These practices can be classified into two parts: firstly, the variable to be measured or phenomena to be observed and secondly, the fault-detection methods applied based on the measured variable or observed phenomena (Jones & Li, 2000). Both parts of the practices are today termed as CMFD. The variable to be measured or phenomenon to be observed includes lubrication oil, smoke, temperature, vibration, pressure, sound (acoustic) and rotational speed, etc. All of the aformentioned have different levels of merit and demerits with their measurement and analyses. The commonly monitored variables used for diesel engines condition monitoring and fault-detection are reviewed in the subsections below.

2.4.1 Visual Inspection Monitoring

Due to the complexity of engines nowadays the use of visual monitoring techniques has improved in recent years, as, a fault which can be missed by all other condition monitoring techniques can be detected by regular visual inspections(David John Moore, 2013; Jones & Li, 2000; Rao, 1996). This technique utilizes the human brain to process gained information so as to give the immediate condition of the machine. It depends on the execution capability of a trained and experienced engineer. Besides the use of senses to visually monitor machines in this technique tools such as light probes, boroscopes and stroboscopes are used to support the inspection so as to make an accurate analysis of the system's running conditions(Charles, 2009). However, during an engine operation not all these visual monitoring techniques can be executed. Hence, systems may have to shut down for visual inspection. Visual inspection is widely applied as a condition checking tool but can be recorded as well to serve trend monitoring purposes.

2.4.2 Lubrication Oil Analysis Monitoring

This technique of condition monitoring analyses the mean element such as the base oil, additives and contaminants, which are contained in the oil. Whilst base oil monitoring test for destructive effects such as oil degradation and viscosity change, additive monitoring examines the chemical degradation and breakdown of the polymers (Jones & Li, 2000). The contaminant monitoring looks for solid, liquid or gaseous contaminants in the oil. Some of the methods used in the analyses include the determination of oil viscosity, magnetic chip detector, Ferrography and Spectrography.

2.4.3 Cylinder Pressure Monitoring

The most commonly used parameter in the study of diesel engine combustion is the cylinder pressure, because its representation encompasses every stroke of the engine cycle. It is usually measured by installing a piezoelectric transducer inside the cylinder. The quality of combustion and heat release rate of the engine is greatly linked to the pressure history and peak cylinder pressure. The cylinder pressure has a direct relationship to the engine's torque and work output. The instantaneous cylinder pressure as a function of the crankshaft rotational angle is a common representation which is used in condition monitoring and evaluation of the engine's combustion quality. The peak cylinder pressure and the crank angle at which it occurs provide information

about the injection and ignition timing, which are vital for engine diagnostics. Some studies carried out on the use of cylinder pressure for engine diagnostics : (Gilkey & Powell, 1985; Leonhardt, Gao, & Kecman, 1995; Lim, Lim, Park, Son, & Kim, 1994) used cylinder pressure to estimate ignition timing and air to fuel ratio of diesel engines, it was used by Leonhardt et al, to monitor the performance of fuel injection pump (1995). Cylinder pressure based diagnostics is yet to be suitable for use within in-service engines and small automotive engines, because the transducers are quite expensive and their installation is considered to be intrusive (Di Leo, 2015).

2.4.4 **Vibration Monitoring**

This condition monitoring method is based on the principle of measuring and analysing the vibration signal generated by the engine. All mechanical equipment in motion produces a vibration profile that encloses a lot of facts about its operating condition and every moving part of the system one way or the other contributes to the profile with its own signature vibration (Robert Bond Randall, 2011; Sinha, 2014). So, should one or several components contain a fault this characteristic signature changes, consequently altering the monitored vibration profile. Vibration monitoring is one of the most widely used variables for fault identification and engine failure prediction. Its acceptance level as a predictive maintenance method for engine maintenance is becoming progressive (Robert Bond Randall, 2011). Thus, to maintenance engineers, the understanding of vibration concept is of massive importance (Rao, 1996). In vibration monitoring, the signal is measured through the use of accelerometers which are installed on the engine component to be monitored. The installation procedures of accelerometers are usually not intrusive and relatively cheap. Several studies (Ahmed Yousef Ben Sasi, 2005; Piersol & Paez, 2009) have demonstrated that vibration analysis has the capability of analysing vibrating machines without interrupting normal operations. Other studies have also demonstrated the prospect of estimating in-cylinder pressure waveform using vibration signals from the engine block (Trimby, 2016). The mixture of various other vibration sources and the impacts of several transmission paths are among some of the difficulties involved in using vibration as a signal for monitoring (Randall, 2011). Vibration monitoring is still not able to provide all-purpose diesel engine condition monitoring because it contains information which is mostly related to the engine’s firing sequence.

2.4.5 Acoustic Monitoring

This method involves the use of microphones to pick acoustic signals from the engine while in operation, and the resulting signal analysed to monitor the conditions of the engine for fault detection. This also include the monitoring and analyses of high frequency acoustic emissions on marine diesel engines. There are significant similarities between data from the acoustic signal and that of vibration monitored waveform. The acoustics characteristics of a diesel engine, which can be used for condition monitoring was developed by (Gu, Ball, & Li, 2000). In their study, the acoustic signal was represented using Wigner-Ville distribution and Continuous Wavelet Transform (CWT), showing the effect which the environment has on the measurement. Acoustic monitoring method is non-intrusive and as such has a high prospect for online condition monitoring. However, its major limitation is the contamination of acoustic waveform by background noise where the measurement is taken (Li .W, 2000).

2.4.6 Exhaust Pressure Monitoring

This method uses the principle that that combustion, injection and lubrication related information can be found in the quality of the engine exhaust quality. This approach can be achieved in two ways: either by chemical analysis of the gases (HC, CO, NO, NO2, CO2 and H2O) emitted during exhaust or physical measurement of parameters such as temperatures, mass flow rate, and noise(David John Moore, 2013; Rao, 1996). Apart from being able to detect fault through this method, it also serves as a statutory safeguard for the environment. Popular in this method is the use of delicate sensors in measuring the temperature or pressure of the exhaust pipe. Although this approach can be utilized for online condition monitoring, it can be very intrusive as the sensor after a short while is broken due to the high temperature of the exhaust gas.

2.5 Key Findings

In this chapter, the fundamentals of the diesel engine cycles have been outlined, actually only some sections of these advanced machines were presented. An overview of the valve train and fuel injection system of the diesel engine has been discussed. The valve train and fuel injection systems of diesel engines are centred mainly on events happening at known pre-set times which are linked by crank angle. Hence, a large enough sample size of data taken from a running engine is expected

to contain the operational effect of these systems for each engine cycle notwithstanding the transient nature of engines. As such, a change in their operational conditions such as abnormal valve clearance or faulty injector would show some discrepancies for a particular event in relation to crank angle. This is one reason why in condition monitoring of engines data used are usually aligned against the crank angle.

The chapter then presented a literature review of common faults in diesel engines and the condition monitoring and fault diagnosis method used in detecting them. Cylinder pressure monitoring based diagnostics is very accurate for diesel engine fault diagnosis but the sensor is very expensive and its installation is intrusive.

CHAPTER THREE

3 OVERVIEW OF IAS Measurement

This chapter provides a significant overview of the IAS generation process for a more enhanced engine diagnostics and monitoring. It will provide a detailed review of the techniques used for IAS measurement and extraction as well as the errors involved in the IAS measurement.

3.1 Introduction

The IAS of diesel engines in recent years is becoming a major interest for real time condition monitoring or diagnosis application. The total dynamic operation of the engine results in the rotation of the crankshaft, thus the IAS contains vital information regarding all combustion and mechanical process which contributes to its rotation (Charles, 2009). Theoretically, any fault or failure should alter the measured IAS. In the use of IAS monitoring for engine diagnostics, the first step is its generation which includes measurement of the angular displacement of the crankshaft and extraction of IAS from the angular displacement (Jia-Dong, et al., 2009; Li et al., 2005). The IAS is usually assessed using angle encoders which are electromechanical devices that convert angular position of the crankshaft to signal (Remond, 1998). The process of acquiring the signal and extracting the angular speed from it is termed the IAS generation process in this thesis. The clear understanding of the IAS generation process is vital for its use for accurate real time engine diagnostics. Li et al., categorized the IAS generation process into two broad groups of time/counter and analogue to digital converter (ADC) – (based methods, based on the mechanism of data acquisition) (2005). In the time/counter based methods, the angular transducer signal is treated as a pulse train and then used to start and stop the time/counter. So as to ensure the pulse train is at transistor-transistor level (TTL), the angular signal from the transducer is conditioned before being fed into the time/counter system. A time/counter system can be realized either in the form of hardware or software. Then different strategies are implemented to extract IAS from the angular displacement signal. These include the measurement of elapsed time (ET) between successive pulses using an interrupt service routine and a timer; counting of the pulse during a prescribed time and a combination of any two of these methods. Li et al., observed that the use of hardware time/counter system for IAS generation process has some limitations (2005). One of which is the inflexibility of the special measurement hardware, because they are often designed for specific applications. However, a software time/counter system is easier to implement for accurate real time engine diagnostics.

In the ADC-based methods, the angular signal from encoders is treated as an ordinary analogue signal. The IAS is extracted by using an efficient signal processing technique on the logged angular signal data. The data can be logged through the use of any general purpose ADC board. Thus this method does not require specific hardware. The main limitation of this method was the large

amount of data required and the low speed of acquisition when compared to the other method. The increase in the memory capacity of computers and ADC acquisition speed has made the ADC based methods more attractive (Gu, et al., 2006; Randall & Luo, 1990; Sweeney & Randall, 1996). Hence, for experimental purpose and because of the objectives of this thesis, the direct ADC-based method of IAS generation was adopted for engine driveline modal properties estimation, condition monitoring and fault diagnosis.

3.2 Instantaneous Angular Speed (IAS) Monitoring

This method is based on the fact that a torque pulse is applied to the crankshaft throw during engine combustion process(André, Girardin, Bourdon, Antoni, & Rémond, 2014). This torque pulse results in a periodic excitation of the engine's crankshaft causing its angular speed to fluctuate in both rigid and flexible modes (Honda, et al., 1989). Whenever there is a combustion or mechanical related fault on the engine, the torque applied to the crankshaft is altered, producing an altered response of engine's angular speed (Ben Sasi, 2005). All IAS based diagnostics methods use common techniques. Firstly, the IAS of one or more components of the engine's driveline is measured. Then once the IAS response is known, the presence of faults can be determined by either threshold criteria, pattern recognition, forcing function reconstruction techniques or a combination of any of these three techniques. These techniques and relevant literature which implemented them are discussed below under signal and model based IAS diagnosis as shown in Figure 3-1 below.

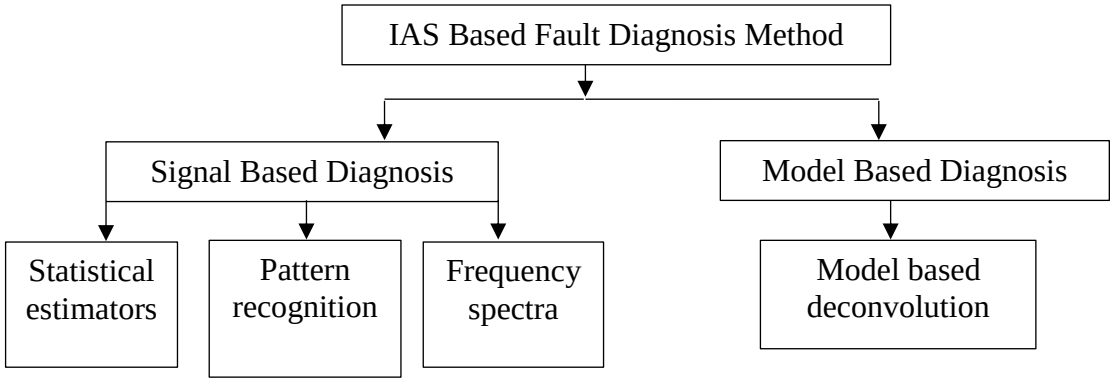

Figure 3-1 IAS based diesel engine fault diagnosis methods

3.2.1 **Signal Based Diagnosis**

The IAS signal based fault diagnosis method consists of techniques which rely mainly on the properties of the observed IAS signal for fault detection. The underlying assumption of the IAS signal based method is either that the observed signal is deterministic with known features or it is a complete black box. Although, some studies classify the black box assumption as data based fault diagnosis, in this thesis both of them are discussed under signal based fault diagnosis. Some of the techniques used in IAS signal based diagnosis include the use pattern recognition technologies, statistical estimator, neural networks, neuro-fuzzy system etc. For instance, Sood et al., based on IAS measurements, proposed three statistical methods (cross correlation, similarity measures and pattern recognition) for engine fault detection (1985). Mauer and Watts, were able to use information from the extracted IAS waveform to detect a faulty cylinder in an 8-cylinder 4-stroke diesel engine (1989). Using the IAS data extracted at an engine speed of 1500 and 2000rpm, they looked at the interval between two consecutive minima of its waveform. Regression lines of the increase and decrease of the signal were calculated and compared with others.

By measuring the IAS of a diesel engine during a free acceleration Mauer, was able to determine the engine's mean available torque (1992). He performed a linear regression on the IAS over a fixed number of engine cycles and proposed that the slope of the regression line is proportional to the mean engine torque.

Lida et al., used a cross correlation technique to filter out measurement noise from the IAS signal and was able to estimate the indicated mean effective pressure (IMEP) for each cylinder in a 4 cylinder engine (1990). Brown and Neil, by comparing the measured IAS signal from engines to

reference patterns in the knowledge database, developed a diagnostic that could identify the misfiring cylinder in engines (1992). Where the database is made up of experimental data taken from the engine operating with known faults under various engine operating conditions. Taraza et al., presented a method of detecting non-uniformities in the contribution of the cylinders to output (2000). Based on information supplied by the lowest harmonic orders of measured IAS, a crankshaft speed variation frequency analysis technique was presented. The phase positions of the lowest three harmonic orders of the IAS were used in identifying the misfiring cylinder. Charles, based on the reliable polar coordinate representation of measured IAS signal, was able to improve the discrimination features of combustion related faults in a 6-, 12-, 16- and 20-cylinder diesel engines (2009). Desbazeille et al., proposed the use of the artificial intelligent system, precisely neural networks for pattern recognition of IAS waveform in normal and faulty conditions (2010). They validated their proposal by using this method in detecting and localizing a fuel leakage fault in a 20-cylinder diesel engine. Gawande et al., based on engine dynamics, developed a mathematical model that shows the effect of fuel quantity on the amplitude of IAS (2015). They were able to demonstrate that, the amplitude of the IAS waveform could be reduced by 55% from the empirical relation found and Fast Fourier Transform (FFT) analysis. The main advantage of using IAS signal based fault diagnosis is that the time and effort required for the development of a model would be saved. This means on the basis of IAS signal based fault diagnosis, relatively simpler fault diagnosis can be developed and be used for onboard engine diagnosis. Despite the excellent prospects and advantage which this method possesses, it is yet to be fully admitted in the diesel engine industry for online condition monitoring and fault detection. Because it is difficult to comprehend a mathematical /physical link of this method. Thus, the method cannot interpret the rationale behind the faults. In signal based diagnosis where neural networks are used it is very difficult to train the network under all possible fault scenarios. A noisy data may also misguide the fault detection algorithm.

3.2.2 **Model Based Fault Diagnosis**

In IAS model based fault diagnosis, firstly, an analytic model built on the fundamental laws of physics is developed for the engine-dynamometer system. In this method, the analytic model combined with the IAS response is used to reconstruct the forcing torque (Williams, 1996). The system model used for the reconstruction ranges from no model, to flexible crankshaft with driveline model. The reconstruction technique can be based on either order domain or state space

deconvolution. In order to take advantage of the combustion process periodicity, the frequency response function of the order domain is formulated with the crank angle being the independent variable in the order domain deconvolution technique (Citron & Chen, 1989). The order domain deconvolution method, can be used for analysis of linear and steady engine operations (Connolly & Yagle, 1993). Although the state space deconvolution method can be utilized on nonlinear and transient engine operations, it suffers a setback of not being able to reconstruct the cylinder pressure at TDC. Hence, most of the studies reviewed use the order domain deconvolution technique.

Citron et al., were able to reconstruct the cylinder pressure waveform for a 4-and 6- cylinder engine by passing back measured IAS signal through a rigid crankshaft and elastic driveline model of the engine (1989). Firstly, the cylinder by cylinder torque fluctuation waveform of the engine was obtained through an order domain deconvolution technique. By using the fluctuation waveform of the engine pressure torque, the average level of the engine torque being developed was established, thereby, providing the waveform of the torque due to cylinder pressure. The cylinder pressure was then obtained from the torque due to cylinder pressure. They further suggested that knowledge of these cylinder pressures and the torques gives the foundation for both open loop and adaptive strategies of engine control.

Connolly and Yagle, using a state space deconvolution were able to reconstruct cylinder pressure from measured IAS (1992,1993). They represented the engine system by a single inertia model and linearized the linear equation of motion by making the independent variable to be velocity squared. The result from the experiment carried out showed that this technique has the prospects of detecting misfire and possibly the severity of misfire.

Taraza, using a steady state, transfer matrix, non-iterative deconvolution approach, investigated the reconstruction of individual cylinder pressure waveforms from measured IAS (1993). In the rigid crankshaft case, multiple engine orders were used simultaneously to solve for each cylinder torque contributions. The prospect of using this method for misfire detection and localization was also emphasized. Models with crankshaft flexibility between each cylinder were also studied.

Shiao and Moskwa estimated the heat release rates and cylinder pressure using a rigid crankshaft, state space, time variant model with the measured IAS as input (1994). The estimated cylinder pressure and heat release rate were used to develop a misfire detection system.

Lim et al., using a rigid crankshaft single degree of freedom model were able to estimate cylinder pressure in 4-cylinder engine (1994). The measured IAS was used as the input for this method. The method used a principle which assumes to know the pressure in the remaining three cylinders when one cylinder fires, thereby reducing the number of unknowns to a single input.

Taraza et al., based on a lumped mass model, established a relationship between the cylinder pressure variation and the IAS of a single cylinder diesel engine operating at a steady state (2005). Using the transfer matrices method, they determined the correlations between the harmonic components of the tangential gas pressure and the harmonic component of the IAS measured from the free end of the crankshaft. The correlation was then used to either predict the IAS when the cylinder pressure is known or to reconstruct the cylinder pressure when the IAS is known. This method has been used to reconstruct cylinder pressure from measured IAS in a 1-cylinder diesel engine only. This is because reconstruction of cylinder pressure from IAS signal using the transfer matrix method for a multi-cylinder is computationally too expensive to implement in real time. Hence, Mocanu, developed an on board fuel identification system for single and multi-cylinder engines, using features such as ignition delay and peak pressure value of a reconstructed pressure waveform (2013). While the cylinder pressure waveform was reconstructed from measured IAS signal using the transfer matrix method for the one cylinder engine, the direct calculation method was utilized for the four cylinder engine.

The features of reconstructed cylinder pressure waveform which were used to identify different fuels can also be used for detecting combustion and mechanical related faults (Mocanu, 2012). The cylinder pressure reconstruction from IAS signal using model deconvolution through order domain method as reviewed has prospects for on board engines diagnostics, because it can identify the faulty cylinder. However, in all the literature reviewed using the aforementioned method the system modal characteristics such as torsional stiffness, resonance frequencies and damping ratios are determined offline through software evaluations using the finite element analysis (FEA). This method and assumption might be valid for engines used as emergency generators but is not valid for automotive engines, because the automotive clutch has dynamic characteristics which vary unpredictably with operating conditions (Williams, 1996). The crankshaft is isolated from the driveline by the soft spring of the clutch which effectively acts as a low pass filter (Al-Durra, et al., 2011; Ali & Saraswati, 2015; Hamedovic, et al., 2005; Hardenberg & Hase, 1979). Engine fault diagnosis, which utilizes frequencies that are below the engine's firing frequency, are mainly

sensitive to modelling assumptions related to the clutch and driveline components. The low resonance frequency if not accurately determined can affect the performance of the IAS model based diagnostics. There is, therefore, the need for an online identification of engine driveline modal properties or characteristics, so as to achieve accurate online diagnostics of the engine. Hence, this thesis presents an online identification of engine driveline modal properties implementing a latest stochastic subspace identification (SSI) method.

3.3 Modelling the IAS Generation Process

In order to generate the IAS of a mechanical rotor system using ADC based method, every part of the generation process is vital. Figure 3-2 below shows a typical IAS generation process.

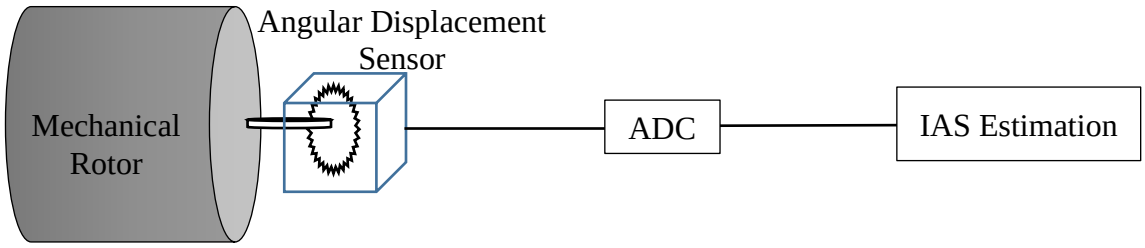

Figure 3-2 a schematic of IAS generation process

3.3.1 Measurement Principle

In reciprocating machines such as diesel engines, there are variations in the angular rotation of the crankshaft rotational motion (Gubran & Sinha, 2014). The variation in angular rotation results to variation in the angular speed in one revolution. Thus, the angular speed of a mechanical rotor is realized in the difference form:

$$\omega = \frac{\Delta\theta}{\Delta t} \tag{3-1}$$

Where θ is the angular displacement of the mechanical rotor and t is the corresponding time duration. So as to know the variation in the angular rotation of the crankshaft in one revolution, a device which produces multiple pulses in every revolution is required. This device could be a

magnetic pick up or hall-effect sensor, optical encoder, potentiometer, incremental shaft encoder or other types of pulse generators (Remond, 1998). These devices contain a stationary part which is the detector and a moving part which is usually mounted to the mechanical rotor as shown in figure 3-3 below. The moving part is shaped circumferentially with uniformly distributed holes, teeth or slots. Since it is mounted with the mechanical rotor it moves rotationally with the rotor (Fengshou Gu, Yesilyurt, Li, Harris, & Ball, 2006).

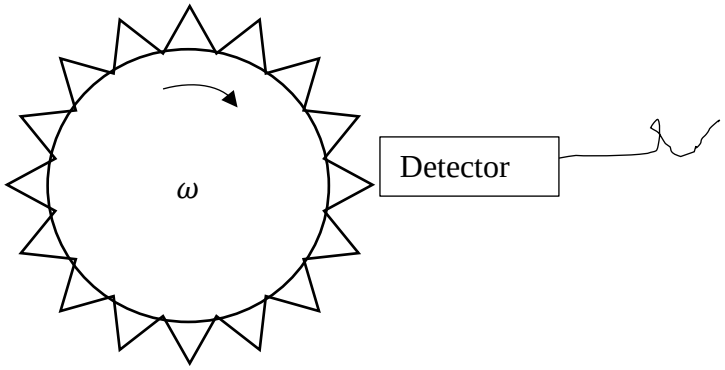

Figure 3-3 angular displacement sensor components

The stationary part of the sensor components converts the motion of the moving part into an electrical signal. The signal then goes through signal conditioning which includes amplification, filtering, shaping and impulse noise removal (Brandt, 2011). These aforementioned processes are usually integrated into the encoder through a conditioning circuitry (Fengshou Gu et al., 2006) Figure 3-4 shows all the conditioning elements usually enclosed within an encoder.

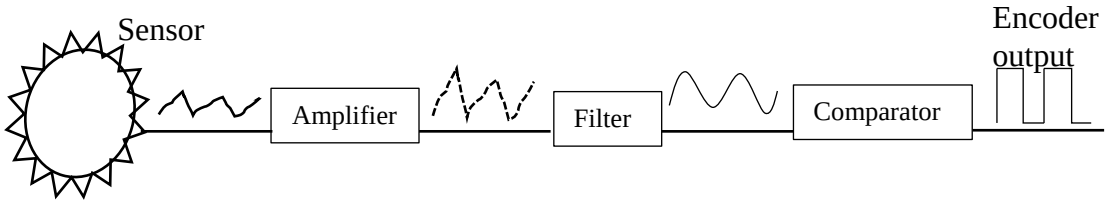

Figure 3-4 signal conditioning elements of encoders

While in shaft encoders both the detecting and moving uniformly part is combined together, in magnetic pick-up encoders they are not. The output signal from the encoder after the comparator can be in the form of a square wave, quadrature wave or before the comparator a simple sinusoidal wave (Fengshou Gu et al., 2006). Therefore, when the crankshaft rotates, the pulse generator produces a pulse for every unit of angular distance. Depending on the number of evenly spaced

division of the shaft generator, the produced pulses are uniformly displaced in-line with the angle of displacement. So, one unit of angular distance of N_p evenly spaced pulse generator is

$$\theta = 2\pi / N_p \ rad \tag{3-2}$$

The ADC converts the analogue speed signal of the pulse generator to digital data, during the measurement process. The digital data consists of time and amplitude information about the speed recorded at a fixed sampling rate. Using appropriate signal processing technique on the recorded time and amplitude information, the IAS can be estimated.

3.3.2 IAS Encoder Signal

The output signal from the encoder as stated in the previous section is a modulated signal (Fengshou Gu et al., 2006). Assuming the frequency of the rotating shaft is constant i.e. the shaft is rotating at a steady speed, the moving parts of the encoder are uniformly distributed circumferentially and there is no influence of noise, the encoder signal exhibits a uniformly periodic waveform $s(t)$. The encoder's output before the comparator can be represented as a sinusoidal waveform for simplicity of analysis

$$s(t) = A_{en} cos(\omega_c t + \varnothing_c) = A_{en} \cos\left(\frac{2\pi}{T_c} t + \varnothing_c\right) \tag{3-3}$$

Where,

A_{en} , is the amplitude of the encoder signal

$\omega_c = \omega N_p$, is the angular frequency of the waveform, N_p is the number of divisions of the moving element or the encoder resolution.

$\omega = \frac{n}{60}$, is the angular speed of the connected shaft in (rev/sec).

n, is the angular speed of the connected shaft in (rpm).

T_c , and $\varnothing_c$ are the period and initial phase of the waveform respectively.

The instantaneous phase of the signal is a linear function of time as shown in the equation below:

$$\begin{aligned} \varnothing_s(t) &= \omega N_p t + \varnothing_c \\ &= \omega_c t + \varnothing_c \end{aligned} \tag{3-4}$$

The angular speed ω has two parts: a fixed part ω_0 and another part $\delta\omega(t)$ which varies with time and can be represented as:

$$\omega = \omega_0 + \delta\omega(t) \tag{3-5}$$

Since, the varying part is a function of time that can be influenced by the dynamics of the mechanical system, the instantaneous phase of the signal can be calculated by replacing ω in equation (3-4) with its new form (3-5):

$$\varnothing_s(t) = (\omega_0 + \delta\omega(t))N_p t + \varnothing_c \tag{3-6}$$

So as to solve for the instantaneous phase at every time t the equation (3-6) in integral form becomes:

$$\varnothing_s(t) = \int_0^t [\omega_0 + \delta\omega(t)]N_p dt + \varnothing_c \tag{3-7}$$

Equation (3-7) can be rewritten as

$$\varnothing_s(t) = N_p\omega_0 t + N_p\int_0^t \delta\omega(t)\,dt + \varnothing_c \tag{3-8}$$

If $\varnothing(t) = N_p\int_0^t \delta\omega(t)\,dt + \varnothing_c$, and the initial phase term in equation (3-8) is ignored the encoder signal for a varying speed can be represented by:

$$\begin{aligned} s(t) &= A_{en}\cos\left[N_p\omega_0 t + N_p\int_0^t \delta\omega(t)\,dt + \varnothing_c\right] \\ &= A_{en}\cos\left[\omega_c t + \varnothing(t)\right] \end{aligned} \tag{3-9}$$

Hence, the signal contains an absolute phase which is proportional to the angular displacement of the shaft. It is a typical frequency-modulated (FM) signal with carrier frequency ω_c and phase deviation $\varnothing(t)$. The varying part of the angular speed $\delta\omega(t)$ is referred to as the modulating signal (D. Vakman, 2000; Gabor, 1947; Pineda-Sanchez et al., 2009). This is a signal format that is well known in vibration, communication and acoustics. The frequency modulated signal is further passed through a comparator circuit, which, transforms it into a square wave. The basic working principles of a comparator is to compare two voltages and outputs either a 1 or 0 to indicate which is bigger. This might introduce error to the signal but that is beyond the scope of this thesis. Therefore, the output of the encoder is a square wave frequency modulated signal which indicates

a peak for every angular displacement of the rotational shaft, depending on the resolution of the encoder. The distance between continuous peaks is $2\pi/N_p$ (Rad), for instances if a 40ppr encoder is used the square wave will have peaks every $\frac{360^\circ}{40} = 9^\circ$. The square wave frequency modulated signal is employed in fibre optics transmission technology. Hence, most of the theories developed in communication engineering can be used to analyse and estimate IAS. The spectrum of a FM signal has a countless number of sideband components, around the carrier frequency, theoretically. In communication engineering, experimental study has shown that, when 98% or more of the FM signal power is contained within the frequency band of interest, then the modulating signal distortion is negligible (Fengshou Gu et al., 2006). This evidence points to Carson's rule for calculating the bandwidth of a FM signal (Boashash, 1992) as shown in the equation below:

$$B_t = 2\left(f_x + \Delta f \right) \tag{3-10}$$

f_x, is the highest frequency of the changing part $\delta\omega$ of the FM signal.

$\Delta f = \frac{1}{\pi} N_p \max\left|\delta\omega\right|$, is the peak frequency deviation.

Since the bandwidth is symmetrically distributed around the carrier frequency f_c, the FM signal's highest frequency components can be calculated as:

$$f = f_c + \left(f_x + \Delta f \right) = N f_r + \left(f_x + \frac{1}{2\pi} N_p \, max\left| \delta\omega \right| \right) \tag{3-11}$$

, where $f_r = \omega/2\pi$, is the rotational frequency.

Hence, this shows that when using an ADC based IAS method, the determination of the sampling frequency is influenced by three factors: (a) the resolution of the used encoder in pulse per revolution (b) the bandwidth of the possible frequency content of the varying part $\delta\omega$ (c) the amplitude of the vary part.

3.3.3 IAS Signal Denoising

Noise is always present at different stages of the IAS measurement process, just like other measurement systems. The first of the noise present in IAS measurement process is the speed fluctuations from the mechanical rotors due to electric supply fluctuations and load uncertainties.

Second are the uncertainties and thermal noise in the measurement process due to the conversion from mechanical motion to an electrical signal, the digitization of the signal and the amplification of the output of the detector. It is difficult to accurately describe the influence of this mentioned noise on the FM signal, due to the complexity of these processes and their interaction. As such, so as to characterize the impacts of the noise, a conventional method developed in communication engineering is employed. In a similar approach used for the analysis of noise impacts in radio signal transmission, the random noise $n_o(t)$ present at the different stages of the IAS measurement is treated as an additional term to equation (3-9). The noise $n_o(t)$, which is assumed to be a zero-mean Gaussian noise, is filtered so that it has a narrow band around the carrier frequency ω_c. Since, the bandwidth of the noise $n_o(t)$, when compared to the carrier frequency ω_c is very low, the noise can be estimated via a spectral pair:

$$n_o(t) \approx n_c(t)\cos\omega_c t - \sin\omega_c t = R_n(t)\cos\left[\omega_c t + \theta_n(t)\right] \quad (3\text{-}12)$$

Through the use of a phasor diagram, the FM signal contaminated by noise is obtained as:

$$\begin{aligned} s_n(t) &= A_{en}\cos\left[\omega_c t + \varnothing(t)\right] + n(t) \\ &= A_{en}\cos\left[\omega_c t + \varnothing(t)\right] + R_n(t)\cos\left[\omega_c t + \theta_n(t)\right] \\ &= R_y(t)\cos\left[\omega_c t + \theta_y(t)\right] \end{aligned} \quad (3\text{-}13)$$

Where angle of the signal with added noise $\theta_y(t)$ is

$$\theta_y(t) = \varnothing(t) + \theta_e(t) \quad (3\text{-}14)$$

$\theta_e(t)$, is the disturbance of the carrier phase angle due to noise. Since, the amplitude of the IAS signal, when compared to that of the noise $R_n(t)$ is much higher, i.e., $A_{en}^2 \gg R_n^2(t)$ the disturbance of the carrier phase angle $\theta_e(t)$ can be estimated by

$$\theta_e(t) \approx \frac{R_n(t)}{A_{en}}\sin\left[\theta_n(t) - \varnothing(t)\right] \quad (3\text{-}15)$$

Thus, the angle used for IAS estimation is

$$\theta_y(t) = \varnothing(t) + \frac{R_n(t)}{A_{en}}\sin\left[\theta_n(t) - \varnothing(t)\right] \quad (3\text{-}16)$$

Assuming an ideal IAS estimation, i.e. an output estimation of $z(t) = {d\theta_y}/{dt}$, results from input of $y(t) = R_y(t)\cos\left[\omega_c t + \theta_y(t)\right]$, the influence of noise on the IAS signal can be characterized by a signal to noise ratio shown below (D. Vakman, 2000)

$$\left(\frac{S}{N}\right) = 3\left(\frac{\Delta f}{f_x}\right)^2 S_\omega \left(\frac{A_{en}{}^2/2}{S_n f_x}\right) \tag{3-17}$$

S_n, is the random noise power

S_ω, is the varying part of angular speed power

Evidently, from equation (3-17), the signal to noise ratio $\frac{S}{N}$ can be enhanced by an increase in the subsequent value of the term $\frac{\Delta f}{f_x}$ known as deviation ratio. Therefore, in order to enhance the signal-to-noise ratio of the FM signal for IAS measurement and diagnostics, an encoder with high resolution should be used if the ADC data acquisition is available. This will also enhance the efficiency of early fault detection and isolation using IAS based condition monitoring.

3.3.4 **IAS Estimation Techniques**

IAS can be estimated either offline or online from the encoder's output signal, depending on the purpose of the estimation. The offline estimation involves the post processing of the sampled encoder data with signal processing techniques. The online estimation involves the use of hardware or software in processing the signal outputs from encoders in real time. For real time condition monitoring and diagnostics using IAS, it is estimated online. However, for an experimental purpose like in this thesis, estimation is carried out offline from sampled encoder outputs using high-frequency data acquisition hardware. Since it has been shown in the previous section that measured encoder signal connected to a rotating shaft is a FM signal, obtaining IAS is thus the estimation of instantaneous frequency (IF) based on the FM signal. Over the years, several approaches have been developed so as to enhance the speed and accuracy of estimating IF. A comprehensive review of these approaches can be found in (Boashash, 1992; Girolami & Vakman, 2002). The signal process techniques utilized in the estimation of IF has been used for grouping

the techniques into the frequency domain, time domain, zero-crossing detection and time-frequency methods (Fengshou Gu et al., 2006). Vakman, has shown that the frequency domain method which uses analytic signals (AS) for IF estimation when compared with the use of conventional time-domain and zeroes-cross detection method, gives higher precision (2000). Gu et al., suggested that the heavy computation involved in the time-frequency domain method hinders the prospect of using this method for IAS estimation, specifically, for real-time diagnostics (2006). For IAS estimation using the ADC based method, the zero-crossing detection method can be grouped under the time domain methods, as the estimation is done in time domain. Hence, it can be said that the time and frequency domain methods have dominated the estimation of IAS for condition monitoring and diagnostics of reciprocating machines such as the diesel engine. The aim of both the time and frequency domain based estimation is to phase demodulate the encoder signals in order to extract the instantaneous deviation in true shaft position relative to the instantaneous mean speed shaft position. Although both methods have their separate merits and demerits, the time domain methods tends to be more versatile in terms of IAS estimation at steady and transient shaft rotation.

3.3.4.1 **Time Domain Based IAS Estimation**

The time domain based estimation principle is very similar to that of the elapsed time (ET) methods. In the ET method, IAS is estimated by measuring the elapsed time between successive pulses using a timer and an interrupt service routine. However, in the case of the direct ADC methods, the analogue signal from the encoder is converted into digital data. The time and amplitude of the signal are recorded at a fixed sampling rate. The unit angular displacement can be calculated using equation (3-2). The elapsed time for the corresponding unit angular displacement can be calculated by detecting the amplitude change of the signal. Suppose, $x(i)$ represents amplitude of the recorded signal, which was sampled at a frequency of Fs for t seconds, using an encoder of resolution of N_p.

$$x(i) = \left[x_i, x_{i+1}, x_{i+2}, x_{i+3} \ldots\ldots\ldots\ldots\ldots x_{if} \right] \tag{3-18}$$

, where $if = Fs * t$ is the total length of sampled data and i is the indices of the sampled data.

The differences in the data can be represented as:

$$dx = [(x_{i+1} - x_i), (x_{i+2} - x_{i+1}), (x_{i+3} - x_{i+2}) \ldots .. x_{if} - x_{if-1}] \tag{3-19}$$

The indices of dx which is greater than unity is part of the signal where there is a significant change in amplitude $ndx = dx > 1$. The difference in the indices ndx that is greater than unity provides a new vector $ndxx$. The indices of the angular displacement can be found by the finding the turning point of the signal. The elapsed time for corresponding angular displacement can be calculated by:

$$d_t = d_n / Fs \tag{3-20}$$

, where d_n are the indices for the angular displacement

The IAS is calculated by:

$$\omega_n(\text{rpm}) = \left(\frac{(2\text{pi}/\ N_p)}{d_n/Fs} \right) /30\text{pi} = \frac{60Fs}{N_p d_t} \tag{3-21}$$

This method is accurate and can be used to estimate IAS for both steady and transient engine operating conditions. However, there is the need for further filtering of the IAS to reduce the noise distortion present in the signal. The step-by-step implementation of this method is discussed briefly below:

a) Apply diff to the FM signal to find the difference between the signal
b) Extract the indices of the resulting signal in (a) that are greater than 1
c) Apply diff to the indices sequence in (b) above and extract the indices that are greater than 1 in the subsequent sequence
d) Extract the indices of the result in (c) above from the (b)
e) Apply diff to the resulting sequence from (d)
f) use equation (3-20) and (3-2) to calculate the elapsed time and unit angular displacement
g) using equation (3-21) IAS can be calculated
h) Using a high-pass FFT filter, the noise distortion can be removed.

3.3.4.2 **Frequency Domain Based IAS Estimation**

The frequency domain methods estimate IAS from the FM signal by implementing a fast Fourier transform (FFT) baseband analysis and is largely reliant on digital signal processing. These methods according to Sweeney and Randall include the frequency domain block-shift transforms, frequency domain zoom demodulation and Hilbert transforms (1996). However, the IAS estimation using the Hilbert transform allows for a more straightforward implementation of noise

suppression (Fengshou Gu et al., 2006). Thus this method is adopted in this thesis for frequency domain based IAS estimation. So as to obtain IAS from the FM signal in equation (3-9), firstly, an analytic representation of the signal is constructed. A filter which shifts each sinusoidal component by quarter cycle can be constructed in order to avoid complicated trigonometrical expressions that are expressible as a sum of many sinusoids. This filter is called a Hilbert transform (HT) filter (Feldman and Seibold, 1999). Analytic representation of a signal is the complex form representation of the signal, where the real part is the original signal, and the imaginary part is the Hilbert transform of the original signal as shown in the equation below

$$w(t)=s(t)+iH[s(t)] \tag{3-22}$$

, where $H[s(t)]$ which represents an HT of the original signal, is defined by

$$\begin{aligned} H\left[s(t)\right] &= \frac{1}{\pi}\int_{-\infty}^{\infty}\frac{s(\tau)}{\tau-t}d\tau \\ &= A_{en}\sin\left[\omega_c t+\varnothing(t)\right] \end{aligned} \tag{3-23}$$

So equation (3-22) can be rewritten as

$$\begin{aligned} w(t) &= A_{en}\cos\left[\omega_c t+\varnothing(t)\right]+iA_{en}\sin\left[\omega_c t+\varnothing(t)\right] \\ &= A_{en}\left\{\cos\left[\omega_c t+\varnothing(t)\right]+i\sin\left[\omega_c t+\varnothing(t)\right]\right\} \end{aligned} \tag{3-24}$$

Since, $e^{ix}=\cos(x)+i\sin(x)$ the equation (3-24) can be written in exponential form as shown below

$$\begin{aligned} w(t) &= A_{en}e^{i(\omega_c t+\varnothing(t))} \\ &= A_{en}(t)e^{i\varnothing_s(t)} \end{aligned} \tag{3-25}$$

Studies (Gu et al., 2006; Ben Sasi, et al., 2004) have shown that from this point of the equation, the IAS can be estimated by two methods. In the first method, the varying angle signal was obtained by elimination of the carrier frequency component in the first form of equation (3-25). This was achieved by multiplying the equation with complex signal $e^{-i\omega_c t}$ and dividing the subsequent result with the amplitude spectrum A_{en} as shown in the equation below.

$$\begin{aligned} w(t)e^{-i\omega_c t} &= A_{en}e^{i(\omega_c t+\varnothing(t))}e^{-i\omega_c t} \\ &= A_{en}e^{i\omega_c t-i\omega_c t+i\varnothing(t)} \\ &= A_{en}e^{i\varnothing(t)} \\ &= e^{i\varnothing(t)} \end{aligned} \tag{3-26}$$

From equation (3-26), the varying angle signal can then be estimated as

$$\varnothing(t) = \tan^{-1} \frac{Imag\left[e^{i\varnothing(t)}\right]}{Real\left[e^{i\varnothing(t)}\right]} \tag{3-27}$$

Then, the IAS is calculated by applying a time differentiation to $\emptyset(t)$.

From the equations (3-25 to 3-27), using this method for frequency based IAS estimation requires five basic steps (Ben Sasi et al., 2004). They are:

1) Band-pass filtering
2) Analytic representation of signal (Hilbert transform)
3) Carrier frequency elimination (frequency shifting)
4) Angle calculation
5) Time differentiation to angle varying signal

Through the use of an FFT based algorithm, the 5 steps above were achieved. The step-by-step procedure of the algorithm are summarized below as follows:

a) The raw encoder signal is uninformed, so as to remove the amplitude modulation or variation caused by encoder misalignment.
b) The encoder signal is transformed to frequency domain via the application of FFT
c) Based on the FFT result calculate the amplitude spectrum and locate the carrier frequency corresponding to the position of the maximum frequency
d) Filter and shift the carrier frequency from the FFT results. These are done in three subs-steps below:
    i) The signal analytic representation form of equation (3-22) is achieved by setting the FFT results in the negative frequency range to zeroes.
    ii) Perform a band-pass filtering around the carrier frequency, by keeping the FFT result around it and setting others in the positive frequency range to zeroes.
    iii) To obtain the angle variation signal in equation (3-26), the filtered FFT block on the right-hand side of the carrier frequency can be shifted to the beginning of the positive frequency range, while that on the left side it is shifted to the negative frequency range of the filtered window.

e) To obtain the complex angle variation in time domain, perform the inverse FFT of the shifted spectrum
f) By implementing equation (3-27) calculate the value of the angle.
g) To obtain the IAS signal differentiate the angle value in (f) above.

In the second method, the derivate $\dot{w}(t)$ is obtained through the application of basic differentiation rules (differentiation rules for product function and function of a function) on the analytic signal w(t) as shown in equation below.

$$\dot{w}(t) = \frac{dA_{en}(t)}{dt} e^{\mathrm{i}\varnothing_s(\mathrm{t})} + \frac{de^{\mathrm{i}\varnothing_s(\mathrm{t})}}{dt} A_{en}(t) \tag{3-28}$$

Applying the differentiation rule for function of function on $\frac{de^{\mathrm{i}\varnothing_s(\mathrm{t})}}{dt} A_{en}(t)$ in (3-28) would result to the following equation

$$\dot{w}(t) = \frac{dA_{en}(t)}{dt} e^{\mathrm{i}\varnothing_s(\mathrm{t})} + A_{en}(t) e^{\mathrm{i}\varnothing_s(\mathrm{t})} \frac{d\mathrm{i}\varnothing_s(\mathrm{t})}{dt} \tag{3-29}$$

If we then divide through by w(t)the resulting equation is

$$\frac{\dot{w}(t)}{\mathrm{w}(\mathrm{t})} = \frac{dA_{en}(t)}{dt} \frac{1}{A_{en}(t)} + \frac{d\mathrm{i}\varnothing_s(\mathrm{t})}{dt} \tag{3-30}$$

The equation (3-30) has a real and imaginary side; the imaginary side contains information regarding the IAS. Hence, IAS can be calculated by

$$IAS = imag\left[\frac{\dot{w}(t)}{\mathrm{w}(\mathrm{t})}\right] \tag{3-31}$$

The main emphasis of this frequency domain method is the implementation of the band-pass filtering in frequency domain. In this method, the convolution due to filtering in the time domain is replaced with multiplication in the frequency domain. This not only reduces computational effort but also allows for the filter types and bandwidth to be adjusted automatically based on the characteristics of analytic signal (D. Vakman, 2000; Vakman, 1994) giving room for optimal noise suppression. Vakman, showed that a Gaussian window is optimal for linear chirp signals (2000). Gu et al., demonstrated that the use of a rectangle window for the band-pass filtering, for this frequency domain method, can significantly reduce noise distortion (2006). Thus the use of a

rectangle window whose width is adjusted based on the spectral width of interest is adopted in this thesis. This method has a high efficiency in implementation, as both the differentiation of the analytic signal and the Hilbert transform can be done in the frequency domain. Step-by-step implementation is discussed briefly below

a) The Fourier transform (FT) sequence in frequency domain is obtained by applying FFT to the FM signal
b) The analytic signal (AS) in frequency domain is obtained by setting to zero the FT sequence in the negative frequency range
c) To perform the band-pass filtering, determine the width of the rectangular window based on the frequency bandwidth of interest and multiply the AS sequence by the rectangular window around the carrier frequency of interest.
d) To obtain the $w(t)$ apply inverse FFT (IFFT) to the band-pass filtered AS sequence
e) To obtain the differentiation signal $\dot{w}(t)$ multiply the band-pass filtered signal in (d) above by a frequency sequence and apply IFFT to the subsequent sequence.
f) Use equation (3-31) to calculate the IAS from the filtered signal.

This frequency method is more numerically stable compared to the other frequency method, hence is adopted in this thesis for the frequency domain based IAS estimation.

3.4 IAS Measurement Performance Parameters and Analysis

Generally IAS measurement methods based on the use ADC, can be characterized by three parameters: minimum measurable speed, maximum measurable speed and measurement error. These parameters are discussed are discussed as follows:

3.4.1 Minimum Measurable Speed

The sampling clock frequency and the buffer size of the data acquisition (DAQ) measurement hardware are used when considering this parameter. A DAQ measurement hardware with a longer buffer size is able to measure a lower speed vice versa depending on the type of DAQ. Because, the pulse duration becomes excessively long, as the angular speed of the shaft approaches zero. This is termed the frequency spectrum resolution. The number of clock units in one pulse must not exceed the maximum number that the DAQ measurement hardware can hold in its register. For

example, the minimum measurable speed for a DAQ measurement hardware with a buffer of 16-bit registers and can operate at 1MHz sampling frequency, is 15.25Hz. In order to measure angular speed smaller than this, a lower clock frequency or larger buffer size must be used, if the angular speed is to be measured accurately.

3.4.2 Maximum Measurable Speed

This parameter is determined by the number of encoder pulses per revolution (resolution) and the sampling rate of the DAQ measurement hardware. In theory, the sampling rate divided by the encoder resolution is the upper bound of the maximum measurable speed. Hence, the maximum measurable speed for the DAQ measurement hardware above using an encoder with 360 PPR is 1389Hz. This result is in-line with the Nyquist criteria where there is a requirement of a minimum two sampling points.

3.4.3 Measurement Error

Generally, angular speed measurement error may be classified into two, based on the sources of the error. Error may occur as a result of the limits of the extraction method or manufacturing imperfections (Li, et al., 2005). Errors that occur due to manufacturing imperfections includes error due to shaft eccentricity, error due to encoder mounting misalignment and error due to the stochastic variation of actual encoder locations as different from the nominal locations (Li, et al., 2005). Studies (Spagnol & Bregant, 2015) to minimize the error from design imperfection have been extensively investigated. Ben Sasi, showed the measurement errors that may result from the inherent features of the measurement principles of time domain based and the first frequency domain based methods (2005). The following section addresses the measurement errors that may result from the inherent features of the measurement principles of the time domain based and second frequency domain based methods.

3.5 Key Findings

In this chapter, an overview of the technologies used for IAS signal measurement has been presented. The IAS generation using general ADC based methods has been modelled as an analogue signal. The features of the general ADC based methods and their respective impact on

estimated IAS has been presented. The IAS model based fault diagnosis method is able to reconstruct the pressure torque which result mainly from the cylinder pressure. The IAS model based diagnosis depends on the development of an analytic model of the engine-load system. Engine fault diagnosis, which utilizes frequencies that are below the engine's firing frequency, are mainly sensitive to modelling assumptions related to the clutch and driveline components. Until today the torsional modal properties used for the development of the analytic model is determined offline. The effect of torsional modal properties on the performance of IAS model based diagnostics has been less studied. Therefore, there is the need for an online torsional modal properties identification of a typical engine-load system for an IAS based fault diagnosis enhancement.

The theoretical basis for one time domain and two frequency domain based IAS estimation algorithms were also presented. While the time domain based IAS estimation technique is expected to be suitable for engine transient and steady operations, the frequency domain based techniques are only suitable for steady engine operation. The frequency domain based IAS estimation using the Hilbert transform allows for a more straightforward implementation of noise suppression. In the Hilbert transform frequency domain based IAS estimation technique the varying angle signal can be obtained either by elimination of the carrier frequency component or the application of basic differentiation rules. The frequency domain based IAS estimation algorithm which obtains the varying angle signal by applying basic differentiation rules is more numerically stable compared to that which uses elimination.

CHAPTER FOUR

4 EXPERIMENTAL FACILITIES AND INSTRUMENTATION

In this chapter the test rig and instrumentation used for IAS based diagnostics are discussed. Firstly the specifications and characteristic of the test engine are discussed briefly. Secondly the test system which includes the encoder and cylinder pressure sensors used for both IAS diagnostics and modal identification are presented. This also includes the description of Sinocera data acquisition hardware and software used for acquiring the encoder and cylinder pressure signals at high speeds. Lastly the engine operating conditions and fault simulation strategy are presented.

4.1 Experimental Engine-Dynamometer System

Experimental test-rig facilities are an important way in which known faults can be seeded and other experimental analysis can be implemented for machinery condition monitoring. This gives room for faults to be investigated and measured in an environment that is safe and instrumented. Also, the accuracy of the data collection and post processing processes are vital in the investigation of condition monitoring techniques such as IAS, because as shown in chapter three, the time domain based IAS estimation method is very sensitive to noisy encoder signal. For this research, the JCB 444 diesel engine test bed, which is available within the automotive laboratory at University of Huddersfield was used. The test-rig was positioned and designed so as to enable easy modification of parts in the engine system such as injection and valve system, to induce common faults found in diesel engines. Hence, this rig will allow faults to be seeded and properly measured, so that the post processing techniques described in the previous chapter can be used to evaluate their condition monitoring applicability. This test rig, as shown in figure 4-1 below, contains a JCB diesel engine connected to an eddy current dynamometer through a flexible coupling. The dynamometer which is rated to handle a maximum power and torque of 210kw and 501Nm, is used to exert a braking force, or load. The entire test bed is placed in a test cell which has an exhaust extraction and ventilation system to maintain room temperature. The rig is equipped with a control panel outside the test cell, which is used to monitor engine temperature, start/stop the engine, and adjust engine operating conditions such as steady speed and variable load and fuel supply. For health and safety, the main fuel supply of the engine is located outside the building in a very secure compartment. Because of the nature of this research the description of the rig is grouped under the following headings: diesel engine and coupling, instrumentation and data acquisition hardware and software. The description and dynamics of the dynamometer and control panel are beyond this research, as such are not discussed holistically.

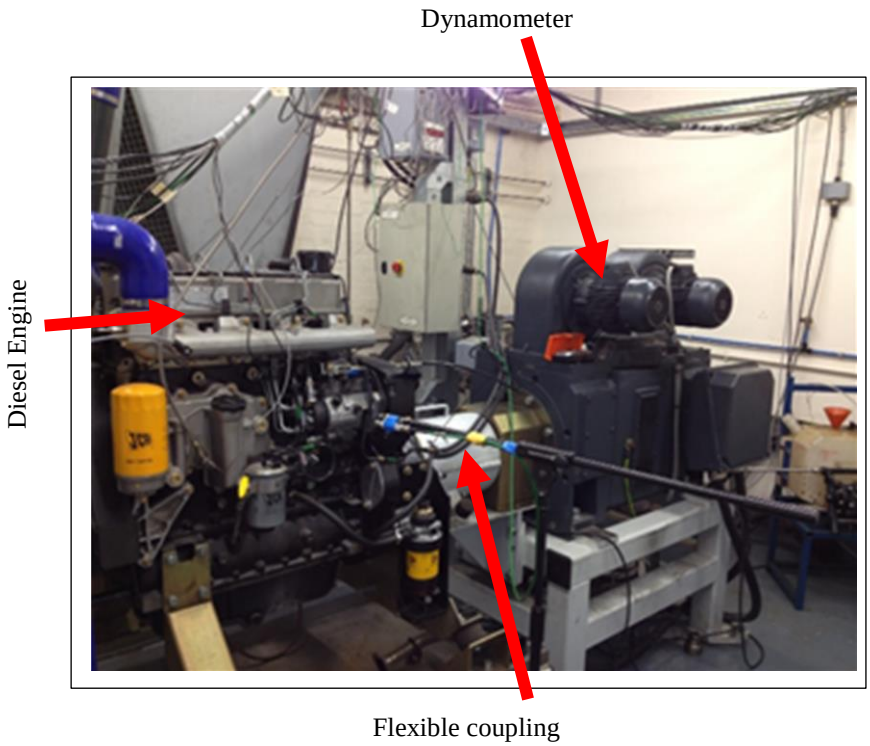

Figure 4-1 diesel engine test rig

4.1.1 **Test Engine**

The type of the JCB 444 diesel engine used in the test bed is the JCB TCA-74 which is a turbocharged and intercooled 4.4 litre engine with serial number U1060311 is shown in figure 4-2 below. This is engine is usually fitted to variety of construction and agricultural machines.

Figure 4-2 JCB TCA-74 engine

The basic engine specification as provided by the manufactures manual is presented in Table 4-1 below.

Table 4-1 basic JCB-TCA-74engine data

Type of engine	Turbocharged and intercooled diesel engine
Number of cylinders	4
Cylinder arrangement	Inline
Combustion cycle	4 stroke
Firing order	1-3-4-2
Compression ratio	17.2:1
Valve per cylinder	4
Nominal bore size	103mm
Stroke	132mm
Valve tip clearance (measured cold)	Inlet 0.35mm
	Exhaust 0.56 to 0.64mm
Combustion system	Direct injection
Fuel injection pump	Rotary mechanical
Maximum power	74.2 kW @ 2200rpm
Rated speed	2200rpm
Dry weight	477kg
Compression variance between cylinder	Not greater than 3.5bar

In chapter two, an overview of the basic diesel engine cycle was presented. It is important to note that due to reasons such as valve and cylinder profiles, type of injection system used and the presence or absence of turbo, engine cycles vary from engine to engine. For the purpose of this research, the various variations that affect Diesel engine cycles are not covered. However, pertinent features of the JCB 444 diesel engine and its expected cycle will be covered. The JCB diesel engine as shown in Table 4-1 above has 4 cylinders, therefore, there will be four combustion cycle over a complete engine cycle of 2 revolutions(720°). This means, there will be one combustion event per cylinder, which will be 180° phased from each other. Table 4-2 below shows the expected engine cycle for the JCB-TCA-74 diesel engine under healthy conditions.

Table 4-2 JCB-TCA-74 engine cycle

Cyl.	IPO $6^{\circ} btdc$	TDC1	EPC $9^{\circ} atdc$	IPC $28^{\circ} abdc$	BDC1	Fuel Inj.	TDC2	EPO $41^{\circ} bbdc$	BDC2
Cyl.1	714°	0°	9°	208°	180°	355°	360°	499°	540°
Cyl.3	174°	180°	189°	388°	360°	535°	540°	679°	720°
Cyl.4	354°	360°	369°	568°	540°	715°	720°	139°	180°
Cyl.2	534°	540°	549°	28°	720°	175°	180°	319°	360°

The valve opening and closing and the fuel injection crank angles for the engine's healthy working conditions were adopted from the manufacturer's manual. This might be slightly different from the reality on the ground, due to the variability discussed above. However, it will be compared with the experimentally estimated values from the engine, so that any deviation from it can be used for fault detection and diagnosis. In order to get the optimal engine operating conditions suitable for the test conditions, the net power, net torque and fuel consumption curve of the engine were adopted from the engine's manufacturer's manual. These curves are shown in Figure 4-3, 4-4 and 4-5 below.

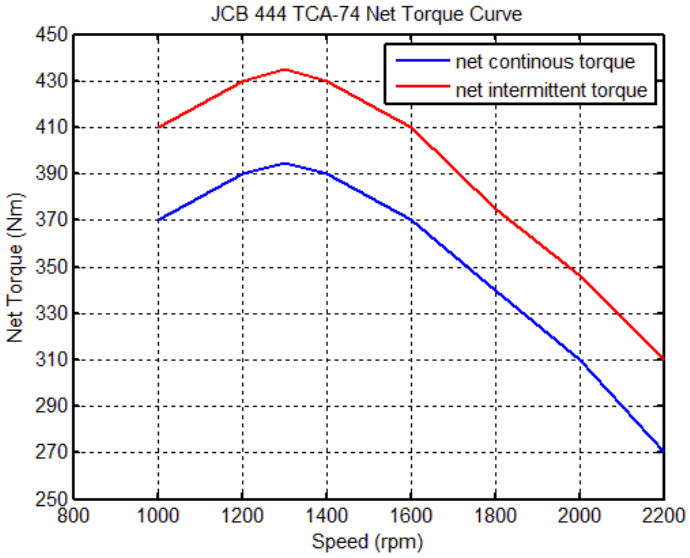

Figure 4-3 research engine's net torque curve

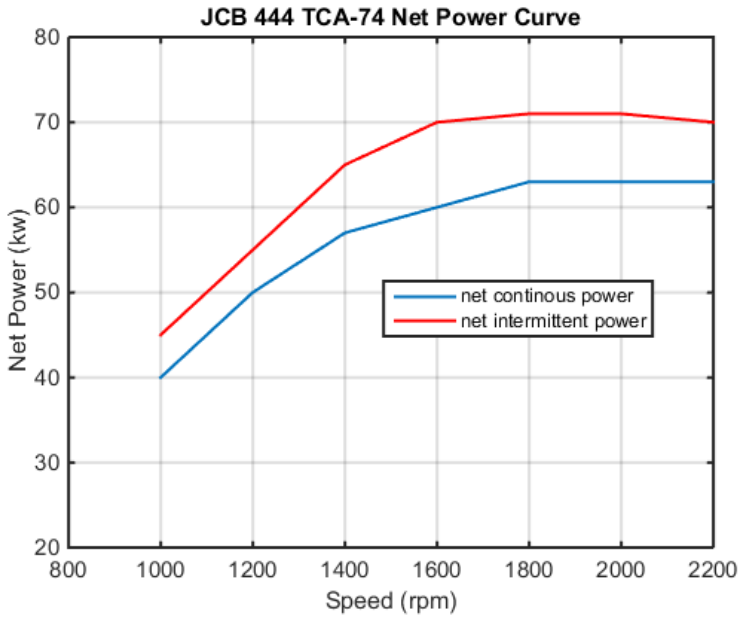

Figure 4-4 research engine's net power curve

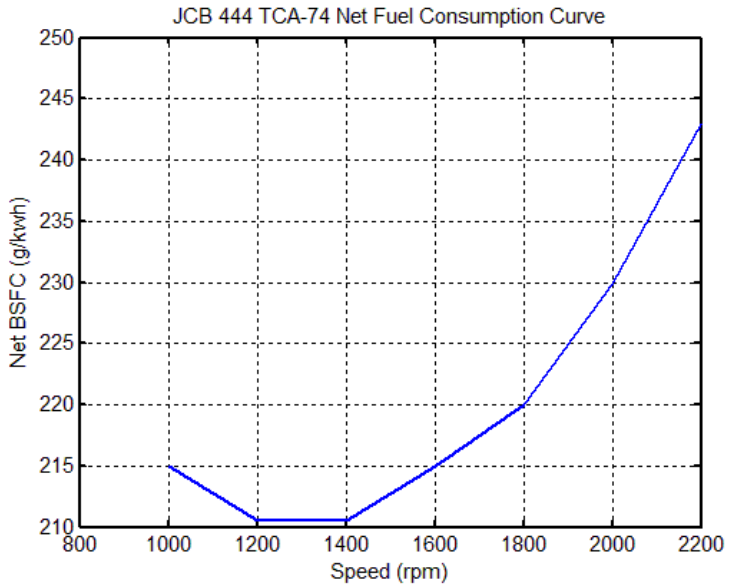

Figure 4-5 research engine's net fuel consumption curve

Assuming intermittent engine operation is to be avoided during the test, from the curve shown above its obvious that the optima operating conditions of the engine is within the speed range of1000-1600 rpm and torque range of 0-310 Nm. This is because the engine can attain the expected net continuous torque at a low fuel consumption rate.

4.1.2 **Flexible Coupling**

The connection of the engine to the dynamometer for engine testing requires the selection of suitable couplings and shaft. The use of incorrect coupling and shaft can result in damage to engine or dynamometer bearings, dangerous level of torsional oscillations and catastrophic failure of the coupling shaft during the test. Hence, the coupling and shaft play a vital role in the design of the experimental test rig, when considering the modal properties of the engine-dynamometer system. The flexible coupling used in the test bed is shown in the figure 4-6 below.

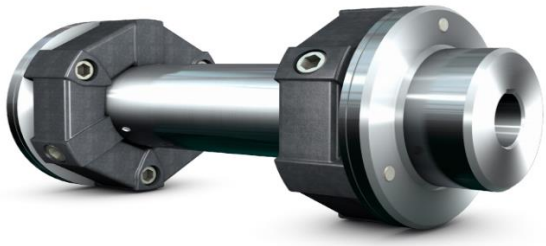

Figure 4-6 centreflex flexible coupling

The coupling is usually designed with a suitable stiffness to ensure that its critical frequency lies outside the operating range of the engine and a suitable degree of damping to ensure that the unit may run through the critical speeds without the development of a dangerous level of torsional vibration. Table 4-3 below shows the centreflex coupling characteristics.

Table 4-3 characteristics of flexible coupling used for JCB engine test rig

Nominal Torque	500Nm
Maximum Torque	1400Nm
Maximum continuous vibratory torque	200Nm
Shore hardness	50 shore
Dynamic torsional stiffness of each coupling	4800Nm

4.2 **Instrumentation**

Experimental work carried out within a laboratory, has a major advantage of full instrumentation of the engine test rig when compared to experimental work carried out in the field. The

instrumentation of the engine test rig not only give room for the measurement of the researcher's interested output but also allows the researcher to measure the effect of the induced fault on the operating conditions of the engine. This section will cover the instrumentation used on the JCB test engine, providing a brief overview of the technology as well as justifying the reason behind the use of these sensors.

4.2.1 Cylinder Pressure Sensor

The first cylinder head of the test engine has been modified and a Kistler pressure sensor model number 6125A has been installed. This sensor was chosen as it meets all the necessary criterion for the conditions which it will be subjected to. The installation of the pressure sensor is purely for experimental works. It will allow the identification of defects from valve and injector problems on combustion parameters such as peak cylinder pressure. It will also ensure accurate alignment of the IAS data with the chosen reference TDC of the cylinder. The output from the installed cylinder pressure will also assist the operator in the safe running of the engine when faults are induced. The pressure sensor produces outputs in voltage, based on the deflection of its diaphragm surface by pressure acting on it. The output in voltage can be equated to the values of the pressure acting on the surface of the sensor. Figure 4-7 summarises the specification of this sensor.

Parameter	Value
Pressure range	0 – 25 MPa
Sensitivity	-15.8 pC/bar
Linear error	± 0.2 FSO
Temperature range	-50° up to 350 C°

Figure 4-7 Kistler type 6125 pressure sensor and specification.

In order to amplify the weak signal output from the pressure signal described above, it was connected to a B&K Charge Amplifier Type 2635 shown in figure 4-8 below. This type of amplifier is useful both in the field and in the laboratory because it can be powered from internal batteries or external direct current power supplies.

Figure 4-8 Face of B&K charge amplifier type 2635 (left), back (right).

4.2.2 **Encoders**

The engine test rig is equipped with three encoders one at the front end of the engine, another one at the flywheel of the engine and the last one is at the dynamometer end of the test rig. Three encoders where placed on the test rig because of the nature of the research objectives. The encoders installed all have different resolutions. The encoder at the front end was designed and constructed in the laboratory, while the others were bought. This section describes briefly the characteristic of these three encoders.

4.2.2.1 **Heidenhain Encoder**

The Heidenhain encoder which measures connected shaft angular position by optical scanning of periodic structure known as graduations is installed at the dynamometer end of the test rig. The installed Heidenhain encoder is shown in figure 4-9 below.

Figure 4-9 Heidenhain ROD 436 1024 27S12-03

This encoder works using the image scanning principle of photoelectric scanning and is contact-free. Specification of the Heidenhain ROD 436 1024 27S12-03 is shown in table below

Table 4-4 Specification of the Heidenhain encoder

Encoder type	Incremental
Output signal	10v to 30v High Threshold Logic(HTL) Quadrature
Resolution	1024 PPR
Power supply	10v-30v
Scanning frequency	Max. 300 kHz

4.2.2.2 **Magnetic Pick-up Sensor (MPUs)**

The second type of encoder used to measure the angular position of the crankshaft is a magnetic pick up sensor. The MPUs mainly contains a coil and permanent magnetic probe. The coil is wound around the permanently magnetized probe. The flux density of the probe's magnetic field is modulated when discrete ferromagnetic objects passes through it. This results into the induction of AC voltages in the coil. For each ferromagnetic material that passes a sinusoidal signal is generated. In engines with gear teeth on the flywheel, this sensor is usually fitted in close proximity to the gear teeth. This is because the output waveform is a function of the air gap between pickup and the gear teeth surface. The number of gear teeth on the flywheel then becomes the resolution

of the encoder. For instance for the JCB engine there are 126 gear teeth on the flywheel. This means there will be 126 pulses for one complete revolution of the crankshaft. The number of gear teeth detected per seconds is dependent on the speed of the engine. The Omron cylindrical proximity sensor E2EG-X1R5C1-M1 shown in the Figure 4-10 below was installed on the flywheel of the engine. It was fixed on the engine through the use of a bolt adapter. The sensor was screwed into the adaptor which is fixed to the engine and close to the surface of the gear teeth on the flywheel by about 2mm as required by the sensor.

Figure 4-10 Omron proximity sensor E2EG-X1R5C1 -M1

4.2.2.3 **Optical Switch and Wheel**

The last type of encoder used in the JCB test rig as shown in figure 4-11 was designed and constructed applying the basic principle of optical encoders as discussed in the previous chapter. The encoder was developed for better mounting unto the engine test rig. In previous chapter the encoder was modelled as a sensor having two parts: a fixed and variable part. The fixed part is usually the sensing part, while the moving part is the number of pulses to generate in one complete revolution of the connected shaft. For instance, in the case of the MPU described above the gear teeth on the flywheel is the moving part, while the MPU is the fixed part. For the encoder at the front end of the test rig a deep gap slotted optical switch was used as the fixed part of the encoding system, while a plastic circular plate with rectangular slits of about 0.5mm width designed using the 3D printing machines was used as the moving part. 180 rectangular slits of breadth 0.5mm was circumferentially drilled on a plate of 150mm diameter.

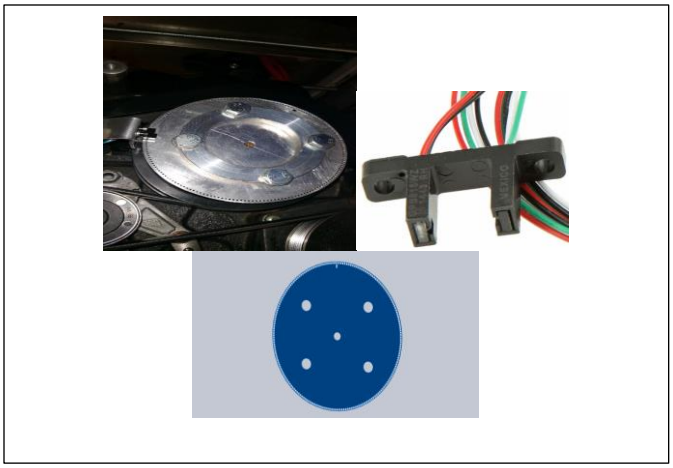

Figure 4-11 optical switch sensor, encoder wheel

4.2.3 **Data Acquisition Hardware and Software**

The Sinocera YE6233 data acquisition hardware, which connects to a PC or laptop directly via usb was used for the data collection. See figure 4-12 for the Sinocera hardware. This hardware allows the channel to measure simultaneously at a sampling rate of 750 kHz per channel. It has in-built pre-amplification which allows the user to increase the gain by 10 and 100 times, which is equivalent to 20dB and 40dB respectively.

Figure 4-12 Sinocera YE 6233 DAQ hardware

The hardware unit also has a built in signal to noise indicator so the user can identify when the system is setup optimally. Table 4-13 below shows the specification of the DAQ hardware.

Table 4-5 performance specifications of Sinocera YE6233 DAQ

Channels	4
Input voltage range	5V to +5V peak
Input Impedance	≥10MΩ
ADC Resolution	16bit Delta-Sigma ADC, Digital Anti-aliasing filter）

Max sampling rate	3MHz with one channel 1.5MHz with two channels 750kHz with four channels
Sampling length	Indefinite (free space available on the hard disk used)
IEPE Supply Gain settings	4mA /24VDC 1; 10; 100mV /mV
High-pass filters IEPE Lower-pass filters	0.3Hz 300Hz

The Sinocera YE7600 Software is a Sinocera general purpose software which supports all DAQ hardware from the company. It is the interface used to interact with the Sinocera unit, allowing the user to change the sampling rate, sampling time, data format, signal sources and also allows the user to condition the signals. The display of the software is shown in Figure 4-13 below.

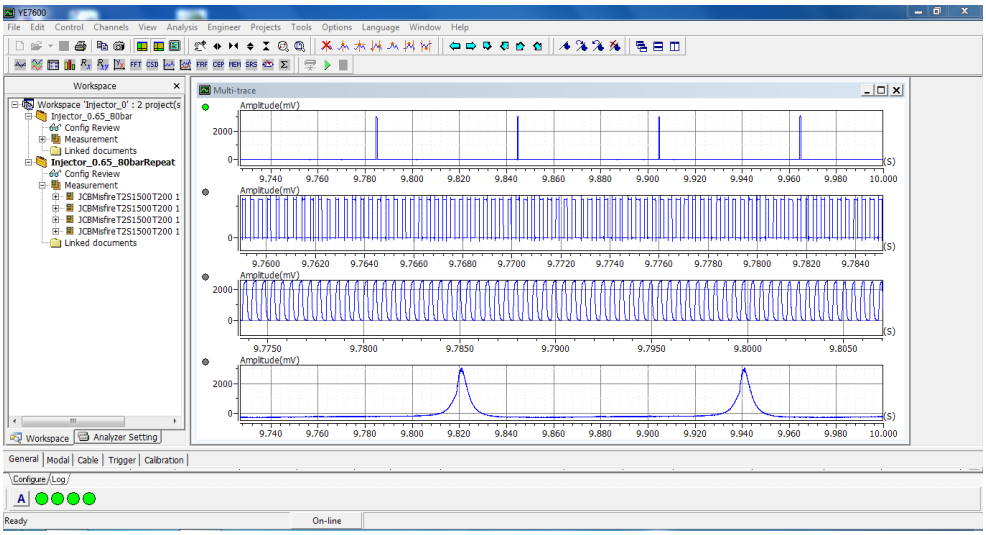

Figure 4-13 Sinocera YE 6233 DAQ software display

4.3 Test Procedures and Fault Simulation

Based on the net power, net torque and fuel consumption curve presented in figure 4-3, 4-4 and 4-5 the test was carried out at three engine speeds (1000rpm, 1300rpm and 1600rpm). Data was collected from the test rig while the engine was operating at steady and transient operating

conditions. For the steady operating conditions, the engine was running at different loads (0Nm 105Nm 210Nm and 315Nm) for each speed given above. Data was collected for transient engine start-up and shutdown operation. The Two classes of faults induced on the engine component are:

1) Injection system related faults such as injector disconnection (complete misfire) or injection pressure reduction
2) Air related faults such valve clearance alteration or turbo charger leakage

4.3.1 Engine Test Procedure

For health and safety purposes, some routine checks are usually carried out before starting the engine. Some of these safety check include: opening the ventilation system of the test cell (the fresh air in and the exhaust air out), manually opening the fuel and water coolant valves, engine oil level check, checking and removing any moisture present in the air filters. This is then followed by switching on the main power supply, control panel and the chiller system. With all the checks done and all valves and power supply switch on, the engine is started from the software. See Figure 4-14 below for the monitor display of the JCB test rig control software. This software gives room for easy change of engine operating conditions such variable speed and load.

Figure 4-14 JCB test rig operation software display

For the steady state test, the engine was run through various operating conditions. These conditions can be seen in the table 4-6 below. For every run, the temperature of the engine was checked periodically to ensure it does not exceed 90 degree Celsius.

Table 4-6 operating conditions for JCB engine

Speed (rpm)	Load (Nm)
1000	0, 105, 210, 315
1300	0, 105, 210, 315
1600	0, 105, 210, 315

The four channels of the Sinocera YE6233 DAQ unit was used and all channels were sampling at 750 kHz. Data was collected during these operating conditions for healthy and faulty cases. However during the complete misfire test the operating conditions were changed to the ones shown in table 4-7 below. The misfire test conditions were changed for safety/test rig health reasons.

Table 4-7 operating conditions for JCB engine with complete misfire test

Speed (rpm)	Load (Nm)
1200	0, 105, 210
1600	0, 105, 210,

1800	0, 105, 210,

The transient test was carried out by collecting data during a start-up, idle speed run and shut down engine operation. The aim of this test was to allow the engine to sweep through a frequency range, so as to be able to determine the modal properties of engine-dynamometer system specifically those patterning to the low frequency vibration mode. This was done through the event trigger feature which is available in the Sinocera software. The one pulse per revolution encoder signal was used as the event to trigger data collection. The schematic representation of the JCB experimental test rig is shown in the Figure 4-15 below.

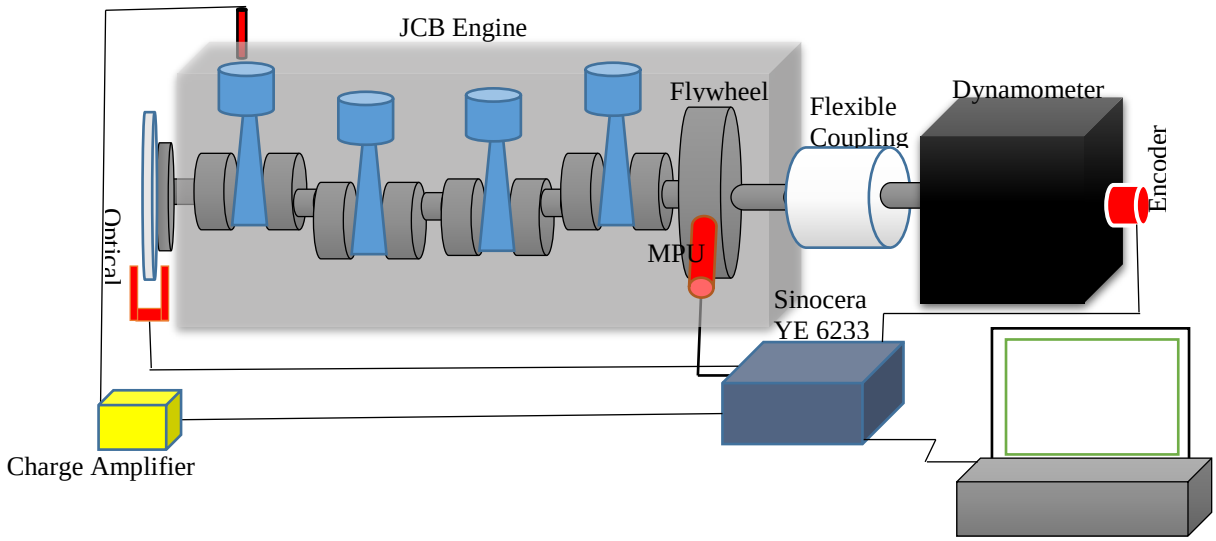

Figure 4-15 schematic diagram of the test rig and measurement system

4.3.2 **Injection System Fault Simulation**

The fuel injection system as described in chapter 2 of this thesis is vital in the dynamics of diesel engines. The injector is one component of the injection system which causes many failures in engines. Hence, engine condition monitoring studies are concentrated on faults related to it. Every cylinder of the JCB engine is fitted with an injector. The components of the injector used for the fault seeding are shown in figure 4-16 below.

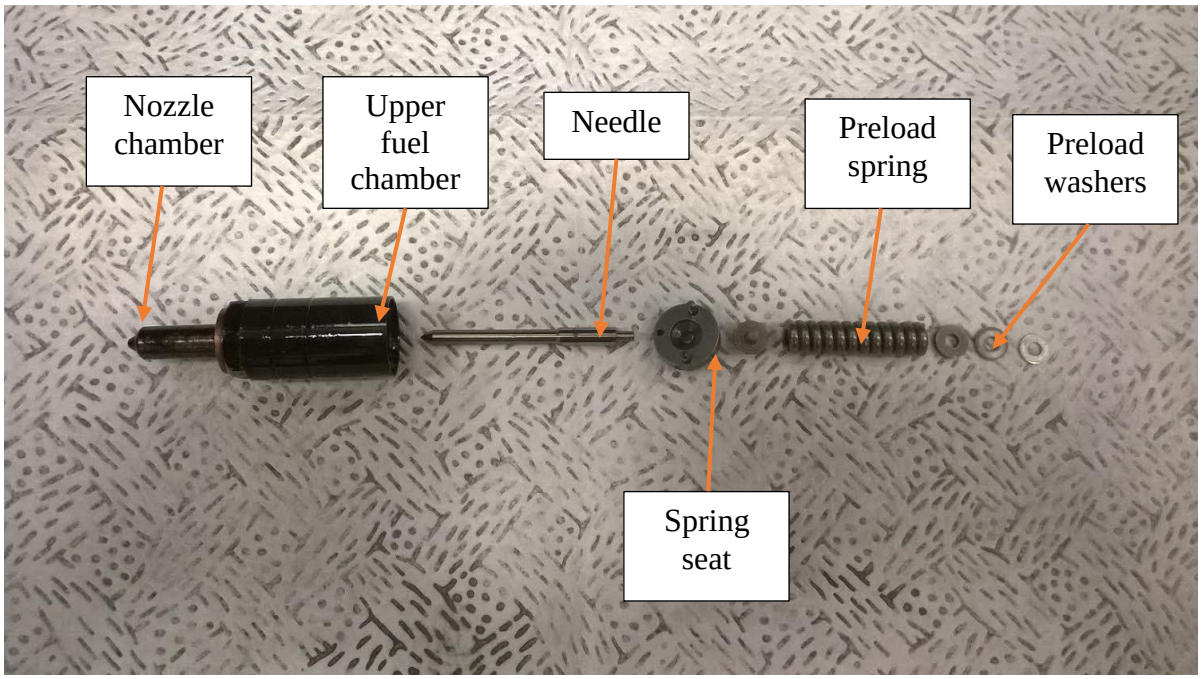

Figure 4-16 component of the JCB diesel engine injector

The opening pressure of the injector (when the lifting force exerted by the fuel in the upper chamber exceeds the force which holds the needle in contacts with its seat) is one important factor that affects the condition of the injection process. The force which holds the needle in contact with its seat depends on the spring stiffness and pre-load washer thickness. Any change in the thickness of the pre-load washer should alter the injection timing and thus affect the peak cylinder pressure. This will have impact in the combustion process and thereby degrading engine performance. In this work the pre-load washer thickness was altered as shown in the Table 4-8 below so as to induce fault in the injection system. See appendix A for the opening pressure of the injector with different alteration in the pre-load washer thickness.

Table 4-8 Injector preload washer alterations

Preload washer	Actual preload washer thickness of injector in Cyl. 1 (mm)	Adjusted value (mm)	Change (%)
Fault severity 1	1.85	0.65	-66
Fault severity 2	1.85	1.30	-33
Fault severity 3	1.85	1.74	-10
Fault severity 4	1.85	2.59	+33

The second fault induced in the injection system was complete misfire in cylinder one three and four. This was achieved by disconnecting the injector from the fuel line. Allowing only air to be compressed in the cylinder with no combustion. The fuel line from the high pressure pump was channelled to another tank through the use of an air tight hose.

4.3.3 **Abnormal Valve Clearance Simulation**

The valve train system is one part of the engine that controls the intake and exhaust of air and used gases from the cylinder. One important part of the valve train is the valve clearance which has been described in chapter two of this thesis. This part of the valve train system can make the engine noisy or lose performance, when it falls out of the manufacturer specified range. Most times the valve clearance of an engine slightly wears out due to usage. Hence, in this work, valve clearance of the first cylinder of the JCB engine was manually adjusted in order to induce faults in the air circulation system of the engine. To do this, the cylinder head of the engine was removed as shown in Figure 4-17 below.

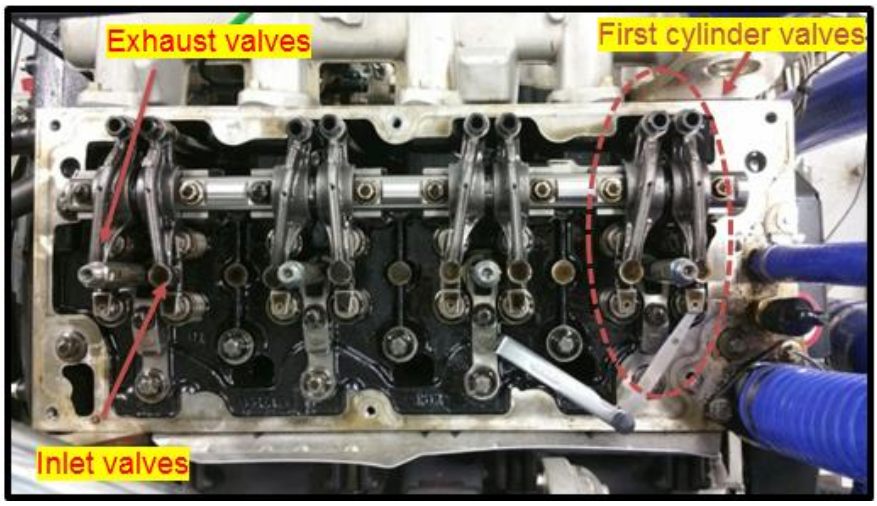

Figure 4-17 inlet and exhaust valves of JCB engine

Then the valve clearance was adjusted by turning a set-screw, which is located at the end of the rocker arm. Turning the screw clockwise moves the rocker arm towards the cam (less clearance), turning the screw counter clockwise moves the rocker arm away from the cam (more clearance). Table 4-8 below shows the original and adjusted valve clearance value of the JCB engine. A 5% abnormal valve clearance was also simulated but this had no effect on the measured IAS. Hence, it was not included in this work.

Table 4-9 abnormal valve clearance alterations

Exhaust Valve	Actual valve clearance of Cyl. (1) (mm)	Adjusted value (mm)	Change (%)
Fault severity 1	0.64	0.84	30
Fault severity 2	0.64	1.00	65

4.4 **Key Findings**

This chapter presented the experimental facilities, instrumentation and simulated faults used in this thesis. The suitable speed and loading range for the experimental engine operation was chosen based on the engine's performance curve. The JCB diesel engine used for the test has optimal engine operation between 1200-1400rpm. It is expected that any fault on the valve train and fuel injection systems would be evident when the engine is operating in any speed within this range. The specifications and operating principles of sensors to measure the single cylinder pressure and

the shaft angular displacement have been presented. It is expected that the three angular displacement measurement sensors placed at front-end, flywheel-end and dyno-end of the system are sufficient for an angular speed based online modal properties identification. The specification of the data acquisitions hardware and software used for the experimental evaluation were also presented. The procedure of inducing the abnormal valve conditions, injector preload washer thickness alteration and complete misfire faults were also discussed.

CHAPTER FIVE

5 MODELS OF ENGINE DRIVELINE TORSIONAL VIBRATION

This chapter presents a finite element and state space models of the test rig engine-dynamometer structures as a three degree of freedom system with the engine, flywheel and dynamometer as individual inertias. It presents the theoretical basis for calculating the total engine torque using relevant engine geometry.

5.1 Introduction

The primary goal of modelling a system such as the engine-dynamometer system is to describe its characteristics for a particular purpose. Hence, a model should in a reliable and sufficient way represents the true characteristics of a system. In an engine-dynamometer system like our test rig and other engine structures, the main source of excitation forces in the engine and inevitably the power train, arises from the crankshaft vibrations. The crankshaft vibration which is due to the oscillatory engine torque, occurs in three-dimension space. Thus, the crankshaft vibration can be grouped into three types: axial, bending and torsional and they all occur at a different frequency range. In this work, the focus is mainly on the torsional vibration of the crankshaft. The motivation is to explore the accuracy of using IAS measurement to deduce cylinder by cylinder combustion information for the purpose of engine diagnostics. Hence, this chapter focuses on explaining and developing a mathematical model which is capable of reproducing the torsional behaviour of an engine-dynamometer system. Due to the nature of this thesis, which majors mainly on the torsional vibration of engine-dynamometer system for IAS based diagnostics, consideration is placed mainly on the rotational dynamics of the engine through the modelling of the crankshaft. The effect of other parts such as the engine mounts are not considered, as, it is assumed to be negligible. This is a norm in most literature modelling the torsional vibration engine for diagnostics purpose (Charles et al., 2009). In this chapter, two methods of modelling vibrating structure are presented. Finite element and state space model were developed, to explaining the torsional vibration behaviour of the system. The state space model was used because its model structure is more suitable for the system identification method described in chapter seven and also useful for the pressure torque reconstruction.

5.2 Engine Geometry

The diesel engine like other rotary machinery has a unique feature which is the peculiar motion of the connecting rod linking the piston pin with the crankpin on the crankshaft. Considering the kinematics of the motion of the mechanism the piston executes a pure translational motion while the crank pin moves in a completely circular path. This is achieved by one end of the connecting rod traveling along a linear path while the other end a circular path, then other parts travels along an elliptical path, hereby making the connecting rod to undergo a swinging type of motion

(Rangwala, 2005). Assuming the crankshaft is rotating at a uniform speed the first objective of most researchers modelling the engine geometry of internal combustion engine is to calculate the piston position in terms of the crank angle. This piston position can be determined by the direct calculation of the downward displacement from the top of the piston. The crank mechanism of one cylinder and its free body diagram is shown in the Figure 5-1 below.

In the figure 5-1 below:

x_p, is the downward displacement of piston

θ, is the crank angle from TDC

r, is the crank radius

l, length of connecting rod

Assuming the crankshaft rotates at a uniform speed the distance moved by the piston x_p is equal to the length DB on the triangle OAC plus a term which is due to the fact that the connecting rod has assumed a slanting position as given by the angle, β. Working by trigonometric functions and identities:

$$DB = r\{1-\cos\theta\} \tag{5-1}$$

The term which is the correction factor is given by AC-BC which by trigonometric functions and identities

$$AC - BC = l\{1-\cos\beta\} \tag{5-2}$$

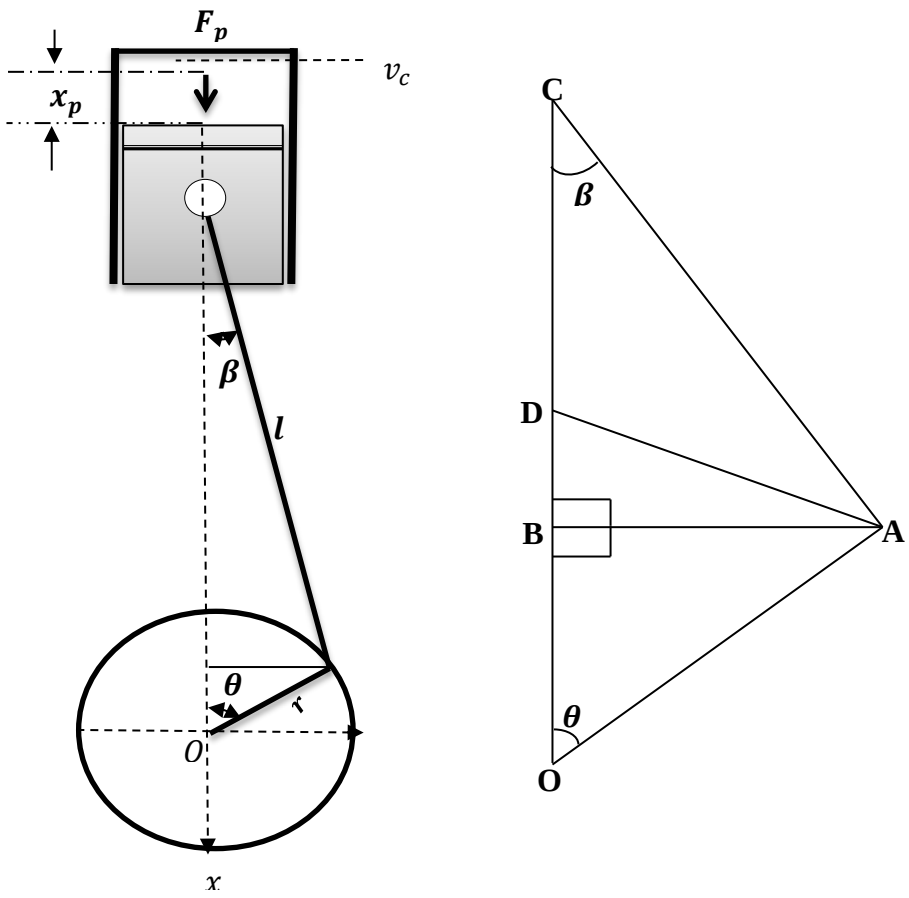

Figure 5-1 crank mechanism and free body diagram

Hence in mathematical form $x_p = DB + (AC - BC)$. Because the basic concept is to express the piston displacement x_p with respect to the crank angle, using sine rule on OAC $\sin\beta = \frac{r}{l}\sin\theta$. Using the trigonometric identity $\sin^2\beta + cos^2\beta = 1$ $\cos\beta = \sqrt{1 - sin^2\beta}$. The piston displacement can be obtained by:

$$x_p = r\{1 - \cos\theta\} + l\left\{1 - \sqrt{1 - \frac{r^2}{l^2}sin^2\theta}\right\} \qquad (5\text{-}3)$$

This expression is not convenient for further calculation due to the square root. It can be simplified further, noting that for most reciprocating machines the ratio r/l is of the order of $1/4$, hence $(r/l)^2$ is $1/16$ as such the second term under the square root sign in equation (5-3) is small when

compared to unity. Expanding into power series and retaining only the first term equation (5-3) becomes:

$$x_p = r\{1-\cos\theta\} + \frac{r^2}{2l}sin^2\theta \tag{5-4}$$

Further simplification can be achieved by using the trigonometric identities

$sin^2\theta = cos^2\theta - \cos 2\theta$ and $\cos 2\theta = 2cos^2\theta - 1$

Piston displacement at any crank angle then becomes

$$x_p(\theta) = \left\{r + \frac{r^2}{4l}\right\} - r\left\{\cos\theta + \frac{r^2}{4l}\cos 2\theta\right\} \tag{5-5}$$

The velocity and acceleration of the piston follow from the differentiation of the displacement with respect to time

$$v_p = \frac{dx_p}{dt} = \frac{dx_p}{d\theta}\frac{d\theta}{dt} \tag{5-6}$$

$$\omega = \frac{d\theta}{dt} \tag{5-7}$$

$$\frac{dx_p}{d\theta} = r\left[\sin\theta + (r/2l)\cos\theta\right] \tag{5-8}$$

$$v_p(\theta) = r\omega\left[\sin\theta + (r/2l)\cos\theta\right] \tag{5-9}$$

$$a_p(\theta) = \frac{dv_p}{dt} = r\omega^2\left[\cos\theta + (r/l)\cos 2\theta\right] \tag{5-10}$$

ω , is the angular speed of the engine.

5.3 Engine Driveline Model

The fluctuating nature of the delivered engine torque is the major cause of the torsional vibration of its crankshaft system. Through the use of torsional elastic elements the engine crankshaft system can be modelled (Fang, et al., 2013; Kiencke & Nielsen, 2005). Although the real system is distributed, simple models consist of linear lumped spring mass-damper systems. Depending on the modelling purpose, the linear lumped spring mass-damper systems can be extended by adding details about the dynamics of various parts (Mendes, et al., 2008; Nickmehr, 2015). The crankshaft

system when in operation must overcome periodic loads, vibration and stresses hence, is faced with the common problem of non-uniform cylinder-wise torque (Honda et al., 1989; J.C. Wachel & Fred R. Szenasi, 1993). In other to reduce this problem there have been recent calculation methods which are able to determine the stress level at the crankshaft critical regions, as well as to estimate the fatigue forces. The result showed that torsional overstress is the major cause of high level of stress in critical region of the crankshaft. See appendix F for the model of the 6 degree of freedom engine-dyno system.

5.3.1 Numerical Model

The dynamic characteristics of a discrete mechanical system like the engine-driveline system, containing p inertias connected through torsional springs and dampers using Finite Element (FE) approximation is described by the following matrix differential equation:

$$[\mathrm{J}]\{\ddot{\theta}(t)\}+[C_t]\{\dot{\theta}(t)\}+[K]\theta(t)=T(t) \qquad (5\text{-}11)$$

, where $J, C_t, K \in \mathbb{R}^{p\times p}$ are the inertia damping and stiffness matrices; $\theta(t) \in \mathbb{R}^p$ is the angular displacement vector at continuous time t; $\dot{\theta}(t)$ is the angular speed vector and $\ddot{\theta}(t) \in \mathbb{R}^p$ is the angular acceleration vector. The vector $T(t) \in \mathbb{R}^p$ is the excitation toque acting on each inertia disc.

Although, the FE model (equation 5-11) is a good representation of the torsional vibration of a typical engine-driveline structure, the main interest of this work cannot be obtained by the FE model. However, it is used as a starting point to derive the other model that is more suited in the context of experimental modelling. This is because the model is in continuous time while the measurement taken in real life experiments are mostly sampled at discrete time.

5.3.2 Model Size Reduction

For real time applications used for diagnostic, the implementation of the engine-driveline model presented above is computationally complex. Because, there is the need for a simple representative torsional vibration model, which when inputted into a complete mechanical/control system can be used to define the dynamics of the system. One way of simplifying the model structure is to reduce

the number of degrees of freedom according to the frequency range of interest (Schagerberg & McKelvey, 2003). The number of degrees of freedom of the new model structure will include those where forces are applied and where responses are needed. Studies have shown that the simplified model structure still show desired performance for specific application such as fuel identification and misfire detection (Schagerberg and McKelvey, 2003; Mocanu, 2012; Nickmehr, 2015). For engine-driveline systems, the degrees of freedom can be reduced by lumping together the entire crankshaft connected with cylinders. So, the Multi-Input Single-Output (MISO) system starting from gas pressure to net torque can now be seen as a system with Single-Input Single-Output (SISO) dynamics (Eriksson & Andersson, 2002). This offers considerable simplification, particularly when deducing information of the combustion process from IAS measurements for diagnostics and other reasons such as fuel identification. There are two approaches to achieving this: single rigid body approach and condensed cylinder approach. In most literatures (Rizzoni, 1986; Iida, et al., 1990; Shiao and Moskwa, 1995 Kiencke and Nielsen, 2000); the single rigid body approach is usually used as a starting point and the dynamic equation is derived with the assumption that the crankshaft is infinitely stiff. This approach is unable to model crankshaft deformations. The condensed cylinder approach has shown great prospects especially in the implementation of IAS engine based diagnostics, as such is adopted in this work. Due to the source of encoder output from the experimental test rig used and the frequency range of interest, the seven degree of freedom torsional vibration model structure is simplified into a three degree of freedom model structure. The inertia of the pulley in front of the engine can be assumed to be negligible as such is condensed with the cylinders while the flywheel and dynamometer are separate inertias, as shown in Figure 5-2 below.

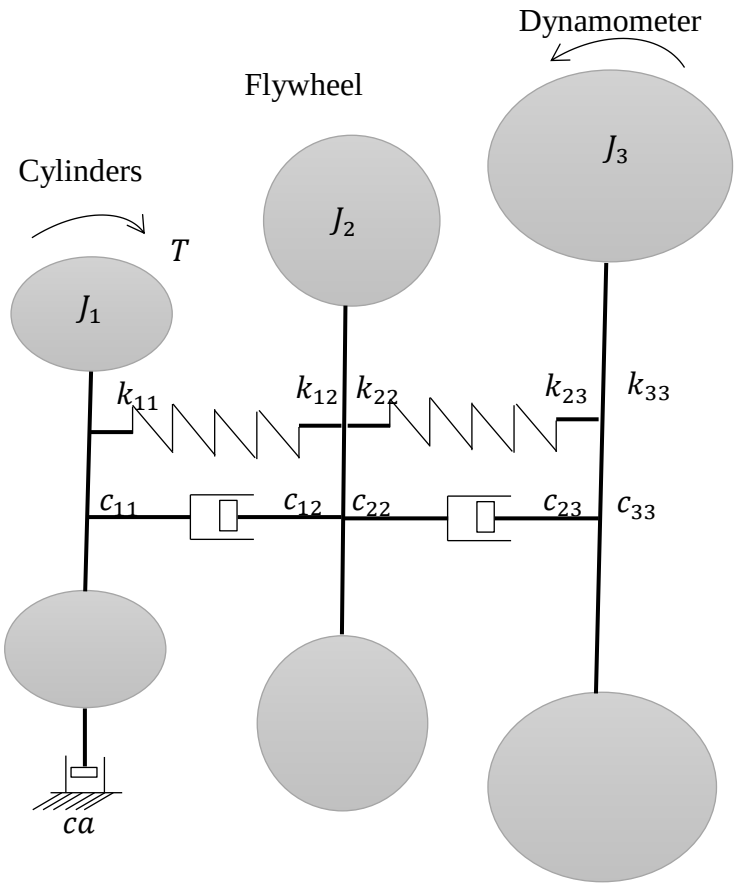

Figure 5-2 simplified model structure of engine-dynamometer system

In order to factorize the differential equation (5-24), the matrices J, C, K are respectively given as

$$\mathrm{J}=\begin{bmatrix} J_1 & 0 & 0 \\ 0 & J_2 & 0 \\ 0 & 0 & J_3 \end{bmatrix}, C=\begin{bmatrix} c_{11} & c_{12} & c_{13} \\ c_{21} & c_{22} & c_{23} \\ c_{31} & c_{32} & c_{33} \end{bmatrix} K=\begin{bmatrix} k_{11} & k_{12} & k_{13} \\ k_{21} & k_{22} & k_{23} \\ k_{31} & k_{32} & k_{33} \end{bmatrix}$$

The using the FE rule damping and stiffness matrices C and K is further simplified as

$$C=\begin{bmatrix} c_1 & -c_1 & 0 \\ -c_1 & c_2+c_1 & -c_2 \\ 0 & -c_2 & c_2 \end{bmatrix} K=\begin{bmatrix} k_1 & -k_1 & 0 \\ -k_1 & k_2+k_1 & -k_2 \\ 0 & -k_2 & k_2 \end{bmatrix}$$

Equation (5-11) then becomes:

$$\begin{bmatrix} J_1 & 0 & 0 \\ 0 & J_2 & 0 \\ 0 & 0 & J_3 \end{bmatrix}\begin{bmatrix} \ddot{\theta}_1 \\ \ddot{\theta}_2 \\ \ddot{\theta}_3 \end{bmatrix}+\begin{bmatrix} c_1 & -c_1 & 0 \\ -c_1 & c_2+c_1 & -c_2 \\ 0 & -c_2 & c_2 \end{bmatrix}\begin{bmatrix} \dot{\theta}_1 \\ \dot{\theta}_2 \\ \dot{\theta}_3 \end{bmatrix}+ \begin{bmatrix} k_1 & -k_1 & 0 \\ -k_1 & k_2+k_1 & -k_2 \\ 0 & -k_2 & k_2 \end{bmatrix}\begin{bmatrix} \theta_1 \\ \theta_2 \\ \theta_3 \end{bmatrix}=\begin{bmatrix} T_1 \\ T_2 \\ T_3 \end{bmatrix} \quad (5\text{-}12)$$

$\ddot{\theta}_1, \ddot{\theta}_2$ and $\ddot{\theta}_3$ represent the angular acceleration of individual inertias

$\dot{\theta}_1$, $\dot{\theta}_2$ and $\dot{\theta}_3$ represent the angular speed of individual inertias

θ_1, θ_2 and θ_3 represent the angular displacement of individual inertias

Connecting the torques T_1(the torque acting on the cylinders), T_2(the torque acting on the flywheel) and T_3(the torque acting on the dynamometer), on each inertia produces the three equation of motion that follow:

$$J_1\ddot{\theta}_1+c_1\left(\dot{\theta}_1-\dot{\theta}_2\right)+k_1\left(\theta_1-\theta_2\right)=T_1 \quad (5\text{-}13)$$

$$J_2\ddot{\theta}_2+c_1\left(\dot{\theta}_2-\dot{\theta}_1\right)+c_2\left(\dot{\theta}_2-\dot{\theta}_3\right)+k_1\left(\theta_2-\theta_1\right)+k_2\left(\theta_2-\theta_3\right)=T_2 \quad (5\text{-}14)$$

$$J_3\ddot{\theta}_3+c_2\left(\dot{\theta}_3-\dot{\theta}_2\right)+k_2\left(\theta_3-\theta_2\right)=T_3 \quad (5\text{-}15)$$

Equation (5-25) is the matrix form of the second order differential equations (5-13, 5-14 and 5-15) and can be used to solve for the angular speed, depending on the method being used for the solution.

The equation (5-12) can be re-written as

$$\begin{bmatrix} J_1 & 0 & 0 \\ 0 & J_2 & 0 \\ 0 & 0 & J_3 \end{bmatrix}\begin{bmatrix} \ddot{\theta}_1 \\ \ddot{\theta}_2 \\ \ddot{\theta}_3 \end{bmatrix}=\begin{bmatrix} T_1 \\ T_2 \\ T_3 \end{bmatrix}-\left\{\begin{bmatrix} c_1 & -c_1 & 0 \\ -c_1 & c_2+c_1 & -c_2 \\ 0 & -c_2 & c_2 \end{bmatrix}\begin{bmatrix} \dot{\theta}_1 \\ \dot{\theta}_2 \\ \dot{\theta}_3 \end{bmatrix}+\begin{bmatrix} k_1 & -k_1 & 0 \\ -k_1 & k_2+k_1 & k_2 \\ 0 & -k_2 & k_2 \end{bmatrix}\begin{bmatrix} \theta_1 \\ \theta_2 \\ \theta_3 \end{bmatrix}\right\} \quad (5\text{-}16)$$

For ease of computation the matrices J, C, K are substituted into the equation, so it becomes

$$J\begin{bmatrix}\ddot{\theta}_1\\ \ddot{\theta}_2\\ \ddot{\theta}_3\end{bmatrix}=\begin{bmatrix}\mathrm{T}_1\\ \mathrm{T}_2\\ \mathrm{T}_3\end{bmatrix}-\left(C\begin{bmatrix}\dot{\theta}_1\\ \dot{\theta}_2\\ \dot{\theta}_3\end{bmatrix}+K\begin{bmatrix}\theta_1\\ \theta_2\\ \theta_3\end{bmatrix}\right) \tag{5-17}$$

Solving for the angular acceleration of each inertia which is a second order derivative of the angular displacement, the equation (5-17) becomes:

$$\begin{bmatrix}\ddot{\theta}_1\\ \ddot{\theta}_2\\ \ddot{\theta}_3\end{bmatrix}=J^{-1}\left\{\begin{bmatrix}\mathrm{T}_1\\ \mathrm{T}_2\\ \mathrm{T}_3\end{bmatrix}\left(C\begin{bmatrix}\dot{\theta}_1\\ \dot{\theta}_2\\ \dot{\theta}_3\end{bmatrix}+K\begin{bmatrix}\theta_1\\ \theta_2\\ \theta_3\end{bmatrix}\right)\right\} \tag{5-18}$$

So as to reduce the order of the differential equation, the first order derivative of the angular displacement $\dot{\theta}_1$, $\dot{\theta}_2$ and $\dot{\theta}_3$ is represented by y_1, y_2 and $y_3$in equation (5-18)

$$\begin{bmatrix}\dot{y}_1\\ \dot{y}_2\\ \dot{y}_3\end{bmatrix}=J^{-1}\left\{\begin{bmatrix}\mathrm{T}_1\\ \mathrm{T}_2\\ \mathrm{T}_3\end{bmatrix}\left(C\begin{bmatrix}y_1\\ y_2\\ y_3\end{bmatrix}+K\begin{bmatrix}\theta_1\\ \theta_2\\ \theta_3\end{bmatrix}\right)\right\} \tag{5-19}$$

Applying the same steps to the equations (5-13, 5-14 and 5-15) and assuming initial conditions of the angular displacement θ_1, θ_2 and θ_3 and that of angular speed $\dot{\theta}_1$, $\dot{\theta}_2$ and $\dot{\theta}_3$ are known, the equations becomes a simplified differential equation which can be solved using any implicit numerical integration method.

$$y_1=\left\{T_1-\left(c_1\left(\dot{\theta}_1-\dot{\theta}_2\right)+k_1\left(\theta_1-\theta_2\right)\right)\right\}/J_1 \tag{5-20}$$

$$y_2=\left\{T_2-\begin{pmatrix}c_1\left(\dot{\theta}_2-\dot{\theta}_1\right)+c_2\left(\dot{\theta}_2-\dot{\theta}_3\right)+k_1\left(\theta_2-\theta_1\right)\\ +k_2\left(\theta_2-\theta_3\right)\end{pmatrix}\right\}/J_2 \tag{5-21}$$

$$y_3=\left\{\mathrm{T}_3-\left(c_2\left(\dot{\theta}_3-\dot{\theta}_2\right)+k_2\left(\theta_3-\theta_2\right)\right)\right\}/J_3 \tag{5-22}$$

5.3.3 Damped Eigenvalues and Eigenvectors

In every vibrating system there is the presence of damping and its functionality is the dissipation of energy. The presence of the damping term in a mechanical system, is partly based on physical observation and partly on mathematical convenience. For a given mechanical system like the engine-dynamometer system, an accurate mathematical model describing the damping force is complicated (Mendes & Zampieri, 2008; Schagerberg & McKelvey, 2003). The assumption of a proportional or viscous damping models are usually adopted, depending on the nature of the

system. For torsional vibration model of engine-dynamometer, the general viscous damping model is usually adopted (Nickmehr, 2015). So as to find the eigenvalues and eigenvectors of the engine-dynamometer system with viscous damping the first order equation (5-19) is reformulated by defining:

$$x(t)=\begin{pmatrix}\theta(t)\\ \dot{\theta}(t)\end{pmatrix}, P=\begin{pmatrix}C & J\\ J & 0\end{pmatrix} and\ Q=\begin{pmatrix}K & 0\\ 0 & -J\end{pmatrix} \tag{5-23}$$

The first order equation derived from equation (5-19) can be represented in the form:

$$P\dot{x}(t)+Qx(t)=\begin{pmatrix}B\\ 0\end{pmatrix}u(t \tag{5-24}$$

, where P and Q are auxiliary matrices for the derivation of the state-space model from the FE model, $x(t)$ is the state vector, B is a matrix that specifies the location of the input or input influence matrix and u is vector describing the input in time. The associated eigenvalue problem is:

$$P\Psi\Lambda_c+Q\Psi=0 \tag{5-25}$$

, where Ψ comprises the complex eigenvectors as columns and Λ_c contains the eigenvalues λ_i [rad/s] and is a diagonal matrix. The structure of Ψ and Λ_c can be represented as

$$\Lambda_c=\begin{pmatrix}\Lambda & 0\\ 0 & \Lambda\end{pmatrix}\Psi=\begin{pmatrix}\Theta & \Theta^*\\ \Theta\Lambda & \Theta^*\Lambda^*\end{pmatrix} \tag{5-26}$$

, Λ and Θ are the eigenvalues and eigenvectors of the original second order system. It can be shown that equation (5-25) satisfy the relation:

$$J\Theta\Lambda^2+C\Theta\Lambda+\mathrm{K}\Theta \tag{5-27}$$

The complex eigenvalues λ_i can be written as:

$$\lambda_i\lambda_i^*=-\xi_i\omega_i\mp j\sqrt{1-\xi_i^2}\,\omega_i \tag{5-28}$$

It can be confirmed that the orthogonality conditions below holds:

$$\Psi^T P\Psi=\begin{bmatrix}\ddots & & \\ & a_i & \\ & & \ddots\end{bmatrix}\Psi^T Q\Psi=\begin{bmatrix}\ddots & & \\ & b_i & \\ & & \ddots\end{bmatrix} \tag{5-29}$$

, where $\begin{bmatrix} \ddots & & \\ & a_i & \\ & & \ddots \end{bmatrix}$ and $\begin{bmatrix} \ddots & & \\ & b_i & \\ & & \ddots \end{bmatrix}$ are called the modal a matrix and modal b matrix

respectively. Introducing equation (5-29) into equation (5-25) yields

$$\Lambda_c = \begin{bmatrix} \ddots & & \\ & \lambda_i & \\ & & \ddots \end{bmatrix} = -\begin{bmatrix} \ddots & & \\ & 1/a_i & \\ & & \ddots \end{bmatrix} \tag{5-30}$$

5.3.4 **Continuous-Time State-Space Models**

An equation similar to the state equation from control theory is obtained, when the second order equation of motion (5-24) is casted into first order form (5-19 and 5-25). This equation generally has a standardized term in $\dot{x}(t)$, which is obtained by pre-multiplying (5-25) by $P^{-1} = \begin{pmatrix} 0 & J^{-1} \\ J^{-1} & -J^{-1}CJ^{-1} \end{pmatrix}$

$$\dot{x}(t) = A_c x(t) + B_c u(t) \tag{5-31}$$

, where $A_c = -P^{-1}Q = \begin{pmatrix} 0 & I \\ -J^{-1}K & -J^{-1}C \end{pmatrix}$ an $B_c = P^{-1}\begin{pmatrix} B \\ 0 \end{pmatrix} = \begin{pmatrix} 0 \\ J^{-1}B \end{pmatrix}$.

The sub-index ‘c’ indicates continuous time A_c, is the continuous time state matrix.

Using equation (5-29) and (5-30), which is the modal decomposition of $P$and Q their orthogonally property, $A_c$can be reformulated as:

$$A_c = -P^{-1}Q = -\Psi \begin{bmatrix} \ddots & & \\ & \dfrac{1}{a_i} & \\ & & \ddots \end{bmatrix} \Psi^T \Psi^{-T} \begin{bmatrix} \ddots & & \\ & b_i & \\ & & \ddots \end{bmatrix} \Psi^{-1} = \Psi \Lambda_c \Psi^{-1} \tag{5-32}$$

$A_c\Psi = \Psi\Lambda_c$, is a typical eigenvalue problem. This indicates that Λ_c contains the eigenvalues while Ψ contains eigenvector of A_c. Not all DOFs of vibrating structures are measured in a real practical torsional vibration experiments. For example in the case of the engine dynamometer system only three DOFs are measured. The observation equation for the vibrating structure is:

$$y(t) = C_a\ddot{\theta}(t) + C_v\dot{\theta}(t) + C_d\theta(t) \tag{5-33}$$

, where $y(t)$ is the outputs C_a C_v and C_d are the output location matrices for angular acceleration, speed and displacement respectively. The equation (5-33) can be transformed into:

$$y(t) = C_c x(t) + D_c u(t) \tag{5-34}$$

, where C_c and D_c are the output matrix and the direct transmission matrix. The direct transmission matrix only requires a term when accelerometers are used, in this work it is assumed to be zero since encoders are used. By combining equation (5-34) and (5-31) the classical continuous state space model is found:

$$\begin{aligned} \dot{x}(t) &= A_c x(t) + B_c u(t) \\ y(t) &= C_c x(t) + D_c u(t) \end{aligned} \tag{5-35}$$

The dimension of the state vector defines the order of the state space model. The equation (5-19) can be represented by equation (5-36), which is the state space form of the equation of motion for the engine-dynamometer model structure and can be used to calculate the response $y(t)$ of the engine-dynamometer system to a given input $u(t)$.

$$\begin{bmatrix} y_1 \\ y_2 \\ y_3 \\ \dot{y}_1 \\ \dot{y}_2 \\ \dot{y}_3 \end{bmatrix} = \begin{bmatrix} 0 \\ J^{-1}T \end{bmatrix} + \begin{bmatrix} 0 & I \\ -J^{-1}K & -J^{-1}C \end{bmatrix} \begin{bmatrix} \theta_1 \\ \theta_2 \\ \theta_3 \\ y_1 \\ y_2 \\ y_3 \end{bmatrix} \tag{5-36}$$

The state vector $x(t)$ comprises of the angular displacement and velocity of all the DOFs. The new state vector is defined as

$$x(t) = Tz(t) \tag{5-37}$$

, T is a non-singular complex square matrix, the process is called similarity transformation. Equation (5-35) can be reformulated by substituting this coordinate transformation of (5-38) into it:

$$\begin{aligned} \dot{z}(t) &= T^{-1}A_cTz(t) + T^{-1}B_cu(t) \\ y(t) &= C_cTz(t) + D_cu(t) \end{aligned} \tag{5-38}$$

It is vital to observe that the transformed matrices $\left(T^{-1}A_cT\ T^{-1}C_cT\ D_c\right)$ shows the same input-output relationship as the original ones. Unlike the state vector

5.3.4.1 **Modal Parameters**

In order to transform the state vector to modal (complex) states a special similarity transformation $x_m(t)$ is applied $x(t) = \Psi x_m(t)$. By substituting T with Ψ in equation (5-38) and inputting the modal decomposition of A_c the modal state space model is obtained as:

$$\begin{aligned} x_m(t) &= \Lambda_c x_m(t) + L_c{}^T u(t) \\ y(t) &= V_c x_m(t) + D_c u(t) \end{aligned} \tag{5-39}$$

, where $L_c{}^T = \Psi^{-1}B_c$ and $V_c = C_c\Psi$.

As defined earlier on the eigenvalue matrix is $\Lambda_c = \begin{pmatrix} \Lambda & 0 \\ 0 & \Lambda \end{pmatrix}\Lambda = \begin{bmatrix} \ddots & & \\ & \lambda_i\lambda_i^* = -\xi_i\omega_i \mp j\sqrt{1-\xi_i^2}\omega_i & \\ & & \ddots \end{bmatrix}$ and the eigenvector matrix is $\Psi = \begin{pmatrix} \Theta & \Theta^* \\ \Theta\Lambda & \Theta^*\Lambda^* \end{pmatrix}$. By taking a closer look at the modal input and output matrices $L_c{}^T$ and V_c the relations to concepts from classical modal analysis are clear. The introduction of the orthogonality condition for P (5-43) and the definitions of P, B_c and Ψ are the modal input matrix can be written as:

$$L_c^T = \Psi^{-1}$$
$$B_c = \begin{bmatrix} \ddots & & \\ & \frac{1}{a_i} & \\ & & \ddots \end{bmatrix} \Psi^T P B_c \begin{bmatrix} \ddots & & \\ & 1/a_i & \\ & & \ddots \end{bmatrix} \Psi^T \begin{pmatrix} B_2 \\ 0 \end{pmatrix} = \quad (5\text{-}40)$$
$$\begin{bmatrix} \ddots & & \\ & 1/a_i & \\ & & \ddots \end{bmatrix} \begin{pmatrix} \Theta^T \\ \Theta^H \end{pmatrix} B_2$$

, where the matrix B_2 chooses the element of the mode shapes corresponding to an input location. Naturally, the last expression of equation (5-40) is called the modal participation matrix, while its rows are the modal participation factors. The super index 'H' indicates complex conjugate transpose.

In the same manner, the output modal output matrix can be re-written by introducing the definition of C_c and Ψ:

$$V_c = C_c \Psi = \begin{pmatrix} C_d - C_a J^{-1} K & C_v - C_a J^{-1} C \end{pmatrix} \begin{pmatrix} \Theta & \Theta^* \\ \Theta\Lambda & \Theta^* \Lambda^* \end{pmatrix} \quad (5\text{-}41)$$

By considering one quantity at a time, the expression in (5-41) can be simplified. Since the main focus of this work is on angular speed the modal output matrix becomes:

$$V_c = C_v \begin{pmatrix} \Theta\Lambda & \Theta^* \Lambda^* \end{pmatrix} \quad (5\text{-}42)$$

By definition the matrix of the measured angular speed selects the components of the mode shapes corresponding to an output location. Being a diagonal matrix, the post multiplication by Λ or Λ^*, scales the mode shapes by their eigenvalues. So, V_c shows the part of the mode shapes that can be observed from measured data.

Therefore, the modal parameters of the engine-dynamometer structure are Λ_c, V_c and L_c^T, and it can be easily demonstrated that they are not sensitive to a change of basis of the state space model.

5.3.4.2 **Model Reduction**

Model reduction is seen as the elimination of certain modes in modal state space model. The first step for model reduction is to rearrange the modal state space model (5-39) to have the modes to be retained nr first:

$$\begin{matrix} nr \\ n-nr \end{matrix}\updownarrow\begin{pmatrix}\dot{x}_{nr}(t)\\ \dot{x}_{e}(t)\end{pmatrix}=\begin{pmatrix}\Lambda_{c_{nr}} & 0\\ 0 & \Lambda_{c_{nr}}\end{pmatrix}\begin{pmatrix}x_{nr}(t)\\ x_{e}(t)\end{pmatrix}+\begin{pmatrix}\mathrm{L}_{c_{nr}}{}^{T}\\ \mathrm{L}_{c_{e}}{}^{T}\end{pmatrix}$$
$$y(t)=\begin{pmatrix}\mathrm{V}_{c_{nr}} & \mathrm{V}_{c_{e}}\end{pmatrix}\begin{pmatrix}x_{nr}(t)\\ x_{e}(t)\end{pmatrix}+D_{c}u(t) \quad (5\text{-}43)$$

, where $x_{nr}(t)$ is the state vector of the reduced system and $x_e(t)$ are the states to be eliminated. By setting the derivative of the states to be eliminated $x_e(t)$ to zero in the state equation, the model reduction is obtained. Introducing the resulting expression for $x_e(t)$ in the observation equation, yields the reduced state space model as:

$$\begin{aligned}\dot{x}_{nr}(t)&=\Lambda_{c_{nr}}x_{nr}(t)+\mathrm{L}_{c_{nr}}{}^{T}u(t)\\ y(t)&=\mathrm{V}_{c_{nr}}x_{r}(t)+\mathrm{D}_{c_{nr}}u(t)\end{aligned} \quad (5\text{-}44)$$

, where $\mathrm{D}_{c_{nr}}=D_c-\mathrm{V}_{c_e}\Lambda_{c_e}{}^{-1}\mathrm{L}_{c_e}{}^{T}=\mathrm{V}_{c_{nr}}\Lambda_{c_{nr}}{}^{-1}\mathrm{L}_{c_{nr}}{}^{T}$

The reduced state space model is a step closer to experimental cases as real life torsional vibration experiments is always band-limited, meaning that experimental data contains information over a frequency bandwidth. Hence, only modes whose frequencies are close to this bandwidth should be observed in the data.

5.3.5 **Discrete-Time State Space Models**

All the equations in the previous section of this chapter were expressed in continuous time, meanwhile in real life applications measurements are taken at discrete time instants. So as to perform simulations and fit models to actual experimental measurement the models need to be changed to discrete time. There is the need to find an analytical solution and expression for the response of an engine-dynamometer structure to a set input that can be evaluated at any time instant t. In most cases researchers had to rely upon a numerical solution method which uses time integration schemes with adaptive time step to stimulate the response of the engine-dynamometer structure. In this thesis the approach used starts by choosing a fixed sampling period[s]. The discretization of the continuous-time equations can then allow for these equations to be solved at all discrete times $k[t]$, where $t=k\Delta t$ and Δt is the sampling period. The behaviour of the time dependent variables between two samples has to be assumed, whenever a continuous-time

equation has been sampled. For example the assumption of a Zero-Order-Hold (ZOH), signifies that the input is piecewise constant over the sampling period (Peeters, 2000). Based on this assumption the continuous state space model equation (5-35) is converted to the discrete time state space model:

$$\begin{aligned} x_{k+1} &= Ax_k + Bu_k \\ y_k &= Cx_k + Du_k \end{aligned} \tag{5-45}$$

, where $x_k = x\left(k\Delta t\right)$ is the discrete-time state vector

$y_k\, u_k$, are the sampled input and output

A, is the discrete state matrix

B, is the discrete input matrix

C, is the discrete output matrix

D, is the direct transmission matrix.

The relation between them and their continuous time counterpart is:

$$\begin{aligned} &A = e^{A_c\Delta t}, B = \int_0^{\Delta t} e^{A_c\tau}\delta\tau, B_c = \left(A - I\right)A_c^{-1}B_c \\ &C = C_c, D = D_c \end{aligned} \tag{5-46}$$

These relationships are standard and are derived in Juang, (1993). If A_c is invertible the second equality for B would be valid. The ZOH sampling doesn't influence the matrices C_c and D_c. The discrete state matrix eigenvalue and eigenvector decomposition is found substituting the eigenvalue and eigenvector decomposition of the continuous state space matrix A_c in equation (5-45):

$$\begin{aligned} A &= e^{A_c\Delta t} = e^{\Psi\Lambda_c\Psi^{-1}\Delta t} \\ &= \Psi e^{\Psi\Lambda_c\Delta t}\Psi^{-1} = \Psi\Lambda_d\Psi^{-1} \\ &= \Psi\begin{bmatrix} \ddots & & \\ & \mu_i & \\ & & \ddots \end{bmatrix}\Psi^{-1} \end{aligned} \tag{5-47}$$

By the series expansion of exponential function the third equality can be proven; the notation of the discrete eigenvalue matrix is defined by the last two equalities. Hence, the continuous

eigenvectors are equal to the discrete ones and the relations between the discrete eigenvalues and the continuous ones is:

$$\mu_i = e^{\lambda_i \Delta t} \Leftrightarrow \lambda_i = \frac{\ln(\mu_i)}{\Delta t} \tag{5-48}$$

Similar to the continuous state model, observed mode shape and discrete modal participation matrix and are written as:

$$\begin{aligned} L^T &= \Psi^{-1} B \\ V &= C\Psi \end{aligned} \tag{5-49}$$

Due to the difference in Bmatrix, the discrete modal participation factors are different compared to the continuous ones. On the contrary, the observed mode shapes are the same in continuous as in discrete.

5.4 Key Findings

In this chapter, finite element, continuous and discrete state space torsional vibration model of the engine-dynamometer system have been presented. The theoretical basis for model size reduction has been presented for both modelling techniques. Model reduction is seen as the elimination of certain modes in FE and modal state space model. Through modal decomposition of the system state matrix eigenvalues and eigenvectors of the system can be computed and modal properties such as resonance frequencies and mode shapes can be obtained.

The chapter also presented relevant equations for computing the pressure and the inertia torque. The fluctuations in the angular speed of diesel engines are excited by the variation in engine torque associated with reciprocating inertia and the pressure cycle in individual cylinders. Thus, it is expected that faults which affects the pressure profile of a cylinder would resurface on the torque associated with it.

The next chapter presents simulation evaluation results using both of the modelling techniques presented in this chapter.

CHAPTER SIX

6 SIMULATION AND VALIDATION OF MODEL

In this chapter the models developed in chapter 5 will be evaluated using the available parameters from the engine-driveline structure of the experimental test rig. A hybrid cylinder pressure profile is created using Matlab curve fitting tool on experimentally measured ones. The resulting cylinder pressure is then used in computing the total indicated torque of the engine at various speed and load conditions. Using the indicated torque as input the mathematical equations of motions were solved numerically in Matlab environment to get the IAS. Using relevant parameters of the system a discrete state matrix is created. The discrete modal parameters and observed mode shapes were computed using a Matlab function which returns the eigenvalues and eigenvectors of the system. A state space model is then created and excited with the calculated torque as input. The angular speed response from the three inertia are collected as the simulated IAS. Impact of modal parameters on the IAS response is then investigated. The simulated result are also validated with experimental ones.

6.1 Introduction

The models (FE and state space models) developed in chapter 5 will now be used to simulate the IAS response of the engine-dynamometer system using relevant parameters of the JCB 444 diesel engine test rig. The first part of the model simulation is the development of a hybrid cylinder pressure profile from measured ones. This was done because instantaneous single cylinder pressure is readily available from the test rig using the pressure sensor described in chapter 4. While, a numerical solution was adopted for the FE model, a state space model simulation technique was implemented in Matlab. Based on a 4^{th} order Runge-Kutta integration algorithm, the numerical solution, solves the set of non-linear and coupled equations (5-20, 5-21 and 5-22). The method uses an adaptive integration step size, meaning a smaller step size is used when the functions to be integrated are not smooth and longer step size when the function are smooth. The simulation of the IAS corresponding to each element of the system then becomes a repeated solution of simultaneous equations for a number of initial value-boundary conditions. During the small time interval of iteration if the interaction that takes place across the boundary of each element and the initial values of the relevant variables are known, the values of all variables can be determined. Results for the model using the numerical solution and state space modelling are discussed in the following sections.

6.2 Engine-Dynamometer Simulation Program

In order to simulate the IAS of the engine at the set operating conditions a computational program of the model was developed in a Matlab programming environment. The equations (5-20, 5-21 and 5-22) were solved so as to get the predicted values of the IAS of the system operating at variable speed and load conditions. The simulation starts with the calculation of the modal properties of the engine dynamometer structure. Then the cylinder pressure simulation was carried out using Matlab curve fitting tools on the experimental single cylinder pressure. The resulting pressure profile was used for computing the torque contribution due to the gas pressure. The total torque contribution was calculated and then used as the excitation force in the numerical solution for the IAS. The following sections discuss and present results from each of these steps.

6.2.1 **Torsional Modal Properties**

The first part of the simulation was the computation of the eigenvalue and eigenvectors of the system matrix. See table 6-1 below for the values of the system properties such as inertia mass effective torsional stiffness and damping ratio used for building the system matrix.

Table 6-1structural parameters of engine-dynamometer system

J_1 inertia of engine's rotating parts	0.2255kg. m^2
J_2 inertia of flywheel plus added adaptor	2.8801kg. m^2
J_2 inertia of dynamometer	0.380kg. m^2
$c_{1,2}$ damping ratio between engine and flywheel	0.18
$c_{2,3}$ damping ratio between flywheel and dyno	0.12
$k_{1,2}$ effective torsional stiffness of engine	7.046e4N/rad
$k_{2,3}$ torsional stiffness of flexible coupling between flywheel and dynamometer	2.3976e3Nm /rad

The inertia used for all three elements where provided for in the manufacturers manual. The torsional stiffness of a unit crankthrow is determined using the modified Ker Wilson formula given below (Guangming & Zhengfeng, 2009):

$$K = \frac{\pi Gs}{32} * \frac{1}{\frac{L_j + 0.4D_j}{D_j^4 - d_j^4} + \frac{L_c + 0.4D_c}{D_c^4 - d_c^4} + \frac{R - 0.2\left(D_j + D_c\right)}{2L_{w1}B_1^3} + \frac{R - 0.2\left(D_j + D_c\right)}{2L_{w2}B_2^3}} \qquad (6\text{-}1)$$

where K, is the crank throw stiffness Gs is the shear elastic modulus L_j , is the length of main journal D_j, outside diameter of pivot journal d_j, inside diameter of main journal D_c, is the outside diameter of crankpin d_c, L_c is the length of the crankpin journal, is the inside diameter of

crankpin, B_1 B_2 are the width on both side of the crankthrow R is the crank radius and L_{w1} L_{w2} are the thickness of the crankthrow on both side. Figure 6-1 below shows the schematic diagram of a unit crankthrow.

Guangming & Zhengfeng showed that the result from this empirical formula is 96% close to the actual stiffness value. From the manufactures manual the crankshaft was made from alloy steel with Rockwell hardness of 50HRC, density of approximately 7850kg/m3; shear modulus is approximately 80Gpa, and Poisson Ratio of approximate 0.3.

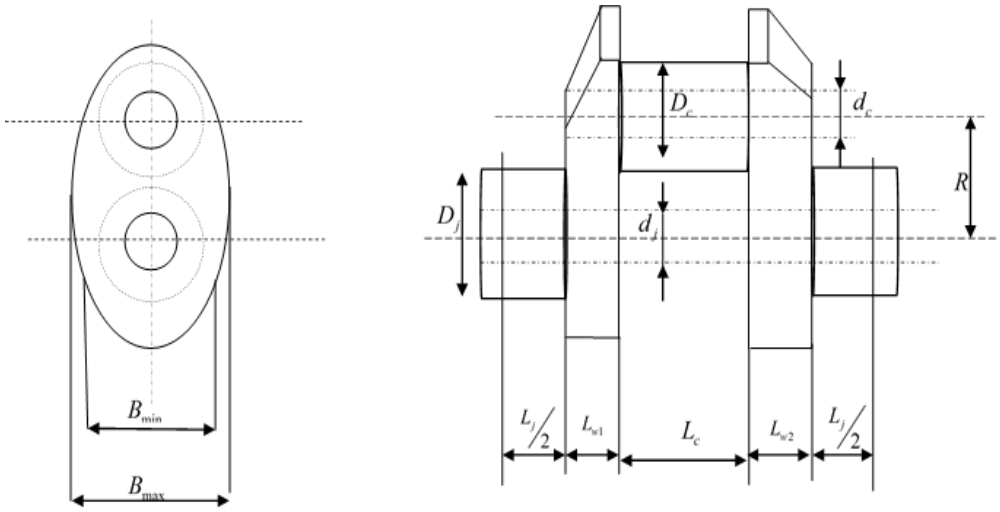

Figure 6-1 unit crankthrow

For high speed diesel engine like the one in this work the crankthrow width B is given by: $B = \sqrt[3]{2B_{max}^3 B_{min}^3 / (B_{max}^3 + B_{min}^3)}$. Table 6-2 below provides the dimensions of a unit crankthrow of the JCB diesel engine

Table 6-2 dimensions of unit crankthrow

L_j (mm)	D_j (mm)	d_j (mm)	L_c (mm)	D_c (mm)	d_c (mm)	R (mm)	L_{w1} (mm)	L_{w2} (mm)	$B1$ (mm)	$B2$ (mm)
38	88	0	22	73	0	66	21	15	48	38

After calculating for the torsional stiffness of a unit crankthrow, the effective torsional stiffness of the engine is calculated by assuming that all the crankthrow of the crankshaft are connected in

series. The stiffness and damping ratio of the flexible coupling was provided in the manufactures manual. The damping ratio between the engine and flywheel is very difficult and complicated to measure. In this work the damping ratio used by Mendes et al., on similar diesel engine was adopted (2007).

MATLAB's "eig" function was used in solving the eigenvalue problem numerically, using the rotational mass inertia, torsional stiffness and damping ratio shown in Table 6-1. The calculated modal properties using the system's dynamic properties is shown in Figure 6-2 below:

The calculated results shows that the system has one rigid vibration mode where all three masses move at the same time and two flexible modes where the engine and the dynamometer moves respectively. The rigid mode occurs at a very low frequency while the flexible modes occurs at two different frequencies (13Hz and 92Hz). These two frequencies of the flexible vibration mode in this work are termed low and high frequency resonances. The vibration amplitude of the high frequency resonance descends from the engine-to-flywheel side of the structure. While that of the low frequency resonance ascends from the flywheel-to-dynamometer side of the system. This is why the encoders placed at the flywheel produces more stable and reliable IAS waveform compared to that from the engine front end and the dynamometer end. These two frequencies are outside spectrum of the engine speed range which is from 900-2200Rpm. As the low frequency mode is just below the engines idle speed while the high frequency mode is above the maximum engine speed. This is a deliberate design by the manufacturers to prevent excessive vibration which could lead to serious damage in any of the system's part during engine running. By the model reduction theory explained in chapter 5, the condensed cylinder model removes most of the high frequency vibration modes of the engine dynamometers structure. See appendix C for the prediction of the vibration mode present in a seven degree of freedom engine–dynamometer system. Since, the low frequency mode of the system is very close to the idle speed of the engine, during engine start-up and shutdown the engine would scan through the low frequency mode. Hence, the coupling used to connect engines to the driven part or load are properly damped to reduce excessive vibration amplitudes during engine's start-up and shutdown. The calculated damping ratio is exact value as the inputted ones.

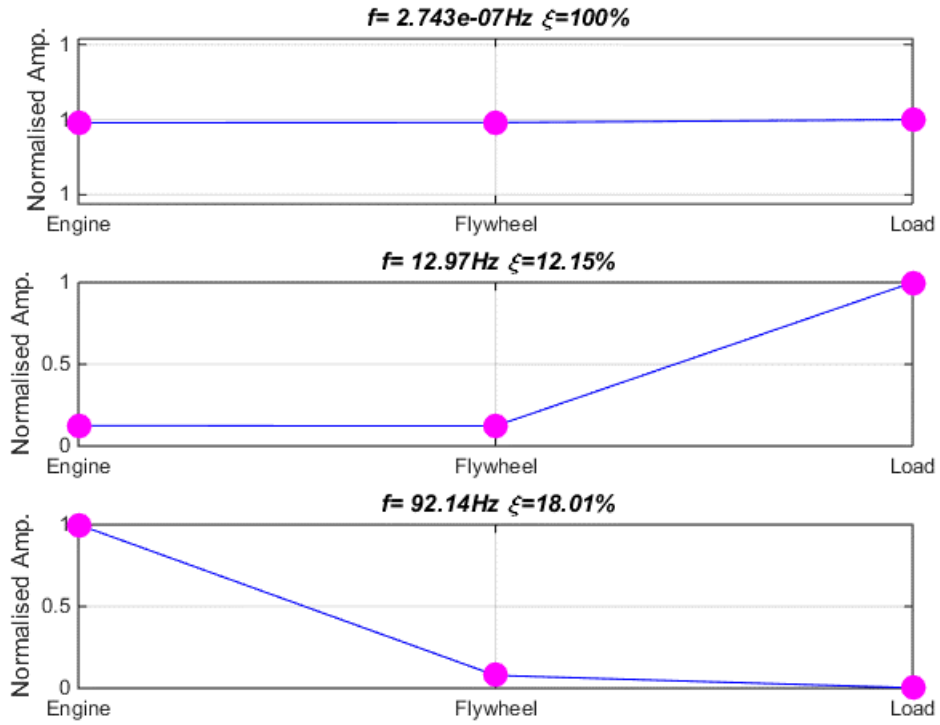

Figure 6-2 calculated modal properties of engine-dynamometer system

6.2.2 **Cylinder Pressure Simulation Result**

In the simulation of IAS using the torsional vibration model, the calculation of the instantaneous cylinder pressure is essential. Generally the concept involves the use of thermodynamics properties of gases, basic heat transfer laws, and standard relationship for compressible fluid flow through an orifice as well as the law of conservation of mass and the law of conservation of energy (J. I. Ghojel, 2010). The model treats the engine's four stroke of intake, compression, combustion (heat release) and exhaust as a sequence of continuous process. While the compression and exhaust stroke is easy to simulate, the combustion strokes is very complex (Gordon P. Blair, 1999). The combustion stroke is usually divided into three phase of ignition delay, premixed combustion and mixing-controlled combustion. This involves the use of several equations and the use Wiebe function to calculate the mass of fuel burnt during the combustion phases (J. I. Ghojel, 2010). This is a very tedious process and is time consuming since, it is not the main focus of this research. Hence, in this work using a Matlab curve fitting tools on the measured single cylinder pressure, a cylinder pressure profile was created for each operating condition of the engine and was used for

calculating the torque due to cylinder pressure. Because the averaged cylinder pressure measurement is a more reliable estimator of the average pressure at that crank angle compared to any individual measurement, the measured cylinder pressure data used in this work was averaged for 24 cycles. Using the one pulse per revolution encoder signal as a reference point the cylinder pressure was then aligned to TDC. See figure 6-3 below for the averaged single cylinder pressure. The use of the polynomial curve fitting Matlab function, on the averaged cylinder pressure as a function of the crank angle, returns the coefficients for a polynomial of 30 degree which best fit the original cylinder pressure.

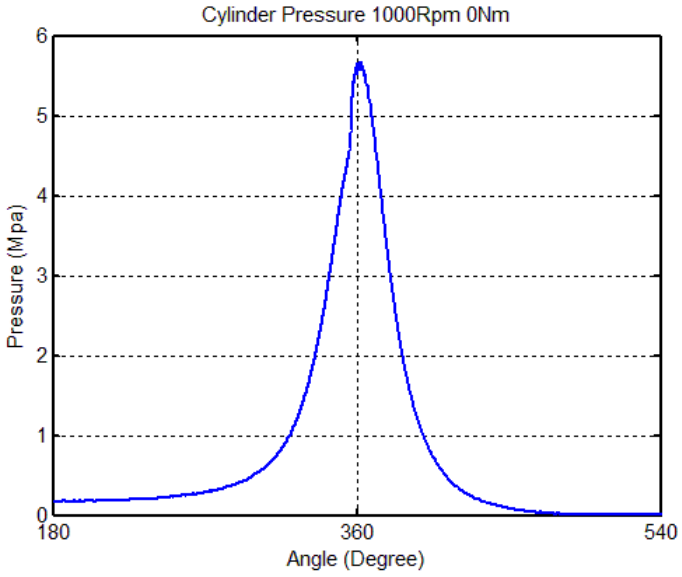

Figure 6-3 averaged smoothed cylinder pressure

These polynomial coefficients can be used to recreate the cylinder pressure profile and can also be altered so as to simulate an induced fault. See Figure 6-4 below for the result of the simulated cylinder pressure using the polynomial coefficient from the curve fitting.

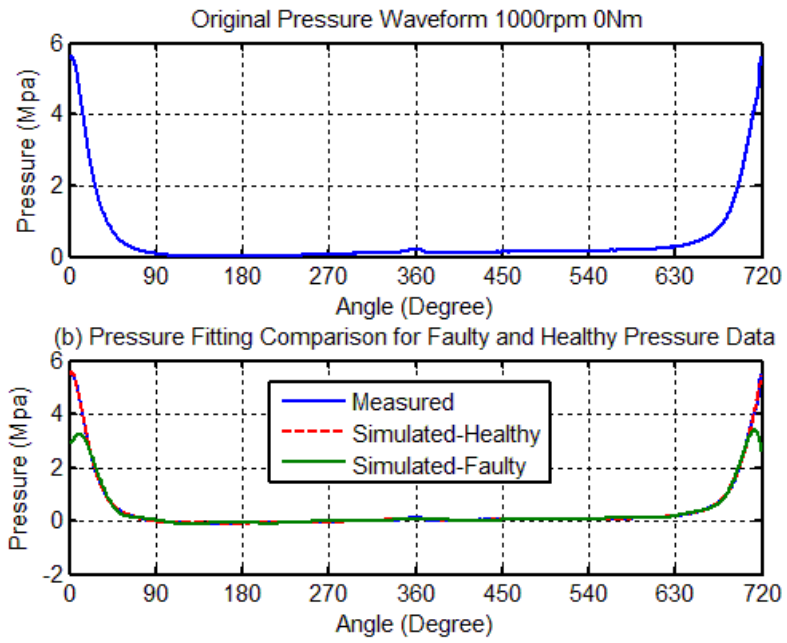

Figure 6-4 simulated single cylinder pressure

Since the model doesn't take into consideration the difference in pressure between cylinders, the simulated cylinder pressure can be duplicated to fire at different crank angles depending on the number of cylinders and firing order of the engine as shown in Figure 6-5 below. This makes the simulation of the cylinder pressure more efficient and easy to manipulate for IAS simulations.

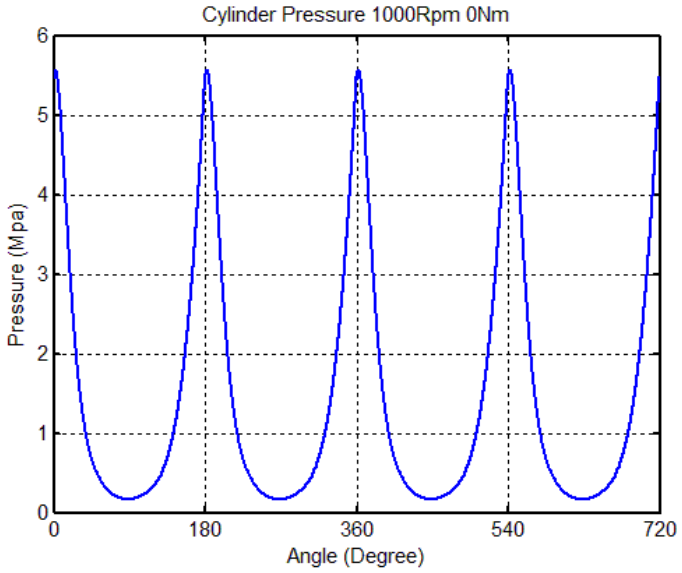

Figure 6-5 simulated cylinder pressure for four cylinder engine

Simulation result at variable speed and load shows that the increase in load results to increase in peak cylinder pressure as shown in Figure 6-6 below.

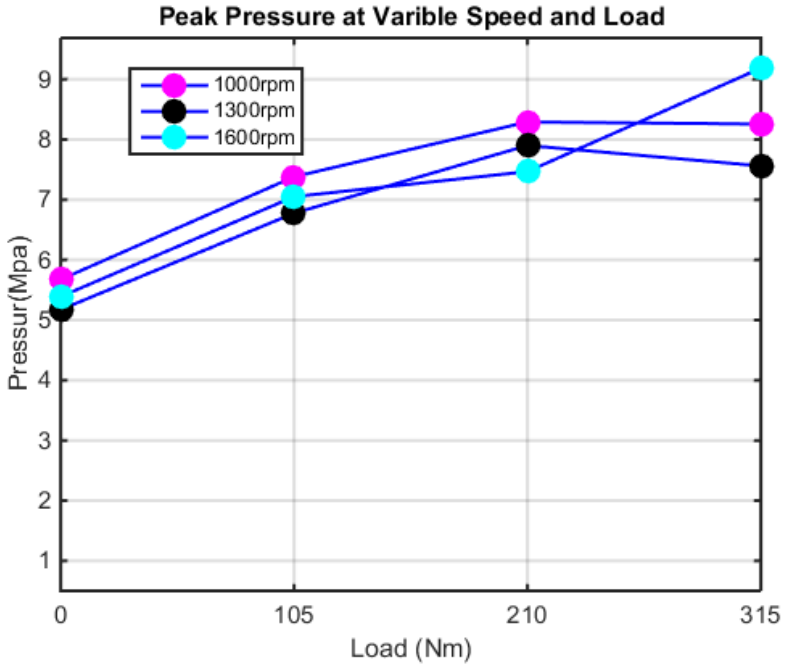

Figure 6-6 peak pressure for four cylinder engine at variable speed and load

However, the relation between the increase in load and cylinder pressure is not linear at every speed. While it is linear across all other loads at 1600rpm except at 210, at the other speeds (1300 and 1000rpm) it is not. Specifically, for the increase in load from 210 to 315Nm at 1000 and 1300rpm, the change in peak cylinder pressure was not linear. While it is fairly reduced by 0.3% at 1000rpm it dropped by 4.3% at 1300rpm. The drop in peak cylinder pressure at 1300rpm for the load increase might be due to combustion dissociation effect. As the engine performance graph indicates the lowest fuel consumption at this speed (1300rpm). Meaning, during this engine operating condition an equilibrium process is evolved in which a minimum energy is achieved from the combustion products. This is usually done to reduce the temperature of the products after combustion. This phenomenon is beyond the study of this work and wouldn't be explained further. Because the pressure signal used for this simulation is from one cylinder only and the model doesn't take into consideration the combustion variability across cylinders. The engine might be designed to compensate for this drop by an increase in the peak cylinder pressure of the other cylinders. Thereby, having no resultant effect on the total engine power torque and IAS.

6.2.3 **Engine Oscillatory Torque Simulation Result**

As discussed in chapter 5 there two main torques which excite the crankshaft of the engine in one revolution: the torque applied due to reciprocating mass and the torque due to cylinder pressure. These two torques are applied to every cylinder of the engine, depending on its firing order. Using the equations in chapter 5 and the simulated cylinder pressure, the two torque applied on each cylinder was calculated. See figure 6-7 below for the simulated applied torques acting on the crankshaft.

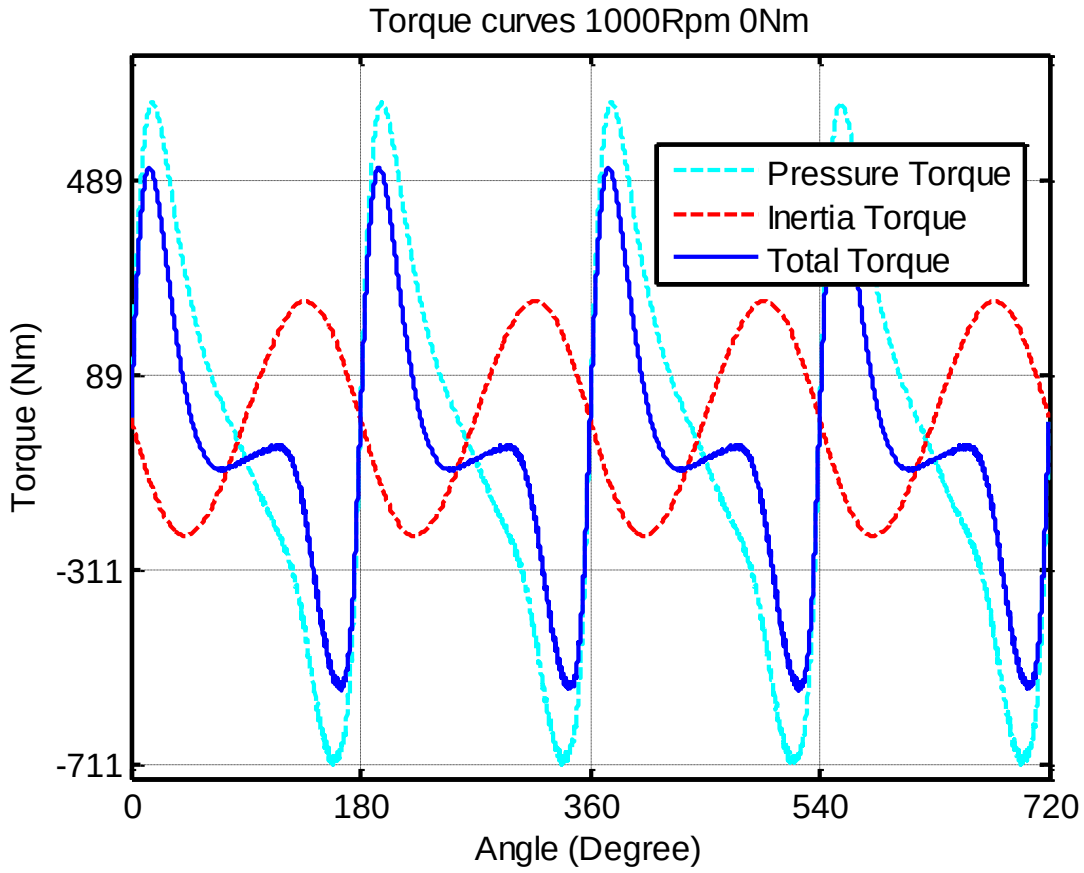

Figure 6-7 applied torque curves of the four-cylinder engine at 1000rpm

The torque contribution from each cylinder of the engine is the main reason for the torsional vibration of the crankshaft. The torque attains its maximum value just after each piston attains TDC. Meaning that the engine generates high torque values after the combustion stroke. The minimum values of torque is attained just before each piston gets to TDC, which is at the compression stroke. This indicates that the engine produces high torque values as a result of a

cylinder firing and a low torque values during the compression stroke of the cylinder. These ups and downs in the value of torque produced is the cause of the torsional vibration of the engine's rotating parts such as the crankshaft. For every cylinder as shown in the torque above, there are two peaks. The high amplitude peak is as a result of the torque due to gas pressure while the low amplitude peak is as a result of the inertia torque. The torque contributions due to individual gas pressure overshadows that due to inertia at low speed even more as the load torque increases as shown in the Figure 6-8. This means that at low speed the torque due to gas pressure is the main contributor to the total engine torque.

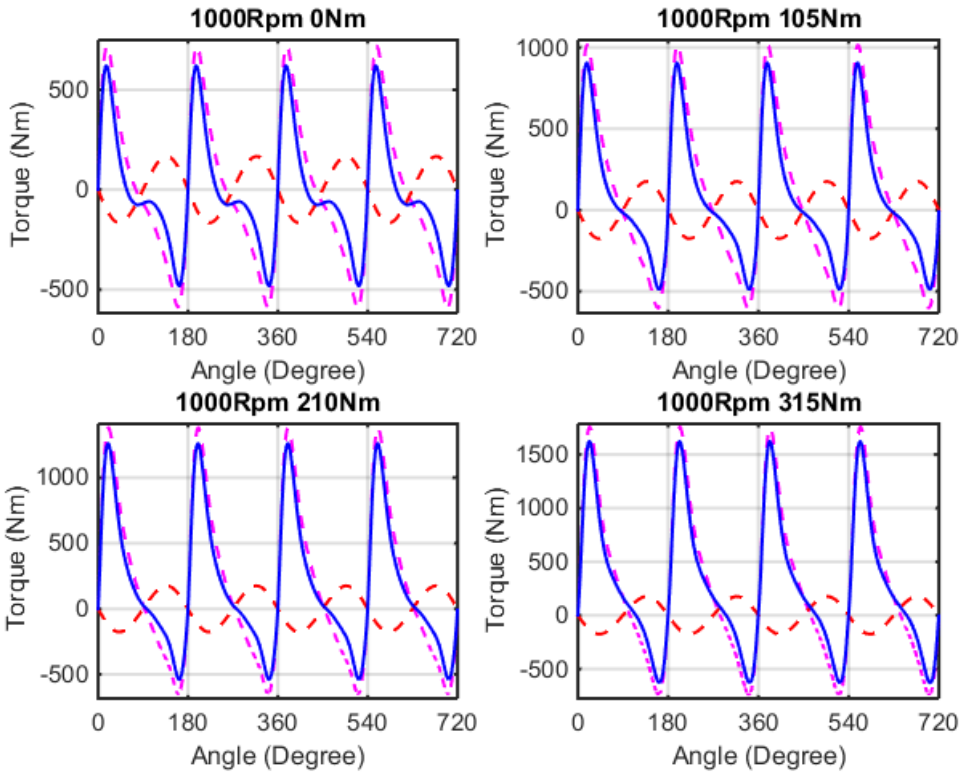

Figure 6-8 applied torque curves of the four-cylinder engine at 1000rpm and variable load

Logically, with increase in speed the contribution from the torque due to inertia apparently increases as shown in the figure 6-9 below.

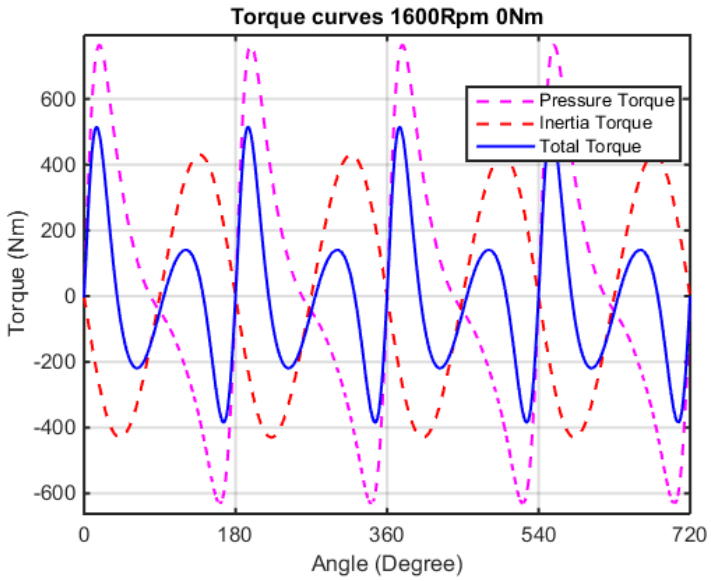

Figure 6-9 applied torque curves of the four-cylinder engine at 1600rpm

However, the contribution from the torque due to inertia decreases as the load increase at this speed as shown in Figure 6-10 below.

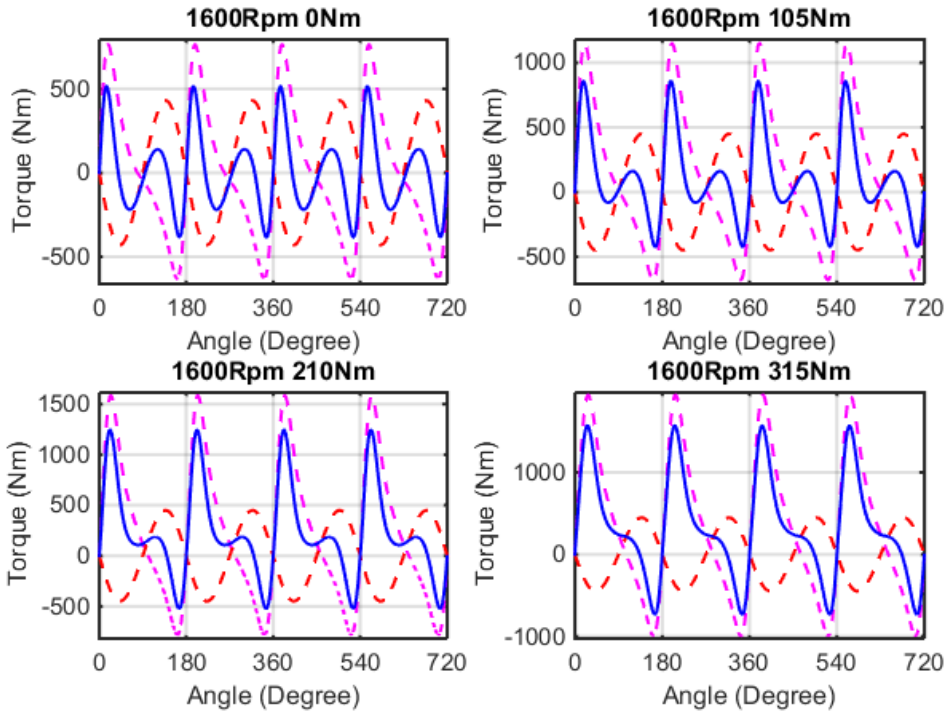

Figure 6-10 applied torque curves of the four-cylinder engine at 1600rpm and variable load

This indicates that the influence of the torque due to inertia on the IAS will be less at 1000rpm than at speeds greater than 1300rpm.

6.3 Numerical Simulation Method Results

The IAS of the engine-dynamometer structure was simulated numerically by solving the equations (5-34, 5-35 and 5-36) using the Matlab ode45 functions. This function solves the system of differential equations by integrating them from an initial set time to a final time with known initial conditions. The ode45 function implements a Runge-Kutta iteration method, using a time step that is adaptable for efficient computation. The simulated IAS shows similar features with the fluctuating net induced torque. It shows the resultant effect of each cylinders cycle on the angular speed. During the compression stroke of each cylinder the angular speed of the engine drops below the average engine speed as shown in the IAS waveform (Figure 6-11).

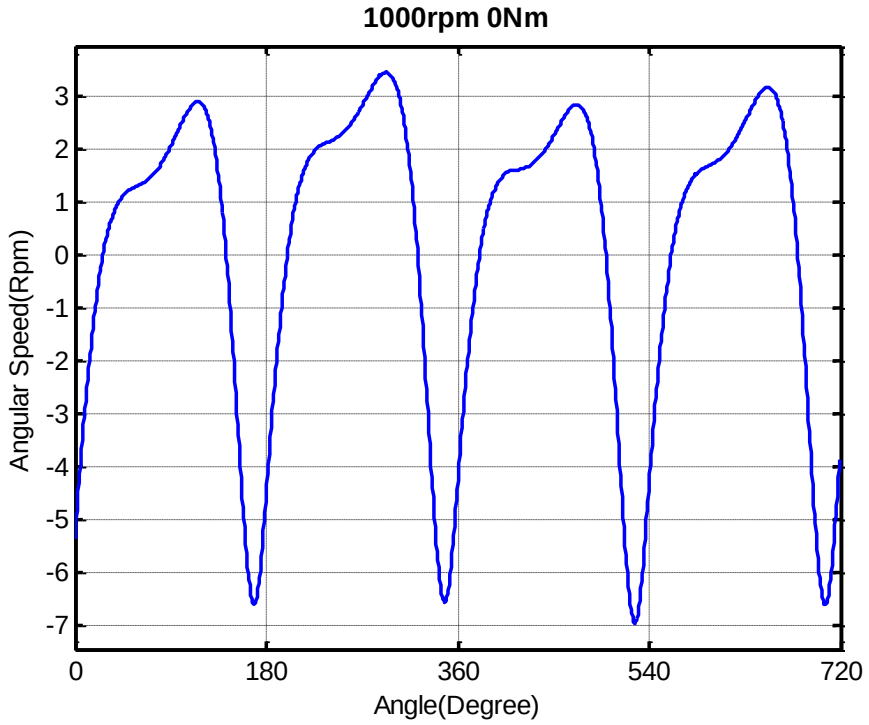

Figure 6-11 simulated IAS waveform for four cylinder diesel engine

Then just after the injection of fuel the angular speed starts to rise until it gets to values that are above the average engine speed. These two phenomenon results into an angular speed waveform

representation with peaks and troughs for each cylinder. The peak results from the combination of the combustion effect and the reciprocating inertia. The effect of the combustion is evident on the left side of the peak while that of the inertia is at the right side. The effect of the reciprocating inertia becomes insignificant with an increase in load as shown in the Figure 6-12 below. It is noticed at no loading condition and as the load increase its impact is overshadowed by the combustion effect at this speed (1300rpm). Although, the effect of the reciprocating inertia becomes significant as the average engine speed increase, this effect also becomes insignificant as the load increases. Therefore, the combustion variability (variation of the cylinder pressure) and the reciprocating inertia are the main cause of the speed fluctuation in engines during steady state operations. So, if there is any alteration in the combustion process the effects of the reciprocating inertia should become more evident in the speed fluctuation waveform and can be used for engine diagnostics.

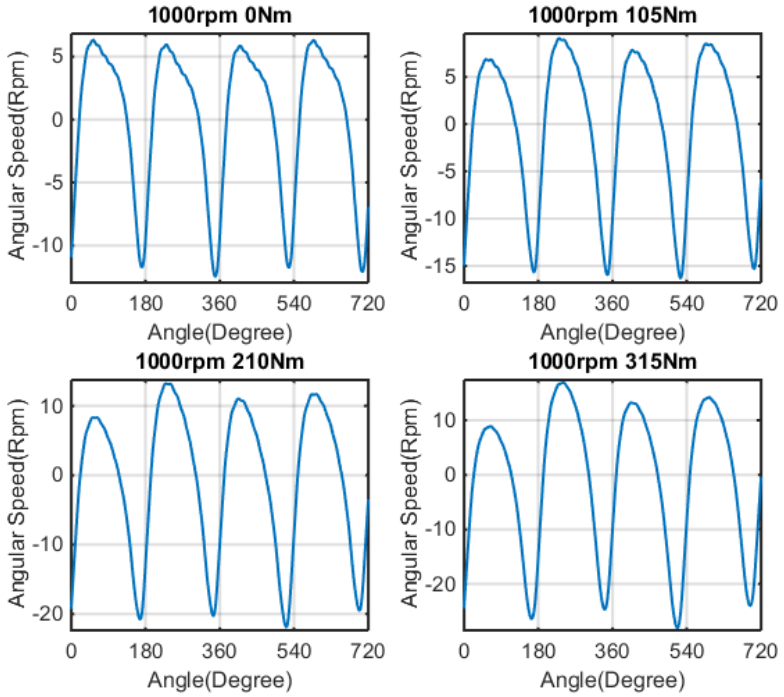

Figure 6-12 simulated IAS waveform at 1000rpm and variable loads

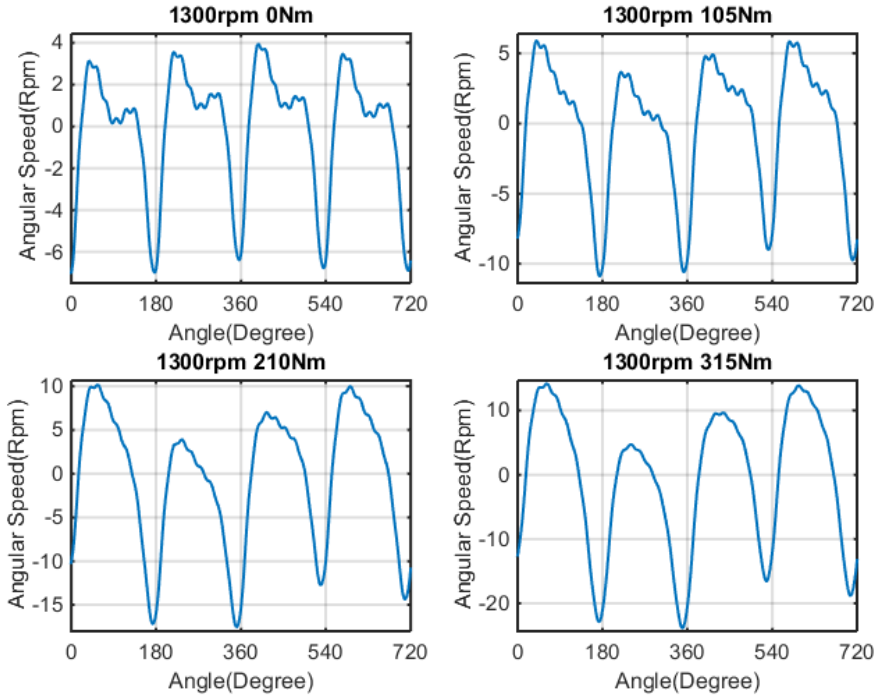

Figure 6-13 simulated IAS waveform at 1300rpm and variable loads

The angular speed fluctuation amplitude increases with increase in load across all speed as shown in the figure 6-14 below. This is in-line with the result from the simulated induced torque. However, the fluctuation amplitude varies across cylinders as in reality cylinder pressure profile varies. But the simulation model used in this work does not take this into account as a single cylinder pressure was used for all cylinder.

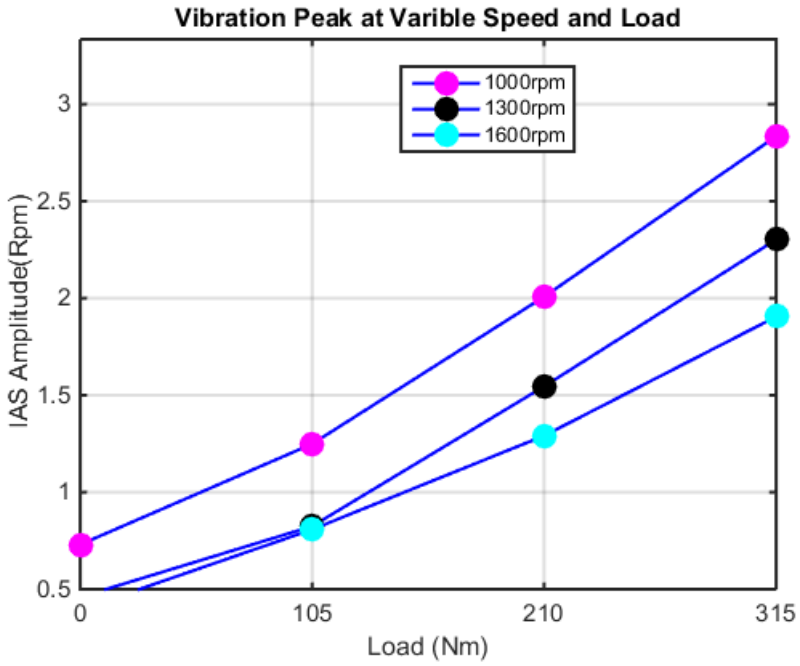

Figure 6-14 peak IAS values for four cylinder engine at variable speed and load

The trends and characteristics of the engine's angular speed fluctuation can also be represented in frequency domain as shown in the figure 6-15 below. The dominant frequency of the angular speed fluctuation waveform in frequency domain is the firing frequency and its harmonics. The firing frequency of the engine moving at 1000rpm (16.7Hz) is 2 times it rotational frequency, which is around 33Hz. Result from the frequency spectrum of the simulated IAS at 1300rpm indicates high amplitudes around 33Hz, 66Hz and 99Hz, which are the firing frequency and its 2nd and 3rd harmonics. This dominance of the firing frequency is a clear indication of the combustion impact on the angular speed fluctuation of engine.

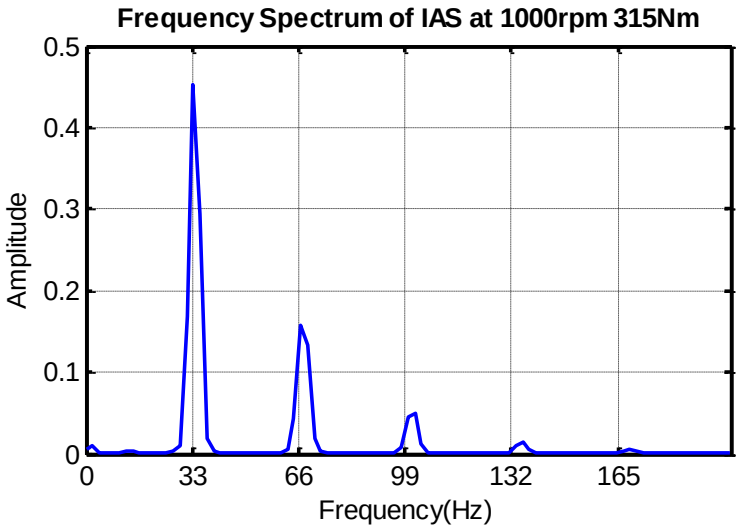

Figure 6-15 simulated IAS in frequency domain

The amplitude of firing frequency and its harmonics shows increase with increase in load across engine speed of 1000, 1300 and 1600rpm as shown in Figure 6-16 below.

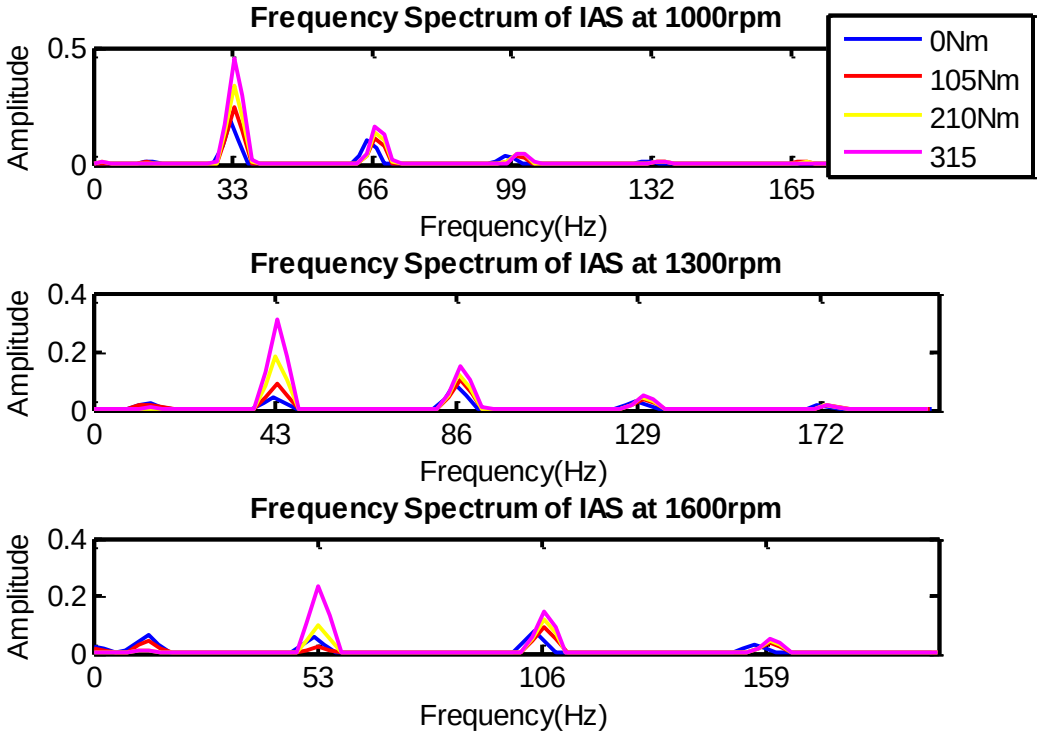

Figure 6-16 simulated IAS representation in frequency domain

The frequency domain representation of the simulated IAS also indicates the presence of some low frequency components which correspond to the engine's rotational frequency and its half order harmonics. For instance, at engine's rotational speed of 1000rpm, there are peaks around 16.67 and 8.3Hz.

6.3.1 Fault Simulation Results

In order to investigate the influence of combustion related fault on the simulated IAS, the peak pressure of the fourth firing cylinder per engine cycle was reduced based on the pressure drop from experimental test rig data. As this is one of the parameters that is easily affected in a real misfire situation. The resulting cylinder pressure profile was then used in computing the torque. When compared with the torque calculated with no fault, result shows reduction in the peak torque value of that cylinder as shown in Figure 6-17 below.

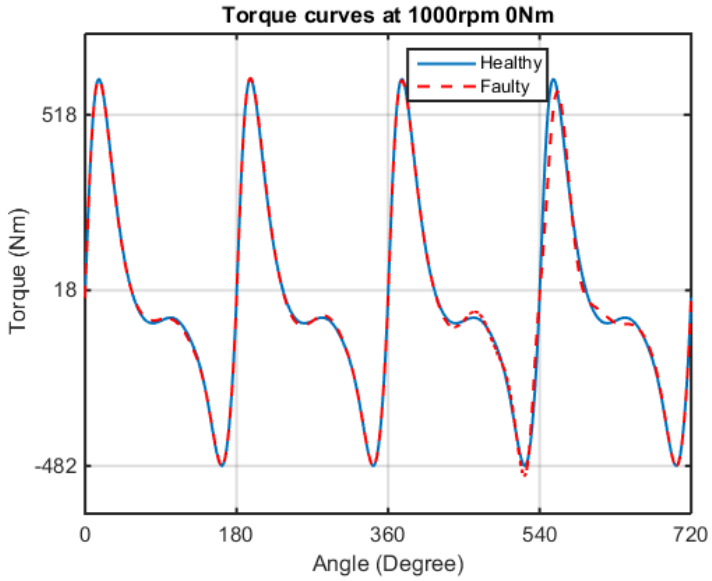

Figure 6-17 simulated healthy and faulty torque curves for four cylinder engine

The reduction in the peak value of the torque as a result of the induced fault becomes significant as the load increases as shown in figure 6-18 below. The simulated angular speed fluctuation waveform using cylinder pressure with misfire in the 4th firing cylinder shows a drop in the peak value that pertains to that cylinder when compared with the waveform of the healthy one as shown in Figure 6-19 below. It also shows an increase in the trough that pertains to the 2nd cylinder. Thus, there is a relationship between the peaks and troughs of the IAS waveform and peak cylinder

pressure and torque of individual cylinders of engines. The result also shows an increase in the peak value of the cylinder firing before the faulty cylinder. This indicates how the engine balances the total power torque contribution from each cylinder's should misfire occur in any cylinder. The reduction in the peak value in the same manner like the torque becomes significant as the applied load increase, as shown in figure 6-20 and 6-21.

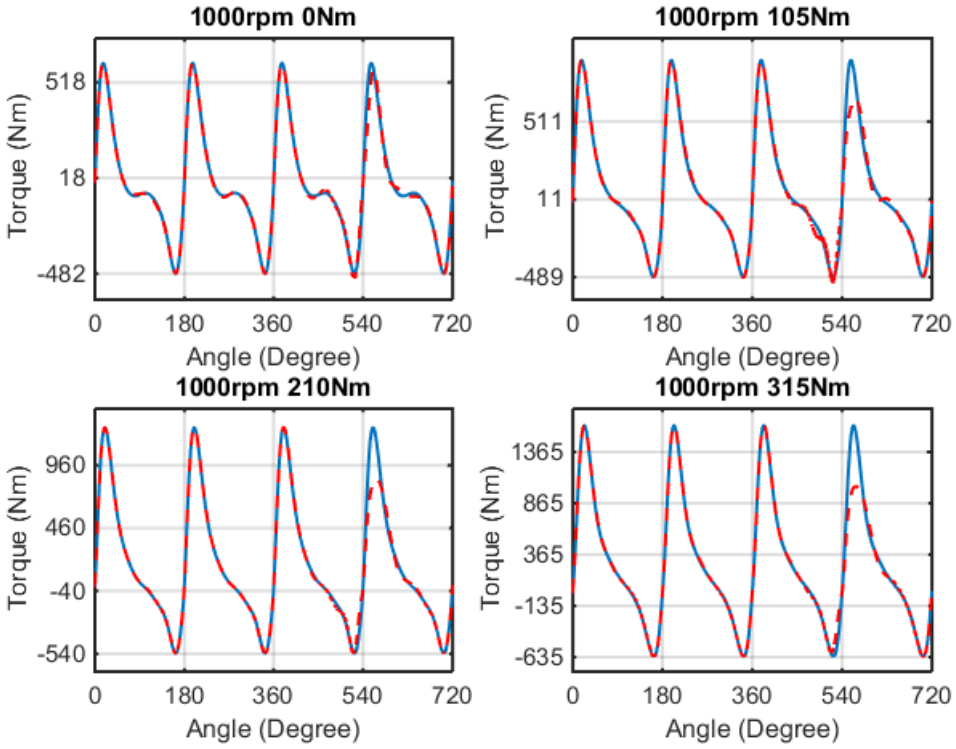

Figure 6-18 comparison between health and faulty torque curves at variable load

.

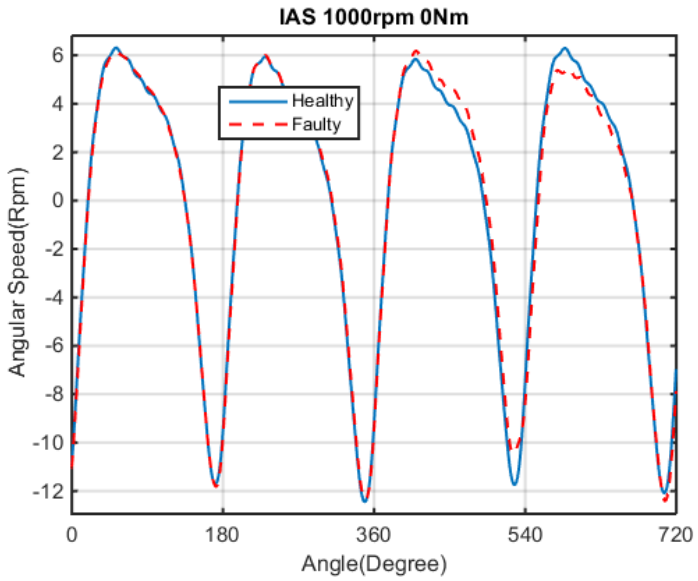

Figure 6-19 comparison between health and faulty IAS waveform of a four cylinder engine

The frequency domain representation of the simulated faulty angular speed fluctuation shows an increase in the peaks of the engine's rotational speed and its half order harmonics when compared to that of healthy ones. The amplitude of these frequencies, which is supposed to indicate a fault in the engine, is very weak and barely significant at the simulated IAS spectrum for 1000rpm 0Nm operating condition as shown in figure 6-23 below. However, as the loading condition increases from 0Nm to 315Nm, the amplitude of the shaft rotational frequency becomes more prevalent in the spectrum of the faulty IAS as shown in the mini-plot of figure 6-22 and figure 6-24. This shows that increase in the amplitude of engine's rotational frequency of IAS frequency domain representation can be used for combustion related fault detection.

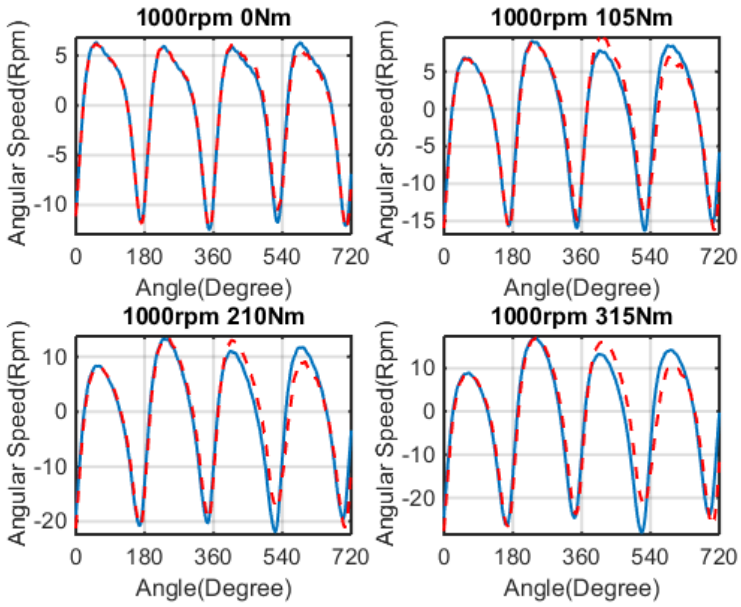

Figure 6-20 comparison between healthy and faulty IAS waveform at variable load

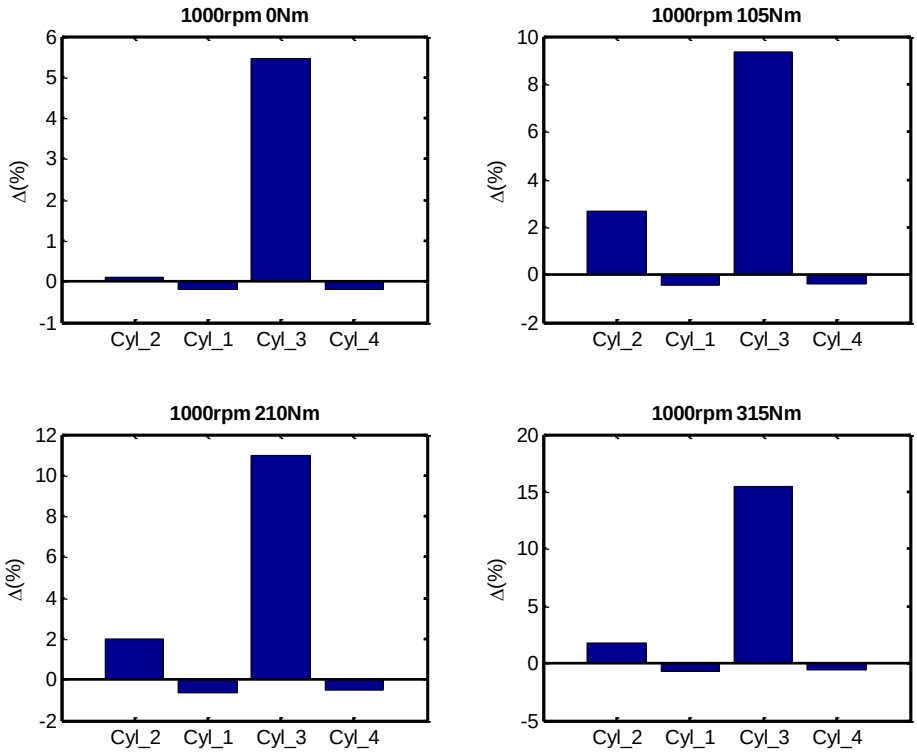

Figure 6-21 difference in trough of simulated healthy and faulty IAS

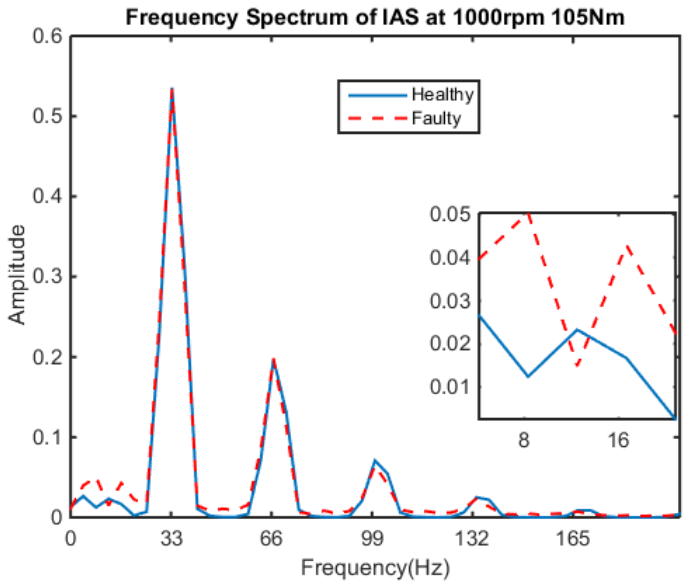

Figure 6-22 spectrum of healthy and faulty IAS at 1000rpm and 0Nm load conditions

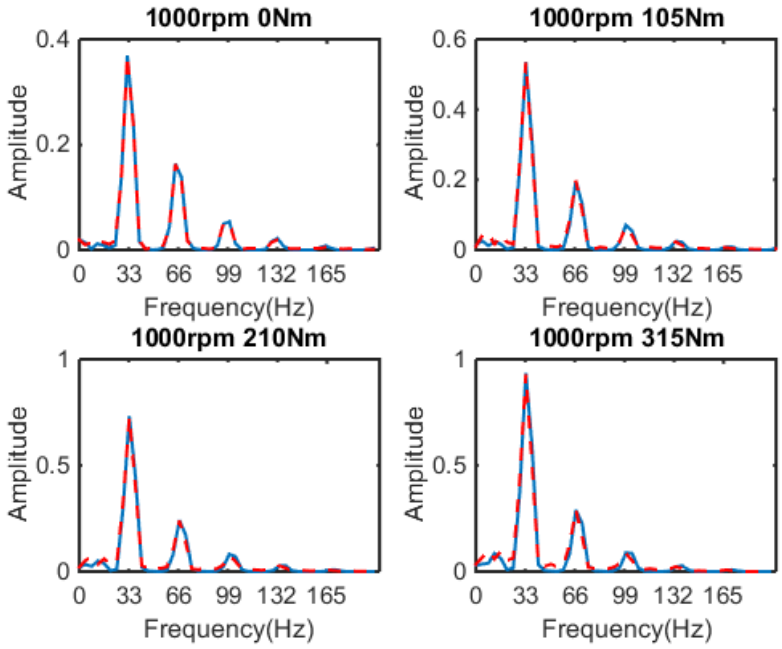

Figure 6-23 spectrum of healthy and faulty IAS at 1000rpm and variable load conditions

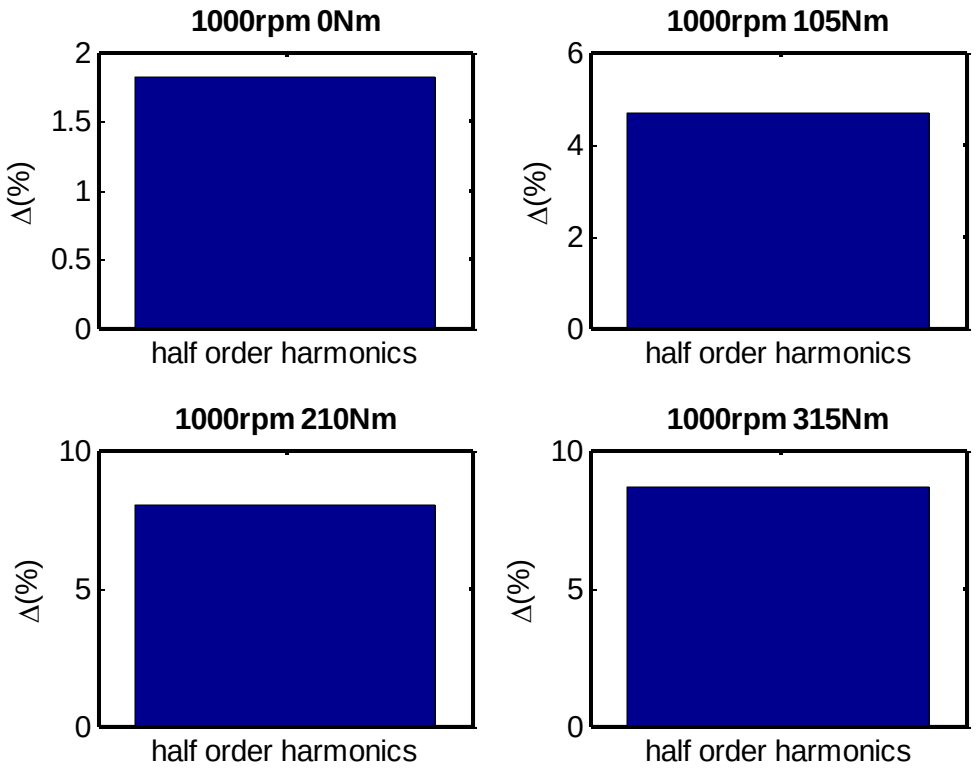

Figure 6-24 change in amplitude of half order harmonics of simulated healthy and faulty IAS

A sensitivity test was carried out with the simulated data. The peak cylinder pressure of the pressure used for calculating the pressure torque was reduced by 5%. The resulting torque was then used for simulating the IAS at variable speed and load conditions. The trough representing each firing cylinder in the simulated faulty IAS waveform compared to that of healthy ones showed no significant change as shown in figure 6-25 below. This indicate that faults which results in 5% pressure drop in a cylinder would be difficult to detect and locate using IAS.

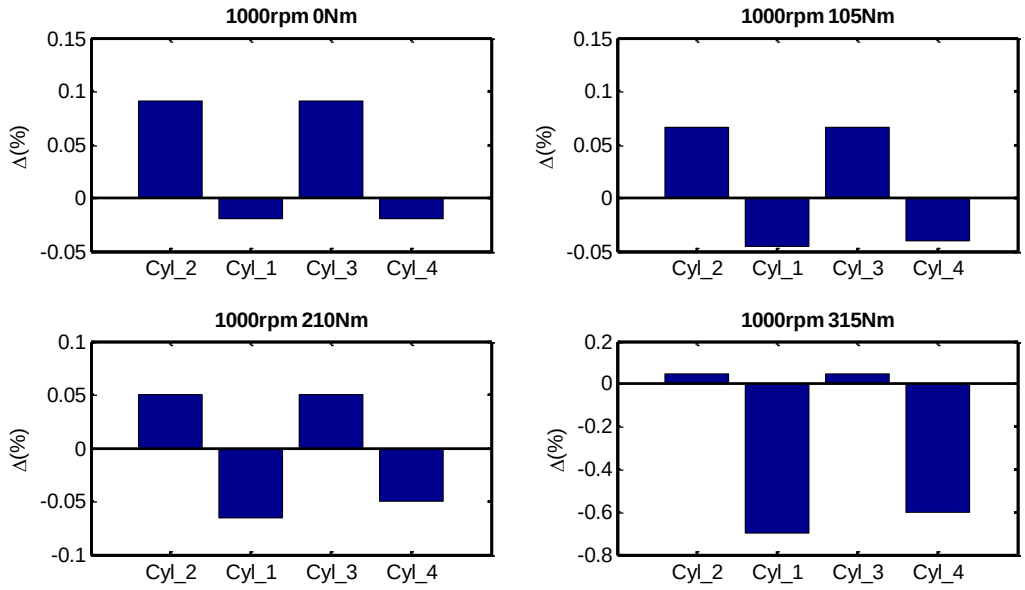

Figure 6-25 change in trough of healthy and faulty IAS at 5% pressure drop

6.3.2 **Model Validation**

The simulated IAS waveform in time domain when compared with the experimentally measured ones shows about 80% correlation as shown in Figure 6-26 below. Both the simulated and experimental IAS waveform shows the influence of the torque due to combustion and reciprocating inertia. Both IAS waveform also shows the increase in vibration amplitude with increase in load across all speeds as shown in figure 6-27. However, the influence of the reciprocating inertia is more prevalent in the experimental IAS waveform than the simulated one at different loading conditions. This could be due to inaccuracy of the system parameters used for calculating the total engine rotational inertia. Thus, limiting the effects of the torque due to reciprocating inertia for the simulated IAS at these loading conditions. Also evident is the variability of the peaks and troughs of the measured IAS waveform in time domain representation across each cylinders. While results from the simulation shows the fluctuation in angular speed across cylinder to be the same, the measured tend to show angular speed fluctuation of two cylinders behaving in similar manners.

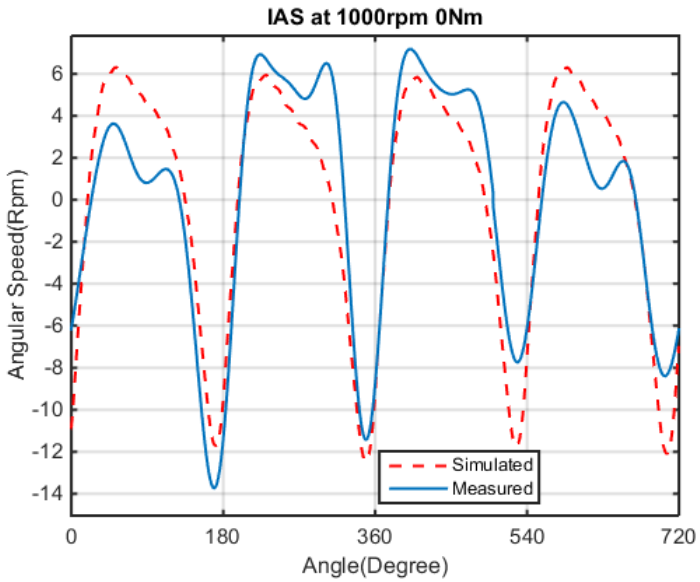

Figure 6-26 comparison between measured and simulated IAS waveform

Specifically the two cylinders that are 180 degree in line with each other. This indicates the different combustion variability across cylinders in real engine operation, which the model doesn't put into consideration. Hence, cylinder pressure parameters such as peak cylinder pressure and pressure rise rate differs across cylinders. The frequency domain representation of both the measured and simulated IAS shows the dominant influence of the firing frequency and its harmonics as shown in Figure 6-28 below. This indicates that the developed model reflects features of the engine combustion process. Hence, the system parameters used for the model can be altered for further IAS simulation evaluation. Because, for IAS model based diagnostics, where the model is used for extraction of the input torque, the accuracy of the system parameters such as the inertia and stiffness is vital. Therefore, there is the need to investigate the influence of these system parameters especially the ones pertaining to the low resonance frequency component, on the diagnostics accuracy of this method. This will be investigated in the next section using a state space model. A state space simulation was chosen because of the computation ease and flexibility of altering the system properties compared to numerical simulation.

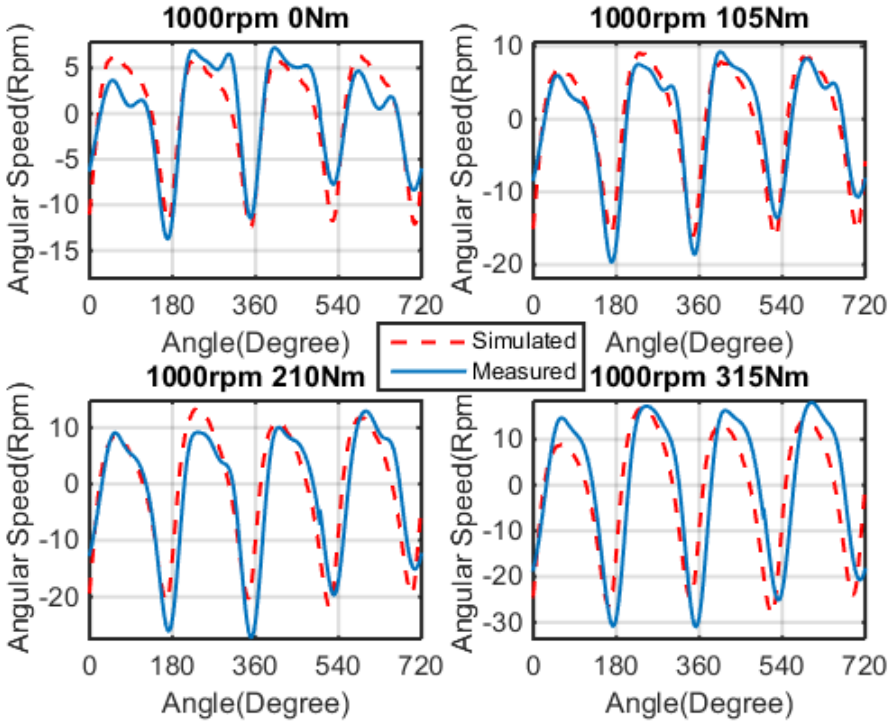

Figure 6-27 healthy measured and simulated IAS waveform at variable load

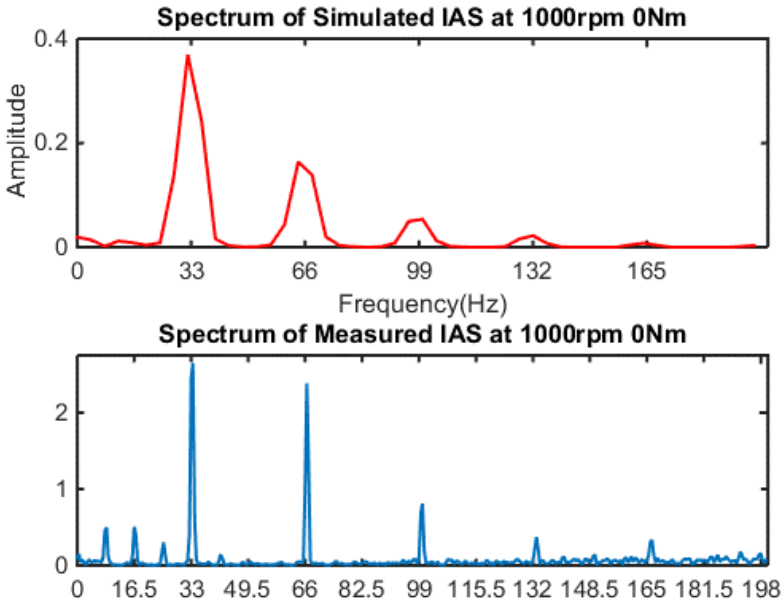

Figure 6-28 spectrum of measured and simulated IAS

6.4 State Space Simulation Results

The state space simulation carried out in this section is not to validate the model as the numerical simulation has already done that. But it is to investigate the influence of modal properties such as resonance frequency on measured IAS response for fault localization. Thus, the input torque used for excitation is a sinusoidal wave whose frequency is that of the engine's firing frequency. This was used for flexibility and easy engine-driveline angular speed response computation with modal parameter alterations. Since, it is the pressure torque that will be reconstructed the torque due to reciprocating inertia will not be considered in the simulation. The pressure torque across each cylinder can be represented as a pure sine wave given in equation (6-2) below:

$$T(\mathrm{t}) = A_T \sin(N_c \pi f_0 t + \varphi) \qquad (6\text{-}2)$$

, where

A_T , is the amplitude of the total torque

$f_0 = 2\left(rpm/60\right)$, is the firing frequency of the engine

rpm, is the average engine speed

N_c, is the number of cylinders

t, is time

φ, is the phase of the excitation torque signal

The simulated engine torque for steady engine operation at 1200rpm is shown in figure 6-29 below. The waveform of the simulated total power torque shows peaks and troughs for every interval of $\frac{1}{f_o}$ an indication of the combustion stroke of each cylinder and the compression stroke of the next cylinder to fire. So, according to the engines firing order 1-3-4-2, the first four peaks correspond to the four cylinders and are periodic for about 120 cycle.

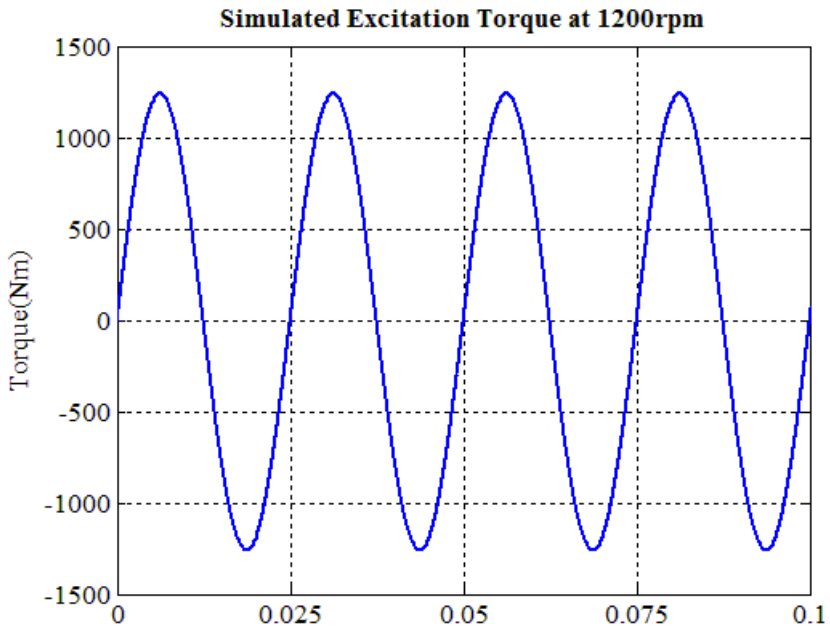

Figure 6-29 simulated excitation torque for a four cylinder engine

6.4.1 **Fault Simulation Results**

A faulty cylinder was simulated by reducing the amplitude of one of the sine wave peaks after every $\frac{cyl}{f_o}$ period by approximately 60%. Where cyl pertains to the index of the cylinder where the fault is induced. For instance a fault in the third cylinder would mean a reduction of the peaks for every $\frac{2}{f_o}$ period as it is the second cylinder to fire in every complete engine cycle (2

revolutions). The simulated excitation torque with a fault in the 3rd firing cylinder of engine cycle as shown in Figure 6-30 below shows reduction in the torque amplitude that corresponds to the cylinder.

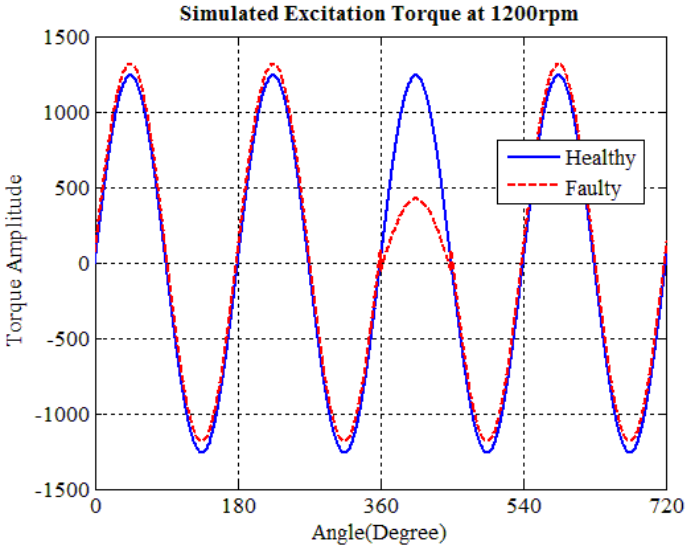

Figure 6-30 simulated excitation torque with fault in 3rd firing cylinder

Firstly, the IAS response of the system was simulated using the same system parameters in section 6.2.1 of this chapter. Followed by the representation of both healthy and faulty IAS in time and frequency domain as shown in Figure 6-31 below.

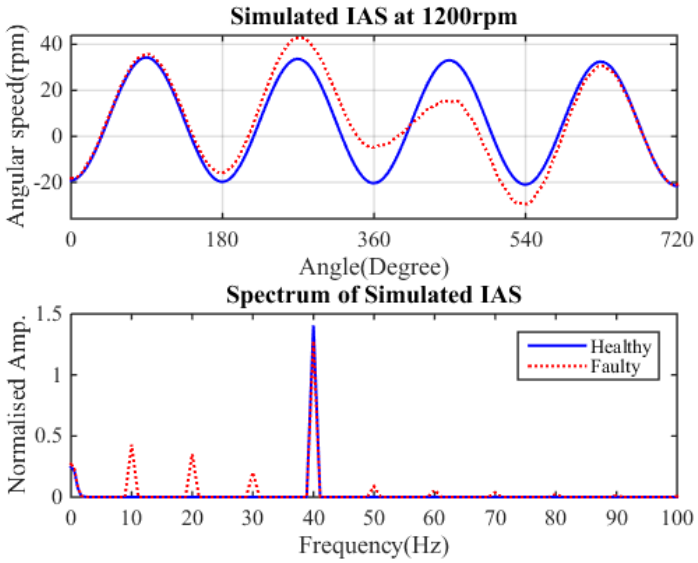

Figure 6-31 faulty and healthy IAS representation in time and frequency domain

Result from the simulated IAS using the state space model shows that during the power stroke of a cylinder the crankshaft angular rotational speed increases, due to produced torque being above the level of the load torque. Then, as the next cylinder to enter the power stroke undergoes compression, while the cylinder in the power stroke expends the combustion energy, the engine speed decreases due to the produced torque dropping below the load torque level. The process is then repeated as the cylinder in compression enters the power stroke. The result is therefore a fluctuating waveform of engine speed vs crank angle that clearly contains information about the cylinder by cylinder engine torque that produced it. The time domain representation of the simulated IAS waveform shows a significant reduction of the peak which results from the combustion of the second cylinder when compared with that of the healthy one. The result also shows an increase in the combustion of the cylinder before the faulty one. This is similar to the IAS simulated in the previous section using the ode45 Matlab function, just that the reduction of the peak due to combustion in the faulty cylinder using this method is more significant than that of the previous one.

The frequency domain representation of the simulated IAS using the faulty excitation torque waveform shows significant presence of the half order harmonics of the engine's rotational frequency compared to the healthy ones. This indicates that the amplitude and presence of the half order harmonics can be used for fault detection using the IAS spectrum. So as to validate this, the

fuel supply line from the high pressure pump of a cylinder was safely channelled into another tank to induce complete misfire in that cylinder. The IAS was measured and estimated at engine operating conditions of 1200rpm 100Nm. The resulting IAS waveform in time and frequency domain was compared with the simulated ones. Figure 6-32 and 6-33 below show the simulated and measured healthy and faulty IAS waveforms.

Result of both simulated and measured IAS waveform in time domain with fault in one of the cylinders shows a reduction in the peak that corresponds to combustion from the cylinder. The result from both simulated and experimentally measured IAS also shows the increase in the amplitude of the cylinder firing before the faulty cylinder. This indicates that the simulated IAS time domain representation of the model contains combustion features of the system and can be used for fault detection.

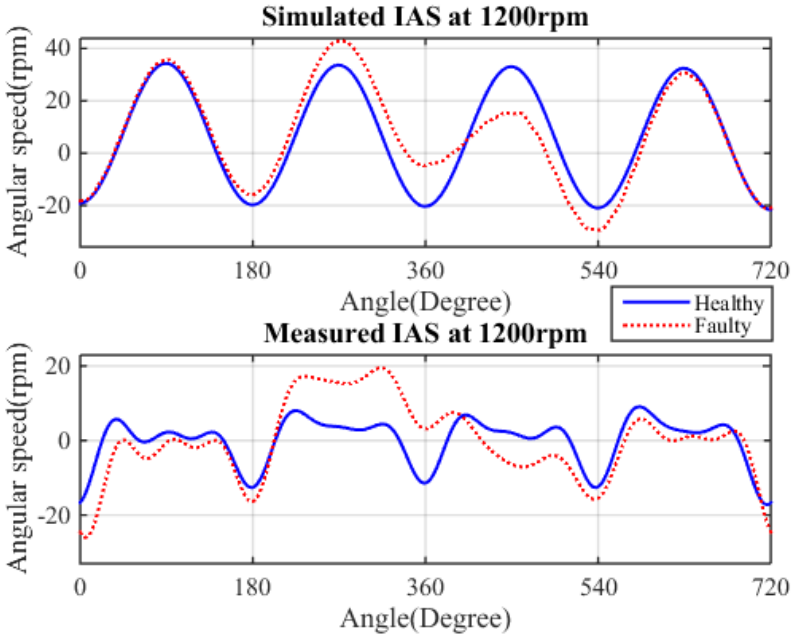

Figure 6-32 measured and simulated IAS in time domain

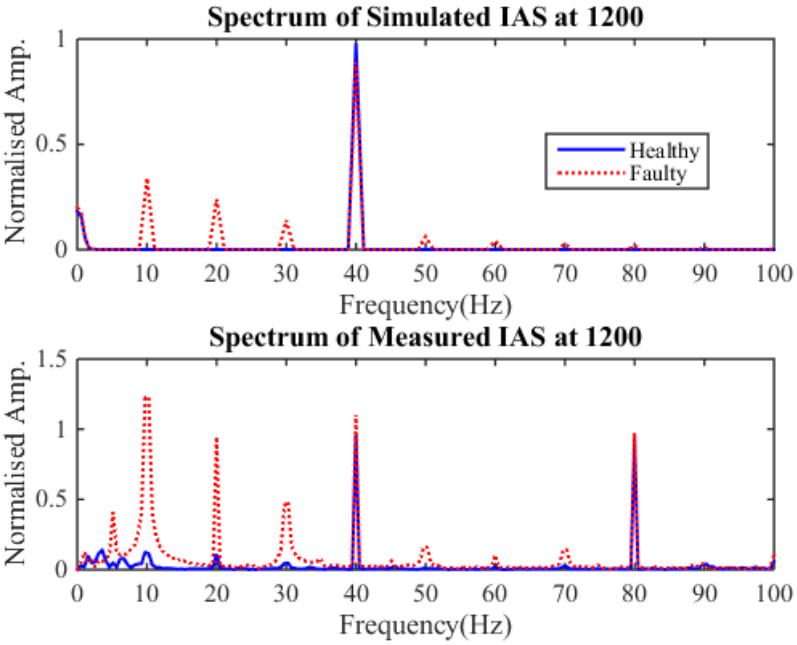

Figure 6-33 frequency domain representation of measured and simulated IAS

Result from the frequency domain representation of both the measured and simulated IAS shows significant increase of the half order harmonics of the engine' rotational frequency. Thus the alteration of amplitude of this frequency can be used for fault detection and quantification.

6.4.2 **Impact of Modal Parameters on IAS**

In order to show the impact of modal parameters on the measured IAS, the inertia of the flywheel is altered for two different occasions. In the first alteration the inertia is reduced while is increased in the second. In the first alteration the value of the present flywheel inertia is reduced by 3% while in the second it was increased by 6.5% of its present value. Table 6-3 below shows the impact of the two alterations on both the low and high frequency resonances.

Table 6-3 effect of adaptor inertia alterations on system's resonance frequencies

Present Frequency (Hz)		After Flywheel Inertia increment (Hz)		After flywheel inertia reduction (Hz)	
Low frequency	12.9	12.7	-1.6%	13.2	+2.3%
High frequency	92.4	91.0	-1.5%	93.8	+1.5%

The alteration in inertia of the flywheel has effect on both the low and high frequency resonance of the engine-dynamometer system as shown in the table 6-3. While 3% reduction of the inertia results in 2.3% and 1.5% increase of the low and high frequency resonance, 6.5% increment results in 1.6% and 1.5% reduction of the low and high frequency resonance respectively.

In order to investigate the effect of these alterations on the simulated IAS, the same excitation torque was used as input for the system with the different frequency alterations respectively. The time and frequency domain representation of the simulated IAS using the altered system properties compared to the original ones are shown in the Figure 6-34 below. The result of the simulated IAS with reduction in the inertia shows a 23% increase in the value of the peak that results from combustion of a firing cylinder and 27% increase in the value of the trough that corresponds to the compression of the next cylinder to fire compared to the one with no alteration. The simulated IAS using the system with flywheel inertia increment shows a 41% reduction in the value of peaks resulting from the firing cylinders and 32% reduction in the value of the trough that corresponds to the compression of the next firing cylinder compared to the one with no alteration. While there is a 22% increase in the amplitude of firing frequency of simulated IAS with 3% inertia reduction, there is a 33% reduction with 6.5% inertia increment compared with that with no alteration. The resonance frequency of the engine-dynamometer system, especially the low frequency component, does influence the amplitudes of the frequency component of simulated IAS.

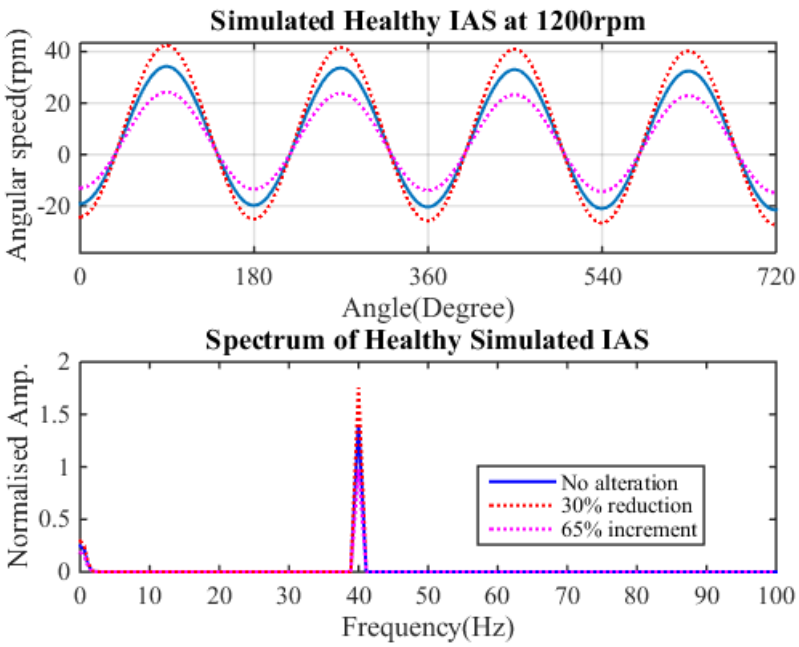

Figure 6-34 time and frequency domain representation of healthy IAS with altered modal parameter

In order to investigate the influence of the alteration on faulty simulated IAS, the same faulty excitation torque was used as input for the system with the different alterations respectively. The result shows that both the 3% reduction and 6.5% increment in the flywheel inertia influences the IAS vibration amplitude in time and frequency domain as shown in Figure 6-35 below. Results shows that while the 3% reduction increase the amplitude of the half order harmonics of the engines rotational frequency, the 6.5% increment reduces it when compared to the unaltered one.

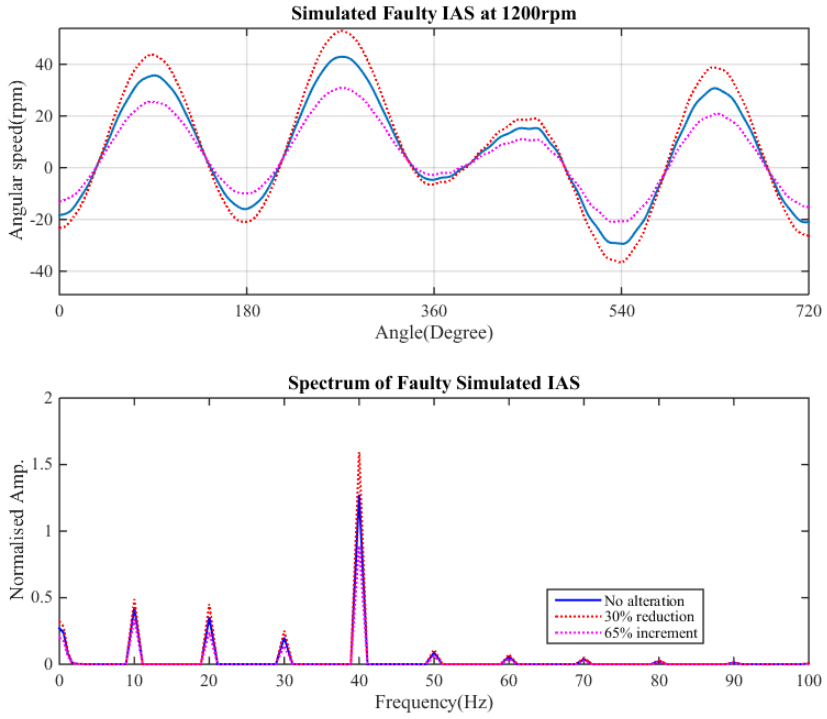

Figure 6-35 time and frequency domain representation of faulty IAS with altered modal parameter

6.5 **Key Findings**

In this chapter the IAS response of a three degree of freedom engine-dynamometer system has been simulated in Matlab environment using numerical and state space modelling methods. Modal properties such as resonance frequency and mode shape of the system has been presented. The three DOF engine-dynamometer system has one rigid and two torsional vibration modes. While the rigid vibration mode occurs at a resonance frequency of (0Hz), the two flexible modes occurs at two different resonance frequencies: a low frequency resonance (13Hz) and high frequency resonance (92Hz). While the vibration amplitude of the high frequency resonance is more significant at the engine side of the system, that of the low frequency resonance is more at the dynamometer side of the system.

A hybrid technique has been used to create a cylinder pressure profile for the numerical simulation. The results of the calculated inertia and cylinder pressure torque using equations from chapter five were presented. The effect of the torque due to reciprocating inertia on the total engine excitation

torque is more significant at high engine speed. Thus, the effect of the torque due to reciprocating inertia is evident in the simulated IAS waveform at high speed. The trough values of the IAS waveform in one engine cycle is related to the peak cylinder by cylinder pressure and pressure torque values. A state space simulation method has been used to study the impact of resonance frequencies on estimated IAS. The low frequency resonance is more sensitive to uniform vibration amplitudes as compared to the high frequency resonance. Alterations in the low frequency resonance alters the peak and trough values of the IAS waveform. Hence, it is expected that alteration in the low frequency resonance would alter the reconstructed peak pressure torque values.

CHAPTER SEVEN

7 STOCHASTIC SYSTEM IDENTIFICATION OF ENGINE-DYNAMOMETER SYSTEM

In this chapter the general concept of operational modal analysis (OMA) and traditional experimental modal analysis (EMA) are introduced. An overview of time and frequency domain based OMA approaches is discussed briefly. The advantages of the stochastic subspace based identification (SSI) technique over other time domain techniques is elaborated. Then, the statistical and identification framework for SSI algorithm is provided. This is followed by the discussion of different types of data used for implementing SSI and the one suitable for the engine-dynamometer system.

7.1 Introduction

The application of modal analysis in vibration-based condition monitoring, structural dynamics modification and analytical model updating in mechanical, aerospace and civil engineering has become prevalent in recent decades (Brincker & Ventura, 2015). Based on the measurements considered for identifying the dynamic properties of the system such as damping ratio, mode shapes and resonance frequency, it can be classified under EMA and OMA. In EMA the excitation forces acting on the structure are controlled and measureable because the test is usually done in the laboratory (Pioldi & Rizzi, 2017). Thus, the excitation force and output (displacement, speed and acceleration) measurements are used to estimates the modal properties of the structures (Brincker, 2014). Although, several EMA identification algorithms ranging from Single-Input/Single-Output (SISO) to Multi-Input/Multi-Output (MIMO) techniques in time, frequency and spatial domain have been developed in the last three decades, some of its limitations are inherent. Some of these limitations includes (Mucheroni & Cardoso, 2006):

1) The complexity involved in using artificial excitation to measure impulse response functions or frequency response functions of large structures or structures in the field.
2) According to Bricker, 2013, Since EMA is mostly carried out in laboratory environment, the results under such controlled conditions might be different under the real operating conditions of the structure.
3) In laboratory environment, component instead of the complete structure is often tested.

In OMA which is also named as output-only, natural-excitation or ambient modal analysis, the natural or normal forces present during the operation of the structure are the excitation forces. Also the test is carried out under real operation conditions in the field. Hence, it is also referred to as stochastic system identification methods, because only the output measurements of the structure in operating conditions is used for its modal properties estimation. The structure while in operating conditions should be subjected to natural or ambient excitations. In recent years, OMA has drawn enormous attentions in both civil, mechanical and aerospace engineering communities. Especially with applications for bridges, towers, buildings and off-shore platforms. Some of the advantages of OMA over EMA includes (Rainieri & Fabbrocino, 2014):

1) It is fast and cheap to conduct as there is no need for intricate excitation equipment.

2) Instead of components, the dynamic characteristics of the complete structure can be obtained.
3) According to Rainieri & Fabbrocino, 2014, due to broadband excitation, the model characteristics under real loading will be linearized depending on the application.
4) Either all or part of coordinates measured can be used as reference point; hence a MIMO identification algorithm must be used for OMA. As14 a result of this, repeated or closed-space modes can be handled with ease, making the analysis appropriate for real world complex structures.
5) Modal properties identified from OMA can not only be used for structural control and dynamic design only but also for damage detection and vibration based condition monitoring of the structure.

Despite its inviting advantages, little has been done in the use of OMA to study the torsional modal properties of mechanical structures such as the engine-dynamometer system. Most studies carried out calculate the torsional modal properties of the engine-dynamometer system offline through the aid of CAD software such as solid works and Ansys workbench (Mendes, 2008). This method is either reliant on the manufacturer providing researchers with the dimensions for engine driveline parts or rigorous dismantling of the engine driveline parts and measuring the engine dimensions. Hence, this chapter presents an online based torsional modal properties identification of a typical engine-dynamometer system for IAS based diagnostics, through the implementation of a stochastic subspace-based identification technique. The next section will provide a brief overview of OMA based identification techniques.

7.2 Overview of Operational Modal Identification Techniques

In operational modal identification techniques, the modal properties of the system are determined without knowing the excitation forces. The excitation forces are normally assumed to be a Gaussian white noise or at least that their spectral densities are all flat. However, it is not compulsory to satisfy that assumption (Brincker, 2014). This is because, the deterministic knowledge of the physical forces acting on the structure can be replaced by the assumption that the physical forces are realization of a stochastic process (a linear filter loaded by white noise) (Peeters, 2000; Brincker & Ventura, 2015; Peeters & De Roeck, 2001). In OMA since the forces are assumed to be unknown, everything is treated from a probabilistic point of view (Brincker &

Ventura, 2015; Lingmi, et ., 2005). Thus, any parameter to be observed is considered as a stochastic variable. For instance if we are to consider a signal $x(t)$, which represents the data of a variable X as a function of time. As it is done normally in statistics and probability theory, a distinction can be made between the actual observed signal $x(t)$ and the variable X which is also represented as a realization X. Recognizing that the exact behaviour of the variable X is unknown and that the disparity of this variable is uncertain, the variable can be described by its probability density function (PDF) $p(x)$. Distinct realizations x of the variable X would have distinct probabilities associated with it. More precisely, the probability of the event that the variable X is present in the small interval $[\mathrm{x};\ \mathrm{x+dx}]$ is related to the PDF $p(x)$ and is defined by:

$$Pr\left[X \in [\mathrm{x};\ \mathrm{x+dx}]\right] = p(x)\,dx \tag{7-1}$$

With the PDF is known, all possible functions such as mean μ_x and variance σ_x^2 can then be calculated. In OMA since we seldom will know the density function the mean and variance are calculated using time averaging as follows :

$$\begin{aligned} \mu_x &= \frac{1}{T_t}\int_0^{T_t} x(t)dt \\ \sigma_x^2 &= E\left[\left(x(t)-\mu_x\right)^2\right] = \frac{1}{T_t}\int_0^{T_t}\left(x(t)-\mu_x\right)^2 dt \end{aligned} \tag{7-2}$$

In OMA, due to large measurements errors in the low frequency region the mean values cannot be used for much in reality, therefore they are removed resulting to a zero mean signal (Brincker, 2013; Brincker & Ventura, 2015). The zero mean output data y_k is available as discrete samples of the time signal and can be transformed to covariance or spectra or used as it is depending on the modal identification technique to be applied. Operational modal identification techniques can be classified under the time and frequency domain.

7.2.1 **Frequency Domain (FD) Techniques**

These group of identification techniques estimates resonance frequencies, modal participation and damping ratios by inspection of spectral peaks and evaluating the height and width of the peaks, hence, they are spectrum driven (Kriel, 2000). Some of these techniques includes peak picking, frequency domain decomposition and frequency domain-polyreference. The aforementioned FD

techniques can be implemented based on EMA and OMA. The EMA FD identification is based on the modal decomposition of the frequency response function (FRF) matrix, gotten from the output and input power spectrum density (PSD) relationship shown in equation (7-3) below:

$$G_{yy}(j\omega) = H(j\omega)^{*} G_{xx}(j\omega) H(j\omega)^{T} \tag{7-3}$$

, where G_{yy} is the PSD of the output matrix

G_{xx} , is the PSD of the input matrix

$H(j\omega)$, is the FRF matrix.

The FRF matrix through poles λ_r and residues R_r can be expressed as partial fractions form:

$$H(j\omega) = \sum_{r=1}^{N} \left(\frac{R_r}{j\omega - \lambda_r} + \frac{R_r^{*}}{j\omega - \lambda_r^{*}} \right) \tag{7-4}$$

The residues $R_r = \phi_r \gamma_r^T$, where γ_r and ϕ_r are modal participation vector and mode shape respectively. While the OMA FD identification is based on the modal decomposition of half power spectrum density, which are computed from FFT of the covariance matrix with positive time lags. Since, the input is assumed to be a white noise $G_{xx}(j\omega)$ equals to constant. Then the modal decomposition of the output PSD matrix $G_{yy}(j\omega)$ can be derived as:

$$G_{yy}(j\omega) = \sum_{r=1}^{N} \left(\frac{A_r}{j\omega - \lambda_r} + \frac{A_r^{H}}{-j\omega - \lambda_r^{*}} + \frac{A_r^{*}}{j\omega - \lambda_r^{*}} + \frac{A_r^{T}}{-j\omega - \lambda_r} \right) \tag{7-5}$$

, the corresponding r^{th} residue $A_r \approx d_r \phi_r^{*} \phi_r^{T}$, and r^{th} pole $\lambda_r = -\sigma_r + j\omega_{dr}$, where $d_r = \gamma_r^{H} G_{xx} \gamma_r$. In the locality of a modal frequency, approximated PSD is:

$$\underset{\omega \to \omega_r}{G_{yy}^{T}(j\omega)} \approx \phi_r \frac{2d_r}{j\omega - \lambda_r} \phi_r^{H} = \alpha_r \phi_r \phi_r^{H} \tag{7-6}$$

Due to their ability to appeal to one's insight by nice plots, they are mainly popular.

However, they tend to be limited by bias problems which results from leakage. The leakage bias tends to result to inaccuracy of the damping estimation in the frequency domain. The identification procedures of the aforementioned FD techniques are briefly summarized in the following subsections.

7.2.1.1 **Peak Picking FD Technique**

Pick peaking (PP) is a conventional FD identification technique which is based on the fact of obtaining modal frequencies at peaks of power spectrum density (PSD) and mode shapes as a column of the PSD matrix at corresponding damped modal frequency. For PP technique to give a reasonable modal property estimate the modes should be well separated. The major advantages of this technique compared to time domain ones is that, it is simpler and faster to implement. However, the PSD peak picking technique is inaccurate for complex structures and the accuracy of the estimated modal frequency is limited to the frequency resolution of the PSD spectrum. Instead of real mode shapes what is obtained is operational deflection shapes. The damping ratio estimated in this method through the half-power point is inaccurate. The PP technique is not usually applied for structure with closely spaced modes. Thus, this technique would not be suitable for a robust structure like the engine-dynamometer system.

7.2.1.2 **Frequency Domain Decomposition (FDD) Technique**

The FDD technique was developed to overcome the weaknesses of the PP technique. In this FD technique, at discrete frequencies $\omega = \omega_i$, singular value decomposition (SVD) of the output PSD is estimated:

$$G_{yy}\left(j\omega_i\right) = U_i S_i U_i^H \tag{7-7}$$

The PSD matrix approximates to a rank one matrix as shown in equation (7-8), when only the r^{th} mode is dominant at the modal frequency ω_r .

$$\underset{\omega \to \omega_r}{G_{yy}\left(j\omega_i\right)} = s_i u_{i1} u_i^H \tag{7-8}$$

Equation (7-8) when compared to (7-6), shows that the r^{th} mode shape can be estimated as the first singular vector at the r^{th} resonance. The rank of PSD matrix will be equal to the number of multiplicity of the modes, in the repeated mode case $\hat{\phi}_r = \mathrm{u}_{\mathrm{r1}}$ .Thus, the singular vector function can rightly be used as modal indication function (MIF). The peaks of singular vector plots can be used to locate modal frequencies and mode shapes can be obtained from the corresponding singular vectors. Closely spaced modes can be detected, since SVD has the ability of separating signal

space from noise space. Three generations of FDD have been developed in recent decades. The first generation could only estimate mode shapes and modal frequencies.

The second generation called Enhanced Frequency Domain Decomposition (EFDD), is able to modal frequencies, mode shapes and damping ratio. The damping ratio and modal frequencies are calculated by applying logarithmic decrement technique on an estimated correlation function of a single degree of freedom (S-DOF) system. The free decay correlation function of a S-DOF system can be obtained by transferring back to time domain via inverse FFT, the singular value data close to the peak with corresponding singular vector that have enough Modal Assurance Criterion (MAC) value (Brincker, et al., 2001). Since, the correlation function of the corresponding S-DOF system is approximated with the inverse FFT of only truncated data, there might be bias error in the damping estimation.

The third generation of FDD, called the Frequency-Spatial Decomposition (FSDD), was developed in the recent decade. The technique uses singular vector that are obtained through the SVD of an output PSD enhanced with spatial measurements (Pioldi & Rizzi, 2017). In several occasions the enhanced PSD in the locality of a mode can be estimated as S-DOF system. Thus, the relevant damping ratio and modal frequencies can be estimated by adopting an S-DOF curve fitter.

7.2.1.3 **Least Square Complex FD (LSCF) Technique**

Major EMA FD modal identification approach is centred on parametric transfer function model denoted by rational fraction function. This lead to the rational fraction polynomial (RFP) FD modal identification technique. Various developed versions of the RFP method were based on least squares solution. So as to deal with noisy measurements in traditional system identification, maximum likelihood (ML) estimators were developed. This was followed with the proposal of a maximum likelihood FD (MLFD) modal identification technique (Pioldi & Rizzi, 2017). This technique which uses FRF measurements for modal identification is an iteration process and is a non-linear estimator. In order to find the initial values for the iterative MLFD technique, a least-square complex frequency-domain (LSCF) technique was introduced. It was found that with much smaller computational effort, the LSCF technique which is based on scalar matrix-function or common-denominator model was able to produce initial values that yielded accurate modal parameters. The LSCF technique suffers from two major limitations:

1) It is difficult to obtain the modal participation factor and mode shapes by using SVD to reduce the residues to a rank-one matrix.
2) Poles that are closely spaced show up as single ones.

Another version of the LSCE technique called polyreference-LSCF which is based on the right matrix-fraction was developed to eliminate the above mentioned limitations.

The aforementioned FD techniques might not be suitable for the identification of the torsional modal properties of the engine-dynamometer system because most spectrum driven modal identification techniques only consider only free decay outputs (Brincker, 2014). The IAS output from the engine-dynamometer system as shown in the later chapter is not necessarily a free decay.

7.2.2 Time Domain Techniques

Many traditional time domain algorithms make use of impulse response function (IRF) measurements for modal properties identification. In OMA, the identification is implemented with covariance or data driven outputs. It is typical in time domain identification to use, parametric models obtained by least square fitting. In reality this is done by solving formulated over-determined set of equations using pseudo inverse of the equation matrix. Some popular time domain modal identification techniques includes: Ibrahim time domain (ITD), polyreference (PR) technique, stochastic subspace identification (SSI) technique and the eigensystem realization algorithm (ERA) (Epaarachchi & Kahandawa, 2016).

All the other time domain techniques mentioned above are dependent on using the correlation function as free decays (Brincker, 2014). However, the experimental output used for the modal identification of the engine-dynamometer system in this work, is the estimated angular speed during the engine's transient shutdown operation. The angular speed estimated during transient engine shutdown operation as shown in the next chapter does not look like that of a decaying sinusoids. Hence all the other time domain techniques discussed above might not be suitable for an IAS based output-only modal identification. The SSI which uses a different approach and is not dependent on establishing free decays from the correlation matrix of the output measurements would be considered. This is because the SSI technique offers a numerically reliable and effective state space model for a complex dynamic system directly from measured data. The concept and theoretical framework for using this technique is discussed fully in the next section.

7.3 Concepts and Statistical Framework for SSI Techniques

The general mathematical framework used in output-only modal identifications involves the use of statistics and concepts such as linear system theory, optimal prediction and stochastic processes (Peeters & DE Roeck, 1999). The general assumption made in output-only modal analysis is that the system behaves linearly and is time-invariant. The linear behaviour of the physical system is regarding to the amplitude of the input and output. The time-invariance means the underlying physical system does not change in time.

7.3.1 Stochastic State-Space Models and Stochastic Components

The discrete state space model developed in chapter 5 is not able to describe real measurement data. To describe a real life measurement data stochastic components are included in the model. Then a discrete-time combined deterministic state space model is obtained:

$$\begin{aligned} x_{k+1} &= Ax_k + Bu_k + w_k \\ y_k &= Cx_k + Du_k + v_k \end{aligned} \tag{7-9}$$

, where $v_k$is the measurement noise due to sensor inaccuracies and w_k is the process noise due to disturbances and modelling inaccuracies. These two vectors are unmeasurable signals and are assumed to be a two correlated zero mean Gaussian white noise processes and can be defined their covariance matrices:

$$E\left[\begin{pmatrix} w_p \\ v_p \end{pmatrix}\begin{pmatrix} w_q^T & v_q^T \end{pmatrix}\right] = \begin{pmatrix} Q & S \\ S^T & R \end{pmatrix}\delta_{pq} \tag{7-10}$$

, where δ_{pq} is Kronecker delta (if$p = q$ then $\delta_{pq} = 1$, otherwise $\delta_{pq} = 0$)), p and $q$are two arbitrary time instants and E is the expected value operator.

However, the main focus for this thesis is a purely stochastic system. In field operations such as nuclear plants where the easiest and only torsional vibration information available are the angular speed responses of the engine-load structure excited by some unmeasurable inputs. From system identification point of view, the lack of input information makes it impossible to distinguish between the noise terms v_k, w_k and the deterministic input u_k. Then the discrete-time stochastic state space model is:

$$x_{k+1} = Ax_k + w_k$$
$$y_k = Cx_k + v_k \tag{7-11}$$

The concept here is that the dynamics of the physical system is represented by the $n \times n$ state matrix A. Given an $n \times l$ input vector indirectly modelled by the noise terms w_k, the state of the system described by $n \times l$ state vector x_k is transformed to a new state x_{k+1}. The state space dimension is the dimension n of the state vector x_k. The forward multiplication of state vector by the $p \times n$ observation matrix C, produces the observable part of the system dynamics. The system response vector y_k is a combination of the some noise measurement and the observable part of the state.

7.3.2 **Properties of Stochastic Systems**

Some well know properties of stochastic system are discussed in this section. It has already been stated in the section 7.3 that the noise terms of the stochastic system can be defined by their covariance matrices given by an equation (7-10). It is also assumed that the stochastic process is stationary with zero mean:

$$E[(x_k \; x_k^T)] = \Sigma, E[x_k] = 0 \tag{7-12}$$

, where the state covariance matrix Σis not dependent on time k. Since, the noise terms w_k, v_k have zero mean and do not depend on the actual state. The output covariance matrices are defined as:

$$R_i = E\left[y_{k+i} \quad y_k^T \right] \tag{7-13}$$

, where i, is an arbitrary time lag. The covariance matrix of the next state is defined as:

$$G = \left[x_{k+1} \quad y_k^T \right] \tag{7-14}$$

The following properties are deduced from stationarity, noise properties and previous definitions:

$$\Sigma = A\Sigma A^T + Q$$
$$R_0 = C\Sigma C^T + R \tag{7-15}$$
$$G = A\Sigma C^T + S$$

And for $i = 1,2$

$$R_i = CA^{(i-1)}G$$
$$R_{(-i)} = G^T (A^{(i-1)})^T C^T \tag{7-16}$$

Since, the output covariance sequence can be obtained from the measured data, the state space matrices can be found by decomposing the estimated output covariance sequence according to equation (7-16). Hence, equation (7-16) is very important because it nearly establishes the solution to the identification problem. This idea will be elaborated upon when discussing the covariance-driven SSI identification approach.

There are two other matrices which play an important role. The extended observability matrix is:

$$O_i \equiv \begin{pmatrix} C \\ CA \\ CA^2 \\ \cdots \\ CA^{I-1} \end{pmatrix} \tag{7-17}$$

It is assumed that the matrix pair $\{A, C\}$ is observable, implying that all dynamical modes of the system can observed in the system's output response. The reversed extended stochastic controllability matrix is defined as:

$$C_i^{ref} \equiv \begin{pmatrix} A^{i-1}G & A^{i-2}G & \cdots & AG & G \end{pmatrix} \tag{7-18}$$

It assumed that the matrix pair $\{A, G\}$ is controllable implying that all the dynamical modes of the system can be excited by the stochastic input.

7.3.3 Optimal Prediction

The optimal prediction of measurements is one of the most important parts of all estimations. In OMA this means the optimal prediction of the measured system response. A predictor is said to predict optimally if the error between the measured and predicted measurement is very low. An optimal predicted system response implies that a model can be estimated in an optimal sense. Assuming there are y_k measurements available from initial time $k = 0$ to $k = t - 1$. If the measurements are collected in the vector

$$y_0^{t-1} = \begin{bmatrix} y_0 \\ y_1 \\ \cdot \\ \cdot \\ y_{t-2} \\ y_{t-1} \end{bmatrix} \tag{7-19}$$

In a Gaussian situation the optimal predictor of $x_t$is obtained by the conditional mean value

$$x = \left[x_t \mid y_0^{t-1} \right] \tag{7-20}$$

The optimal predictor of the state vector x_t at time t is the mean value of x_t for all given measured system response y_k from $k = 0$ to $k = t - 1$. The prediction error is difference between x_t and $\hat{x}_t$ defined as:

$$\varepsilon_t = \hat{x}_t - x_t \tag{7-21}$$

The error is the part of $x_t$that cannot be predicted by $\hat{x}_t$. By formulating a similar condition mean the system response y_k can be predicted.

$$\begin{aligned} \hat{y}_t &= E\left[y_t \mid y_0^{t-1} \right] \\ &= E\left[\left(Cx_t + v_t \right) \mid y_0^{t-1} \right] \\ &= C\hat{x}_t \end{aligned} \tag{7-22}$$

7.4 Main Principles of SSI Techniques

Modal identification usually begins by adopting a certain model that represents the system. In section 7.3.2 of this chapter the innovation and stochastic state space model was studied, hence the type of model used for SSI is clear. SSI techniques can be divided according to the type of data they require for modal identification. The SSI technique that requires raw time data is termed data-driven SSI, while the one that requires covariance data is called covariance-driven SSI. The main principles of both the data and covariance-driven SSI techniques are given in appendix E.

7.4.1 Data-Driven SSI vs. Covariance-Driven SSI

There are similarities as well as differences between these two robust subspace output-only identification techniques. The first similarities are that both subspace techniques start with a data-reduction step. In the covariance-driven subspace algorithm the raw time histories of the data Hankel matrix are converted to the covariance of the Toeplitz matrix. Thus the number of elements are reduced from $\left(r+l\right)i \times j$ to $li \times ri$. While in the data-driven subspace identification a reduction step is implemented by projecting the row space of the future outputs into the row space of the past reference outputs. This projection is computed by means of QR-factorization of the data Hankel matrix. Because only the R-factor is further needed in the algorithm, a significant data

reduction is obtained. Another similarity is that both algorithms proceed with the singular value decomposition. The differences between these two algorithms seems to be their advantage over one another. The covariance-driven identification is computationally faster than the data-driven identification (Peeters and Roeck, 2000). Because the use of the Fourier transform in the covariance-driven data reduction step is less time consuming than a slower QR-factorization used in the data-driven counterpart. Although, the use of the Fourier transform in the covariance-driven identification algorithm makes it less accurate due to leakage error, it has more computational prospect for the online modal properties identification of a dynamic system like the engine-load system. Hence, the covariance-driven subspace identification algorithm is adopted in this work for an output-only modal identification of a typical engine-dynamometer system.

7.5 **Key Findings**

This chapter has presented theoretical basis and equations for prospective IAS based OMA of the engine-dynamometer system. It has discussed relevant OMA techniques and their limitations when considering modal identification of the engine-dynamometer system using IAS signal. Time and frequency domain OMA techniques such as FDD, ERA, LSCF, ITD and PR all depends on establishing free decay from the measured response except for the SSI. The angular speed of the engine-dynamometer system during engine transient operations does not resemble a free decay. This makes the SSI more robust and reliable OMA technique to be used for an IAS based modal properties identification.

A stochastic state space model of the system has been also presented. The concepts and statistical framework of using the SSI OMA technique were presented. Based on the data type used, SSI techniques can be classified as either data-driven or covariance-driven. The covariance-driven SSI is computationally faster compared to the data-driven counterpart. The covariance-driven reference based SSI algorithm was identified as a prospective OMA technique to be used for online identification of torsional modal properties of the engine-dynamometer system. The next chapter presents an experimental and simulation evaluation of an IAS based on-line modal properties identification of a typical engine-dynamometers system.

CHAPTER EIGHT

8 SIMULATION AND EXPERIMANTAL EVALUATIONS

In this chapter, the covariance-driven subspace identification technique described in chapter 7 was implemented using a simulated system response under random excitations and an experimental system response during transient engine shutdown operation. Two types of random signal are used as excitation input for the simulated evaluation. Firstly, a stationary random signal generated in Matlab is used as excitation input for the state space model in chapter 6, then the system response was generated and used for implementing an SSI based modal identification algorithm. Secondly, a non-stationary random signal, is also used as excitation input and the system response generated and used for implementing the SSI based modal identification algorithm. This was then validated with an experimental system response from a transient engine shut-down operation. Finally the characteristics of the identified modal properties is used for engine misfire detection.

8.1 Simulation Study of IAS Based Identification

Before implementing the subspace identification technique with experimental data a simulation study is carried out. The simulation evaluation conducted is used to ascertain the accuracy of the technique because in a simulation the actual modal properties are known and can be compared with the extracted ones from the identification algorithm. The simulation evaluation is used to study the system responses under stationary and non-stationary random excitations. The stationary random excitation is used because in OMA the excitation forces are normally assumed to be a Gaussian white noise or at least that their spectral densities are all flat. Due to the dynamic of the engine operations, the stationary random input does not completely describe the excitation torque acting on the crankshaft. Hence, a non-stationary random excitation is used.

8.1.1 Data Generation

The discrete state space model of the engine-dynamometer system developed in section 6.4 was used for the simulation evaluation in this chapter. The only difference is that instead of a deterministic input, two types of random inputs are used for excitations. The impact of the excitation torque on a unit crankthrow during engine run up or run down operations can be assumed to be a brief input signal. This brief input signal can be simulated in Matlab as a unit impulse. So for a multi-cylinder engine there would be multiple impulses of different amplitudes acting on different location across the crankshaft. Since, there is no mathematical formula for modelling these multiple impulses it can be assumed to be a transient non-stationary random input. The non-stationary random input is created in Matlab by generating a signal with 4 impulses and the position of each impulse in the signal is randomly chosen. In order to randomly choose the position of each impulse in the signal the Matlab ‘rand’ function is employed. The generated signal is then used for the excitation of the engine inertia in the discrete state space model. The figure 8-1 shows the time and frequency domain representation of the system outputs (angular speed) under a non-stationary random input. Since the Matlab ‘rand’ function is employed for choosing the position of the impulses, every time the program is executed 4 different positions are selected synonymous to four cylinders making the process a random one. Every time the program is executed the angular speed responses from the engine, flywheel and dyno inertia are saved. The program was executed 8 times

making available 8 dataset which is sufficient for the implementation of the covariance-driven SSI algorithm.

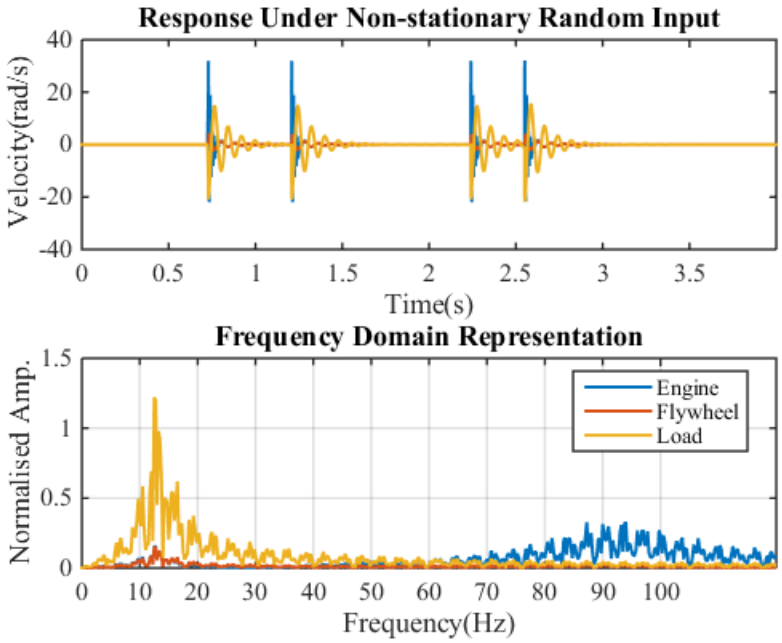

Figure 8-1simulated IAS under a non-stationary excitation

The second input used for the excitation is generated using the Matlab ‘rand’ function which produces a different uniformly distributed pseudorandom numbers every time it is executed. The generated random input signal was passed through a low pass FFT filter with band coefficients which corresponds with frequencies of <0Hz and < 150Hz. This frequency band was chosen because of the calculated low (13Hz) and high (92Hz) frequency resonances of the engine-dynamometer system (section 6.21). The resulting time domain angular speed outputs due to excitation from a stationary random input and their corresponding frequency domain representation is shown in the figure 8-2. Both simulations are more or less in-line with the real life situation where the engine-dynamometer system is excited by an unknown but assumed to be white Gaussian distributed forces. And the outputs are measured with encoders placed at the different locations (front end, flywheel end and dynamometer end) along the system. However, the non-stationary input best describes the excitation input and the output of system during the engine run up and run down operations. The stationary random input is too generic to describe the excitation input during engine run up and run down operations.

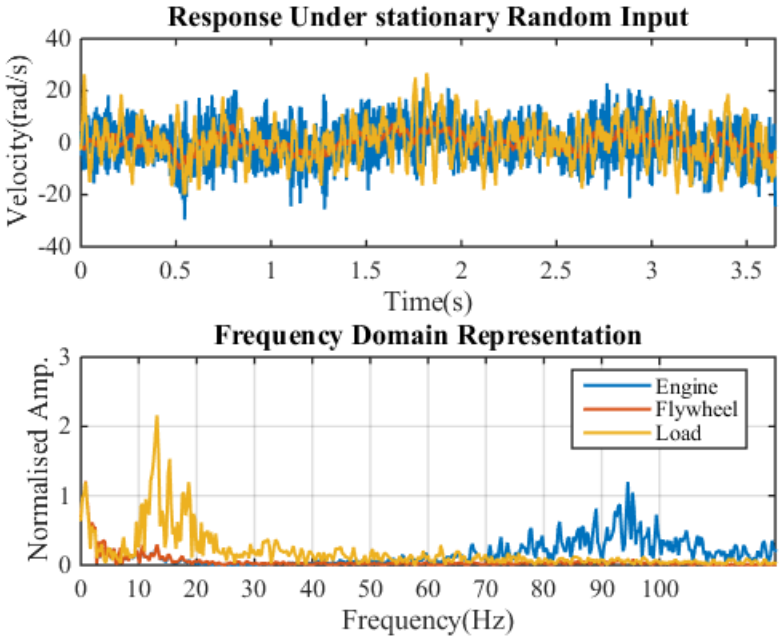

Figure 8-2 simulated IAS under a stationary random excitation

The time and frequency domain representation of the system response under stationary and non-stationary random excitations indicates the presence of both high and low frequency components. The number of oscillations per second in the time domain representation of each inertia varies from engine to dynamometer reference points. While that from the engine inertia shows more oscillations per second indicating the presence of a high frequency component, the ones from the dynamometer shows fewer cycle per second indicating the presence of a low frequency component. The frequency domain representation of the system response under stationary and non-stationary random excitation indicate peaks around 13Hz and 92Hz, which corresponds to the calculated low and high frequency resonances in section (6.2.1) Since the frequency domain representation of the responses of both stationary and non-stationary excitations show similar characteristics, they are both used for the implementation of the SSI algorithm. In order to account for measurement error in the estimated IAS during engine shutdown operation a Gaussian white noise sequence of 0.5 average power was added to the simulated signal from both non-stationary and stationary random excitations (Peeters and De Rock, 1999). The added noise would make the identification algorithm more challenging and identification of the structural poles more difficult because the noise introduces additional poles to the data.

8.1.2 Covariance-Driven Reference-Based Identification Algorithm

Generally in most SSI algorithms the data initially goes through some pre-processing steps such as detrending, filtering and differentiation/integration etc. However, most of these pre-processing steps are optional depending on the nature of the signal. Some of these pre-processing steps sometimes adds or removes some frequency component which might be relevant. Hence, the algorithm adopted in this thesis utilizes the simulated and measured angular speed signal. The identification technique adopted in this work is expected to use the covariance between the outputs from all the channels and a limited set of reference channels. However, due to the limited amount of sensors used in this work all three signals are used as reference in both simulated and experimental evaluations.

The step by step procedure of applying the identification algorithm to the generated data is listed as follows.

1. The first step in this algorithm is the computation of the auto correlation functions from the data. Using the FFT frequency domain method. This method is computationally faster to implement when compared to the direct method. Through trial and error a time lag of 1024 and data segment of 4096 was suitable for the correlation functions.
2. The resulting correlation signals is passed through some threshold criterion so as to reduce added noise before averaging. Firstly, the root mean square value of the correlation functions is calculated. Using the minimum and maximum values of the calculated root mean square values as sub intervals the probability density function (PDF) is estimated using the Matlab 'hist' function. Then a minimum and maximum threshold condition obtained from the estimated PDF is put in place during the averaging of the correlation functions. See figure 8-3 below for a segment of the correlation signal and the averaged correlation signal.
3. The system matrices A and C are then calculated after arranging the averaged correlation signal in a block Toeplitz matrix using the equation (7-71) and (7-72). The number block rows i of the Toeplitz matrix was chosen such that ri is greater than the chosen maximum

model. Using a minimum and maximum model order of 20 and 60 the matrices O_i, C_i^{ref} were computed, from which the system matrices and modal parameters are estimated.

4. The modal parameters are then calculated using equation (5-61), (5-62) and (5-63).

The stabilization diagram was constructed according to the following criteria: mode shape vector (MAC) 5%, damping ratio 1% and eigenfrequency 1%.

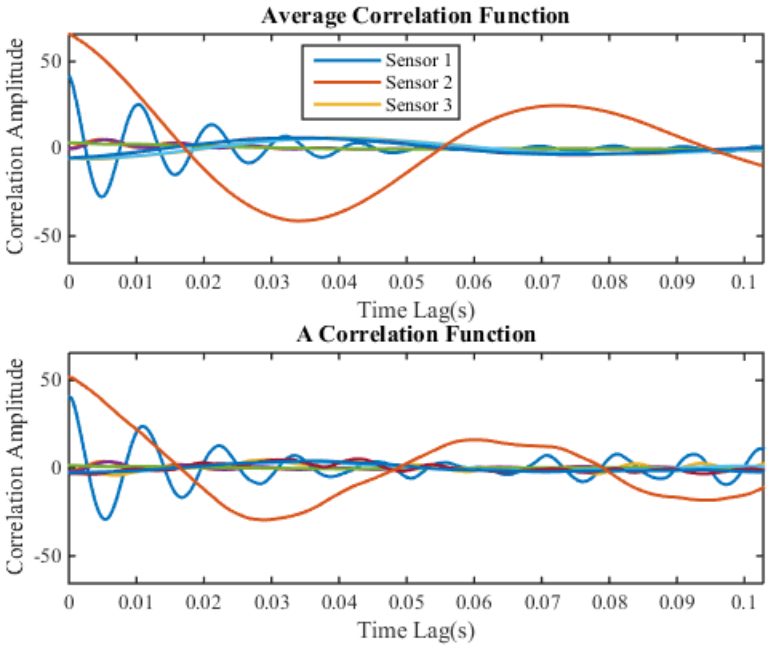

Figure 8-3 Averaged correlation function

The result from the implemented algorithm is discussed in the next section

8.1.3 **Stationary Excitation Results and Discussions**

Results from the stabilization diagram of the IAS simulated under stationary random excitation shown in figure 8-4 shows stable modes with some spurious poles from 0-100Hz. After applying the three conditions explained in equation (7-72) (see appendix E) three modes around 3Hz, 13Hz and 92Hz are found to be stable and are further used for modal properties identification. The 13Hz and 92Hz frequency component is in line with the predicted resonance frequencies. However, the 3Hz frequency component is not present in the predicted resonance frequencies. This frequency component might be as a result of the noise added to the signal

The identified mode shapes associated with 13Hz and 92Hz frequencies shown in figure 8-5 is 80% correlated with the predicted ones. However, there is some disparity between the predicted damping ratio and the identified ones as shown in table 8-1.

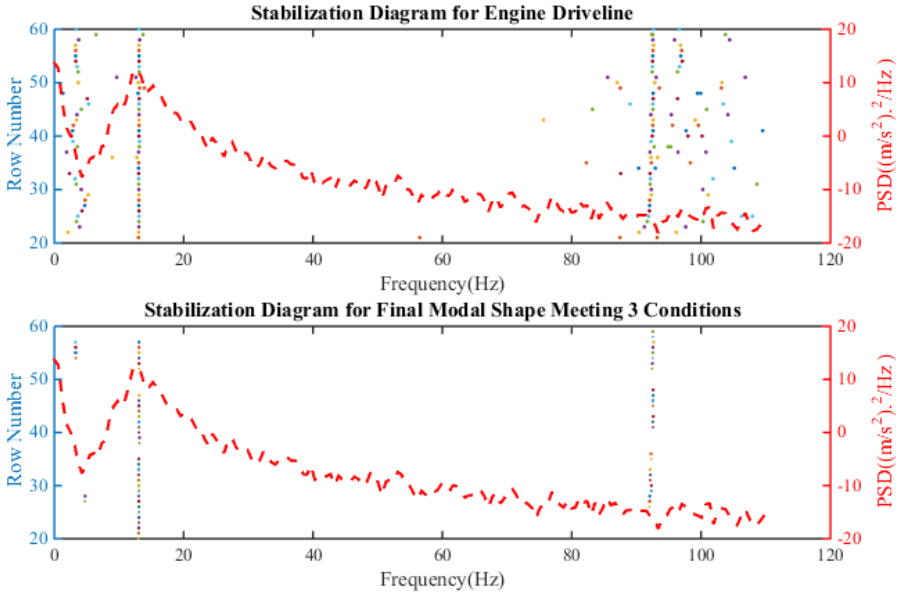

Figure 8-4 stabilization diagram for stationary random excitation

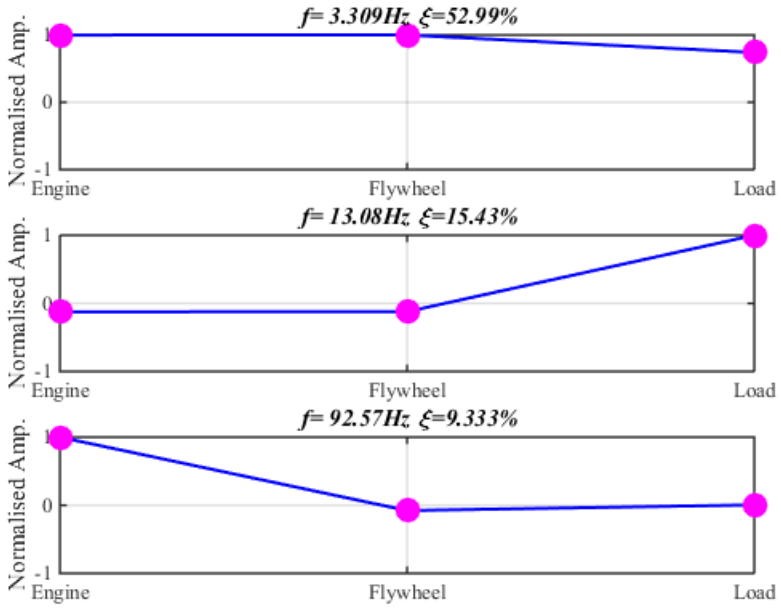

Figure 8-5 identified modal properties for stationary random excitation

Table 8-1 comparing identified and predicted modal properties for stationery random input

Mode	Predicted resonance frequency (Hz)	Identified resonance frequency	Predicted damping ratio	Identified damping ratio
1	Nil	3.3	Nil	0.5
2	12.9	13.1	0.12	0.15
3	92.2	92.6	0.18	0.09

8.1.4 **Non-stationary Excitation Result and Discussion**

Just like that of the stationary random input results from the stabilization diagram of the IAS simulated under non-stationary random excitation shown in figure 8-6 shows stable modes with some spurious poles from 0-100Hz. After applying the three conditions two stable modes around 13Hz and 91Hz frequency component are found and are further used for modal properties identification. The 13Hz and 91Hz frequency component is in line with the predicted resonance frequencies. In this case there is no presences of the 3Hz frequency component. The identified mode shapes associated with 13Hz and 91Hz frequencies shown in figure 8-7 is about 80% correlated with the predicted ones. However, there is also some disparity between the predicted damping ratio and the identified ones as shown in table 8-2.

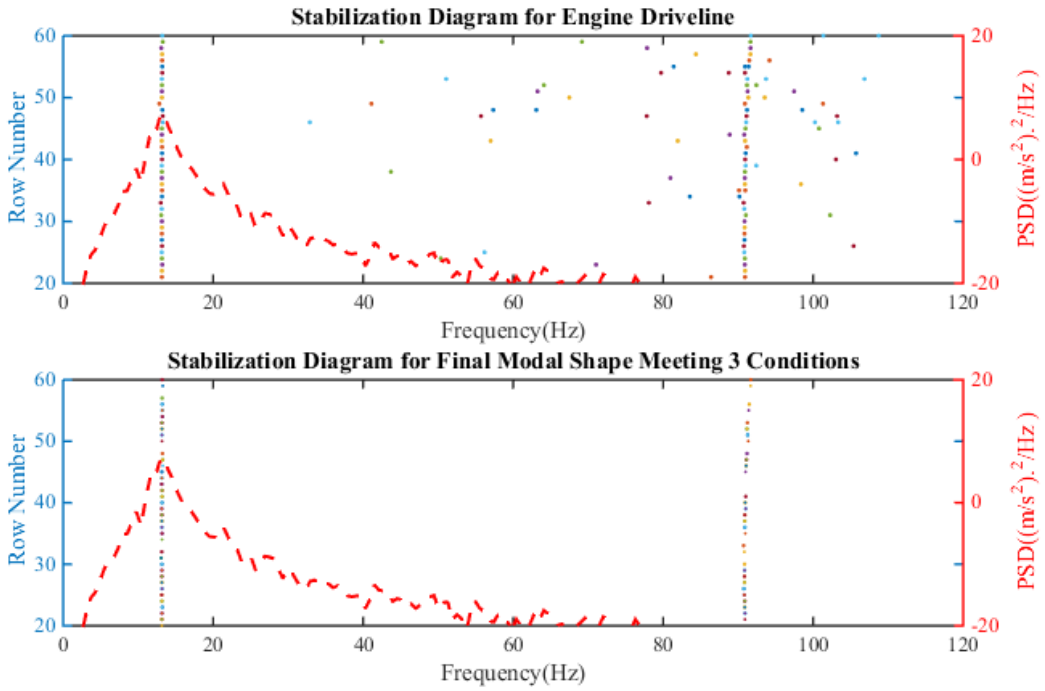

Figure 8-6 stabilization diagram for non-stationary random excitation

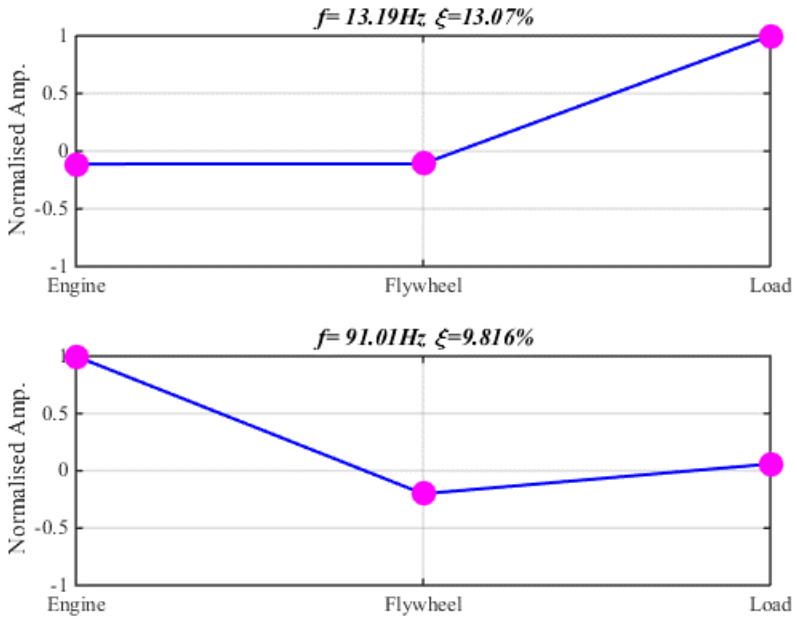

Figure 8-7 identified modal properties for non-stationary random excitation

Table 8-2 comparing identified and predicted modal properties for non-stationery random input

Mode	Predicted resonance frequency (Hz)	Identified resonance frequency	Predicted damping ratio	Identified damping ratio
1	12.9	13.2	0.12	0.13
2	92.2	91.0	0.18	0.09

8.2 Experimental Study of IAS Based Identification

The data used for the experimental evaluation was acquired from the JCB diesel engine test-rig described in section 4.2. The test-rig has three encoders installed at the front end, flywheel end and dynamometer end of the engine, which is in line with the reference points used in the simulation study.

Theoretically three engine transient operations can be considered for output-only modal identification; run up and run down, start-up and shut-down operations. Although, during the run-up and run down operation the engine sweeps through a significant frequency range, it is not considered in this work because of the significant presence of some forcing frequencies (firing frequency). The start-up operation of engines is usually very complex, it's categorized into the cranking, run-up and transition to idle phase. During the cranking phase the engine-dynamometer system is not under the influence of the combustion forces. Because the engine pumps only air as the starter motor transmits torque to the crankshaft through a large gear ratio to overcome the inertia and friction of the engine at standstill (Mohire and Burde, 2010). During the other two phases of engine start-up operation, the influence of the combustion forces is prevalent as the engine performs an ascending sweep through a suitable frequency range which is usually below the engines idle frequency. This indicates that the IAS estimated during engine start-up operation might not be a reliable response for output-only modal identification. During the shutdown operation, fuel supply is cut off in the injector pump. So, instead of combustion forces, there is only the presence of a gradually decaying compression pressure in the cylinder. Therefore, the system would perform a descending sweep through a suitable frequency range. Since, the

compression pressure is a decaying one, some of the system's torsional natural vibration mode should become eminent.

8.2.1 **Test Procedure and Signal Processing**

Using the event trigger option of the Sinocera data acquisition system and the one pulse per revolution signal as the trigger, the angular displacement of the engine driveline was sampled at a sampling frequency of 750 kHz during start-up, Idle and shut-down operation of the engine. The test was repeated under the same condition for eight times so as to enhance the accuracy of identified modal properties using the covariance-driven SSI algorithm. Before the correlation function matrix is estimated the data from the engine's operations shown in figure 8-8 below went through some initial pre-processing steps. The first step was to check the quality of the raw data as it comes out of the data acquisition system. The saved raw data is then calibrated and IAS estimated using time domain based technique described in section 3.3.4.1. This was then followed by resampling of the data for easy computation. The signal was then classified into the different engine operating conditions of start-up. Idle and shut down. While the estimated IAS for engine start-up and idle operation is not further processed, that of the shutdown operation is saved and used for the implementation of a covariance-driven SSI algorithm. The estimated IAS for the engine's shut-down operation shown in figure 8-9 shows the speed performing a descending sweep from 900rpm to 0rpm. The time and frequency domain representation of the estimated IAS shown in figure 8-9 shows similar trend with that of the simulated ones. The time and frequency domain representation indicates the presence of both high and low frequency components. The number of oscillations per second in the time domain representation of each encoder varies from engine to dynamometer reference points of the system. While that from the engine shows more oscillations per second indicating the presence of high frequency component, the ones from the dynamometer shows fewer cycle per seconds indicating the presence of low frequency components. While the part of signal showing more oscillation per second is more visible at initial part of the signal, that showing fewer oscillation per second is at the later part of the signal. This feature of the signal shows the non-stationary nature of the signal indicating the difficulty involved in using the signal for output-only modal properties identification. Thus, the SSI technique which is very robust was chosen above all other time domain OMA techniques.

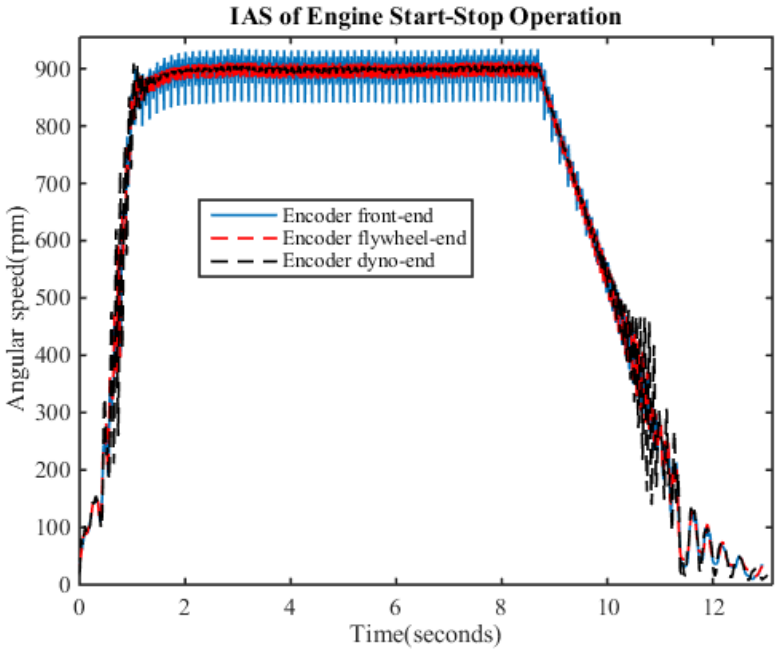

Figure 8-8 angular speed response of engine start-stop operation

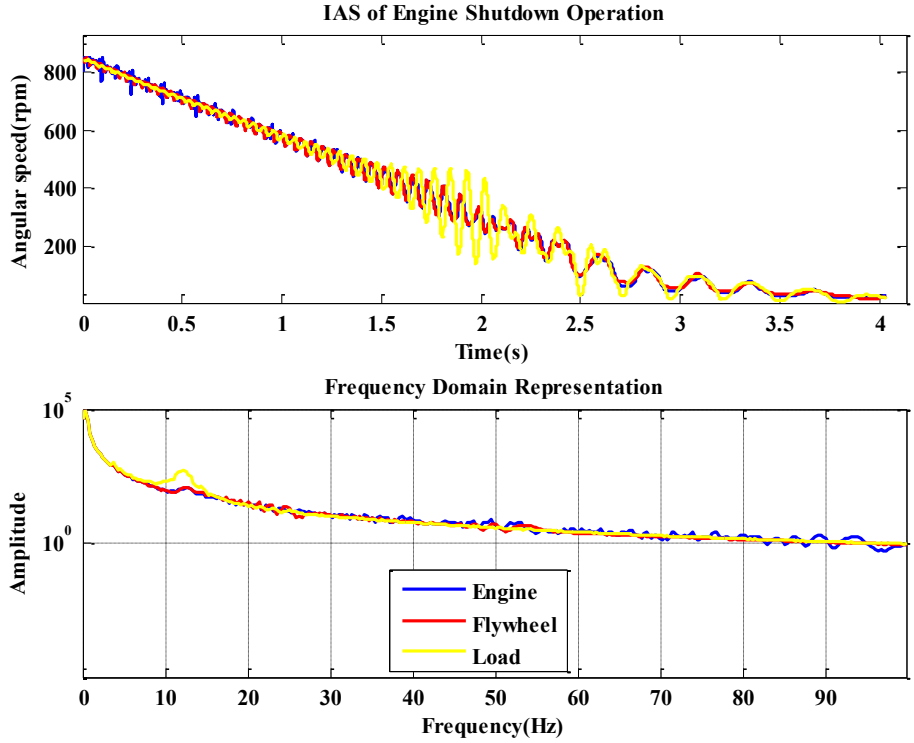

Figure 8-9 IAS time and frequency domain representation for shut-down operation

.

The frequency domain representation of the measured IAS show peaks around 13Hz and other frequency components. The amplitude of the low frequency (13Hz) component is more at the dynamometer reference point compared to the other reference points of the system. In likewise manner the amplitudes of the other frequency (40Hz, 60Hz and 90 Hz) component is more visible at engine and flywheel reference point compared to that of the dynamometer. The aforementioned trend is also evident in the spectrum of the simulated outputs using both stationary and non-stationary inputs shown in section 8.1.1. However the spectrum of the simulated output using non-stationary random input is closer to that of measured IAS of engine shutdown operation, because it is more sensitive to vibration amplitude as shown in appendix C.

8.2.2 IAS Based Identification with Results and Discussion

The IAS data estimated during transient engine shut-down operation is then used for implementing an output-only modal identification using the same covariance-driven subspace algorithm as with the simulated cases. The main difference between the algorithm used for the simulated IAS under random excitations and the measured IAS during transient engine shut down operation is the introduction of some iterative process in the step 2 of the algorithm used in section 8.1.2. This iterative process is added due to the non-stationary nature of the measured IAS. Rather than passing the entire correlation functions through the threshold criteria, they are divided into three segments. This means that 3 separate segments of the correlation function is averaged and used for the modal properties identification. Using a minimum and maximum model order of 20 and 97 the matrices O_i, C_i^{ref} were computed for each sections, from which the system matrices and modal parameters are estimated. The stabilization diagram for each section, chosen based on trial and error was constructed according to the following pre-set criteria: mode shape vector (MAC) 50%, damping ratio 20% and eigenfrequency 1050%. The stable modes for all segments and their resonance frequencies is further passed through two selection criteria. The first is to select the modes whose frequencies occurs at certain rate over orders. The second is to remove the harmonic components present among the selected modes leaving behind only torsional structural component.

The stabilization diagram of the first segments shown in figure 8-10 shows stable modes with some spurious poles from 0-100Hz. After applying the three conditions explained in equation (7-72) three modes around 22Hz, 44Hz and 79Hz is found to be stable.

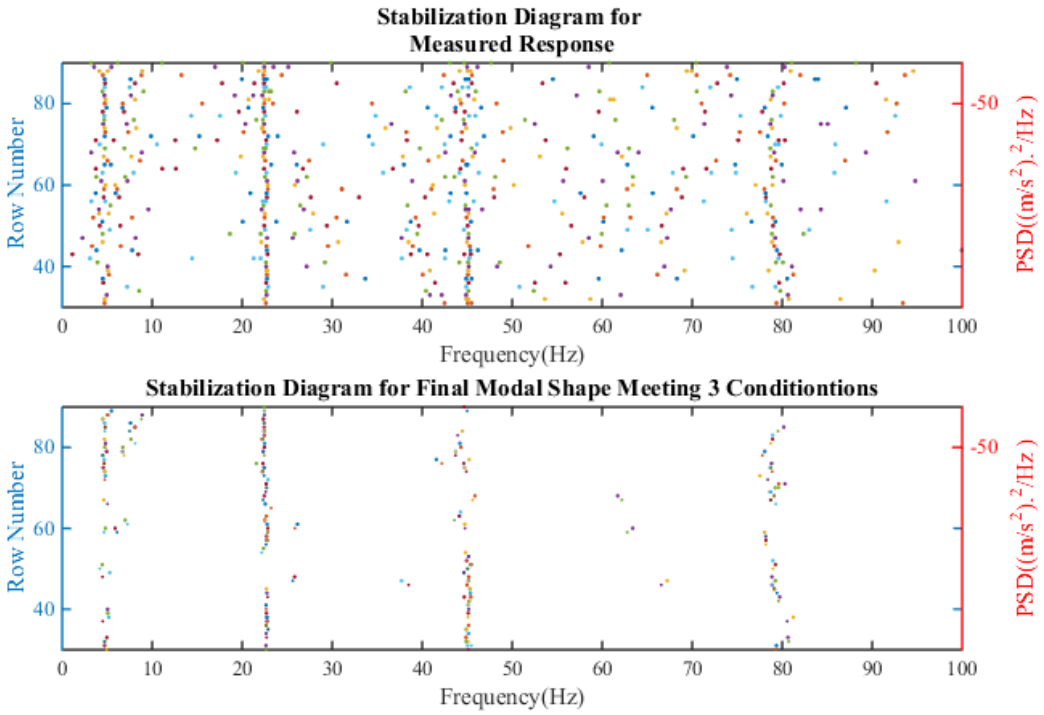

Figure 8-10 stabilization diagram of first segment

The 22.4Hz and 45.1Hz frequency component can been regarded as a harmonic components of the result from the crank shaft rotational frequency. These two frequency component are not anyway related to the torsional structural property of the system because they are within engine operating speed range. The 79Hz frequency component cannot be attributed to any harmonic component and is far away from the engine speed range. Thus, the 79Hz frequency component is further used for the modal properties computation.

The stabilization diagram of the second section shown in figure 8-11 shows stable modes with some spurious poles from 0-70Hz

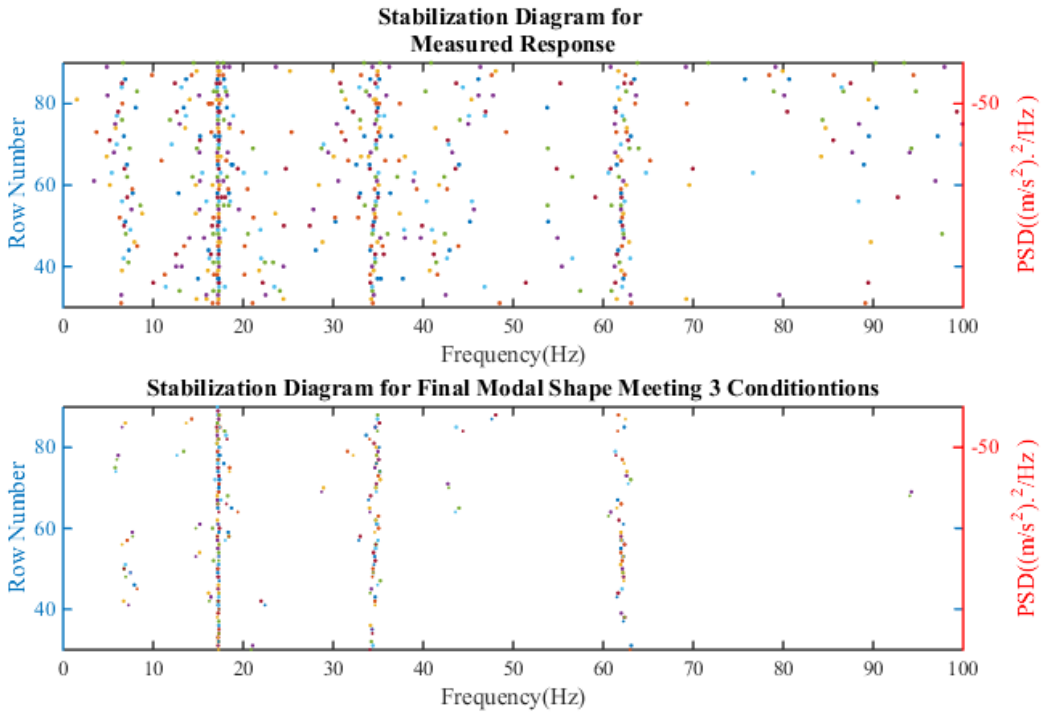

Figure 8-11 stabilization diagram of second section

After applying the three conditions three modes around 17.2Hz, 34.9Hz and 62.1Hz are found to be stable. The 17Hz and 34Hz frequency component can been seen as a harmonic component of resulting from the shaft rotational frequency. These three frequency component are not anyway related to the torsional structural properties of the system because they are also within engine operating speed range. The stabilization diagram of the third section shown in figure 8-12 shows stable modes with some spurious poles from 0-70Hz. After applying the three conditions two modes around 4.9Hz, and 12.5Hz are found to be stable. These two frequency component are below the engine operating speed range and cannot be attributed to any harmonic component of the shaft rotating frequency. The 12.5Hz frequency component is very close to the predicted low frequency resonance of the engine-dyno system. The 5Hz frequency component might result from the translation vibration of the rotating shaft.

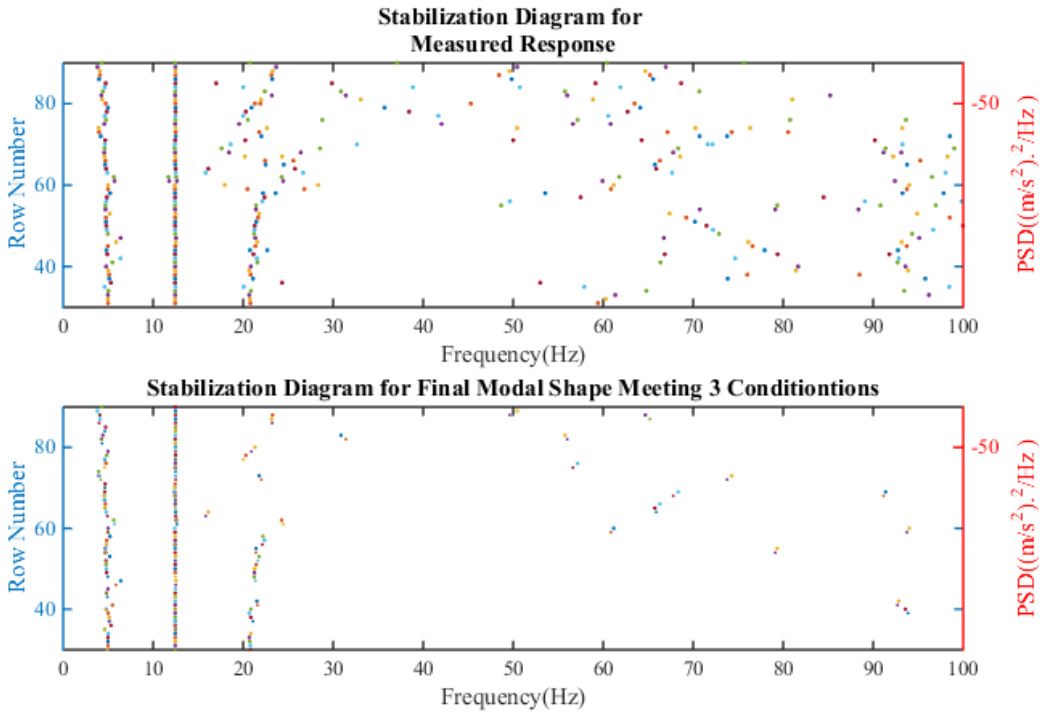

Figure 8-12 stabilization diagram of third section

From visual inspection of the mode shapes of all the stable modes (see appendix B), the mode shape associated with most of the harmonic components are very correlated and different from that of 12.5Hz and 79.0Hz. The estimated mode shape associated with 12.5Hz and 79.0Hz frequency component are shown in figure 18-13. The predicted and identified mode shape associated with the high and low frequency resonance are about 80% correlated. However, there is also some major disparity between the predicted modal properties and the identified ones as shown in table 8-3. Firstly there is about 15% error in the estimation of the high frequency resonance as compared to 3% for the low frequency resonance. This error margin might be due to the inaccuracies involved with the use of the covariance-driven SSI algorithm as stated in previous chapter of this thesis (section 7.4.1). Another reason might be due to the excitation amplitude needed for this vibration mode to be excited. Simulation results using the non-stationary random input (see appendix C) indicates that the excitation amplitude affects the amplitude of the high frequency vibration mode more compared to the low frequency vibration mode.

Table 8-3 predicted and identified modal properties for measured IAS

Mode	Predicted frequency (Hz)	Identified frequency (Hz)	%Δ	Predicted damping ratio	Identified damping ratio	%Δ
1	12.9	12.5	-3%	0.12	0.03	-75%
2	92.2	79.0	-14%	0.18	0.02	89%

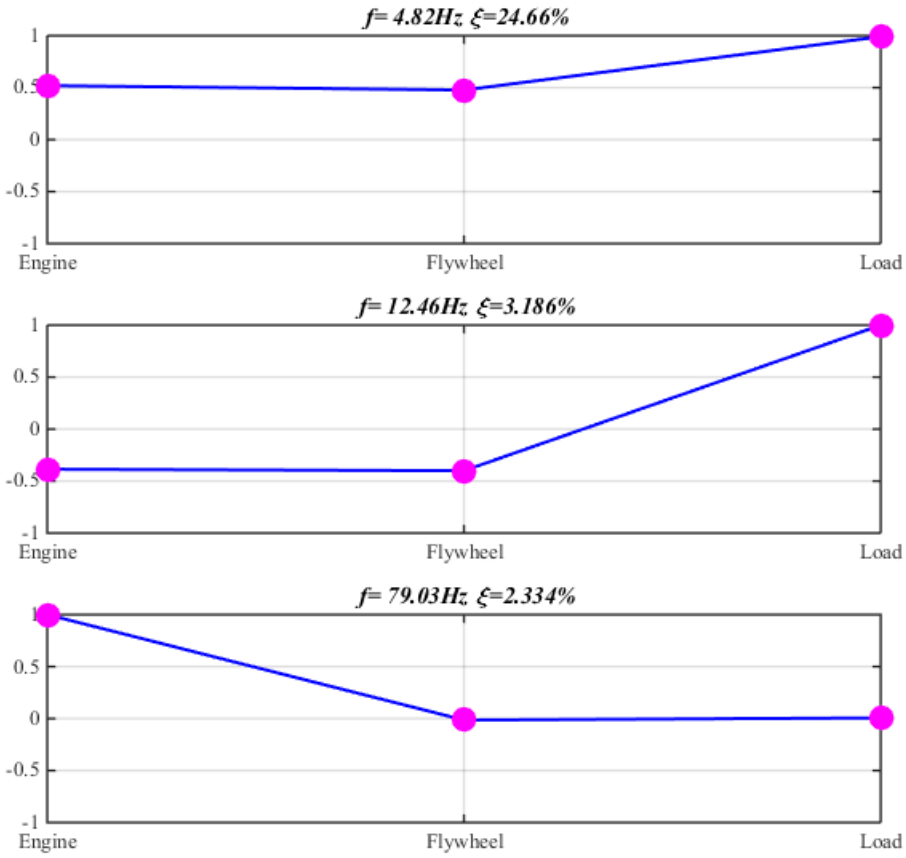

Figure 8-13 identified modal properties for measured IAS

When the amplitude of this vibration mode is very low it can be masked by measurement noise which makes it difficult for identification especially when the output-only is used. Moreover, a large error margin is also found between the predicted damping ratios and estimated ones.

This is very typical with damping ratio estimation using output-only modal identification. As consistent estimation of damping ratio from experiments can be notoriously difficult. Hence, the

accurate estimation of damping ratio using both OMA and EMA techniques is still an ongoing research area.

8.3 Modal Properties Based Engine Diagnostics

So as to further study the dynamics of the engine-dynamometer system, a start-stop test was carried out on the system with complete misfire induced in the first, third and fourth cylinders of the engine respectively. These cylinders were chosen due to their position relative to the engine. The first and fourth cylinder is at the extreme left and right of the engine while the third cylinder is at the middle of the engine. The estimated angular speed response during these individual cases as shown in the figure 8-14 shows a lower idle speed for each of the misfire cases. This means there is a drop in the total torque produced by the engine in every misfire case.

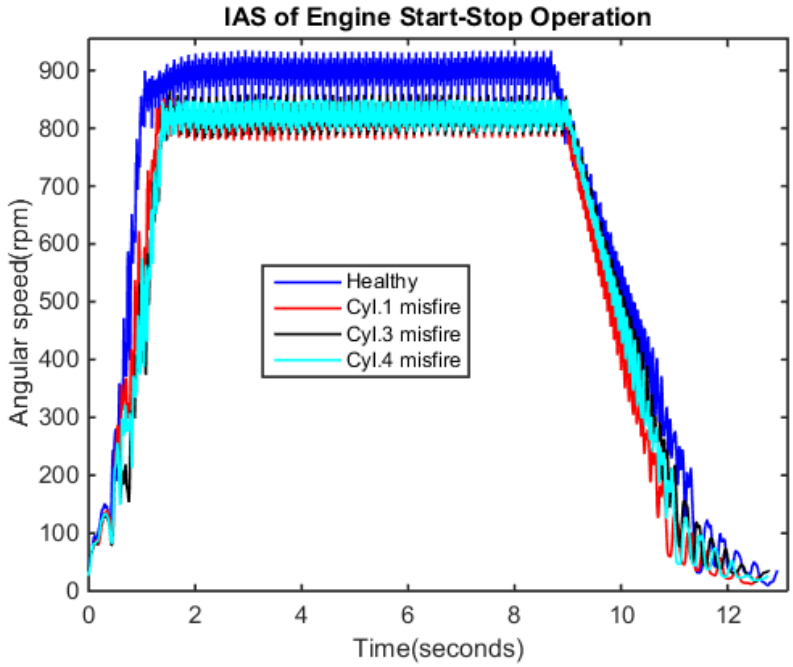

Figure 8-14 response of engine start-stop operation for healthy and misfire cases

The frequency domain representation of respective estimated IAS with complete misfire shown in the figure 8-15, show some alterations around the low frequency component frequency component compared to that with no misfire. The amplitudes around the other frequency component especially the <90Hz seems to be decreasing. This decrease in the amplitude of the high frequency component suggest a change in the vibration excitation during shutdown with misfire in the engine.

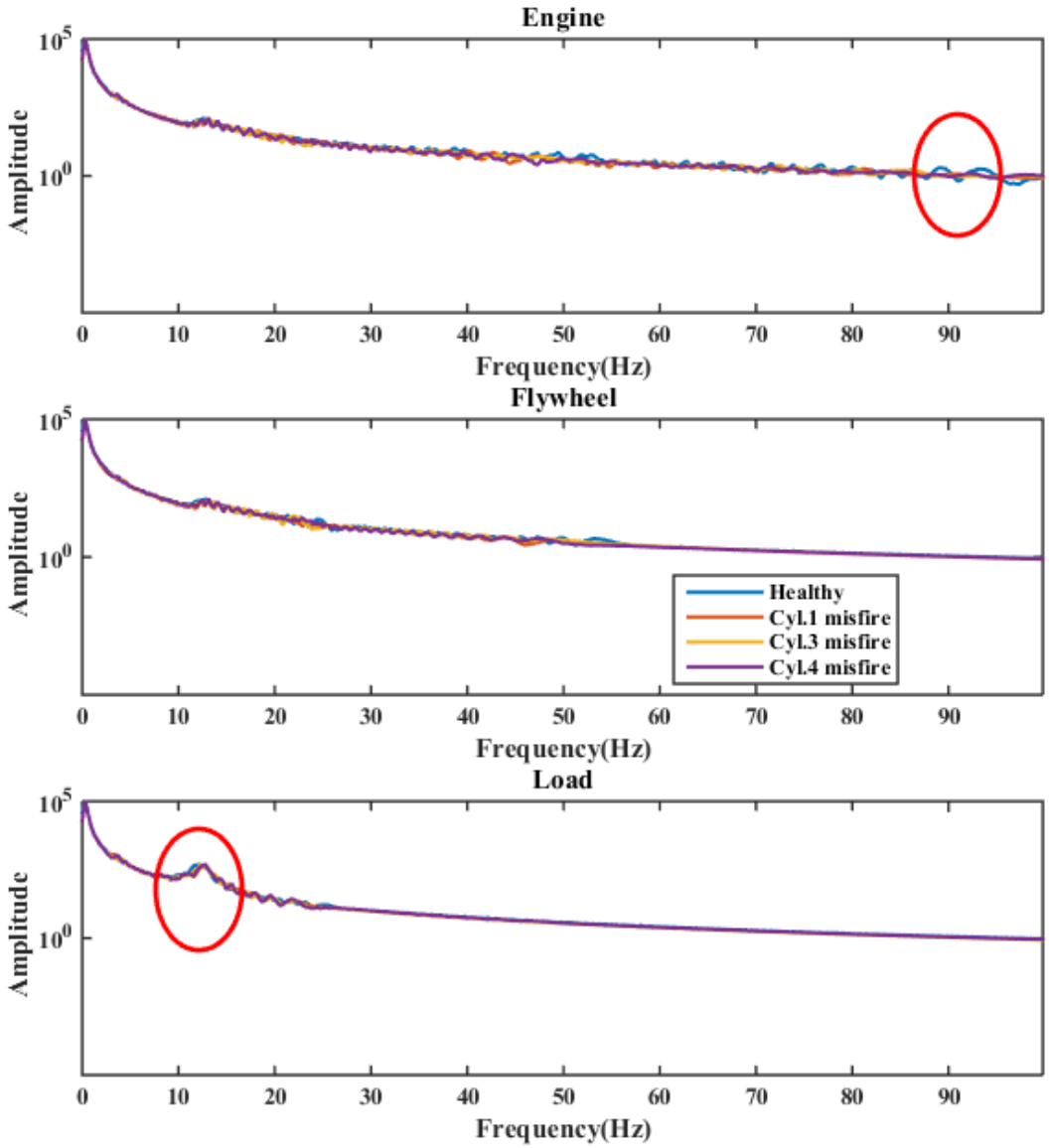

Figure 8-15 frequency domain representation of estimated IAS with misfire

The modal parameters of the system were extracted using the covariance-driven subspace identification algorithm used in the previous section. The mode shape of IAS response with complete and no misfire shown in the figure 8-16, indicates that the mode shape low frequency resonances is more reliable for complete misfire detection. Because, the estimated mode shape of the low frequency vibration mode using the measured outputs of engine with faults show features that can be used for diagnosis. The mode shape of the low frequency vibration mode with faults shows more amplitude at the engine flywheel side of the system compared to that with no fault.

The estimated mode shape of the high vibration mode using the measured outputs of engine with faults shows no meaningful feature that can be used for diagnosis. Hence, the high frequency vibration mode is not sensitive to perturbation resulting from engine faults

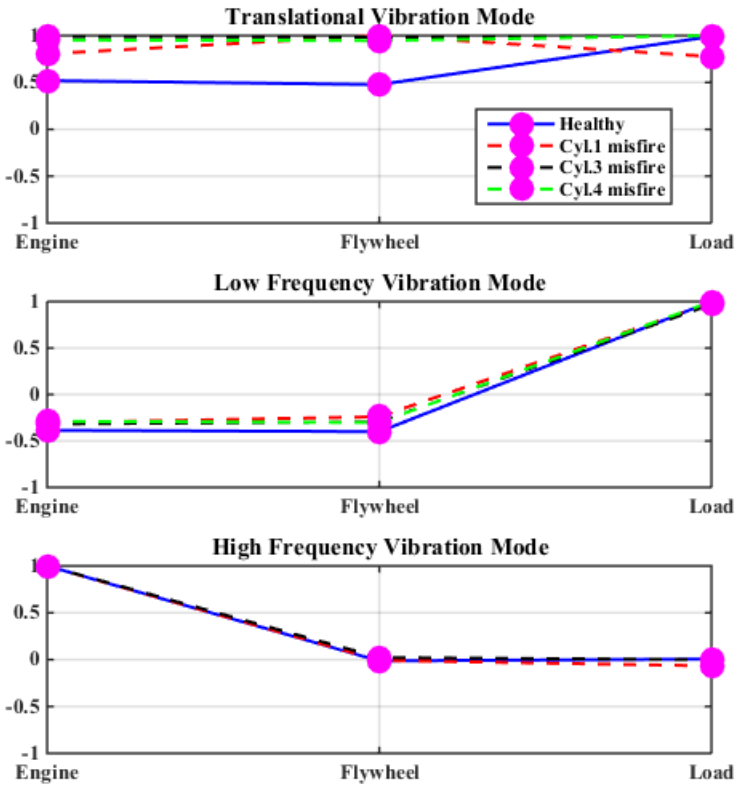

Figure 8-16 mode shape of healthy and faulty engine

The estimated frequency and damping ratio of the low and high frequency vibration mode shown in the table 8-2, indicates a 5-14% increase in the estimated low frequency resonance with misfire compared with the no misfire case. This means complete misfire in any cylinder results in the mass distribution of the flywheel and adaptor moving a bit further from its rotational axis thereby altering its rotational inertia. Noticeably, the high frequency resonance remains almost unaltered with the faults. More so, the algorithm was unable to estimate high frequency resonance with misfire in the 4^{th} cylinder.

Table 8-4 estimated frequency and damping ratio of healthy and faulty responses

Modes	Identified properties no misfire case		Identified modal properties 1st cylinder misfire				Identified modal properties 3rd cylinder misfire				Identified modal properties 4th cylinder misfire			
	f (Hz)	ξ	f (Hz)	%Δ	ξ	%Δ	f (Hz)	%Δ	ξ	%Δ	f (Hz)	%Δ	ξ	%Δ
1	12.5	0.03	13.7	9.6	0.08	160	13.1	4.8	0.05	67.3	13.1	4.8	0.035	15.4
2	79.0	0..02	79.1	0.0	0.04	100	79.1	0.0	0.06	200	Nil	Nil	Nil	Nil

8.4 **Key Findings**

In this chapter results of simulation and experimental evaluation of IAS based on-line modal identification of an engine-dynamometer system has been presented. The results of the simulated evaluation was implemented using stationary random in and a non-stationary random signals as inputs. The output response using the non-stationary random input is closer to the real engine-load response compared to that of the stationary random input.

The covariance-driven SSI technique when implemented with simulated angular speed output from a three DOF engine-dynamometer system can extract the two flexible vibration modes. The frequencies and modal shapes associated with each flexible vibration modes are very similar with the predicted ones.

The experimental evaluation results presented were implemented using IAS signal measured during transient engine shut-down operation. IAS outputs during transient engine shut-down operation is sufficient enough for output-only modal identification of an engine-dynamometer system. The covariance-driven SSI technique when implemented with IAS from engine transient shut down can extract the flexible vibration modes. The frequencies and modal shapes associated with each flexible vibration modes are very similar with predicted ones. The frequency associated with the low vibration mode can be more accurately determined using the covariance-driven SSI algorithm. However, the damping ratios obtained from the implementation of the SSI technique has large errors. This is very typical with damping ratio estimation using output-only modal identification. As consistent estimation of damping ratio from experiments can be notoriously

difficult. Hence, the accurate estimation of damping ratio using both OMA and EMA techniques is still an ongoing research area.

IAS of engine shutdown operation.

The identified modal properties were used to study the system behaviour during individual cylinder misfire. The mode shape of the low frequency resonance showed characteristics for each cylinder misfire. A complete misfire in any cylinder alters the inertia of the flywheel thereby altering the resonance frequency of the engine-dynamometer system. It is expected that this change in resonance frequency, especially of the low frequency resonance, if taken into consideration during IAS model based diagnostics would enhance its diagnosis performance.

CHAPTER NINE

9 IMPLEMENTING IAS BASED DIAGNOSIS

In this chapter, IAS signal and model based diagnostics are implemented using IAS estimated from the JCB diesel engine test rig described in chapter four. IAS is estimated from the engine under three different fault conditions described in chapter 4. The chapter starts with the time and frequency domain representation of the IAS estimated at varying speed and load conditions for both healthy and faulty cases. This is then followed with an IAS model based diagnostics which considers the effect of modal properties, specifically the low frequency resonance, on the extracted cylinder pressure torque.

9.1 Introduction

The estimated IAS used in this chapter was done using the Hilbert demodulation frequency domain technique which is more numerically stable and robust for engine steady state conditions. The IAS based diagnostics implemented in this chapter is done with IAS estimated from engine under three fault conditions: complete misfire in cylinder 1 and 4, abnormal exhaust valve clearance conditions and the injector preload washer thickness alterations. The speed and load condition of the engine were altered during the complete misfire test for the health of the test rig. These faults were chosen due to their relevance in real day-to-day engine operations and the components altered are vital to the engine's valve train and fuel injection systems described in chapter 2. For the implementation of IAS signal based diagnostics, the time and frequency domain representation of estimated IAS from healthy and faulty engine conditions will be compared. While for the model based IAS diagnostics the state space model developed in chapters 5 is used for the reconstruction of the cylinder pressure torque from the estimated IAS of both healthy and faulty engine conditions.

9.2 Signal Based Diagnostics

As discussed in chapter 2, IAS signal based diagnostics are methods which uses the time domain representation of the signal for fault detection. While there are several methods that have been used for fault detection in this method, because of the main focus of this thesis, the time domain waveform as well as the frequency domain representation of the estimated IAS is used. The following sub-sections presents and discusses results from respectively faults using the signal based methods.

9.2.1 Misfire Diagnosis

Firstly, the IAS waveform characteristics in line with the engine operating cycle as shown in figure 9-1 show trough and peak speed values for every half revolution. This makes it four trough and peaks speed values for every two revolutions (one engine cycle), which is expected for a four cylinder engine. These four peaks and trough speed values corresponds to compression and combustion effect of each cylinder respectively. As explained previously in chapter 6, the peak speed values result are due to the produced torque exceeding the load value. Hence, should the

IAS waveform be in this form at any speed and load condition the time domain representation if properly processed should be able to detect and localize the fault.

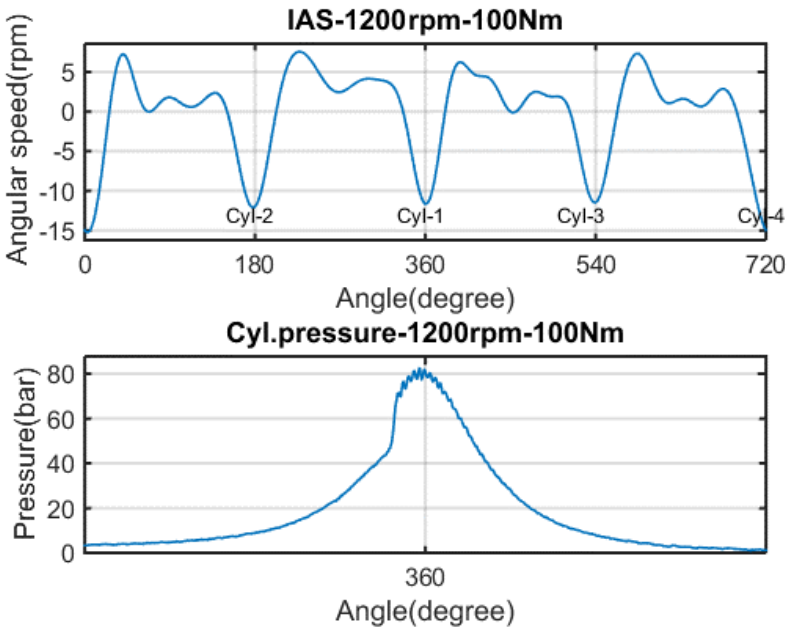

Figure 9-1 IAS waveform and 1st cylinder pressure of diesel engine at 1200rpm

However, this is not the case at higher speed as shown in the Figure 9-2 below, at high speed the IAS waveform shows about 2 peak speed values and a trough speed value at every half revolution. This is because the effect of the torque due to reciprocating inertia caused by the acceleration and deceleration of the piston becomes more and more important as speed increases. So, at reasonably high speed this effect masks the peak due to combustion for respective cylinders, making the IAS waveform look different compared to that at low speed. In this situation the four firing per engine cycle (720 degree) are not clearly seen. In this case, it would be difficult to use the time domain representation for fault detection and localization. This is a major weakness of the signal based IAS diagnostics, which can be obtained in the model based IAS diagnostics.

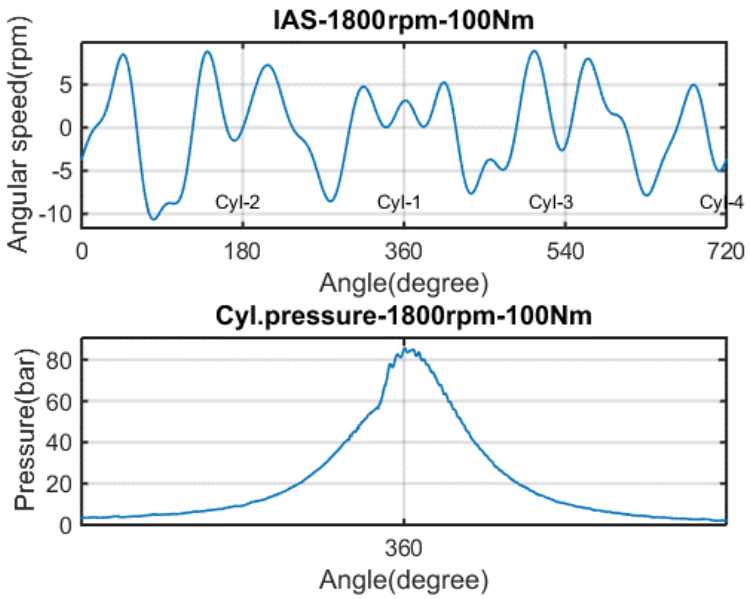

Figure 9-2 IAS waveform and 1st cylinder pressure of diesel engine at 1800 rpm

9.2.1.1 **Time Domain Based Diagnosis**

Complete misfire was induced in the first and the fourth cylinder of the JCB diesel engine. The first cylinder pressure shown in figure 9-3 indicates an alteration in peak pressure value with a complete misfire in any cylinder. With a complete (100%) misfire in the first cylinder, there is about a 20% drop in the peak pressure value compared to the healthy case as shown in the figure 9-4. However there is a 20% increase in peak pressure value with a complete misfire in the fourth cylinder. This suggests the manner in which the engine compensates for the reduction in the pressure torque contribution in one cylinder. It can be presumed that the reduction in the peak cylinder pressure resulting from complete misfire in the first cylinder would be compensated for by an increase in other cylinder.

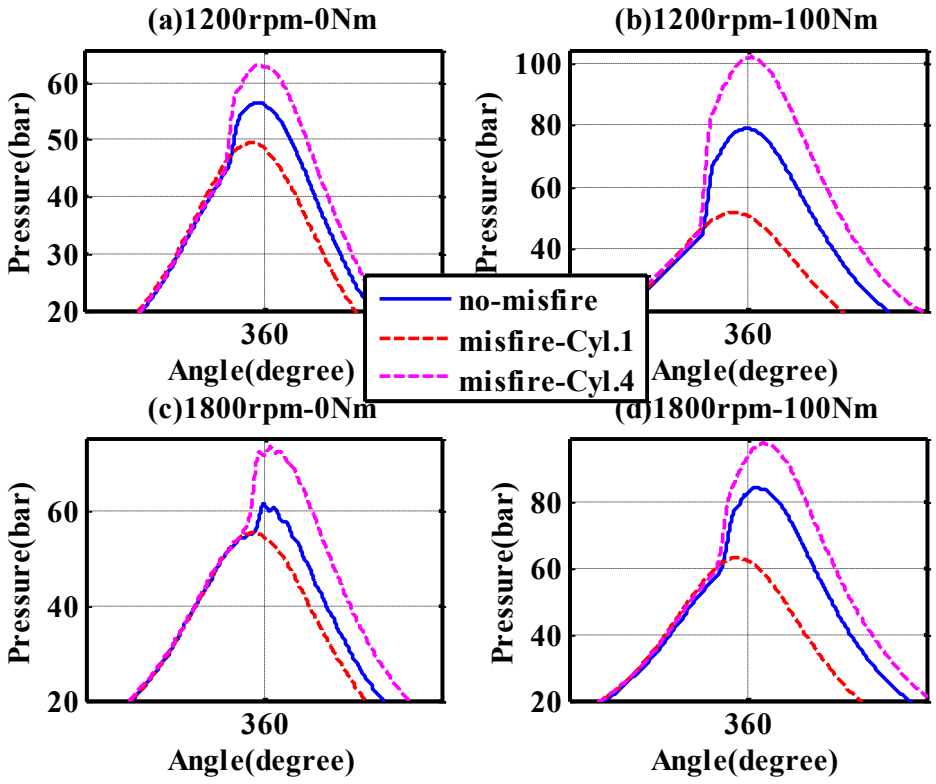

Figure 9-3 1st cylinder pressure of healthy and faulty diesel engine

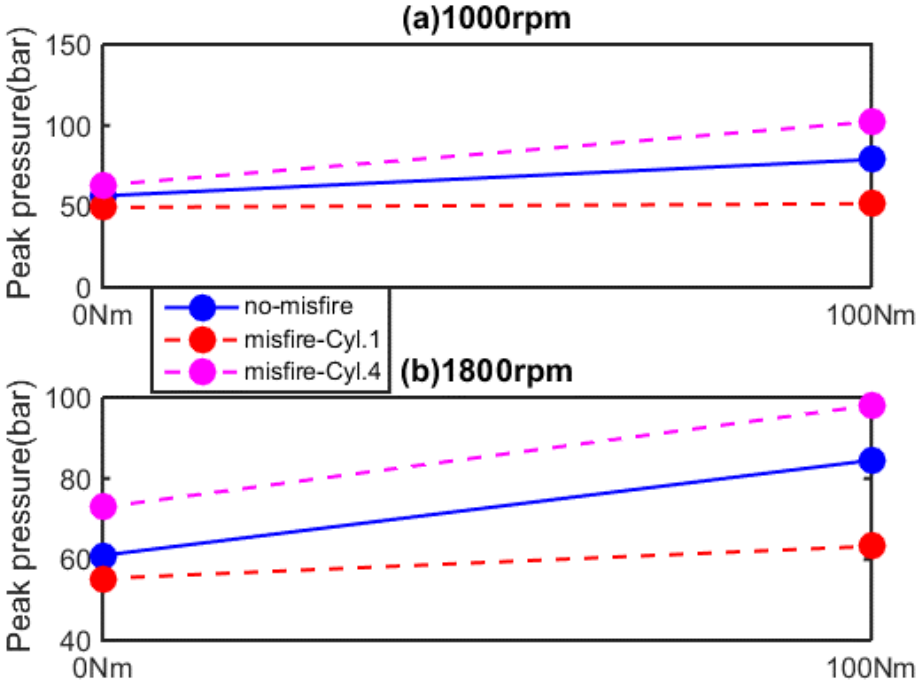

Figure 9-4 peak 1st cylinder pressure of healthy and faulty diesel engine

Since, there was only a pressure sensor in the first cylinder this relation cannot be ascertained. However, with a clear IAS waveform of healthy and both complete misfire cases, this relation is expected to surface. The IAS time domain representation of the healthy and faulty engine conditions shown in the Figure 9-5, show a clear distinction between both faults at 1200rpm-0Nm and 100Nm. Although the IAS waveform at 1800rpm-100Nm also shows a distinction between complete misfire, it is not as evident as that of 1200rpm-100Nm.

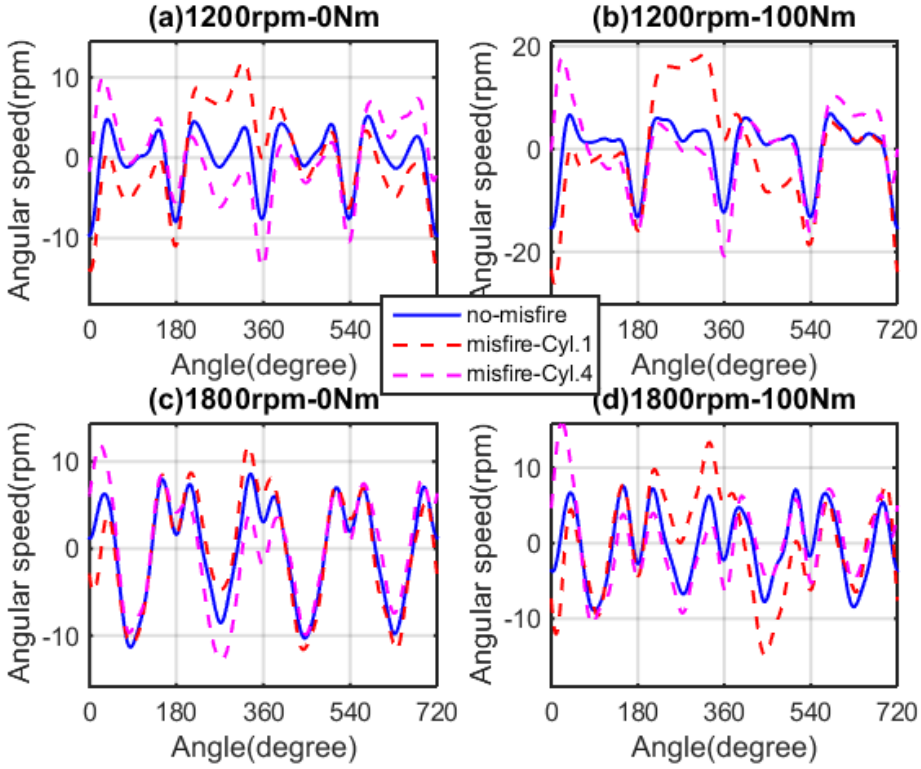

Figure 9-5 IAS of healthy and complete misfire cases of a diesel engine

So as to show a clear IAS waveform which can be used for the dynamic characteristics of the engine during individual cylinder misfire, the IAS waveform at 1200rpm-100Nm for healthy and faulty conditions were chosen as shown in the figure 9-6. The IAS waveform of complete misfire cases compared to that of no-misfire case shows significant alteration in the trough speed values that pertains to that cylinder. With complete misfire in the first cylinder the trough speed value that pertain to the 1st cylinder increases from about -10rpm to 5rpm. While that with complete misfire in the 4th cylinder increase from -15rpm to about 0rpm. This indicates that there is a relationship between the trough speed values, which represents the transition from compression to combustion in a cylinder and the peak cylinder pressure values. Because, the first cylinder pressure

plot, shown in figure 9-3, shows about 40% reduction in peak pressure value with complete misfire in the first cylinder. This means that the peak cylinder pressure is inversely proportional to the trough speed value that pertains to the cylinder. The presumption of how the engine balances a reduction in pressure torque contribution of a cylinder is clearly apparent in the IAS waveform results. With complete misfire in the 1st and 4th cylinder, the trough speed values that pertains to the cylinders with no misfire reduces, suggesting an increase in their peak pressure values. The trough speed value of cylinder 2 and 3 shows about 35% reduction for complete misfire in the 1st and 4th cylinder.

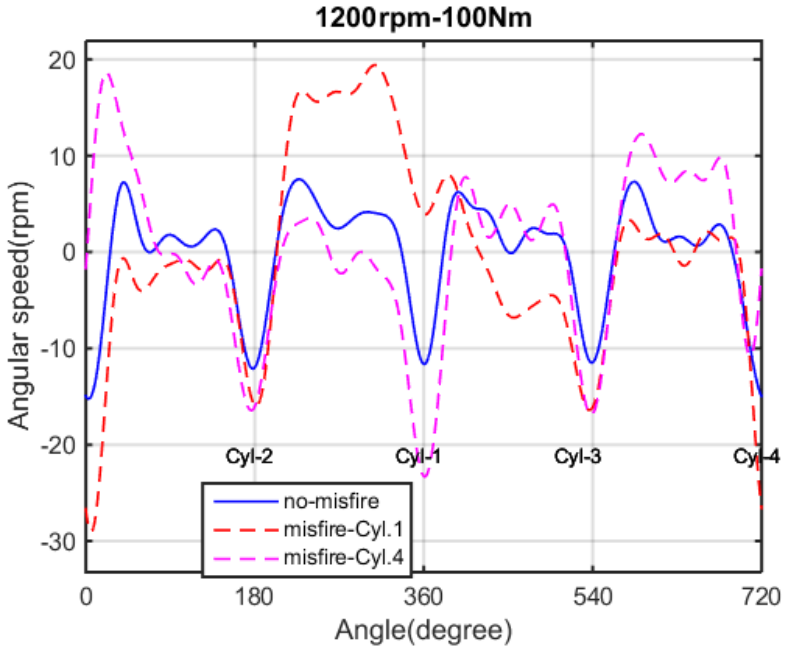

Figure 9-6 IAS of healthy and complete misfire cases at 1200rpm-100Nm

While, the trough speed value that pertains to the 1st cylinder shows a significant 100% reduction for complete misfire in the 4th cylinder, the trough speed value that pertains to the 4th cylinder also shows significant 90% reduction for complete misfire in the 1st cylinder. This explains the reason why there was about 40% increase in peak pressure of the 1st cylinder when there was a complete misfire in the 4th cylinder and vice versa. This indicates that in a four cylinder in-line engine, the cylinders at the extreme ends (free-end and the flywheel-end), plays vital role in balancing the total pressure torque contribution in case of complete misfire in any cylinder. Therefore, the trough speed values of IAS waveform at low speed can be used for complete misfire detection and localization as shown in the figure 9-7.

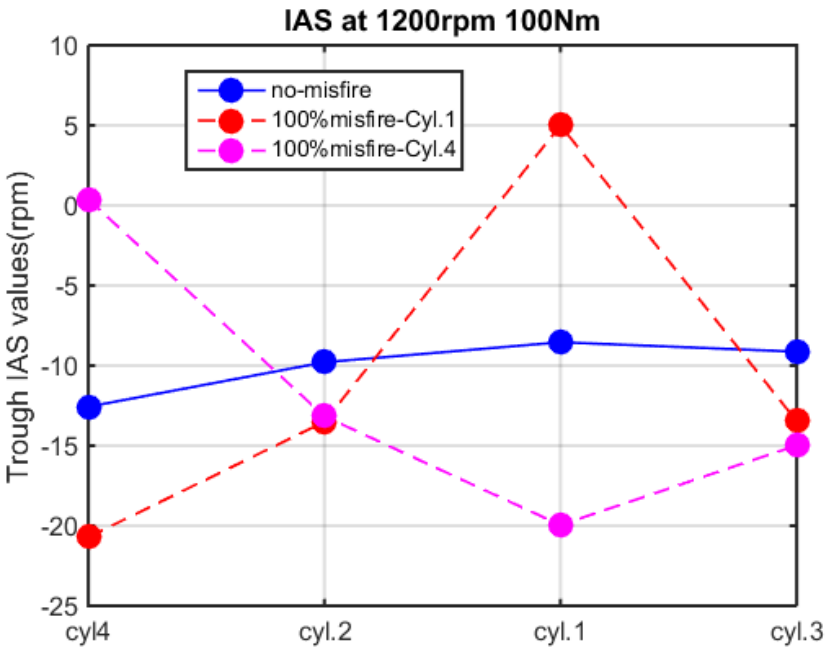

Figure 9-7 IAS trough values for healthy and misfire engine conditions

There is an increase in the trough values that pertains to the misfiring cylinder when compared to their values at healthy engine condition. The level of increase of the IAS trough values can be used for misfire detection to a certain degree. However, this method is only viable at low engine speed because at reasonable high engine speed the trough speed values that pertains to individual cylinders are masked by the torque due to reciprocating inertia. Thereby making it difficult to use this technique for early misfire diagnosis.

9.2.1.2 **Frequency Domain Based Diagnosis**

This IAS based diagnosis method involves the representation of the estimated IAS in frequency domain. The techniques used range from using the amplitude to the phase information of the firing frequencies and it's high and low order harmonics (Charles et.al. 2009). However, for this thesis this method is only used for fault detection purposes only. The frequency domain representation of IAS estimated from the different engine conditions shown in figure 9-8, indicates significant increase in the amplitudes of some low frequency component for the faulty cases. This phenomenon is mostly evident at 100Nm of both 1200rpm and 1800rpm engine speed.

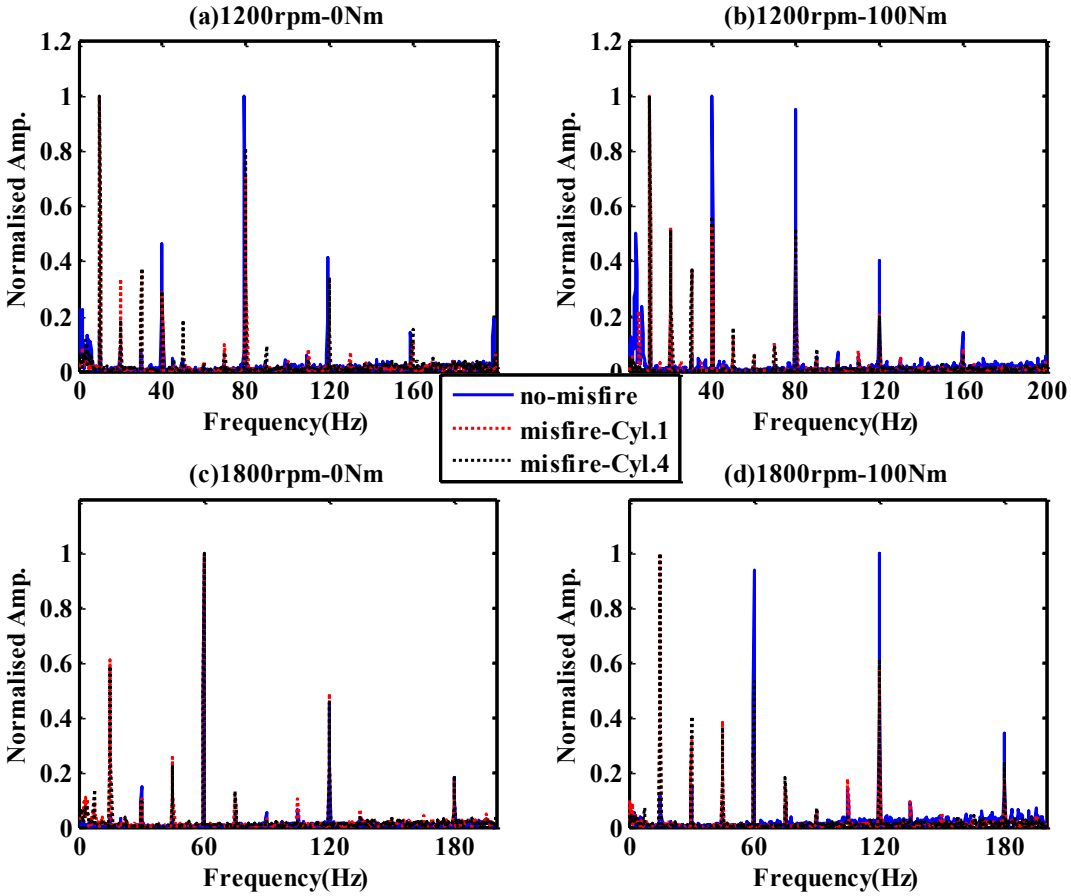

Figure 9-8 frequency domain representation of IAS for healthy and faulty engine conditions

So as to further the discussion, the frequency domain representation of 1200rpm-100Nm is plotted alone as shown in figure 9-9 below. IAS spectrum of complete misfire in the 1st and 4th cylinder of the engine, shows a significant amplitude increase around lower frequency components of 10Hz, 20Hz and 30Hz compared to the healthy case. The amplitude of the 10Hz frequency component is more significant compared to the firing frequencies and its harmonics. These frequency components correspond to the one and half order (1.5 of 20Hz), half order (0.5 of 20Hz) harmonics of the engine's rotational frequency as well as the engine's rotational frequency (20Hz). Normally, in the IAS spectrum of a 4-cylinder in-line diesel engine, the amplitude of the firing frequency or its 1st amplitude is dominant depending on the loading conditions. This is because the firing orders of most in-line engines are designed so that the combustion pressure from each cylinder minimizes any torsional vibration in the crankshaft. However, the combustion pressure of each cylinder is never the same; hence there is some imbalance in the engine's crankshaft rotation which results in

the presence of the rotational frequency and its half and one half order harmonics. The presence of misfire in any of the cylinders will increase the amplitude of these harmonic components. Hence, the presence and amplitude of half order and one and half order harmonics of the engines rotational frequency can be used for engine fault (misfire) detection.

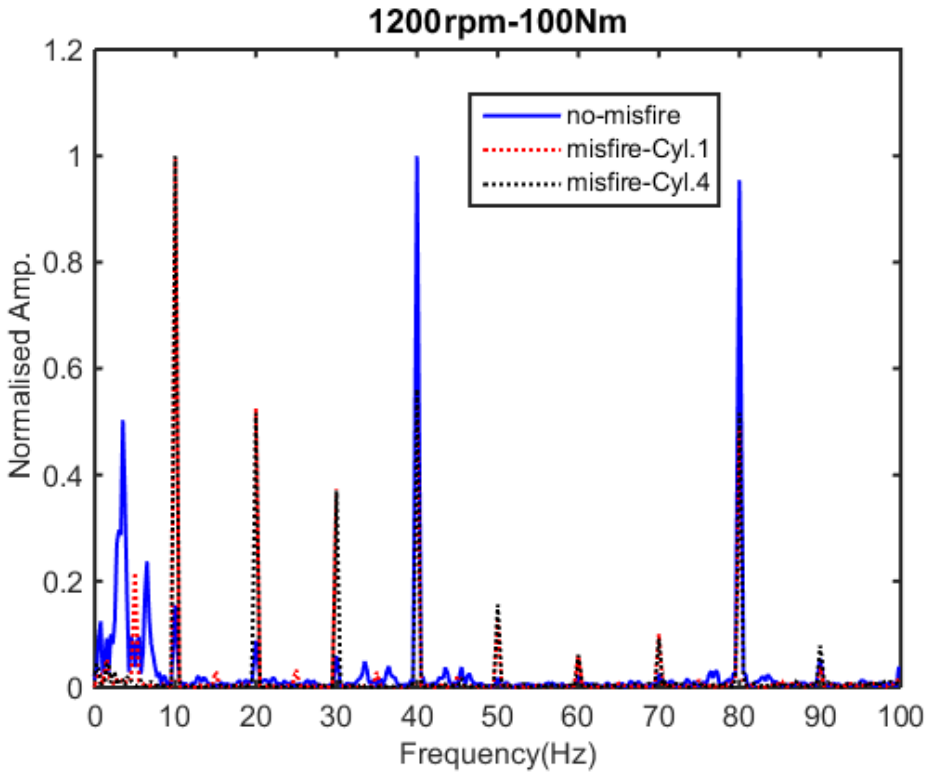

Figure 9-9 spectrum of healthy and faulty IAS at 1200rpm-100Nm

So as the evaluate this phenomenon at higher speed and the same loading condition the IAS spectrum of the engine at 1800rpm-100Nm was plotted alone as shown in the figure 9-10. IAS spectrum of complete misfire in the 1st and 4th cylinder of the engine at 1800rpm-100Nm also shows a significant amplitude increase around low frequency components of 15Hz, 30Hz and 45Hz compared to the healthy case. These frequency components corresponds to the one and half order (1.5 of 30Hz), half order (0.5 of 30Hz) harmonics of the engine's rotational frequency as well as the engine's rotational frequency (30Hz).The amplitude of the 15Hz frequency component which corresponds to the half order harmonics of the engine's rotational frequency is more significant compared to the firing frequency. This indicates that contrast to the IAS time domain representation diagnosis method, the frequency domain representation diagnosis method can be used for fault detection at both high and low engine speed operating conditions.

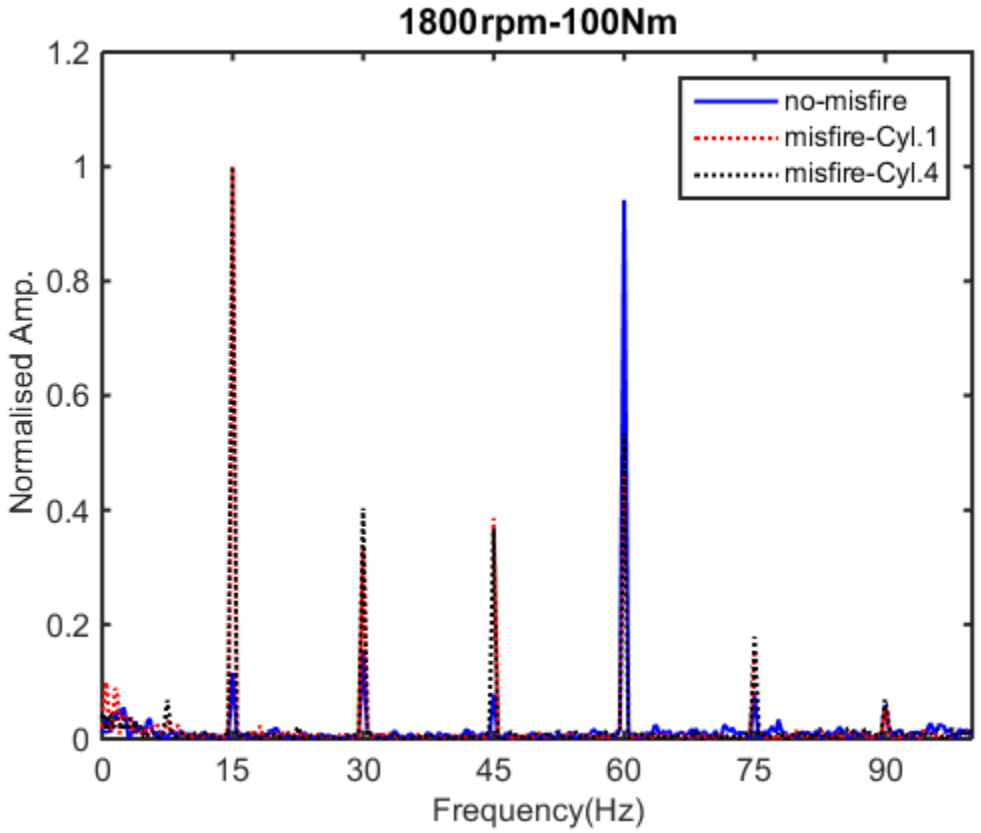

Figure 9-10 spectrum of healthy and faulty IAS at 1800rpm-100Nm

9.2.2 **Abnormal Valve Clearance Diagnosis**

As discussed in earlier chapter, the valve train of diesel engines are important for its day-to-day operation. As they control air intake and exhaust of gas in and out of the cylinder. Studies have shown that, a faulty valve train can have a diverse impact on the engine's combustion performance. The valve clearance is an essential part of the valve as it enables the engine to breathe (intake air and exhaust of gas) freely. Several studies have used cylinder pressure profile and engine body vibration for valve clearance fault detection.

9.2.2.1 **Time Domain Based Diagnosis**

The 1st cylinder pressure of the engine (JCB diesel engine) operating with 65% increment of its original exhaust valve clearance shown in figure 9-11, indicate some reduction in the peak cylinder pressure at specific speed and load conditions. The 1st cylinder pressure of the 30% increment tends to shows a close match with that of the original clearance.

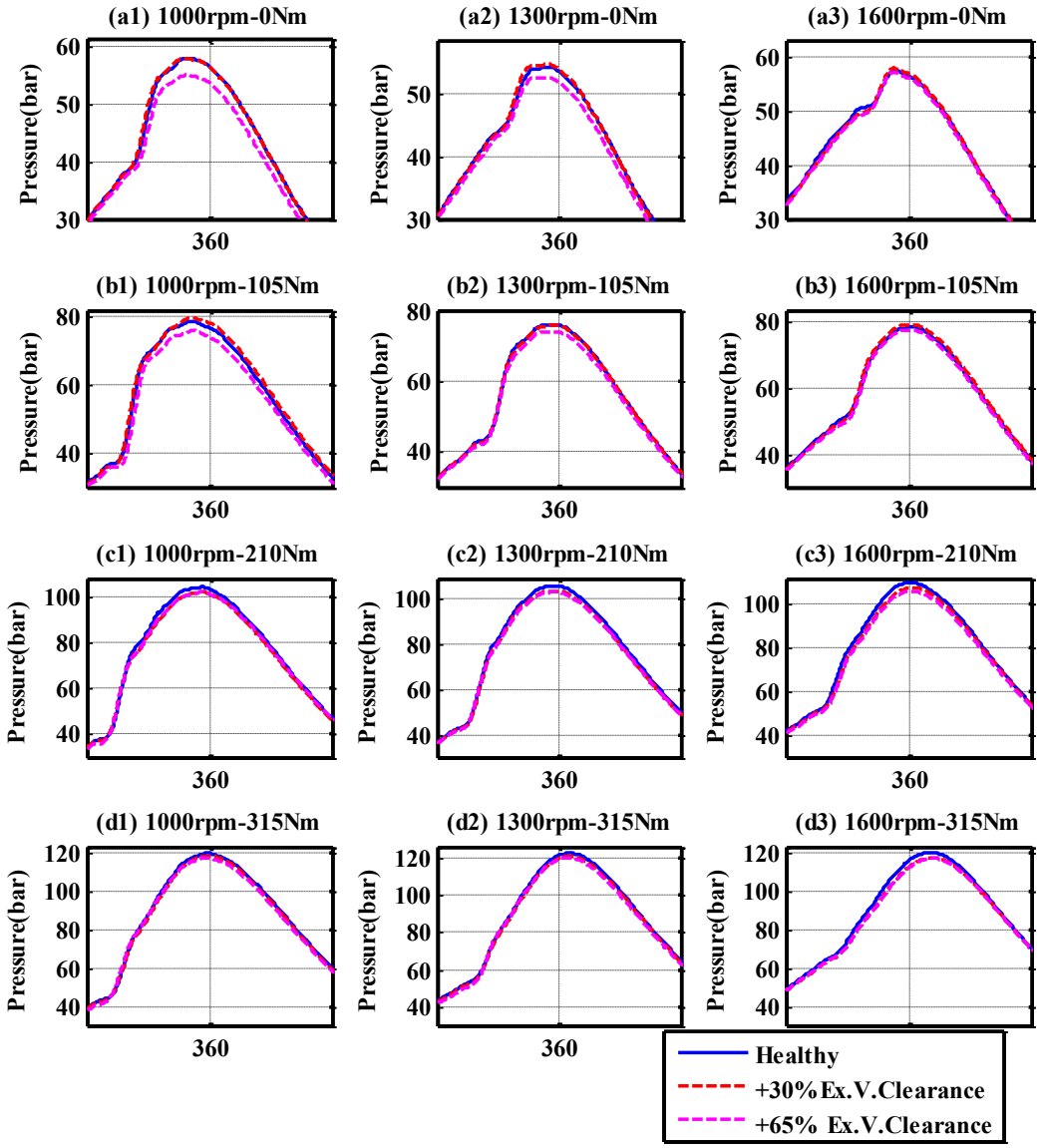

Figure 9-11 cylinder pressure of healthy and abnormal exhaust valve clearance

The peak cylinder pressure of exhaust valve clearance abnormality of two severities (30% and 65% increment) and that of a normal one at various speeds and varying load increments shown in

figure 9-12, show, some peak pressure reduction at 1000rpm at all loading conditions. Although there is some peak pressure reduction, this reduction does correspond with the degree of the fault severity. However, at some speed and load conditions specifically at 1300rpm-210Nm the result tends to correspond with the degree of the fault's severity.

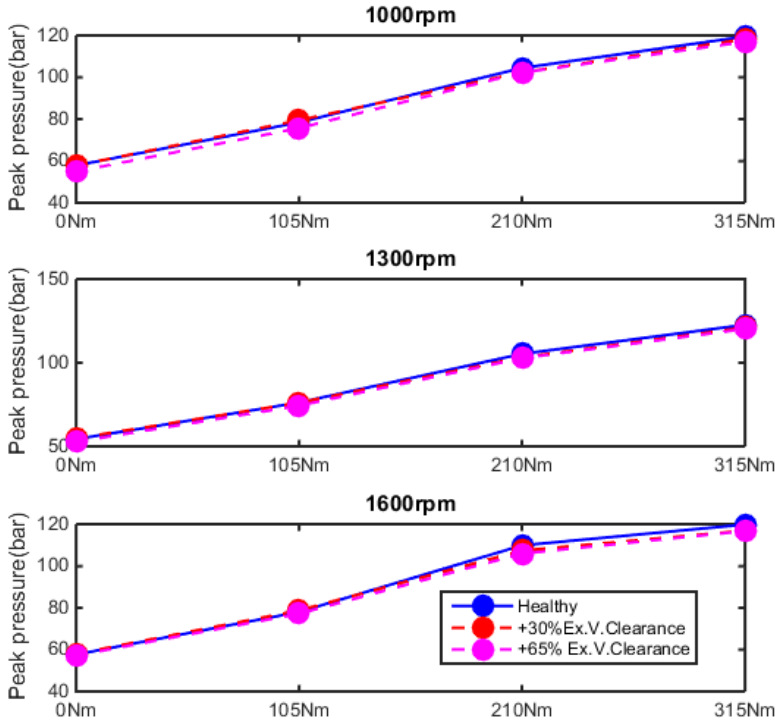

Figure 9-12 peak cylinder pressure for healthy abnormal exhaust valve clearance

The IAS time domain representation of the engine with valve clearance abnormalities shown in figure 9-13, 9-14 and 9-15, shows that the time domain representation might not be viable for early exhaust valve clearance fault detection in diesel engines. As there is no significant difference between the IAS waveform of the healthy engine condition and that of the faulty case, except for some alteration in the peak values of the faulty case at 1000rpm.

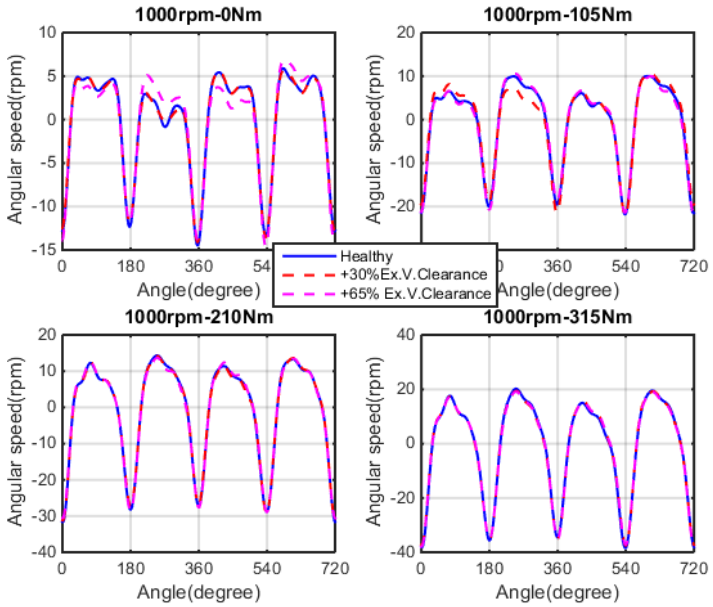

Figure 9-13 IAS waveform of normal and abnormal valve clearance at 1000rpm and variable loads

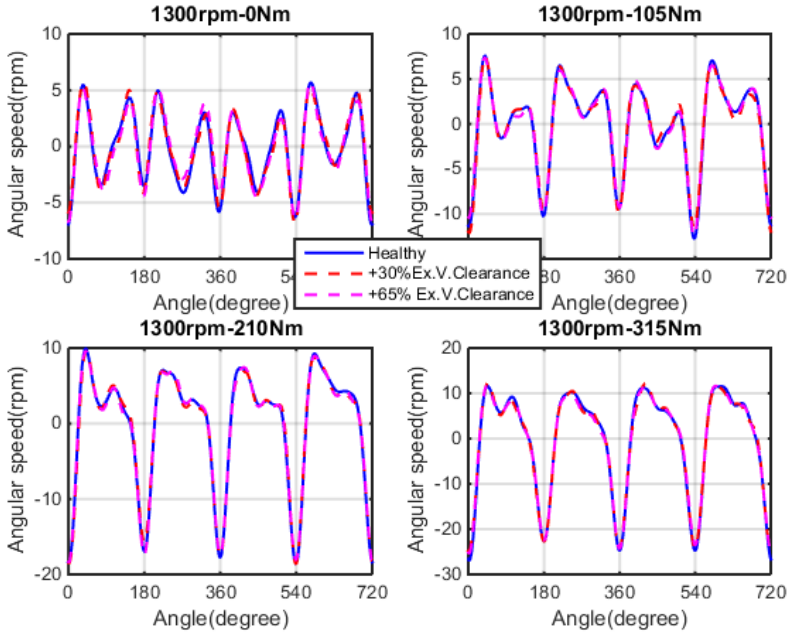

Figure 9-14 IAS waveform of normal and abnormal valve clearance at 1300rpm and variable loads

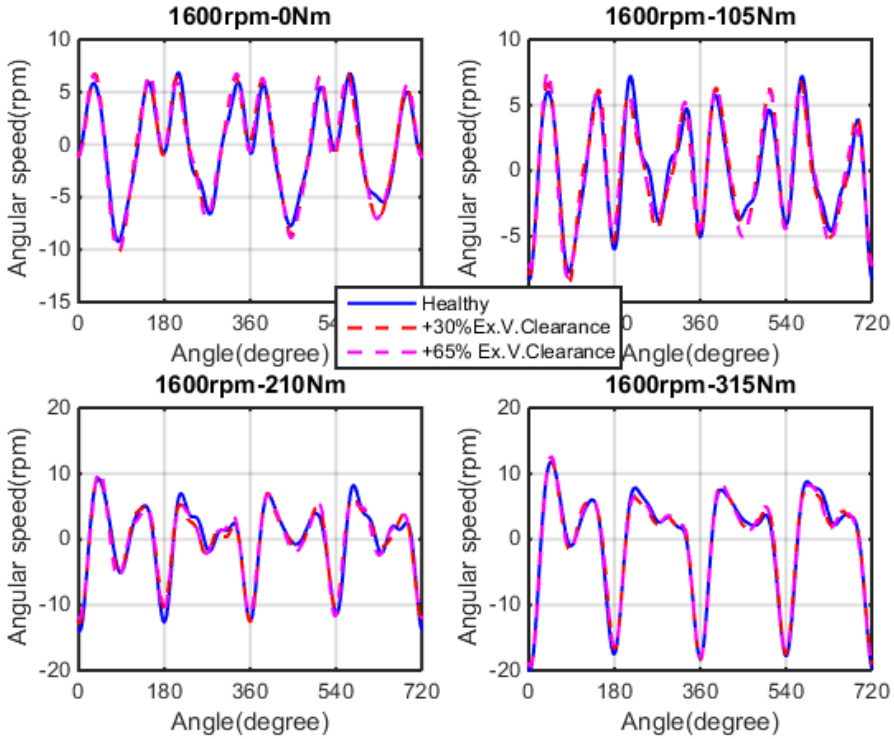

Figure 9-15 IAS waveform of normal and abnormal valve clearance at 1600rpm and variable loads

9.2.2.2 **Frequency Domain Based Diagnosis**

The IAS frequency domain representation of the engine with valve clearance abnormalities shown in figure 9-16, 9-17 and 9-18 shows abnormalities in the amplitude of the low frequency components compared to that with normal valve clearance. The abnormality in amplitude of the low frequency components tends to vary across engine speed and loading condition. The IAS spectrum results across all speeds show an increase in amplitude around low frequency component for the faulty cases and the increase is more evident at 105Nm loading condition. So as to further investigate the IAS spectrum for abnormal exhaust valve clearance detection, the frequency range of the spectrum was limited to that of half the firing frequency at all speed and loading conditions.

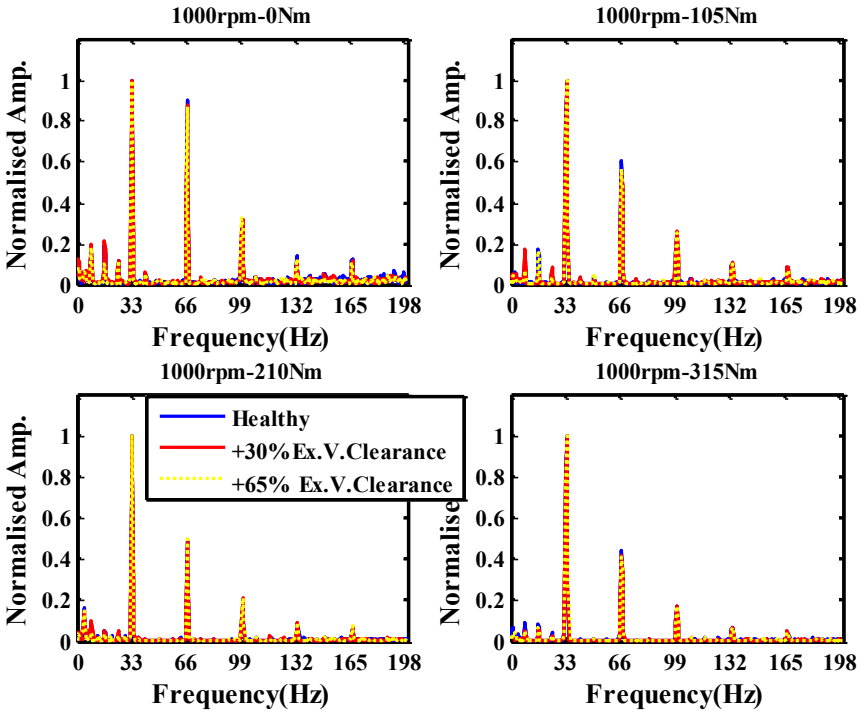

Figure 9-16 IAS spectrum of normal and abnormal valve clearance at 1000rpm and variable loads

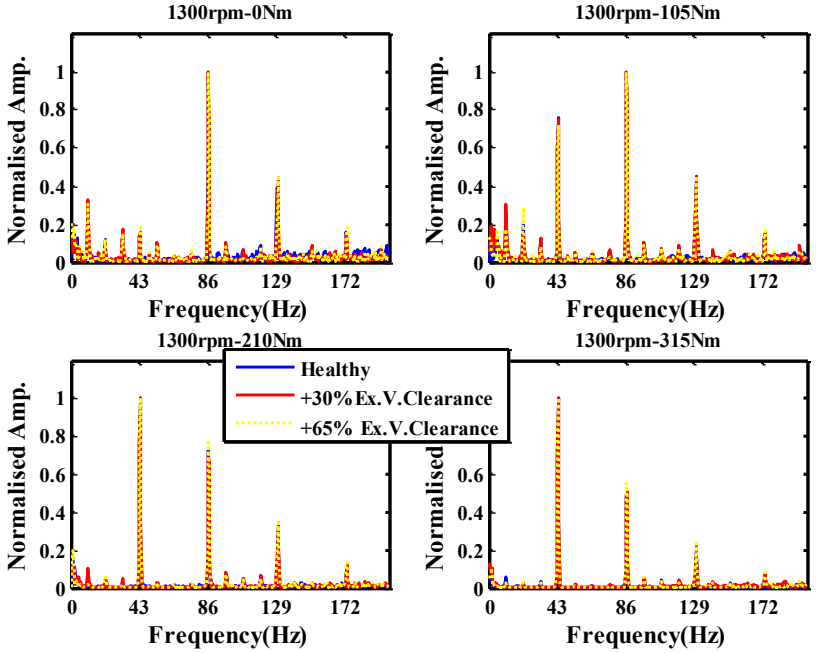

Figure 9-17 IAS spectrum of normal and abnormal valve clearance at 1300rpm and variable loads

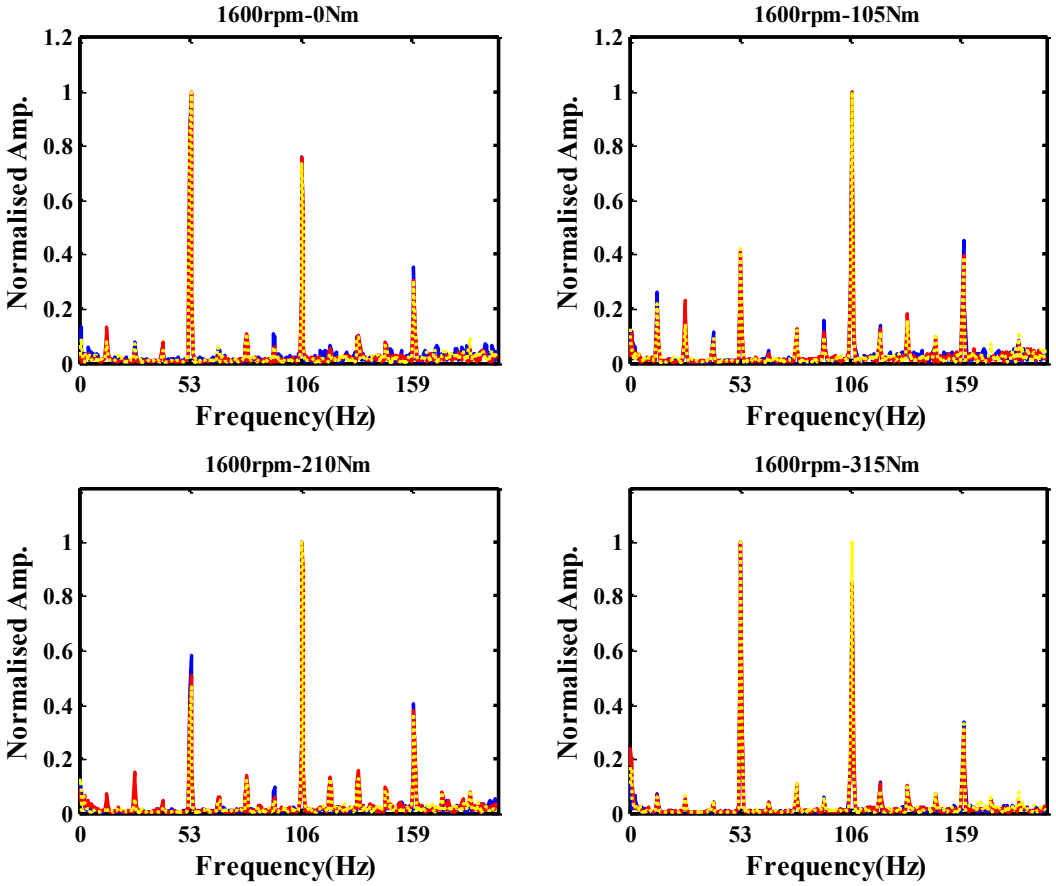

Figure 9-18 IAS spectrum of normal and abnormal valve clearance at 1600rpm and variable loads

The IAS spectrum shown in figure 9-19 below shows that these low frequency components where there is increase in amplitude corresponds to the half (0.5 of shaft rotational frequency) order harmonics of the crankshaft's rotational frequency. The increase in the amplitude of this frequency components tend to vary across speed and loading condition. While there is no significant amplitude increment, around the half order harmonic components for the faulty cases at 1000rpm-0Nm, there is at 1300rpm-0Nm and 1600rpm-0Nm. This is not the case at the next loading condition, as there is a significant amplitude increment around the half order harmonic frequency component for the faulty case at 1000rpm-105Nm specifically the 35% valve clearance increment. There is a significant increase in the amplitude of the half order harmonics of the shaft's rotational frequency component and the shaft rotational frequency components for individual cases at 1300rpm-105Nm. This indicates that IAS frequency domain representation can be used for exhaust valve clearance faults in a diesel engine. However, it cannot identify the cylinder where the fault

is located. Hence, the need for a more robust technique that can detect the fault and as well as identify the cylinder where the faults is located. The IAS model based diagnostics technique which reconstructs the pressure torque from the measure IAS would be considered for the abnormal exhaust valve clearance localization.

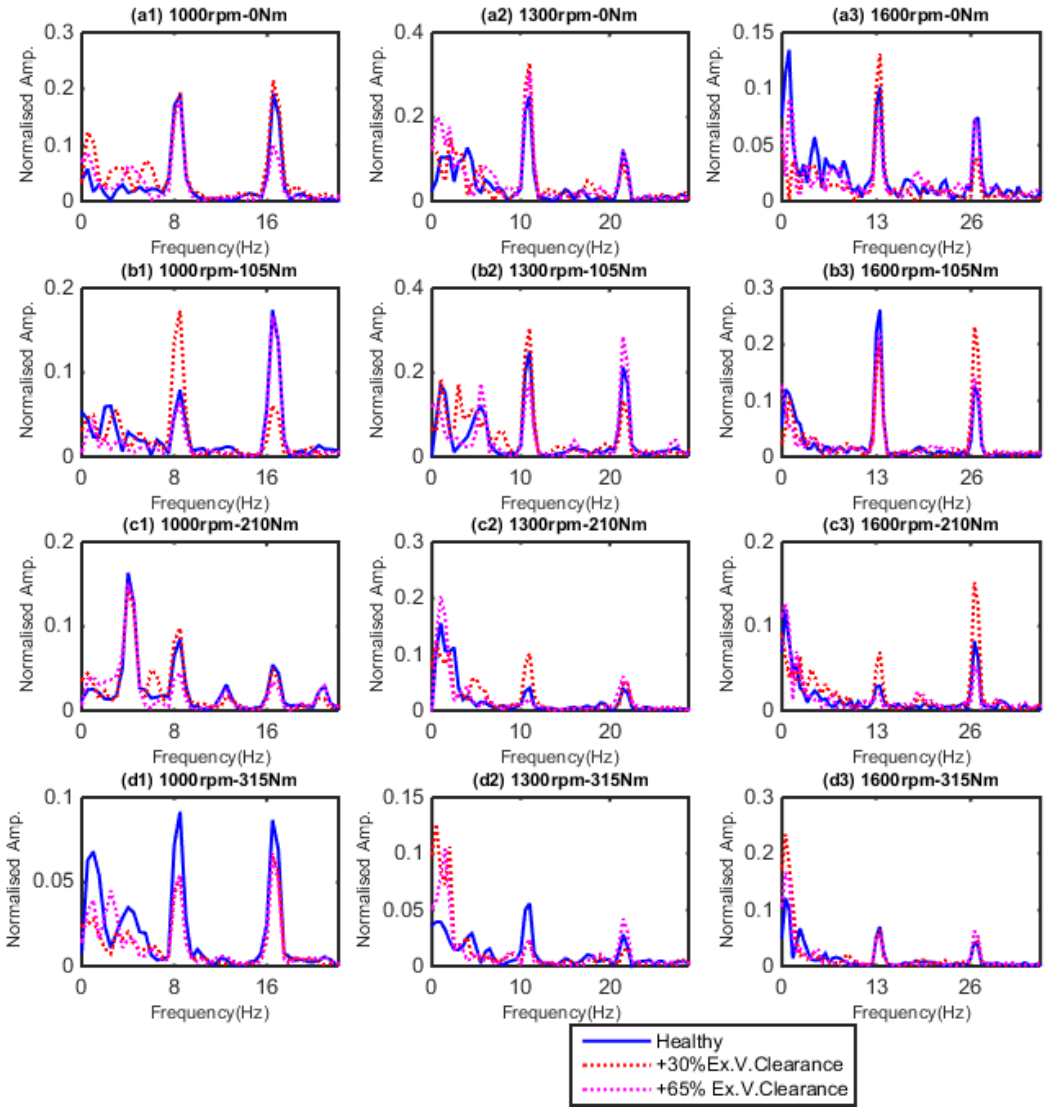

Figure 9-19 low frequency components of IAS spectrum for normal and abnormal valve clearance

9.2.3 **Injection Fault Diagnosis**

The diesel fuel injection system plays a vital role in the engine performance efficiency. Studies have shown that the injectors of diesel engines gets weak and tired over time. So as to induce an abnormal working condition in the injection system, the thickness of the preload washer inside the injector was reduced by 10%, 33% and 66% of its original value and increased by 33% of its original value. This washer, together with the spring as discussed in chapter 2 acts as a preload which should be exceeded for the needle of the injector to lift and fuel injected into the cylinder. Firstly, the opening pressure of the injector with different washer thickness set values were manually tested using a manual operated injection machine see (appendix A for description and result) The results showed that the increase in the washer thickness causes an increase in the opening pressure of the injection. While the reduction of the washer thickness causes a reduction in the injection opening pressure.

9.2.3.1 **Time Domain Based Diagnosis**

The 1st cylinder pressure of the engine (JCB diesel engine) operating with 33% and 66% reduction and 33% increment of the preload washer thickness shown in the figure 9-20, shows an abnormal pressure profile compared to the healthy case. The result shows that the cylinder pressure profile for 66% reduction of the preload washer thickness shows a consistent increase in the peak cylinder pressure value at 0Nm across all speed (100rpm, 1300rpm, and 1600rpm) compared to the healthy case. While that of the 33% increment shows consistent reduction in the peak cylinder pressure compared to the healthy case at 0Nm across all speeds. This is in contrast to the cylinder pressure profile result at 315Nm across all speeds where there is a reduction in the peak cylinder pressure for all of the fault severities. However, the cylinder pressure profile of the 10% and 33% reduction compared to that of the healthy case shows no consistent alteration pattern at 0Nm across all speeds (100rpm, 1300rpm, and 1600rpm), hence, would not be reliable for the fault diagnosis. The 66% reduction and 33% increment in washer thickness shows increment and reduction of peak cylinder pressure at 1000rpm-0Nm compared with that for the healthy case. There is a clear distinction between all severities of the injector fault for the cylinder pressure profile at 210Nm across all speed. The result shows reduction in peak cylinder pressure as the severity of the fault increases at this engine operating condition.

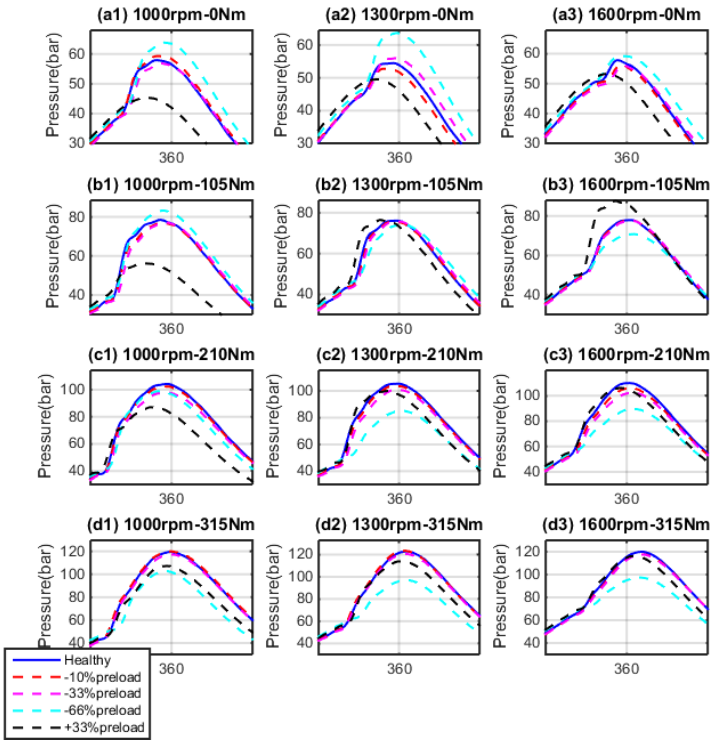

Figure 9-20 cylinder pressure for healthy and faulty injector

The peak cylinder pressure of injector faults with four severities (10%, 33%, and 65% reduction and 33% increment of the injector's washer thickness) and that of a normal one at different speed and varying load increment shown in figure 9-21, shows, consistent behaviours across speed which can be used for fault detection. The peak cylinder pressure of 33% washer thickness increment compared to that of healthy shows consistent reduction in its value at 1000rpm across all loads (0Nm, 105Nm, 210Nm and 315Nm) only. While that of 65% reduction compared to the healthy case shows increment at 1000rpm low loads (0Nm and 105Nm) and reduction at 1000rpm high loads (210Nm and 315Nm). Since the cylinder pressure is the main component of engine pressure torque, the peak cylinder by cylinder pressure torque values should provide features that can be used for fault detection and localization.

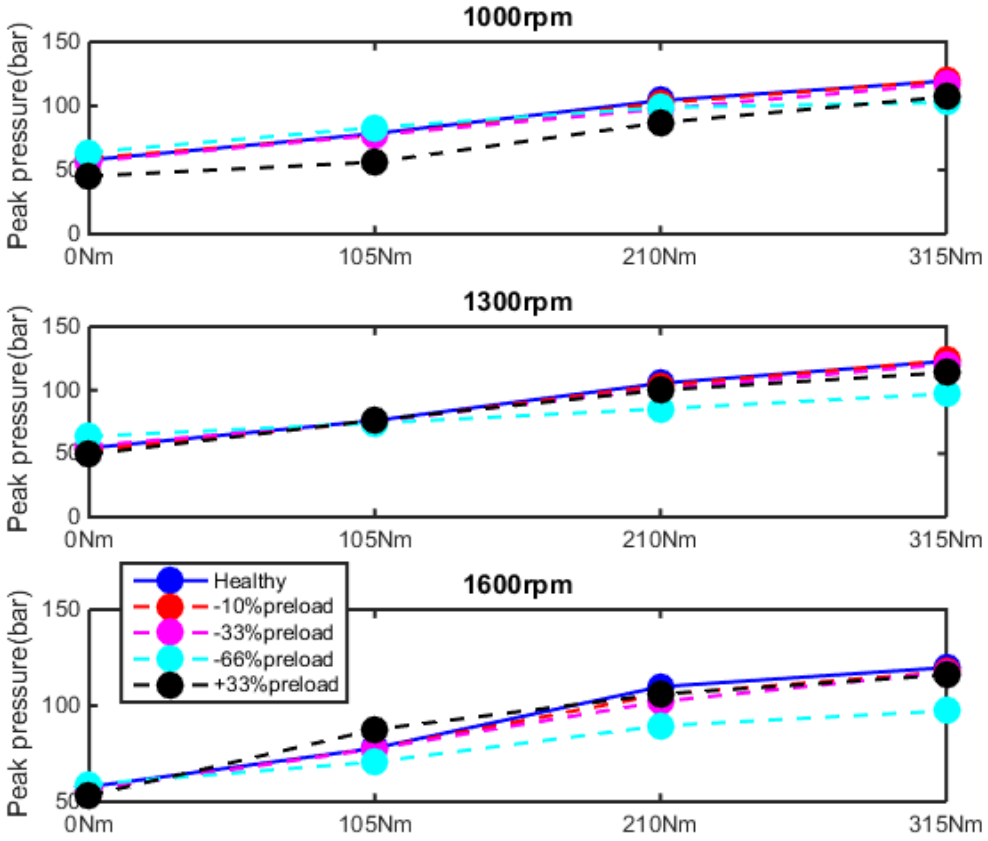

Figure 9-21 peak cylinder pressure for healthy faulty injector

The IAS time domain representation of the engine with faulty injector shown in figures 9-22, 9-23 and 9-24 show some abnormalities compared with that of healthy injector. The result indicates abnormal IAS waveform for the 65% reduction and 33% increment of washer thickness at low loads (0Nm and 105Nm) across all speed (1000rpm, 1300 and 1600rpm). The abnormality tends to reduce as the load approaches 315Nm across all speeds. The IAS waveform of 10% and 33% reduction also shows some abnormalities at these speed and load conditions but they are not consistent and are not like that of the extreme severities. Although there are some difference between the IAS waveform of engine with healthy injector and that of the faulty case, because of the main aim of this research which is centred on IAS model based diagnosis, it would not be processed further.

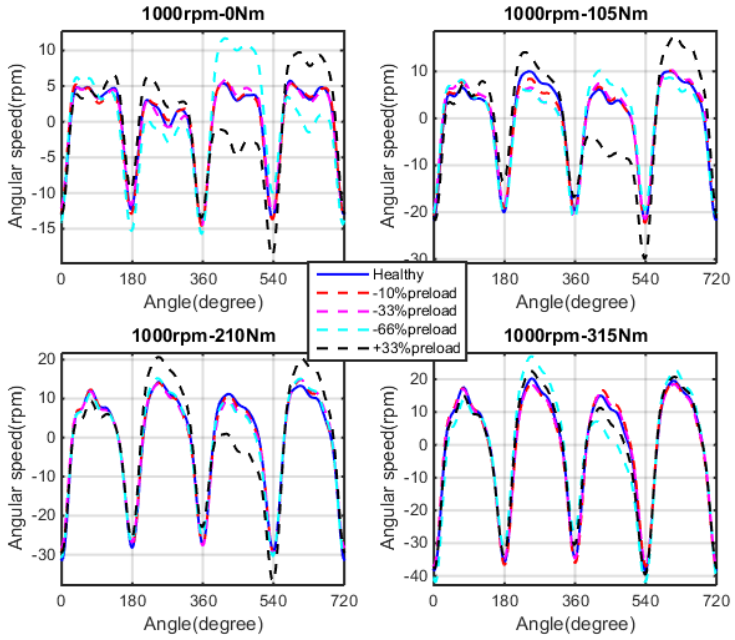

Figure 9-22 IAS waveform of healthy and faulty injector at 1000rpm and variable loads

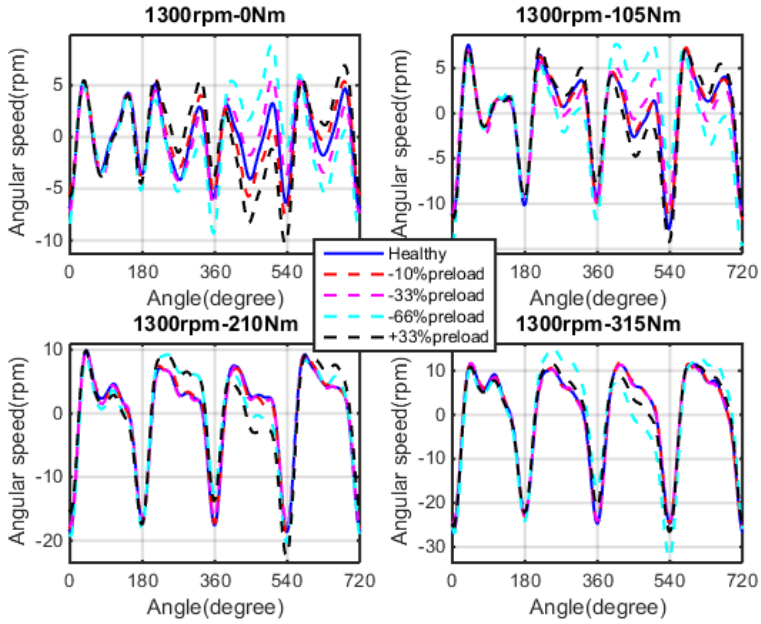

Figure 9-23 IAS waveform of healthy and faulty injector at 1300rpm and variable loads

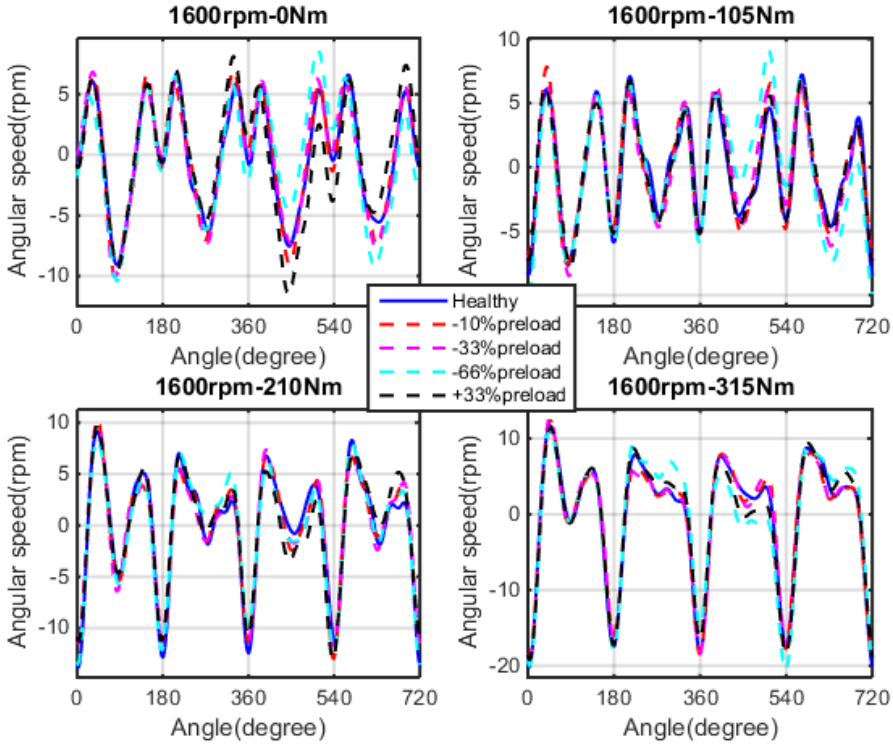

Figure 9-24 IAS waveform of healthy and faulty injector at1600rpm and variable loads

9.2.3.2 **Frequency Domain Based Diagnosis**

The IAS frequency domain representation of the engine with injector fault shown in the figures 9-25, 9-26 and 9-27 show abnormalities in the amplitude of the low frequency components compared with that of healthy injector. The increase in amplitude of the low frequency components tends to vary across engine speed and loading condition. Increases in the amplitude of the low frequency component for extreme (65% reduction and 33% increment) cases of the fault are more evident across all engine speed and varying load conditions. The increase in the amplitude seems to reduce with an increase in the loading conditions across all speed. In order to further investigate the IAS spectrum for injector fault detection, the frequency range of the spectrum was limited to that of half the firing frequency at all speed and loading conditions.

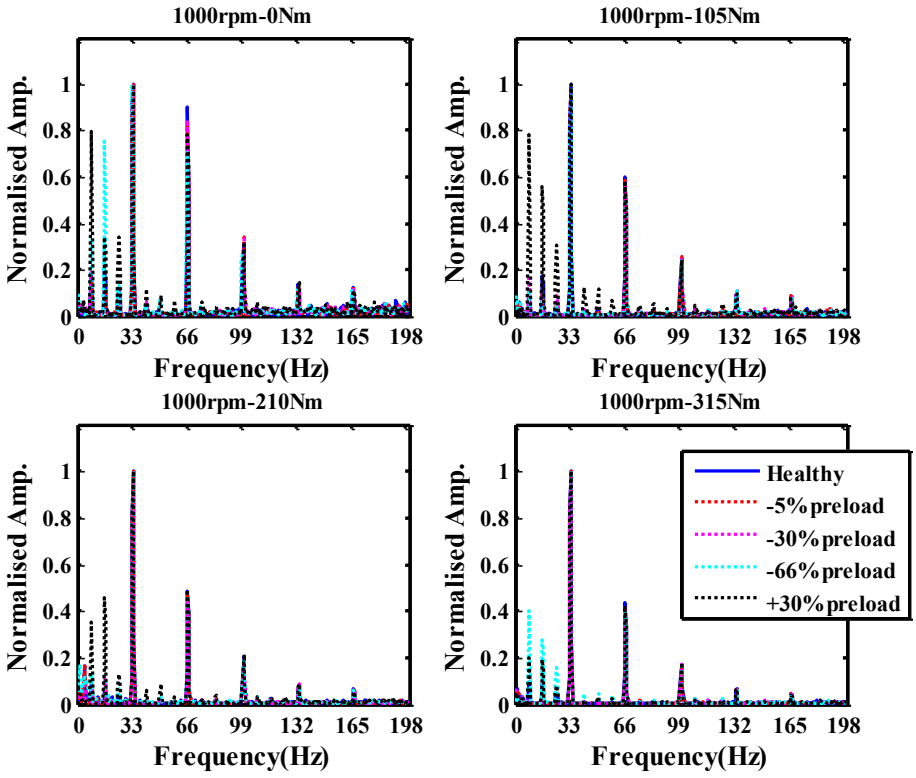

Figure 9-25 IAS spectrum of healthy and faulty injector at 1000rpm and variable loads

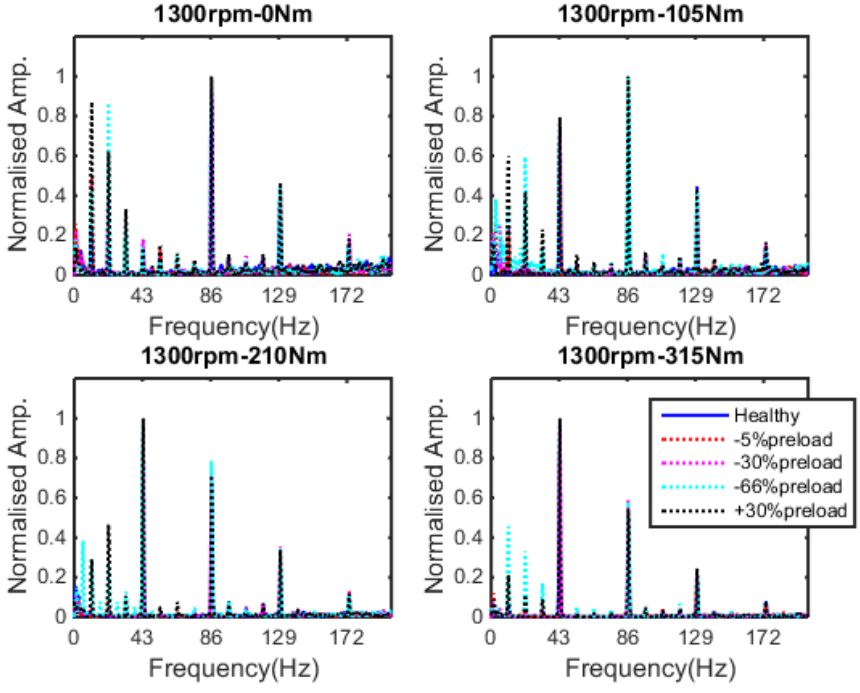

Figure 9-26 IAS spectrum of healthy and faulty injector at 1300rpm and variable loads

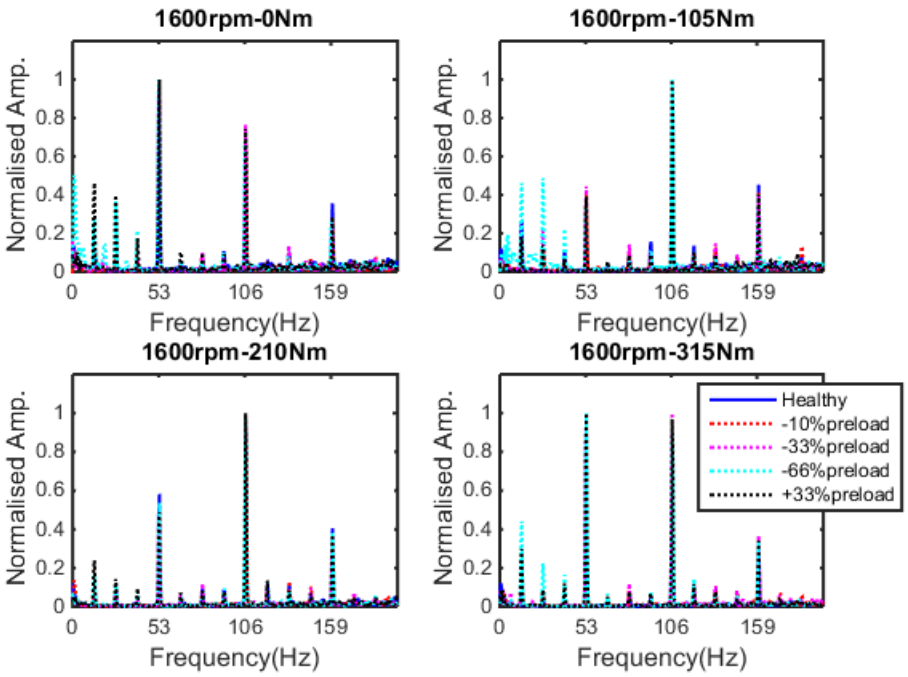

Figure 9-27 IAS spectrum of healthy and faulty injector at 1600rpm and variable loads

The IAS spectrum shown in the figure 9-28 below shows that these low frequency components corresponds to the half (0.5 of shaft rotational frequency) and 1st (shaft rotational frequency) order harmonics of the crankshaft's rotational frequency. While, the spectrum of 1300-0Nm engine condition shows amplitude increment at both low frequency components for all severities of the fault, that of 1600rpm-0Nm only showed increment for extreme cases of the fault (65% reduction and 35% increment). The spectrum of estimated IAS at the average engine speed of 1000rpm shows significant amplitude increment at both 8Hz and 16Hz frequency component for only the extreme case of the fault across all loading conditions except at 210Nm where there is increment around only the 16Hz (shaft' s rotational frequency) component. This means that at low engine speed early case of this fault would only be detected at 210 Nm load condition using the frequency dominion representation method. The spectrum of estimated IAS at the average engine speed of 1300rpm shows significant increase in amplitude at both 10Hz and 20Hz frequency components for all severities of the fault at 0Nm and 210Nm loading conditions. This indicates that IAS frequency domain representation can be used for detecting an injector fault of different severities in a four cylinder diesel engine. However, it cannot identify the cylinder where the fault are located. Hence, the need for a more robust technique that can detect the fault and as well identify

the cylinder where the faults is located. The IAS model based diagnostics technique which reconstructs the cylinder pressure torque from the measured IAS would be considered in the next section.

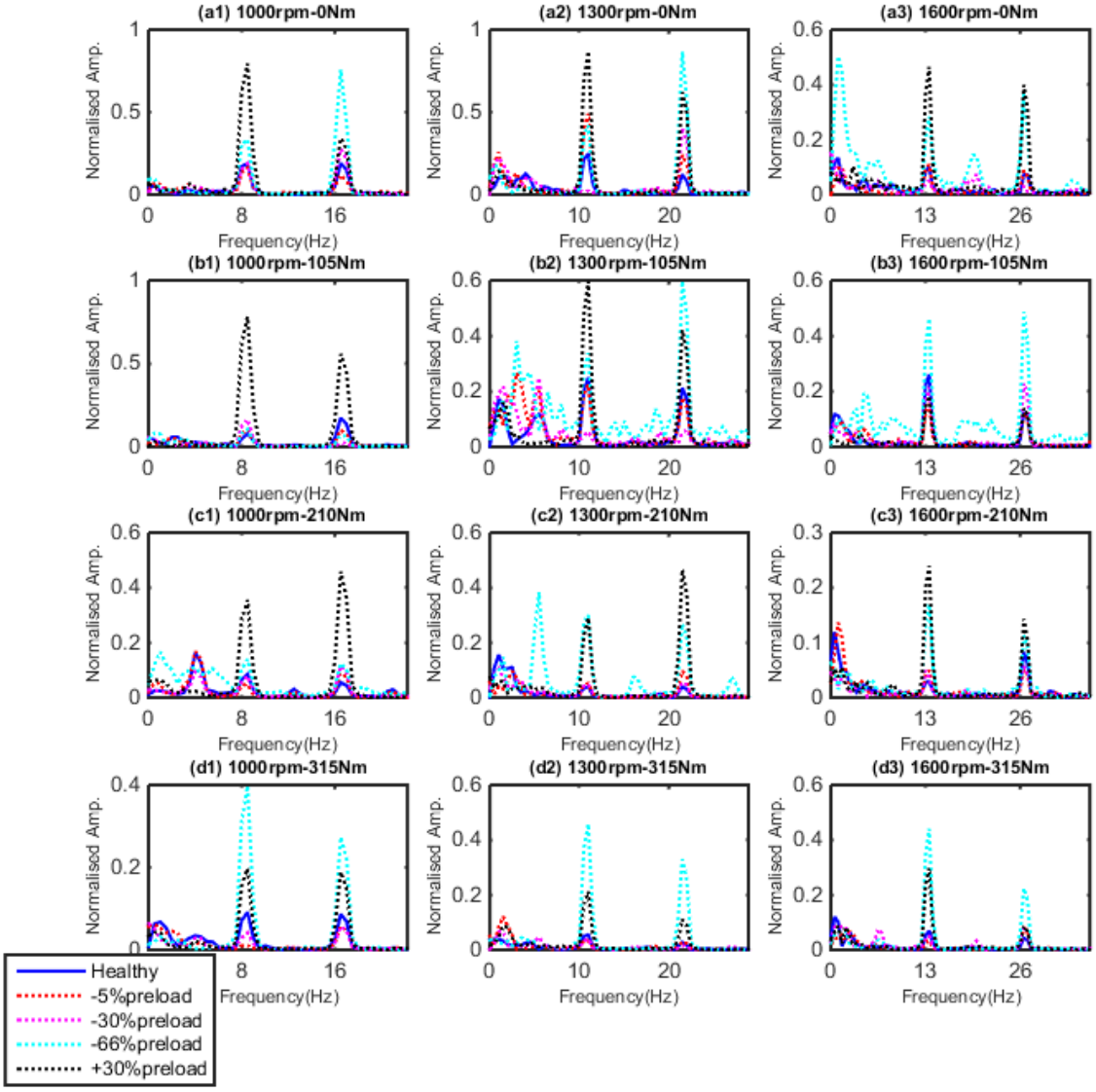

Figure 9-28 low frequency component of IAS spectrum for healthy and faulty injector

9.3 **Model Based Diagnostics**

Although, the IAS signal based diagnosis can detect fault (misfire, abnormal valve clearance and faulty injector) in engines, its ability to identify specific faulty cylinders is still less mature. The

model based diagnosis which reconstruct the applied forcing torque by combining measured angular speed response with an analytical system model, has shown more prospects in identifying specific faulty cylinders. The primary goal of this diagnostic method is to use measured IAS response of the engine-load system to reconstruct the forcing torque applied by respective cylinders. The applied forcing torque is then used to estimate individual cylinder pressure torque contributions. The pressure torque can be reconstructed either by applying a deconvolution algorithm on the measured IAS or direct computation of the torque from the measured IAS. The direct computation method is based on the assumption that the engine-load system is very rigid. Thus, does not take into consideration the low frequency resonance of the system. Though this method is computationally easy to implement compared to the other deconvolution methods, the rigid body assumption affect the accuracy of the calculated torque. The direct calculation method consist of the following steps:

1) The measured IAS is smoothed through the use of a low pass FFT filter and the averaged for 24 engine cycles
2) The resulting signal from (1) is then differentiated so as to obtain the angular acceleration of crankshaft.
3) To obtain the engine torque, the angular acceleration signal obtained in step (2) is multiplied by the total mass inertia of the engine
4) The torque due to the reciprocating inertia is calculated using equation (5-23) and subtracted from the engine torque to yield the pressure torque.

The direct computation method is not always reliable for fault detection compared to the deconvolution techniques. The order domain deconvolution algorithm can be done either through the use of a transfer matrix or frequency response matrix. The order domain deconvolution algorithm where frequency response functions are formulated with a crank angle as the independent variable is adopted in this work.

9.3.1 Order Domain Deconvolution Method

This method takes advantage of the periodicity of the combustion process. While the magnitude and phase of the measured IAS response are the inputs for this deconvolution process, the applied order domain system torques are the outputs. Although some researchers have included multiples of the firing frequency so as to obtain additional information, recent order domain diagnostic

method limits analysis to firing order only. To formulate the frequency response function of the engine-load system, the simplified model structure of engine-load system in chapter 5 is used. The first step in this method is to derive the equation of motion of the system. The three equations of motion below results when torques are equated on each inertia of the system:

$$J_1\ddot{\theta}_1 + c_1\left(\dot{\theta}_1 - \dot{\theta}_2\right) + k_1\left(\theta_1 - \theta_2\right) = T_E \tag{9-1}$$

$$J_2\ddot{\theta}_2 + c_1\left(\dot{\theta}_2 - \dot{\theta}_1\right) + c_2\left(\dot{\theta}_2 - \dot{\theta}_3\right) + k_1\left(\theta_2 - \theta_1\right) + k_2\left(\theta_2 - \theta_3\right) = T_2 \tag{9-2}$$

$$J_3\ddot{\theta}_3 + c_2\left(\dot{\theta}_3 - \dot{\theta}_2\right) + k_2\left(\theta_3 - \theta_2\right) = T_L \tag{9-3}$$

, where T_3 and T_1 are the load and engine torque respectively. Assuming that the load torque input at the inertia J_3 and the engine torque at inertia J_1 can be denoted by:

$$T_E = T_e e^{j\omega t}$$
$$T_L = T_l e^{j\omega t} \tag{9-4}$$

The solution for the resulting angular displacement of the i^{th} inertia, ignoring the initial condition response may be denoted as:

$$\theta_i = A_i e^{j\omega t} \tag{9-5}$$

The following equation is derived for the angular speed and acceleration after calculating the first and second derivative of the angular displacement:

$$\dot{\theta}_i = j\omega A_i e^{j\omega t} = B_i = j\omega A_i$$
$$\ddot{\theta}_i = -\omega^2 A_i e^{j\omega t} \tag{9-6}$$

The equations of motion can be expressed in matrix form below:

$$[R]\{\Theta\} = \{T\} \tag{9-7}$$

, where

$[R]$, is the system matrix obtained by substituting for angular displacement (9-5), angular speed and angular acceleration (9-6) in the equations of motion (9-1, 9-2 and 9-3):

$$R=\begin{bmatrix} -\omega^2 J_1 + c_1 j\omega + k_1 & -c_1 j\omega - k_1 & 0 \\ -c_1 j\omega - k_1 & -\omega^2 J_2 + c_1 j\omega + c_2 j\omega + k_1 + k_2 & -c_2 j\omega - k_2 \\ 0 & -c_2 j\omega - k_2 & -\omega^2 J_3 + c_2 j\omega + k_2 \end{bmatrix}$$

(9-10

$\Theta = \begin{pmatrix} A_1 \\ A_2 \\ A_3 \end{pmatrix}$, is the angular displacement vector for the three inertia (engine, flywheel and load)

$T = \begin{pmatrix} T_1 \\ T_2 \\ T_3 \end{pmatrix} = \begin{pmatrix} T_E \\ 0 \\ T_L \end{pmatrix}$, is the forcing torque amplitude acting on each inertia

The equations above governs the response of the three degree of freedom engine-load system to a single frequency input. However, in practical sense the engine torque is composed of frequency components which contains significant energy for the first 24 harmonics of cycle speed. Through the use Fourier decomposition, the engine torque can be represented as a series of sine waves:

$$T_E(\mathrm{t}) = \bar{T}_E + \sum_{m=1}^{n} + T_{E,\mathrm{m}} \sin\left(\omega_m t + \phi T_m\right) \qquad (9\text{-}11)$$

The subscript m represents the m^{th} Fourier component while $\bar{T}_E$, denotes the mean engine torque and ω_m is the forcing frequency. Since the system response is the superposition of the responses to all the torque components in the input, the angular speed at the flywheel is given by:

$$\dot{\theta}_2(\mathrm{t}) = \bar{\theta}_2 + \sum_{m=1}^{n} + \theta_{2,\mathrm{m}} \sin\left(\omega_m t + \phi_{2,m}\right) \qquad (9\text{-}12)$$

, where $\phi_{2,m}$ is the phase at the 2nd inertia due to m^{th} the harmonic. Then, it can be assumed that the amplitude of the IAS waveform is proportional to the engine pressure torque through the range of engine speeds of interest. This means a measure of the engine torque can be calculated from the engine speed and its fluctuation amplitude. However, experimental and theoretical studies (Citron, et. al, 1989) have suggested some difficulties exist in using this assumption. The assumption is not supported at certain speeds for some engines. Firstly, this is due to the effect of inertia torque. Secondly, the simple firing frequency response is distorted by some engines drivetrain system vibrational characteristics. There are two cases that can be considered when using this method: constant drivetrain load and fluctuating drivetrain load. The case considered in this work is the

case where the drivetrain load torque is essentially constant over the engine torque expansion interval. The engine torque fluctuation waveform is the only external input driving the IAS under this condition. As shown in the 3x3 matrix below, there are nine possible transfer functions for all combinations of degrees of freedom where torque is applied and where angular displacement are taken:

$$\begin{bmatrix} \frac{\theta_1}{T_E} & \frac{\theta_1}{T_2} & \frac{\theta_1}{T_L} \\ \frac{\theta_2}{T_E} & \frac{\theta_2}{T_2} & \frac{\theta_2}{T_L} \\ \frac{\theta_3}{T_E} & \frac{\theta_3}{T_2} & \frac{\theta_3}{T_L} \end{bmatrix} \tag{9-13}$$

This matrix provides the relation between the angular displacement from individual inertia and the corresponding torque acting on them. To solve for transfer functions for a three degree of freedom system is a very cumbersome task, symbolic programs such Maple, Mathematica or Matlab are usually employed. Rather than solving for individual transfer function, the inverse of the system matrix$[R]$, would produce another 3x3 matrix[r], which corresponds with respective transfer function. Then the amplitude of the torque component $T_{E,m}$ is given by:

$$\begin{aligned} r_{2,1} &= \frac{\theta_2}{T_{E,m}} \\ T_{E,m} &= \theta_2 * \frac{1}{r_{2,1}} = \frac{\dot{\theta}_2}{|j\omega|} * \frac{1}{|r_{2,1}|} \end{aligned} \tag{9-14}$$

, where $|j\omega|$ and $|r_{2,1}|$ represents the absolute value of $j\omega$ and $r_{2,1}$ respectively. The total engine torque wave excluding the mean can be calculated by:

$$T_E(\mathrm{t}) - \bar{T}_E = \sum_{m=1}^{n} + T_{E,\mathrm{m}} \sin\left(\omega_m t + \phi T_m\right) \tag{9-15}$$

The phase of engine torque component is given by:

$$\phi T_m = \phi_{2,m} + \varphi_{2,m} - \frac{\pi}{2} \tag{9-16}$$

, where $\phi_{2,m}$ the phase of the speed component is, $\varphi_{2,m}$ is system phase shift (negative of the phase of $r_{2,1}$) and $\frac{\pi}{2}$ arises from the relationship between displacement and speed. The pressure torque

fluctuations $T_p(t)-\bar{T}_E$ is obtained by subtracting the inertia torque fluctuation from the calculated total engine torque fluctuations $T_E(t)-\bar{T}_E$. The inertia torque fluctuation is calculated by using the equation (5-23). The mean engine torque can $\bar{T}_E$ be obtained from the engine pressure torque fluctuation plot because at TDC the pressure torque is supposedly to be zero. Since the torque radius for any cylinder at TDC is zero and no other cylinder contributes to the pressure torque at that point. Hence, the value of the pressure at TDC must be equal to negative of the mean engine torque. The value of the mean engine torque when added to the pressure torque fluctuation waveform then yields the cylinder pressure torque.

9.3.2 Pressure Torque Reconstruction Results

The measured angular speed signal was decomposed into its Fourier components as shown in equation 9-12. The reconstructed signal shown in the Figure 9-29 shows a very strong correlation compared to the measured one. This shows that the frequency component extracted from the measured IAS waveform is enough to reconstruct the total engine torque fluctuation, which comprises of both the inertia and pressure torque.

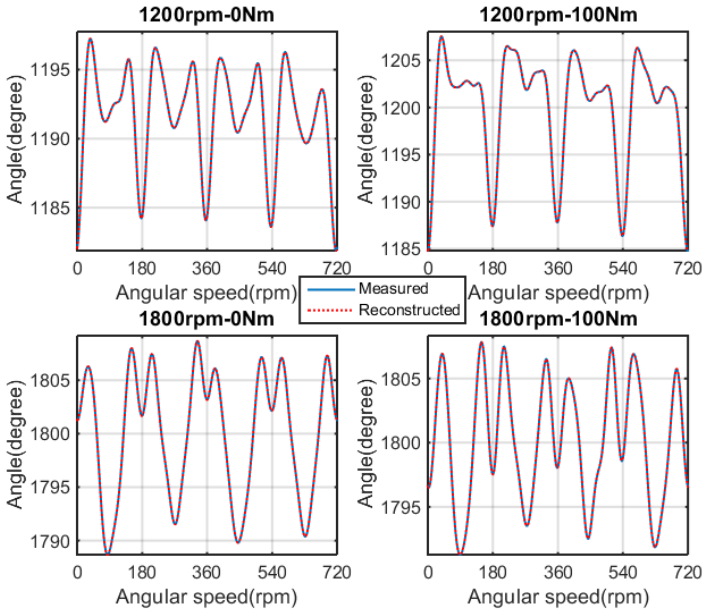

Figure 9-29 measured and reconstructed IAS using 24 harmonic component

So as to show the impact of resonance frequency specifically the low frequency component on extracted pressure torque, the inertia of the flywheel was altered by 10% increment and decrement.

Table 9-1 shows a 0.6 % increment and decrement in the value of the low resonance frequency component with the 10% alteration of the flywheel inertia.

Table 9-1 effect of flywheel inertia alterations on system's resonance frequencies

Resonance Frequency (Hz)		10% flywheel Inertia reduction (Hz)		10% flywheel inertia increment (Hz)	
Low frequency	12.9	13.1	+0.6%	12.8	-0.5%
High frequency	92.3	93.0	+0.4%	91.2	-0.3%

Result of the reconstructed pressure torque shown in figure 9-30 shows 9% increase in the peak pressure across all cylinder when there is a 10% increase in the flywheel inertia. While that of 10% reduction also shows a 9% percent reduction in peak torque pressure across all cylinder.

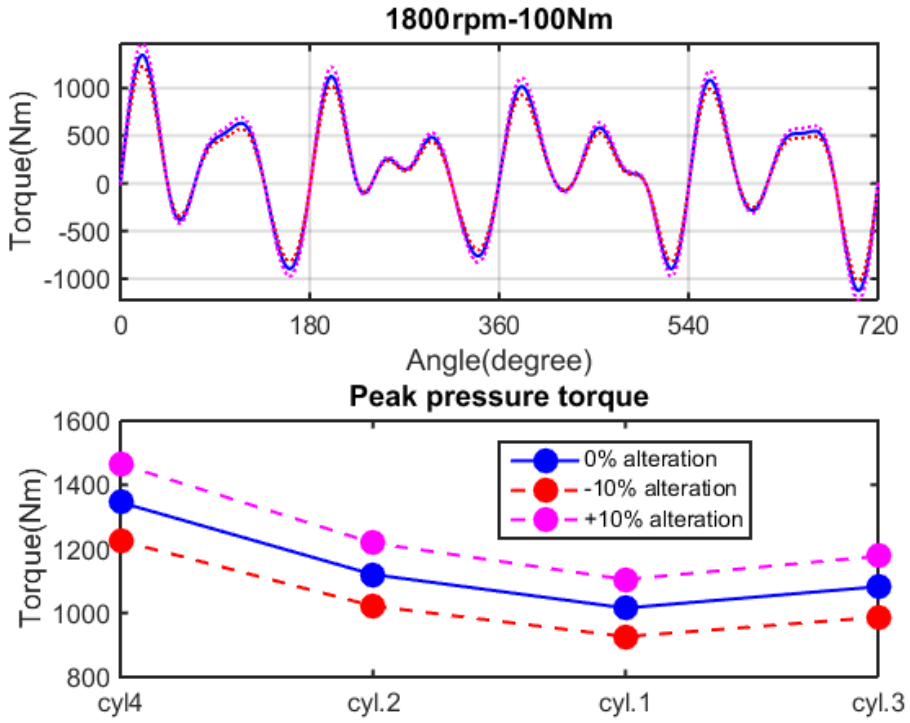

Figure 9-30 the impact of flywheel inertia alteration on reconstructed pressure torque

This indicates that 0.6% alteration of the low resonance frequency component of the engine-load system can alter the accuracy of the reconstructed peak pressure torque values. This alteration can affect its use for early and accurate fault diagnosis. The pressure torque reconstructed using the order domain technique with adjusted low resonance frequency was compared with the one

calculated using measured cylinder pressure and that reconstructed using the direct method. The pressure torque reconstructed using the revised modal properties in line with the extracted low resonance frequency components as shown in the figure 9-31, shows a very close correlation to that of the calculated one compared to the one reconstructed from the same IAS using the direct method. This indicates that the pressure torque reconstructed from measured IAS using the order domain deconvolution technique can be more reliable for early and accurate fault diagnosis, if the resonance frequencies of the engine-load system, especially the low resonance frequency components is close to its real time value. One way of determining the real time resonance frequencies of the three degree of freedom engine-load system has been presented in earlier chapter of this thesis.

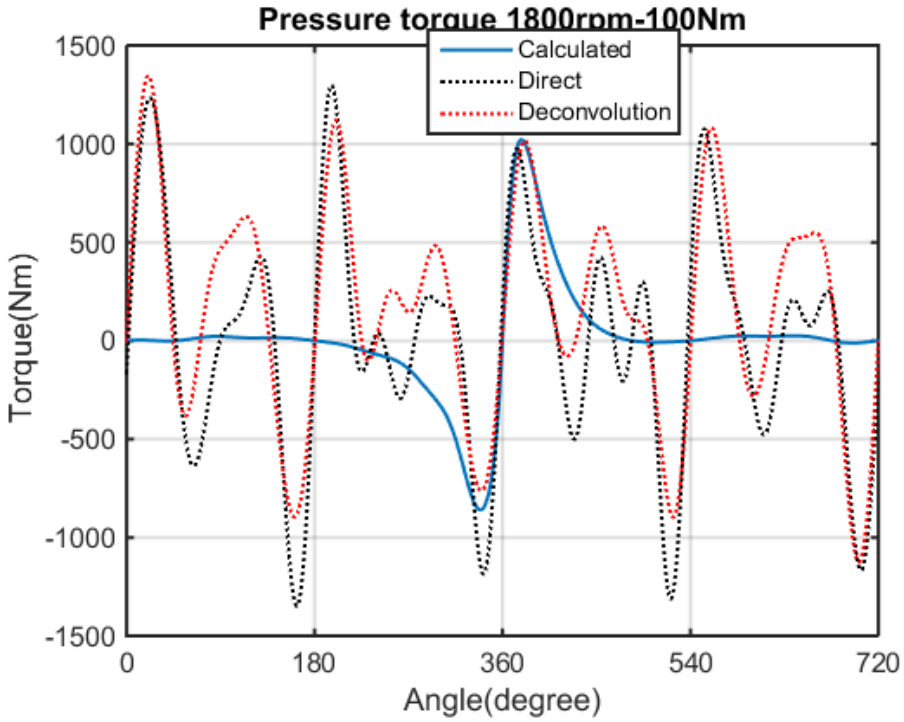

Figure 9-31 comparing pressure torque reconstruction methods

9.3.3 **Fault Diagnosis Result**

In order to evaluate the effect of using the real time resonance frequencies on the IAS model based diagnostics, the real and the altered low frequency resonance provided in table 9-1 is used for IAS model based misfire diagnostics. Using the altered estimated low frequency resonance, the reconstructed pressure torque for healthy and complete misfire in the 1st and 4th cylinder shown in figure 9-32, indicates a reduction in the peak torque value that pertains to that cylinder. So as to

quantify the drop in peak pressure torque value for complete misfire in respective cylinders the peak torque that pertains to individual cylinder is shown in the figure 9-33 below. The result shown in figure 9-34, indicates about a 21% drop in peak pressure torque value for a complete misfire in the 1st cylinder compared to the one reconstructed for healthy case at 1200-0Nm steady engine operating condition. The drop in the peak pressure torque seems to increase with increase in load at the same speed. This phenomenon is repeated at 1800rpm-0Nm and 100Nm steady engine operations. This is also the case for complete misfire in the 4th cylinder as shown in the figure 9-35. There is about 10% reduction of the peak torque value of the 4th cylinder at 1800rpm-0Nm and 34% reduction at 1800rpm-100Nm.

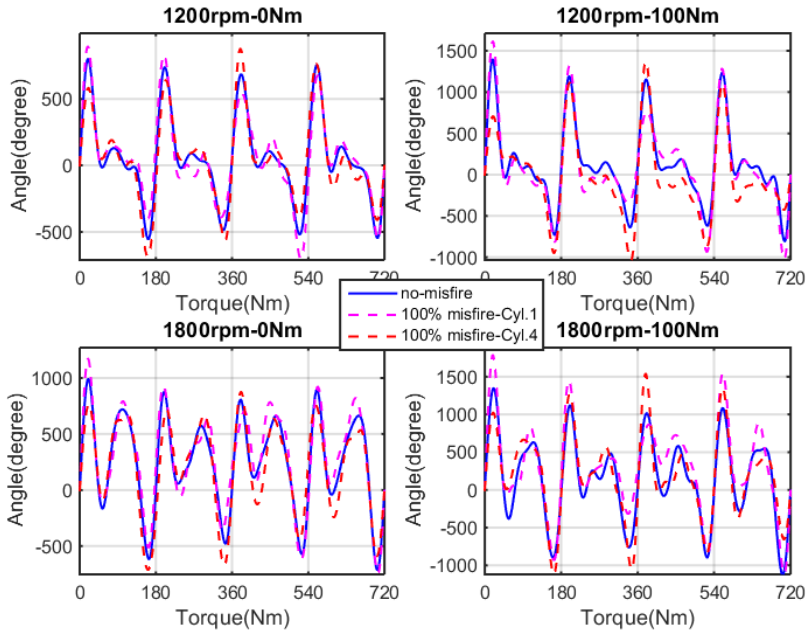

Figure 9-32 reconstructed pressure torque of healthy and faulty engine

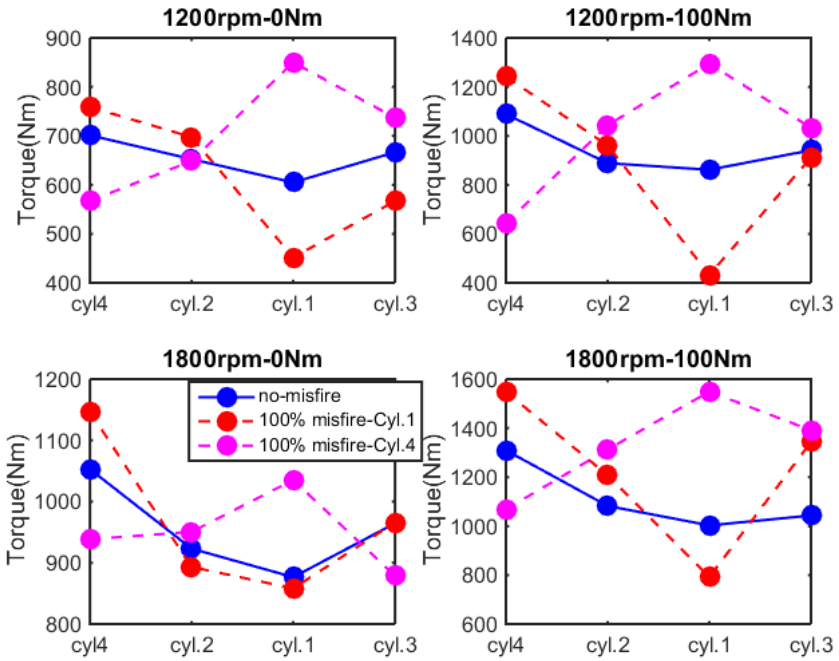

Figure 9-33 cylinder by cylinder peak pressure torque values of healthy and faulty engine

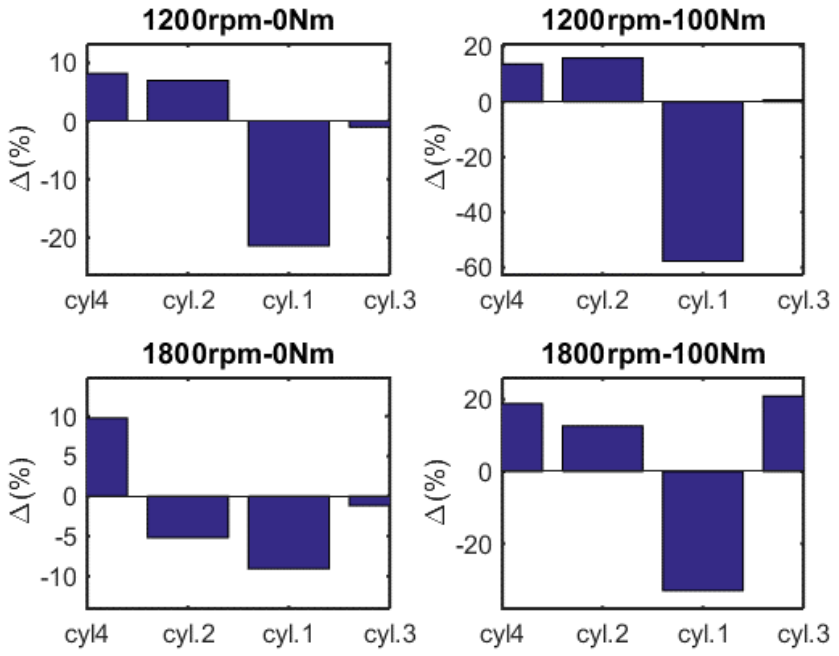

Figure 9-34 change in peak pressure torque across cylinder for 100% misfire in 1st cylinder

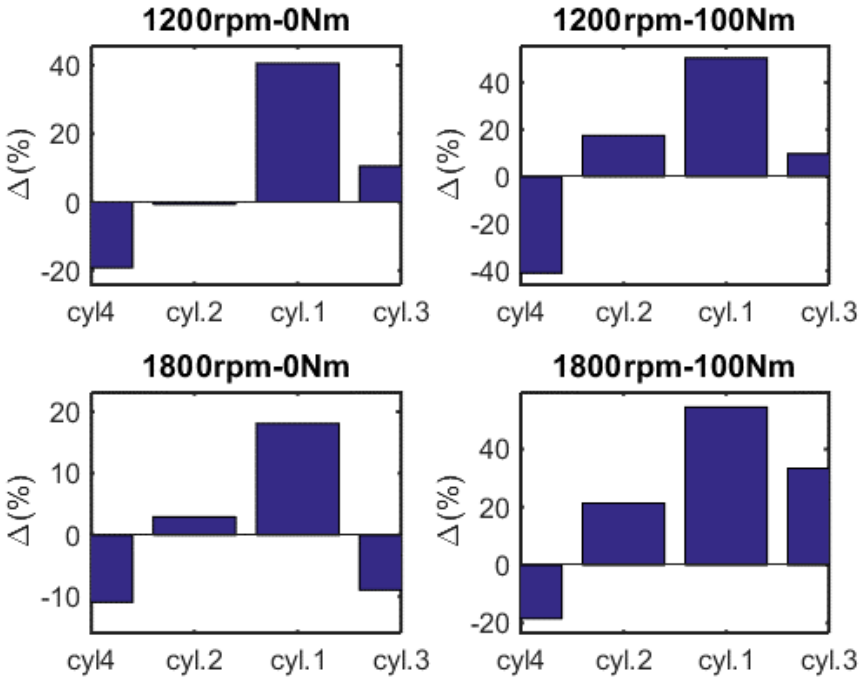

Figure 9-35 change in peak pressure torque across cylinder for 100% misfire in 4th cylinder

Hence, misfire in a cylinder of a four stroke inline diesel engine can be identified by the drop in the peak pressure torque values that pertains to that cylinder. Also evident is the increase in the peak pressure torque value of other cylinders. For complete misfire in the first cylinder, there is an increase in the peak pressure torque of cylinders 2 and 4 (both of their crankpins are 180 degrees to that of the misfiring cylinder) at 1200rpm-0Nm. While there is reduction in the peak pressure torque of the 3rd cylinder (its crankpin is in phase with the misfiring cylinder). This is not the case at 1800rpm. There is an increase in the peak pressure torque of the 4th cylinder and reduction in that of the 2nd 3rd and 1st cylinder at 1800rpm-0. Then at 1800rpm-0Nm, there is an increase in all other cylinders except that with the complete misfire. This phenomenon is the same for complete misfire in the 4th cylinder. This might be a way in which the engine tries to compensate for the loss of pressure torque from the misfiring cylinder. This might affect the use of cylinder by cylinder peak pressure torque value for early misfire localization.

In order to compare the percentage drop in peak pressure with that of the peak pressure torque the measured single cylinder pressure for healthy and complete misfire was used for calculating the pressure torque. The figure 9-36 shows the percentage drop in peak pressure and that of the calculated pressure torque.

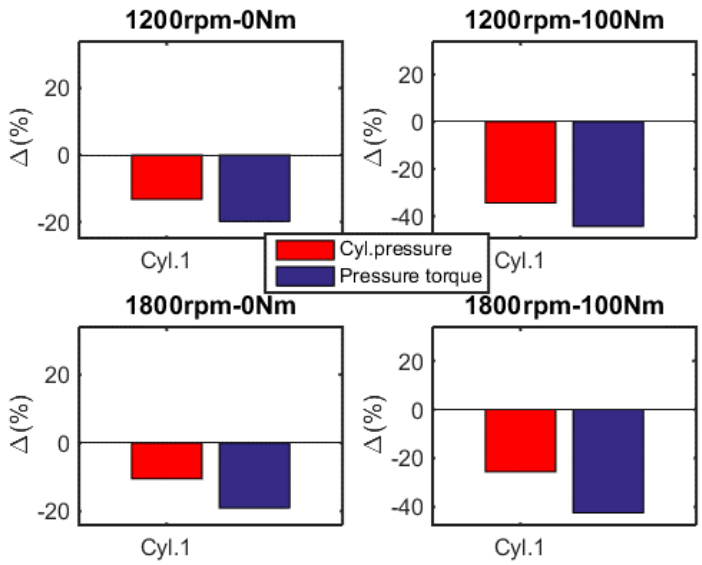

Figure 9-36 drop in peak pressure and calculated pressure torque

A drop in peak cylinder pressure indicates a drop in the peak pressure torque across all speed and loading conditions. However, there is a deviation in the percentage drop in the calculated pressure torque compared to that of the reconstructed ones using the altered estimated low frequency resonance shown in figure 9-34. While the change in the calculated pressure torque at 1200rpm-100Nm shows about 42% drop in its peak values for complete misfire in the 1st cylinder, the reconstructed one using the offline estimated low resonance frequency shows a 58% drop.

The low frequency resonance was set to its real time estimated value by adjusting the inertia of the adaptor attached to the flywheel. The change in reconstructed pressure torque using the real time estimated low frequency resonance shown in figure 9-37, is closer to that of the calculated ones. The change in the reconstructed pressure torque at 1200rpm-0Nm using the real time estimated low frequency resonance indicates a 35% drop in its peak value for complete misfire in the 1st cylinder.

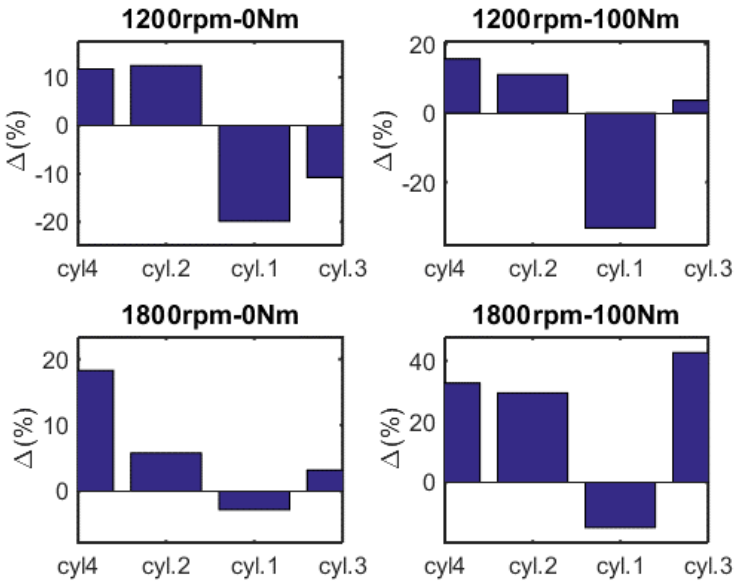

Figure 9-37 change in peak pressure torque across cylinder using real time resonance frequency

The reconstructed pressure torque of engine with healthy and faulty injector with four severities shown in figures 9-38 and 9-39 shows some alteration in peak torque values which can be used for cylinder by cylinder diagnostics. The reconstructed pressure torque tend to show similar trends around low (0Nm) and high (210Nm and 315Nm) engine loading condition across all speed.

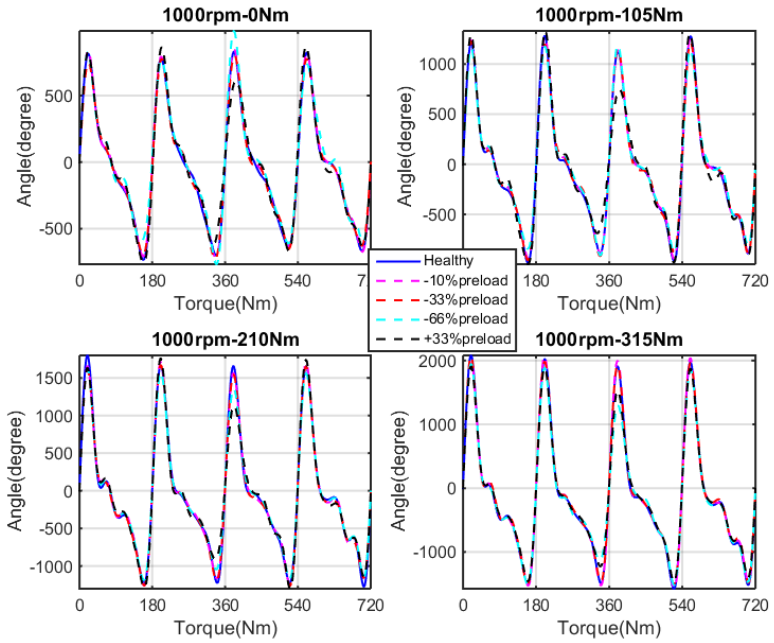

Figure 9-38 reconstructed pressure torque for healthy and faulty injector at 1000rpm

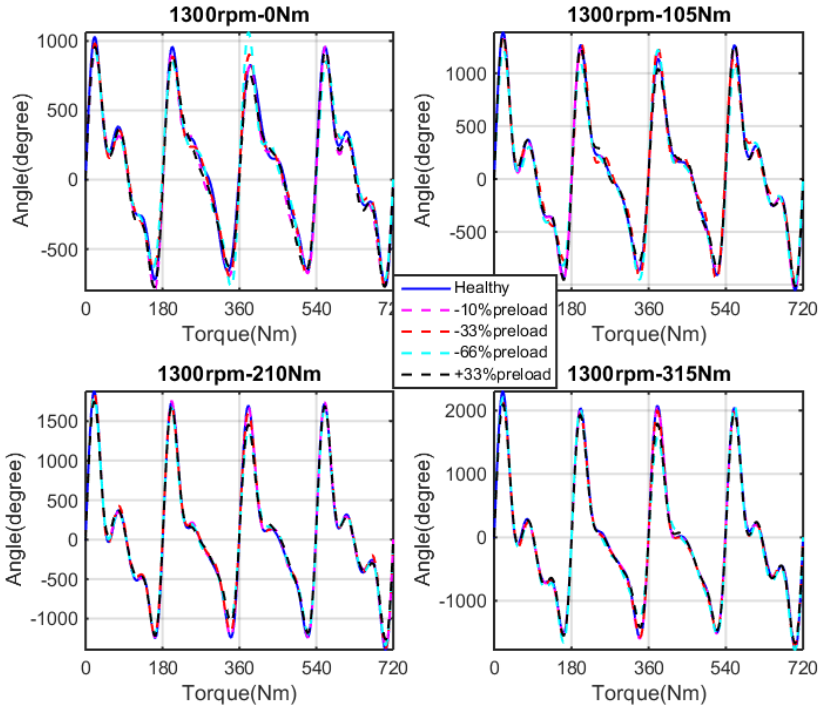

Figure 9-39 reconstructed pressure torque for healthy and faulty injector at 1300rpm

The peak pressure torque values for healthy and faulty injectors with four different fault severities shown in figure 9-39 below shows characteristics which can locate the faulty cylinders at all severities.

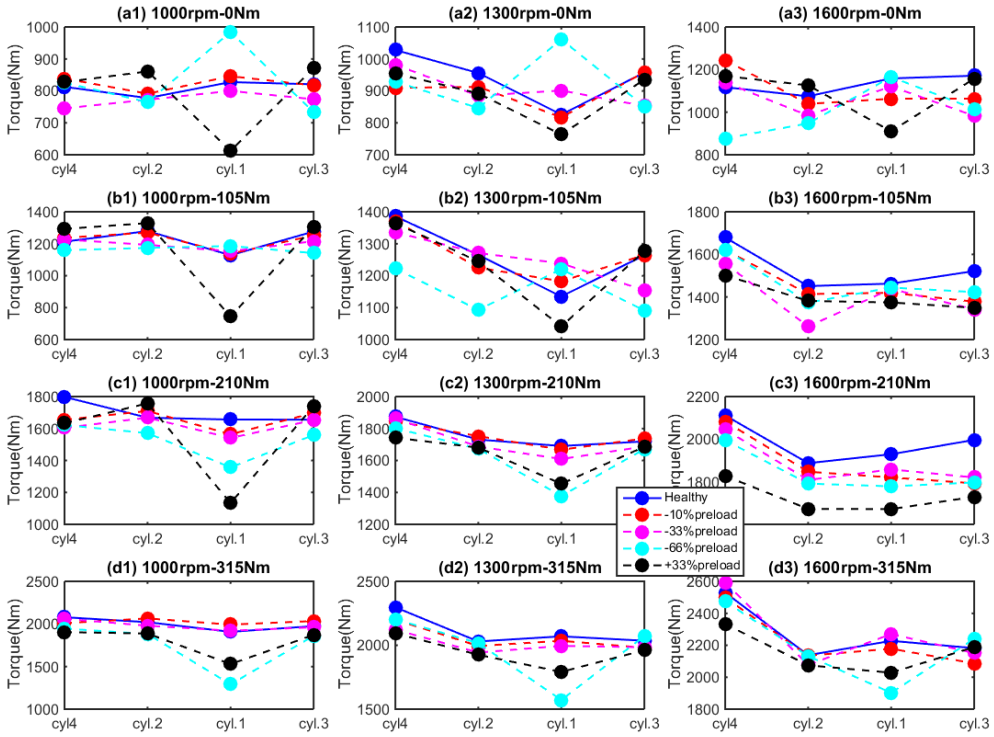

Figure 9-40 peak pressure torque for healthy and faulty injector

Result (9-40 (a1), (a2) and (a1)) shows that at low (0Nm) engine loading condition across all speed 66% reduction in the injector's preload washer thickness of a cylinder results to increase in the peak pressure torque values that pertains to that cylinder when compared with that of other cylinders. While at the same loading condition 33% increment of this parameter causes reduction in the peak pressure torque values of the faulty compared with other cylinders. As the load increases to 105Nm, this trend is no longer the same across all speeds for both fault severities. Although there is increase in the peak pressure torque of the faulty cylinder at 1000rpm-0Nm (9-40 (b1)) and 1300rpm-0Nm (9-40 (b2)), when compared to that of other cylinders there is no difference for the 65% reduction preload washer thickness. However, that of the 33% increment still shows a reduction in peak pressure torque of the faulty cylinder compared to the other cylinders. The peak pressure torque values of all cylinders at 1600rpm-105Nm shows a very

strange characteristics for all the fault severities. The peak pressure torque values at 1300rpm-210rpm (9-40 (c2)) shows distinctive features that can be used to identify the faulty cylinder at all severities of the fault. This corresponds with the engine performance curve in chapter 4 where the engine optimal operation is at 1300rpm. Hence, the clear features for cylinder misfire localization are found at this speed as shown in figure 9-41 below.

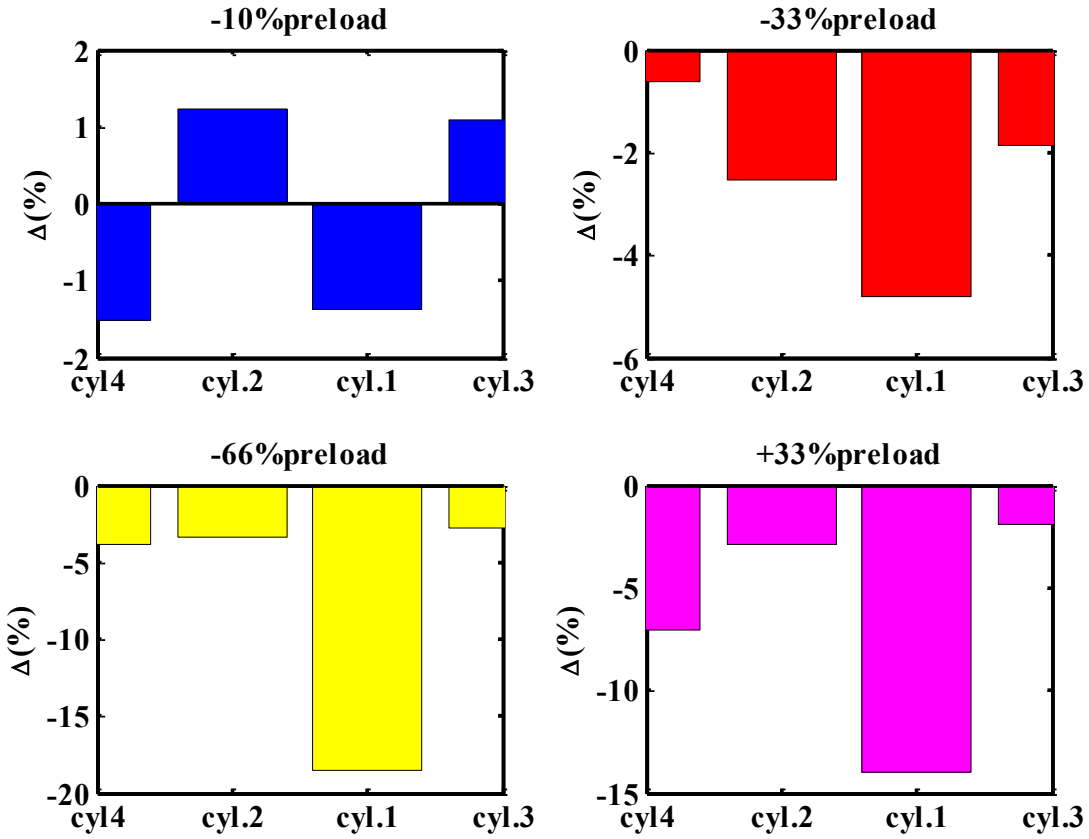

Figure 9-41 drop in pressure torque at 1300rpm 210Nm injector fault

The drop in peak pressure torque relative to cylinder one, which is the faulty cylinder, tends to become significant as the severity of the fault increases. However, at 10% preload washer thickness reduction, there is no significant drop in the peak pressure torque relative to the faulty cylinder. This means that a 10% reduction of preload washer thickness fault might be difficult to isolate using this technique.

The peak pressure torque values for normal and abnormal exhaust valve clearance with two severities shown in figure 9-42 shows alteration in peak values but not after any particular pattern.

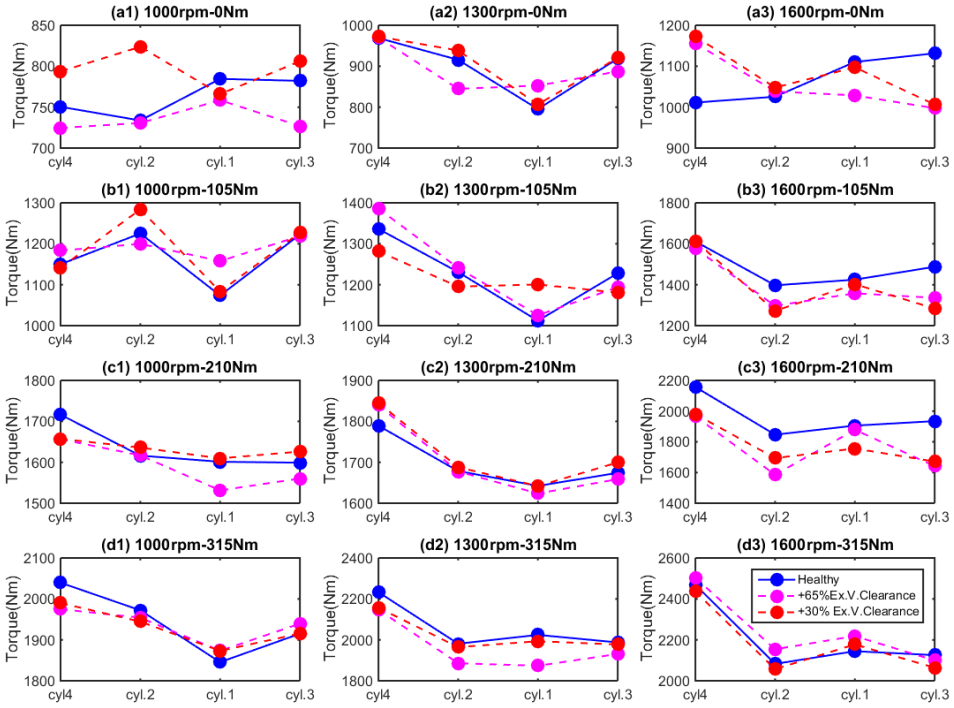

Figure 9-42 peak pressure torque for normal and abnormal valve clearance

This might be due to the non-linear pattern in which the engine balances loss in pressure torque in any cylinder and the severity of the fault. However, at the same speed and load conditions as that of the injector fault (1300rpm-210Nm) (9-41(c2)) the cylinder with the abnormal valve clearance shows a lower peak pressure torque values compared to other cylinders as shown in figure 9-43 below. The drop in peak pressure torque relative to cylinder one, which is the faulty cylinder, tends to become significant as the severity of the abnormal valve increased from 30% to 65%. A 5% abnormal valve clearance was seeded but the impact was not significant on the reconstructed pressure torque.

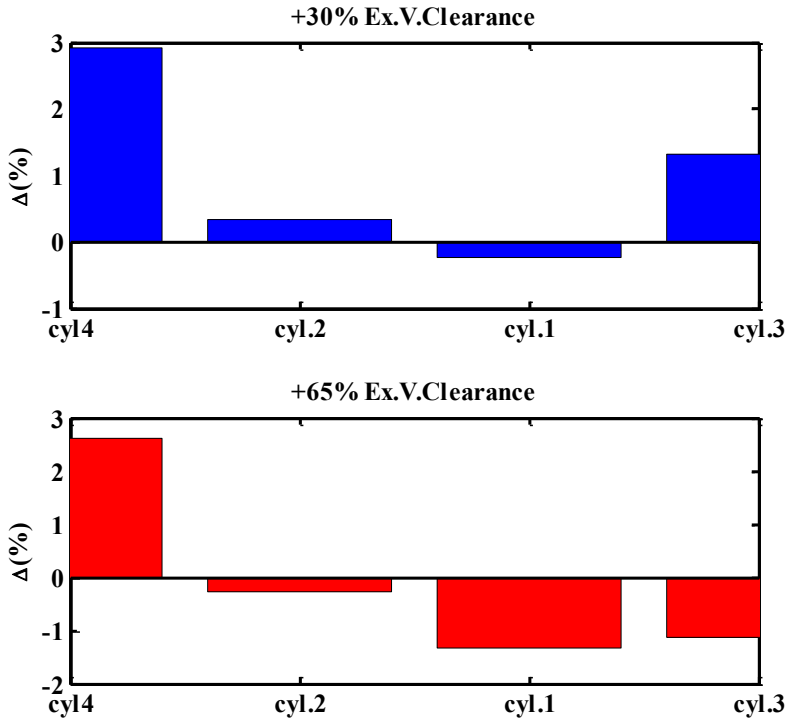

Figure 9-43 drop in pressure torque at 1300rpm 210Nm abnormal valve clearance

9.4 Key Findings

IAS based fault diagnosis has been implemented through the simulation of a complete misfire, abnormal valve clearance valve condition and faulty injectors in a four cylinder diesel engine. The IAS waveform and frequency domain representation method have been used for signal based fault diagnosis.

The trough values of IAS waveform can detect and localize complete misfire in a four cylinder diesel engine at low speed where the effect of the torque due to inertia is not dominant. However, the use of these trough values for abnormal valve clearance and partial misfire is not reliable due measurement discrepancies associated with the IAS waveform.

The frequency domain representation of the estimated IAS shows the presence and increase in amplitudes of the half order harmonics of the engine speed for all three faults. The frequency domain representation of estimated IAS shows an increase in the amplitude of the engine speed frequency component and its half order harmonics for all severities of the injector fault. However,

this increase in amplitude does not show any regular pattern that corresponds to the fault severities. The IAS frequency domain representation is reliable for fault detection but not always sufficient for fault localization.

The order domain deconvolution technique which reconstructs the pressure torque from the measured IAS has been used for the model based fault diagnosis. The reconstructed IAS waveform using 24 Fourier components of the original signal is about 90% correlated with the original signal. The reconstructed pressure torque using the real time identified low resonance frequency shows a close correlation with the calculated pressure torque using the measured single cylinder pressure. Alterations to the low frequency resonance of the engine-dynamometer system results to the alterations in peak values of the reconstructed pressure torque. Hence, the real time low frequency resonance should be considered in the implementation of IAS model based fault diagnostics. The online estimated low frequency resonance of a three DOF engine-dynamometer system, when used in IAS based diagnostics can enhance the fault diagnosis performances of this method

The peak values of reconstructed pressure torque using the estimated real time low frequency resonance can be used for faulty injector and abnormal exhaust valve clearance diagnosis.

CHAPTER TEN

10 CONCLUSION AND RECOMMENDED FURTHER WORKS

This chapter encapsulates the set project objectives as defined in section 1.2.2 and relates them to the achievements of the research work. The main conclusions drawn from this research work conducted are presented in line with the set project. Furthermore, an explicit summary of the main contributions of the work carried out to knowledge is also highlighted. The last section of this chapter presents areas of possible future work that might help advance subjects topics in the field of engine condition monitoring.

10.1 Review of Project Objectives and Achievements

Improving engine-monitoring techniques is paramount especially in this era where environmental pollution is on the increase and environmental regulations are becoming more stringent than ever. Most global nations like the UK and France in accordance with the 2015 Paris agreement on climate change, are beginning to set targets to reduce automobile emissions. There is, therefore, the need to improve engine monitoring techniques to comply with these stringent regulations and to ensure that the engine during its entire operational life performs optimally. The development of an online modal identification method that can further enhance early and accurate engine fault diagnosis was the primary scientific and technical objectives of this research project. The signal from an encoder which is often used to construct the IAS waveform for fault detection has been utilized for online output-only torsional modal properties identification. As defined in section 1.2.2 the project was split into three areas: IAS extraction and measurement implication: modal analysis of engine driveline and IAS based fault diagnosis. The individual part of the project is subdivided into distinct research objectives and achievement, which are listed below.

10.1.1 IAS Extraction and Measurement Implication

- **Objective -01:** To study, develop and implement a non-intrusive IAS measurement strategy for data collection from the engine.
- **Achievement-01**: An extensive CI engine test facility was developed featuring relevant encoders which measure the IAS at three locations front-end, flywheel and dyno-end (section 4.2). The sensor at the front-end of the engine was developed by applying basic working principles encoders and was readily available and cheap. The Sinocera DAQ used was able to sample the encoder signal at 750 kHz thereby enhancing the IAS measurement accuracy.

- **Objective -02:** To investigate and implement IAS extraction algorithms for transient and steady engine operating conditions.
- **Achievement-02**: the theoretical basis of a time domain and frequency domain based IAS extraction algorithm were studied and implemented. The time count extraction algorithm was used to estimate IAS at transient engine start-up and shutdown operation (section 8.2).

The Hilbert demodulation extraction algorithm was used to estimate IAS at engine steady operation (9.2).

10.1.2 Modal Analysis of Engine-Dynamometer System

- **Objective -03**: To develop a torsional vibration model for typical engine driveline, so as to simulate IAS data from the engine under steady and random excitation.
- **Achievement-03**: The IAS of steady engine operation at variable speed and loads was simulated numerically by developing both the finite element and discrete state space model in a Matlab environment (section 6.3 and 6.4). The pressure torque was calculated using a hybrid cylinder pressure profile produced from measured single cylinder pressure. The inertia torque was calculated using relevant engine parameters. The total engine torque was used as input force acting on the corresponding inertia for the numerical simulation using the finite element model. While the input force was modelled as a sinusoidal wave whose frequency is the engine's firing frequency for the numerical simulation using the state space model (section 6.4). The IAS of the engine under transient operation was simulated using pseudo-random number generated in Matlab as input for the state space model simulation (section 8.1). The modal properties such, resonance frequencies and mode shapes of the engine-dynamometers was calculated using the relevant system parameters like torsional stiffness, inertia and damping ratio as supplied in the manufacturers manual (section 6.2). The inertia of the flywheel adaptor was altered, and its impact on the calculated resonance frequency and mode shape was investigated (section 6.4). The effect of the altered resonance frequencies, due to the flywheel inertia alteration, on simulated IAS was also investigated. The low resonance frequency component showed more consistent sensitivity to flywheel inertia alteration.

- **Objective -04**: To explore which of engine's transient operations can be considered as random excitation and to implement output only modal analysis using data from an engine's transient operation.
- **Achievement-04**: The general study of modal analysis techniques that can be used for IAS based output-only modal analysis was investigated through a literature survey which reviewed suitable OMA technique (section 7.2). Both OMA time and frequency domain techniques were evaluated against an IAS based online modal properties identification of

a typical engine-dynamometer system (section 7.2). The covariance-driven reference based SSI technique due its robustness and ease of computation was identified for a prospective IAS based modal properties identification. The dynamics of engine operation at start-up, idle and shut-down operation were investigated by reviewing engine transient operation (section 8.2). The presence of misfire in the engine during start-up and idle operation makes the shut-down operation a prospective transient operation to be used for an SSI based output-only modal analysis.

- **Objective -05**: To develop and implement output only modal analysis using IAS outputs from random excitation of engine-load system and transient engine operation.
- **Achievement-05**: The IAS output simulated from random excitations of the engine-load system was used in identifying the modal properties of the engine-dynamometer system through the implementation of a covariance-driven reference based SSI technique (section 8.1.2). The IAS of transient engine operation has been used to identify the online modal properties of the engine-dynamometer system by implementing a covariance-driven reference based SSI technique (section 8.2). The cylinder (1, 3 and 4) of the engine was induced with a complete misfire respectively and encoder response during engine shut-down operations were measured and IAS estimated (section 8.3). The modal properties such as resonance frequency and mode shapes of the engine-dynamometer system were identified using the estimated IAS of individual cylinder misfire. The result showed that misfire in a cylinder does affect the extracted modal properties to certain degree.

10.1.3 IAS Based Fault Diagnosis

- **Objective -6**: To study IAS signal and model based diagnosis.
- **Achievement -6**: The general study of IAS based diesel engine fault diagnosis was investigated through a literature survey which reviewed relevant previous work on IAS signal and model based fault diagnosis (section 3.2). The IAS model based fault diagnosis has shown more prospect in not only the detecting a fault, but also identifying the faulty cylinder. Detailed steps and equations of implementing the IAS model based fault diagnosis, where the pressure torque is reconstructed from the IAS were presented (9.3).

- **Objective -7**: To implement IAS signal and model based diagnosis by introducing a specific quantified fault into the engine.
- **Achievement -7**: Abnormal valve clearance and injection faults were induced in the test engine respectively (section 4.3.2 and 4.3.3). The IAS of the engine with the respective faults was estimated using the Hilbert demodulation extraction technique (section 9.2). The time domain waveform of estimated IAS for engine healthy and faulty operations and were compared. The IAS waveform trough values which represents each cylinders transition from compression to combustion were used to diagnosis the complete misfire fault in the respective cylinders. The IAS frequency domain representation was used for detecting abnormal valve clearance and injection faults. The peak value of the cylinder pressure torque reconstructed from measured IAS was used in identifying the faulty cylinder with the abnormal valve clearance and injection fault.

- **Objective 8**: To explore the effect of accurate modal properties in model based fault diagnosis
- **Achievement -8**: The cylinder pressure torque was reconstructed using the identified modal properties of the engine-dynamometer system by altering the inertia of the flywheel to achieve the desired low resonance frequency (section 9.3.1). The cylinder pressure torque was also reconstructed using an altered inertia of the flywheel. The result showed that any alteration in the flywheel inertia affects the peak pressure torque reconstructed.

10.2 Conclusions from Research Conducted

This research work is aimed towards the online identification of modal properties of engine-dynamometer system from measured IAS for accurate engine fault detection and location. This has been conducted through experimental and simulation evaluations. Furthermore, a novel IAS based online output-only engine-dynamometer modal properties identification which enhances IAS model based fault diagnosis has been developed. The conclusions listed below can be drawn from the research conducted.

Conclusion one: IAS has been estimated from encoder signal during engine start-up and shut-down operation by the time count technique. The estimated IAS shows the engine speed sweeping through suitable frequency range. It can be concluded that the time count estimation technique is suitable for transient engine operation.

Conclusion two: A three DOFs engine-dynamometer system consisting of engine, flywheel and dynamometer has been developed to simulate IAS for engine fault diagnostics. The simulation and experimental results showed thesame characteristics for healthy and faulty condition. The three DOFs is sufficient and computationally easy to study engine-load system for fault diagnostics.

Conclusion three: IAS has been simulated using hybrid cylinder pressure profile obtained from a measured single cylinder pressure to calculate the cylinder pressure torque. The time and frequency domain representation of the simulated IAS at variable speed and load showed a very close correlation with the measured ones. It can be concluded that the hybrid cylinder pressure profile obtained from single cylinder pressure reduces computation ease of simulating IAS for engine fault diagnosis.

Conclusion four: The impact of altered resonance frequency on IAS was simulated using a state space model of the engine-dynamometers system. An increase in the low resonance frequency component of the system resulted in an increase in the IAS amplitudes across all cylinder and reduction in the trough values which represent the transition from compression to combustion and vice versa. It can be concluded that the IAS of a typical engine-load system where the dynamometer represent the load in the case is sensitive to the low frequency vibration mode.

Conclusion five: The IAS estimated during engine transient shut-down operation was used for implementing an online output only modal properties identification of the engine-dynamometer system. The estimated IAS during engine shut-down operation can be used for online modal properties identification of an engine-dynamometer system for IAS model based diagnostics.

Conclusion six: A simulation and experimental evaluation of IAS based covariance-driven SSI technique was developed and implemented. The identified mode shapes and resonance frequencies

from the simulated outputs under random excitations were about 80% with their calculated values. The identified low and high frequency resonances and their mode shapes using the IAS estimated during transient engine shut-down operation, were about 80% correlated with the calculated and simulated ones. However, the error margin for the high frequency resonance was high. It can be concluded that covariance-driven SSI technique can be used to identify online the torsional modal properties of a typical engine-load system especially the low frequency vibration modes for early and accurate engine fault diagnostics.

Conclusion seven: The modal properties of the engine-dynamometer system were obtained during respective cylinder misfire, so as to study the system's mode shape characteristics under misfire conditions. There was an increment of the low frequency resonance obtained during misfire in respective cylinders. Inherently, the mode shape of the low frequency resonance showed unique characteristics for individual cylinder misfire. This characteristics can be used to diagnose cylinder by cylinder misfire in a four cylinder diesel engine. It can be concluded that the identified mode shape of the low frequency resonance can be used for complete misfire detection in a four inline four stroke diesel engine.

Conclusion eight: The altered low resonance frequency used for the pressure torque reconstruction showed alterations in the peak pressure torque value. The closeness of the low resonance frequency to its actual value would further enhance the accuracy and quantification capabilities of the IAS model based diagnosis.

Conclusion nine+6: The signal based IAS diagnosis was implemented for complete misfire in the 1^{st} and 4^{th} cylinder. The IAS waveform trough values which represents individual cylinder's transition from compression to combustion was used to detect and locate the faulty cylinder. However, this method was not feasible for abnormal valve clearance and injector fault location. The frequency domain representation of all three faults showed the presence of low frequency components which is the half order harmonics of the shaft rotational frequency. The IAS model based diagnostics which takes into consideration the identified real time resonance frequency of the engine-dynamometer system was able to detect and locate all three faults showing a consistent effect of their severities at specific speed and load (1300rpm-210Nm) engine operating condition.

It can be concluded that the IAS model based fault diagnosis of a four cylinder diesel engine which takes into consideration the identified online modal properties enhances its accuracy and quantification capabilities.

10.3 Contribution to Knowledge

The research work conducted in this thesis seeks to introduce the impact of online modal properties identification techniques in IAS based condition monitoring and fault diagnostics. The main contributions to knowledge from this work are listed below:

Contribution one: The three degree of freedom engine-dyno torsional vibration is sufficient for an IAS based model-based diagnostics.

Contribution two: The IAS time count algorithm can be used to extract encoder signal with varying frequency range. Until now there has been no published research using this extraction technique for transient engine shut-down operation.

Contribution three: This research work shows for the first time the impact of modal properties on the simulated IAS using a three DOF state space model of an engine-dynamometer system.

Contribution four: This research work shows for the first time that the excitation forces during transient engine shutdown operation can be modelled as a non-stationary random input and the output used for implementing a covariance-driven SSI algorithm.

Contribution five: This research presents a novel online IAS based output only torsional modal properties identification using a covariance-driven SSI technique.

Contribution six: The research work shows for the first time the impact of cylinder misfire on the mode shape of a typical engine-load system. This can be used for online misfire detection and localisation as the model is computationally easy to implement and the sensor are cheap and readily available to install.

Contribution seven: The research work has provided a new strategy of using real time low frequency resonance component of a typical engine-load system for IAS model based diagnosis of diesel engine with a misfire, an abnormal valve clearance and injection faults.

10.4 Recommended Further Research Work

A lot of preliminary research and study have been undertaken to understand OMA techniques, transient engine operations and signal processing techniques for the accurate estimation of IF in a noisy signal. In order for more extensive research to be undertaken the following further works are recommended.

Recommended work one: In this thesis only the covariance-driven SSI technique was implemented using IAS extracted during transient engine shut-down operation. Further research should be conducted on the use data driven SSI technique to identify the modal properties of the engine-dynamometer system using the estimated IAS during shut-down operation. As studies have shown that the data driven is more accurate than the covariance driven SSI. Also the data-driven permits the identification of Kalman gain which can be used to predict the system response.

Recommended work two: In this research work the modal properties of the engine-load system were identified during transient engine shut-down operation. In special cases like in nuclear gas plants where engines are only shut-down few times in a year it will be difficult to obtain IAS response for the modal properties identification. So, further research should be conducted on the use of IAS estimated at other engine transient operations like change in speed or load for output only modal properties identification.

Recommended work three: In this research the impact of the modal properties on reconstructed pressure torque was only investigated. Further research is needed to investigate the impact of the modal properties on reconstructed cylinder pressure using the order domain deconvolution technique.

Recommended work four: In this research study the modal properties of four cylinder engine-dynamometer system was identified, but there is no evidence if the same results would be obtained

for 6-cylinder engine or other types of engine. There is the need to extend this IAS based output-online modal properties identification technique to other types of diesel engines.

Recommended work five: In this work, the pressure torque reconstruction was done assuming a constant drivetrain load torque. It will be essential to investigate the effect of the modal properties on reconstructed pressure torque using a fluctuating drivetrain load torque.

APPENDIX A

Injector Opening Pressure Measurement

The injector was placed in a merlin injector tester as shown in the figure A-1 below and pressure was then applied manually until the needle lifts and fuel is injected inside the tester's chamber and a manual pressure gauge indicates the opening pressure of the injector. This test was carried out for healthy and different severities of the injector fault and the opening pressure noted and tabulated in table A-1 below.

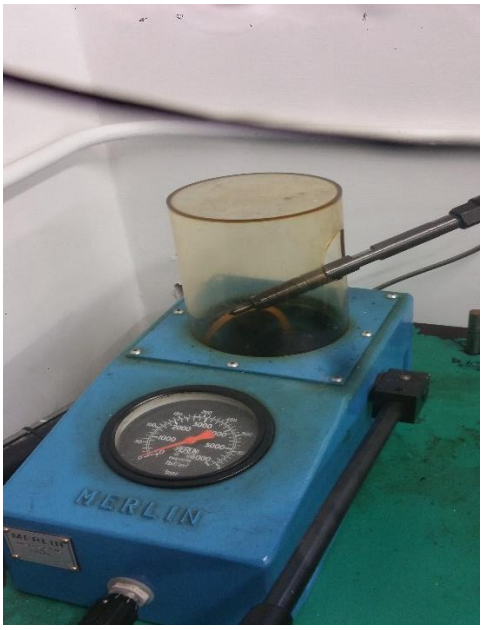

Figure A-0-1 merlin injector tester

Table A-0-1 opening pressure of injector with different washer thickness

Sn	**Washer thickness (mm)**	**Opening pressure (bar)**
1	1.85	270
2	0.65	80
3	1.74	260
4	1.30	240
5	2.59	400

APPENDIX B

IAS Based Covariance-driven SSI Algorithm

The following steps were implemented for the online torsional modal properties identification of a typical engine-load system using measured angular speed signal from engine flywheel and dyno reference point of the system. Firstly the raw angular displacement data shown in figure B-1 below is saved for 8 start-up, idle and shutdown operation.

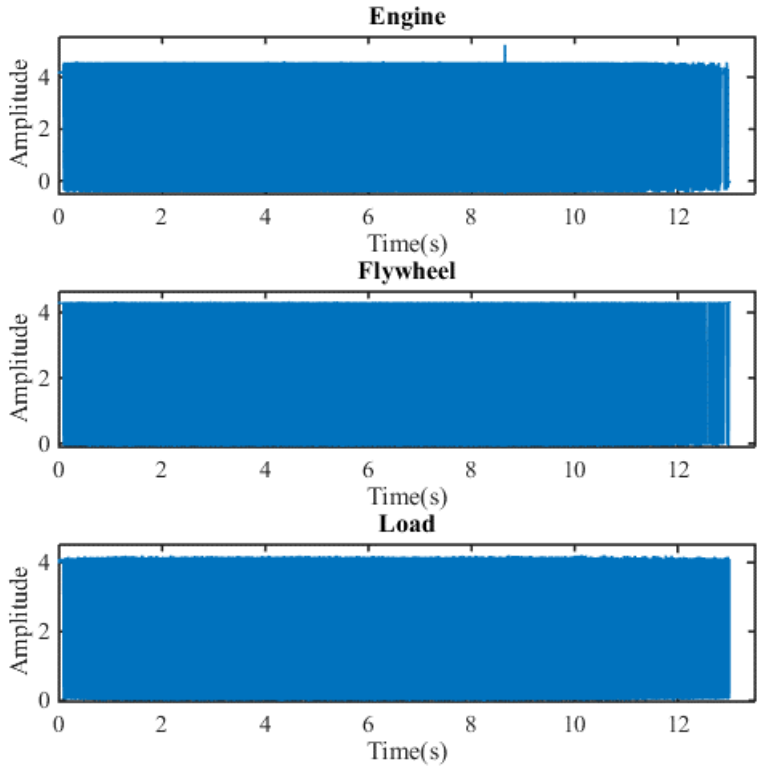

Figure B-0-1

Then the raw encoder signal is used for the estimation of IAS using the time count algorithm described in chapter 3 of this thesis. The frequency domain algorithm cannot be used because the signal contains several frequency components. Because of the high sampling frequency (750 kHz) used the signal is resampled to 10 kHz through a cubic spline interpolation. The estimated IAS is then separated into start-up (transient), idle (steady) and shutdown (transient) engine operations.

The IAS of the engine shutdown operation is considered for the modal properties identification in this work due to the minimum influence of combustion frequency compared to that of the start-up operation. The 8 IAS of the engine shutdown operation is cascaded as shown in figure B-2 below.

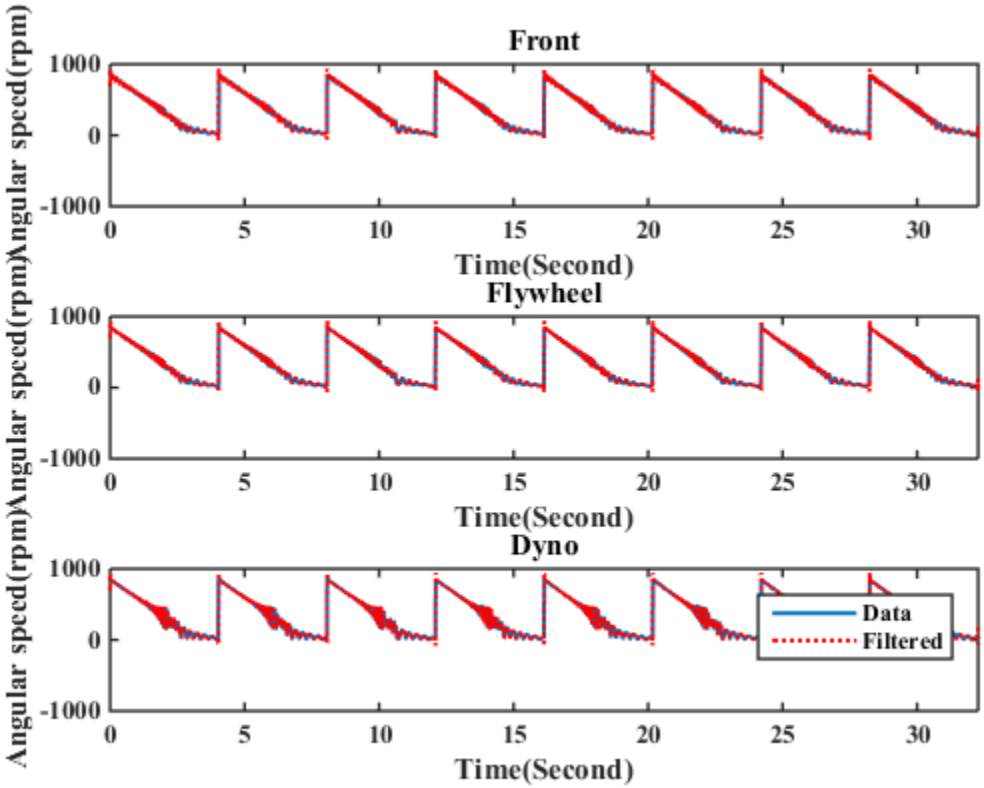

Figure B-0-2 Cascaded IAS signals

The signal is passed through a low pass filter to remove any unwanted noise. Several pre-processing options were considered before using the un-processed IAS data for the identification procedure. Firstly, the option of detrending the signal is considered as shown in the figure B-3 below. However, the result obtained is not satisfactory due to the omission of the low frequency component. Secondly the option of differentiation to angular acceleration is considered as shown in figure B-4 below. The obtained result is also not satisfactory as the presences of other frequency components were prevalent. It can be suggested that these two pre-processing methods add or removes relevant frequency component from the IAS signal. So the use of un-processed measured IAS data only is considered in this work.

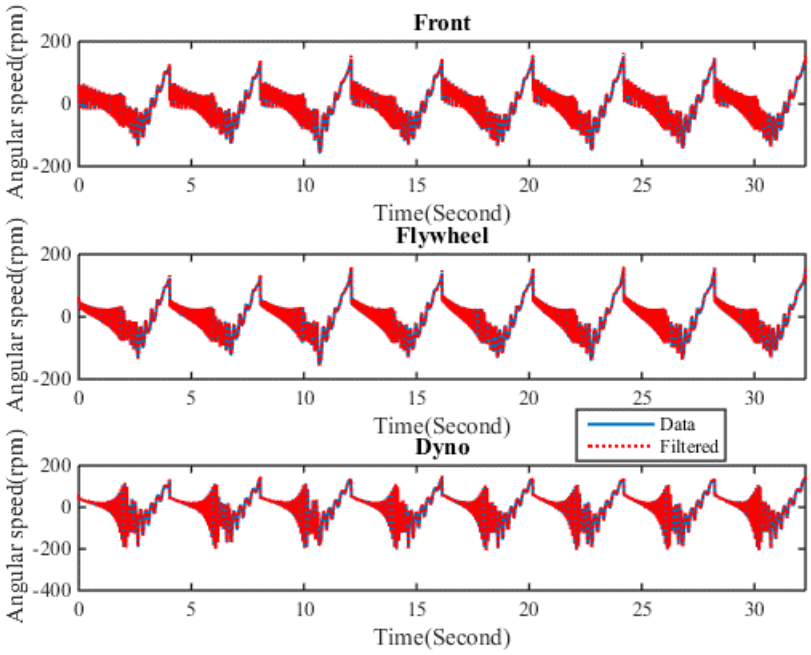

Figure B-0-3 detrended IAS data

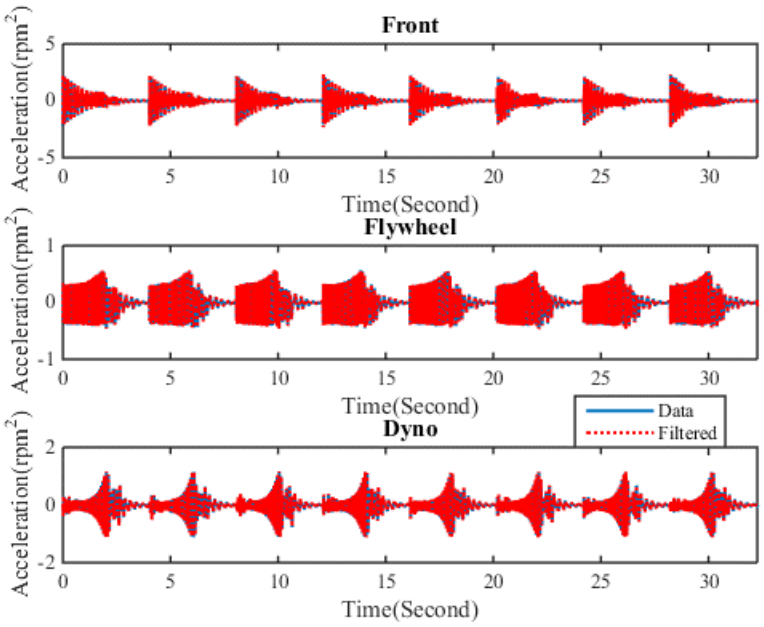

Figure B-0-4 instantaneous angular acceleration

Then the correlation function of the IAS signal was estimated using a sufficient data segment and a lag time.

The correlation function is averaged using a threshold criteria gotten through the calculation of the PDF of the signal. Due to the non-stationary nature of the IAS signal three different segment of the correlation function is averaged and used for the modal properties identification. The amount of segment is obtained through a trial and error method. The averaged correlation function of a segment of the data is shown in the figure B-5 below.

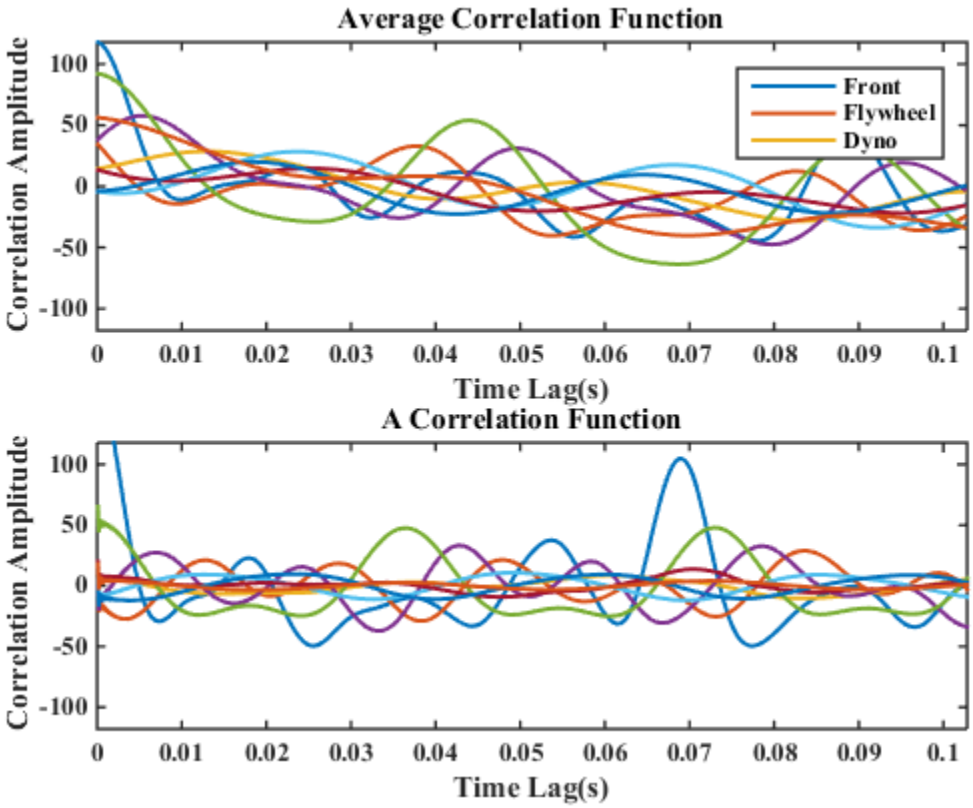

Figure B-0-5 correlation function of measured IAS

The modal properties for each segment is computed over selected orders and passed through a stabilization criteria and only the stable modes is saved and used for further selections. Only the frequencies which occur above certain rate is selected. Figure B-6 below shows the rate of frequency over order for the 1st data segment. The modal properties of the selected frequencies is saved and used for further selections as there are still some presence of harmonic components For example figure B-6 shows the presence of a 22Hz and 44Hz frequency component. These two can be said be in some sort of harmonic relationship. This is also evident in their mode shapes shown in figure B-7.

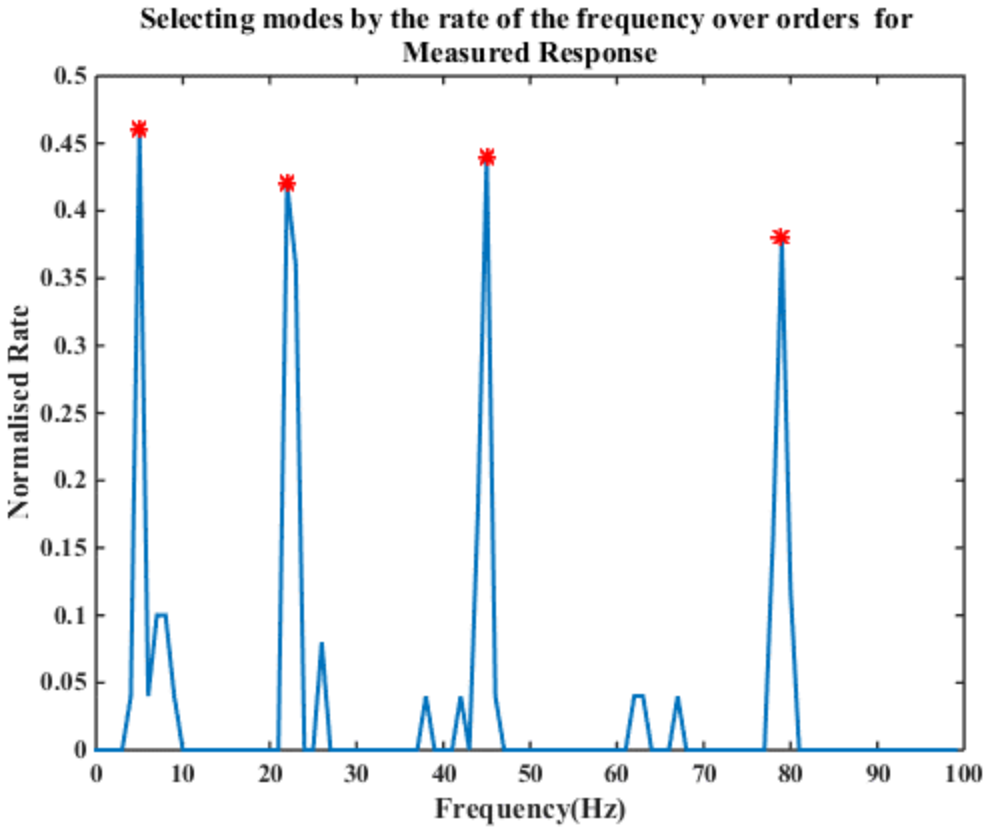

Figure B-0-6 rate of frequency over orders for 1st segment

The mode shapes of all the selected frequency component shown in figure B-7 Below indicates the presence of harmonic components. The last selection stage is the removal of the harmonic component leaving only the torsional modal properties of the engine-load system. This procedure is repeated for the IAS estimated from engine with induced faults.

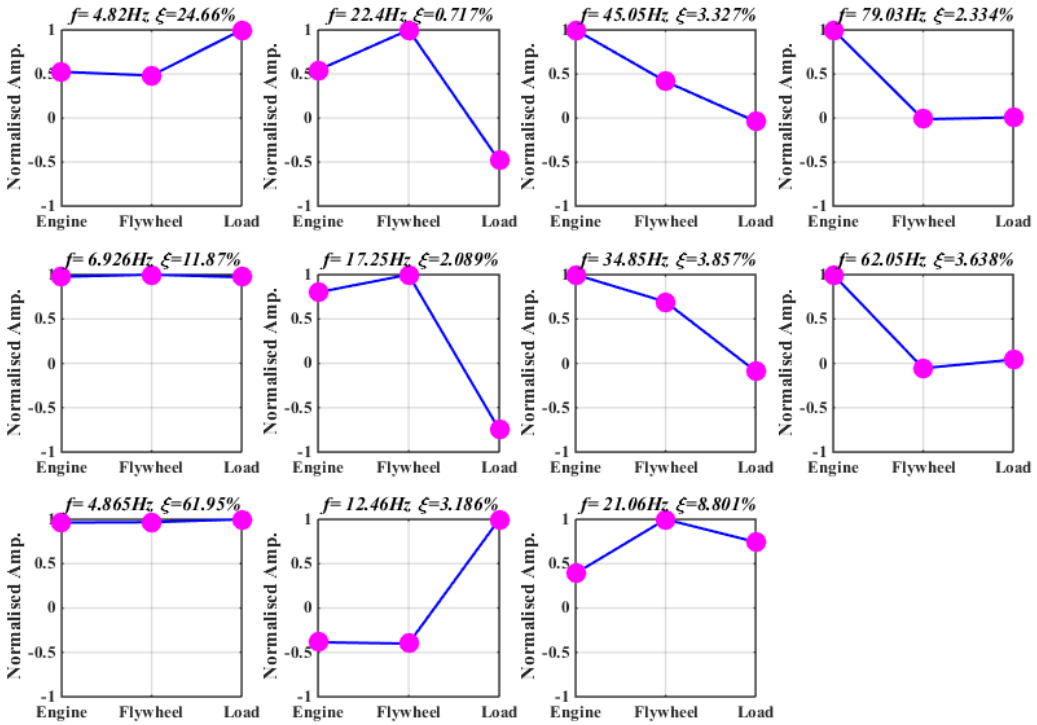
f= 4.82Hz ξ=24.66%
f= 22.4Hz ξ=0.717%
f= 45.05Hz ξ=3.327%
f= 79.03Hz ξ=2.334%
f= 6.926Hz ξ=11.87%
f= 17.25Hz ξ=2.089%
f= 34.85Hz ξ=3.857%
f= 62.05Hz ξ=3.638%
f= 4.865Hz ξ=61.95%
f= 12.46Hz ξ=3.186%
f= 21.06Hz ξ=8.801%
Normalised Amp.
Engine
Flywheel
Load

Figure B-0-7

APPENDIX C

Vibration modes of a 7 Degree of Freedom Engine-Dyno System

The system parameters used in building the system state matrix is shown in table C-1 below.

Table C-0-1

J_1 Pulley	0.0035kg. m^2
J_2 1st Crankthrow	0.056kg. m^2
J_3 2nd crankthrow	0.056kg. m^2
J_4 3rd Crankthrow	0.056kg. m^2
J_5 4th Crankthrow	0.056kg. m^2
J_6 Flywheel	2.881kg. m^2
J_7 Load	0.38kg. m2
c_1	0.02
c_2	0.04
c_3	0.04
c_4	0.04
c_5	0.05
c_6	0.12
k_1	2.01e5N/rad
k_2	1.02e5N/rad
k_3	1.02e5N/rad

k_4	1.02e5N/rad
k_5	1.2e6N/rad
k_6	2.25e3N/rad

So as to show all the possible vibration modes of the engine-dyno system a seven degree of freedom state space model of the system is developed in Matlab and the modal properties calculated. The predicted mode shapes and associated frequencies are shown in figure C-2 below.

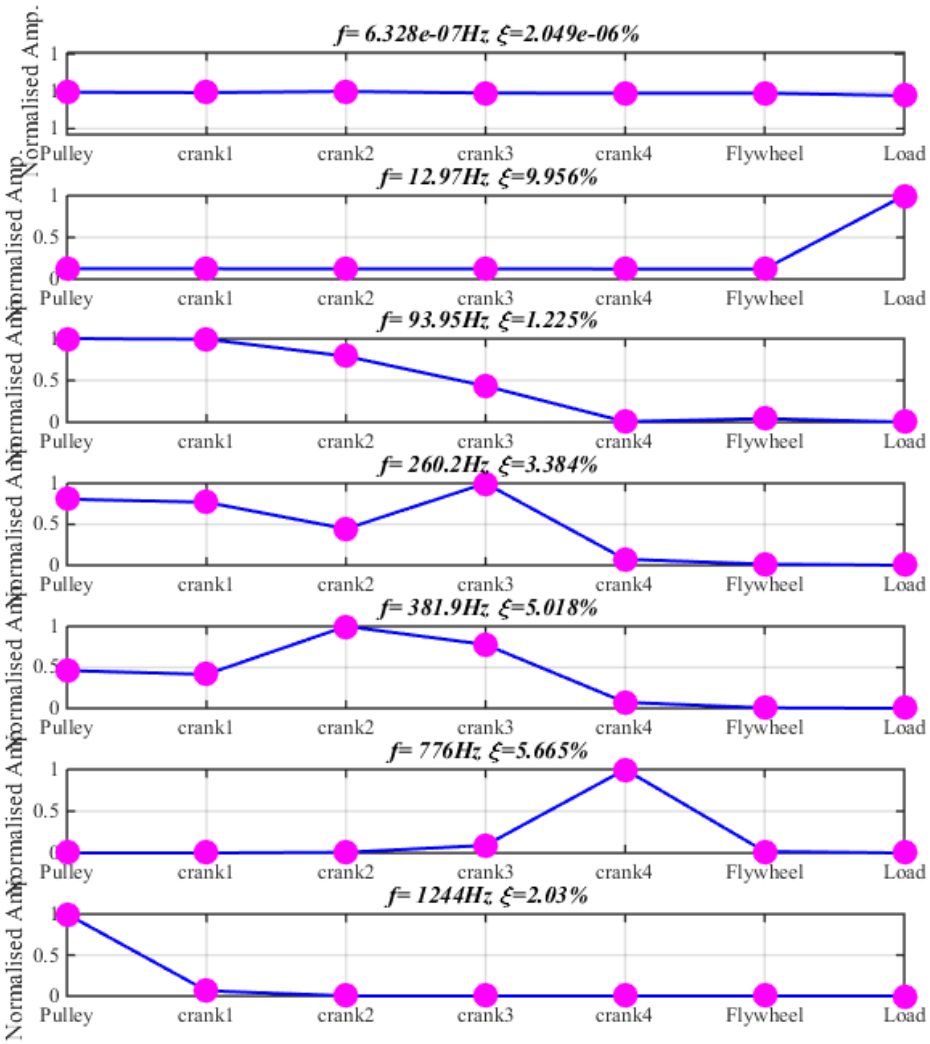

Figure C-0-1 vibration modes of 7DOF engine-load system

The predicted mode shapes of the 7DOF engine-load system indicates a rigid mode, one low vibration mode and five high vibration modes. A low frequency (<13Hz) resonance indicating more amplitudes at the load side of the system is shown and five high frequency (93Hz 260Hz, 381Hz, 776Hz and 1244Hz) resonances indicating movement around the engine side of the system.

APPENDIX D

Effect of Excitation Dynamics on Simulated System Output

In order to study the effect of excitation dynamics on the two vibration modes of the engine-load system, the amplitude of the non-stationary random input is varied by thrice. The non-stationary random input was chosen because it describes the excitation input during engine shutdown operation more compared to the stationary random input. The figure D-1 below shows the frequency domain representation of the outputs subjected to a non-stationary input of different amplitudes.

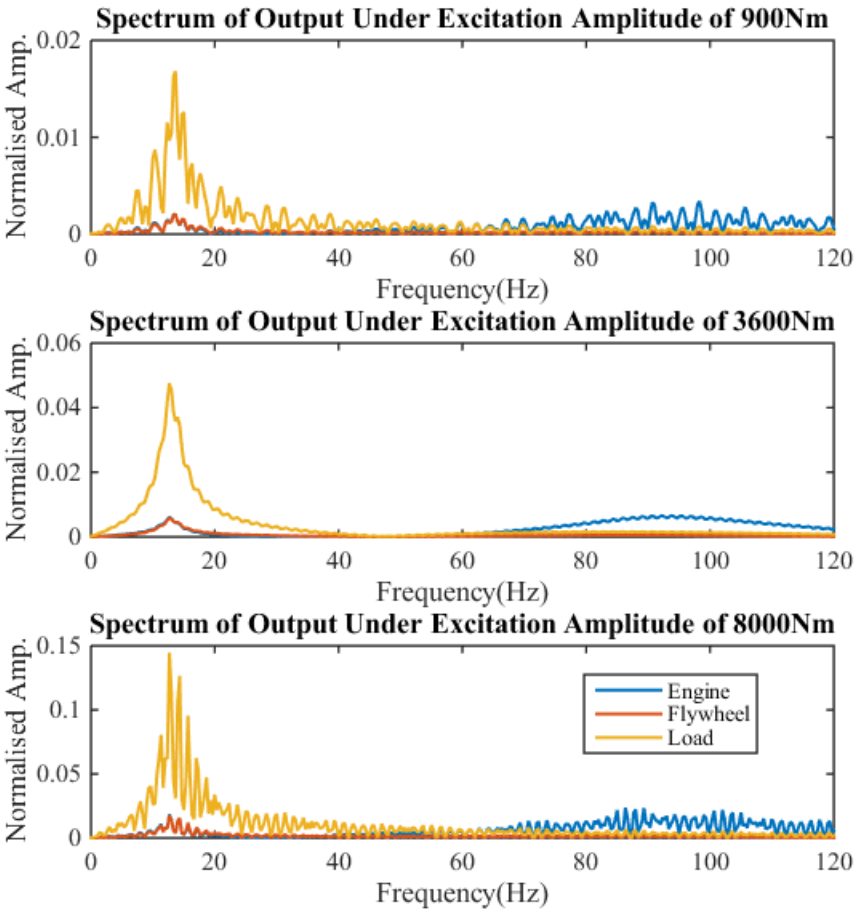

Figure D-0-1 frequency domain representation of output under different excitation amplitudes

Both the low and high frequency vibration mode are sensitive to excitation amplitudes as shown in figure D-1. However, because of the damping in the engine side of the system the low frequency vibration mode shows more increase in amplitude with increase in excitation amplitude. Another feature of the input which affect the excitation of the vibration modes is the distance between each impulse. The Matlab ‘rand’ function is used to randomly select the position of each impulse in the input. Table D-1 below provides the position of each impulse in the input used for the excitation in figure D-1.

Table D-0-1 position of impulse

Excitation amplitude	Position of impulse 1	Position of impulse 2	Position of impulse 3	Position of impulse 4
900Nm	88755	75517	117247	155935
3600Nm	89110	90165	26223	5131
8000Nm	60939	66679	137275	200957

Taking into consideration that the total length of the input is 300001 the 900Nm and 8000Nm excitation impulses are distributed in positions which are greater than half of the excitation signal length while that of the 3600Nm is distributed in positions that is less than half of the excitation signal length. The frequency domain representation of the output under 3600Nm excitation amplitude is less noisy and the amplitude of the high frequency vibration mode is clearer compared to the others. This suggest that the position distribution of the excitation impulse can affect the noise in the measured system output.

APPENDIX E

Kalman Filter and the Innovation Model

For a linear and time-invariant system, the Kalman filter relates response predictor and the state predictor as follows:

$$\begin{aligned} \hat{x}_{t+1} &= A\hat{x}_t + K_t e_t \\ e_t &= y_t - C\hat{x}_t \end{aligned} \tag{E-1}$$

, where the matrix K_t is called the non-steady Kalman gain and e_t is called the zero-mean $\hat{x}_t$ Gaussian white noise processes. The non-steady-state covariance matrix of the predicted state vector is defined as P_t the Kalman gain K_t can be estimated as:

$$\begin{aligned} K_t &= \left(G - AP_tC^T\right)\left(R_0 - CP_tC^T\right)^{-1} \\ P_{t+1} &= AP_tA^T + \left(G - AP_tC^T\right)\left(R_0 - CP_tC^T\right)^{-1}\left(G - AP_tC^T\right) \end{aligned} \tag{E-2}$$

The last part of equation (E-2) is called the Ricatti equation. On the basis of the previous predicted state $\hat{x}_t$ and the response y_t the Kalman filter predicts the state $\hat{x}_{t+1}$.

The Kalman filter (E-1) during start-up will experience a transient phase where the state prediction will be non-steady. But, when the system matrix is stable the filter enter a steady state as time get closer to infinity. At this steady state the covariance matrix of the predicted state $\hat{x}_t$ becomes constant, $P_t = P$ and $K_t = K$. The steady state Kalman filter is now defined as

$$\begin{aligned} \hat{x}_{t+1} &= A\hat{x}_t + Ke_t \\ e_t &= y_t - C\hat{x}_t \end{aligned} \tag{E-3}$$

The steady state Kalman gain is now estimated as:

$$\begin{aligned} K &= \left(G - APC^T\right)\left(R_0 - CPC^T\right)^{-1} \\ P &= APA^T + \left(G - APC^T\right)\left(R_0 - CPC^T\right)^{-1}\left(G - APC^T\right) \end{aligned} \tag{E-4}$$

The last part of equation (E-4) is called the algebraic Ricatti equation. If all matrices except P is known, the equation (E-4) can be solved using eigenvalue decomposition. The covariance matrix of the innovations is:

$$R_e = R_0 - CPC^T \tag{E-5}$$

Rearranging equation (E-1), the following state space model is obtained:

$$\begin{aligned} \hat{x}_{t+1} &= A\hat{x}_t + Ke_t \\ y_t &= C\hat{x}_t + e_t \end{aligned} \tag{E-6}$$

This is called the innovation state space model. This equation compared to the stochastic state space model (7-11) has the following difference: the prediction of the state vector replaces the state vector in (7-11) and the double input processes in (7-11) have been converted into a single input process called the innovations. From the equation (E-3) if many state of the stochastic state space model (7-11) can be predicted, then A and C matrices can be estimated using the least regression problem below:

$$\begin{bmatrix} \hat{x}_{i+1} & \hat{x}_{i+2} & \cdots & \hat{x}_{i+j} \\ y_i & y_{i+1} & \cdots & y_{i+j-1} \end{bmatrix} = \begin{bmatrix} A \\ C \end{bmatrix} \begin{bmatrix} \hat{X}_i \end{bmatrix} + \begin{bmatrix} \rho_w \\ \rho_v \end{bmatrix} \tag{E-7}$$

, where $\hat{X}_i$ is the Kalman filter state sequence gathered from the Kalman filter state estimates, defined as:

$$\hat{X}_i = \begin{pmatrix} \hat{x}_i & \hat{x}_{i+1} & \cdots & \hat{x}_{i+J-1} \end{pmatrix} \tag{E-8}$$

Since the innovations (input process) are assumed to be a Gaussian white noise and A and C are assumed to be time-invariant, this approach is effective even if the predicted state $\hat{x}_i$and $\hat{x}_{i+1}$ originates from a non-steady Kalman filter.

Data-Driven SSI Technique

The data-driven SSI technique uses the raw output data y_k which is available as discrete samples of the time signal, without any further pre-processing to obtain covariance matrix. Generally, a lot of sensors (which are mostly accelerometers) are used in modal analysis experiment since the spatial resolution of the experimental mode shapes is determined by the positions and amount of sensors used. This makes measurements used for modal analysis applications contain some

redundancy. In theory all the signal carry the same information on damping ratios and modal frequencies if none of the sensors is placed at the node of a mode (Peeters & De Roeck, 2001). So, to reduce the redundancy some signals can be partially omitted during the identification process. Resulting in identification algorithms that are faster and requires less computer memory, without losing accuracy. To yield the full mode shape the omitted sensors are again included in the end. This approach termed referenced based identification techniques is adopted in this work. The principles outlined in this section are that of the referenced based data-driven SSI technique. Assuming l amount of outputs are divided into a subset of r properly selected sensors and $l-r$other sensors arranged so as to have the reference sensor output first:

$$y_k = \begin{pmatrix} y_k^{ref} \\ y_k^{\sim ref} \end{pmatrix}, y_k^{ref} = Ly_k, L = \begin{pmatrix} I_r & 0 \end{pmatrix} \tag{E-9}$$

, where y_k^{ref} are the outputs from the reference sensor and $y_k^{\sim ref}$ are from the others; $L$is the selection matrix that selects the references. In OMA, the choice of the reference sensor corresponds to that of the input location in traditional EMA. Therefore, candidates for reference outputs should be sensors placed at optimal locations on the structure such that all modes of vibration are present in the measured data (Rainieri & Fabbrocino, 2014). It is essential in the development of identification techniques to gather the output measurements in a block Hankel matrix with $2i$ block rows and N Colums. The first and last i blocks have r and l rows. It is assumed that $N \to \infty$, for the statistical proves of the techniques. The Hankel matrix H^{ref} can be split into a future and past reference part:

$$H^{ref} = \frac{1}{\sqrt{N}} \left(\begin{array}{cccc} y_0^{ref} & y_1^{ref} & \cdots & y_{N-1}^{ref} \\ y_1^{ref} & y_2^{ref} & \cdots & y_N^{ref} \\ \cdots & \cdots & \cdots & \cdots \\ y_{i-1}^{ref} & y_i^{ref} & \cdots & y_{i+N-2}^{ref} \\ \hline y_i & y_{i+1} & \cdots & y_{i+N-1} \\ y_{i+1} & y_{i+2} & \cdots & y_{i+N} \\ \cdots & \cdots & \cdots & \cdots \\ y_{2i-1} & y_{2i} & \cdots & y_{2i+N-2} \end{array} \right) = \begin{pmatrix} Y_{0|i-1}^{ref} \\ Y_{i|2i-1} \end{pmatrix} = \begin{pmatrix} Y_p^{ref} \\ Y_f \end{pmatrix} \begin{matrix} \updownarrow ri \\ \updownarrow li \end{matrix} \tag{E-10}$$

The output data need to be scaled by a factor of $\frac{1}{\sqrt{N}}$ so as to be consistent with the definition of the output covariance matrix (7-13). The subscripts of $Y_{i|2i-1}$ are that of the first and last element in the first column of the block Hankel matrix. The subscripts p and f stand for past and future. By dividing H^{ref} into two parts of i block rows, the matrices Y_p^{ref} and Y_f are defined. Another splitting

up is gotten by adding one block row to the past references and neglecting the first block row of the future. In this new division, $l-r$ block rows are left over because the references are only a subset of the outputs. These rows are represented by$Y_{i|i}^{\sim ref}$:

$$H^{ref} = \begin{pmatrix} Y_{0|i}^{ref} \\ \hline Y_{i|i}^{\sim ref} \\ \hline Y_{i+1|2i-1} \end{pmatrix} = \begin{pmatrix} Y_p^{ref+} \\ \hline Y_{i|i}^{\sim ref} \\ \hline Y_f^- \end{pmatrix} \begin{matrix} \updownarrow r(i+1) \\ \hline \updownarrow l-r \\ \hline \updownarrow l(i-1) \end{matrix} \tag{E-11}$$

In the implementation of data-driven subspace algorithms, the RQ-factorization of the data Hankel matrices is very important. The RQ-factorization when applied to the Hankel matrix of equation (E-11) yields:

$$H^{ref} = \begin{pmatrix} Y_p^{ref} \\ \hline Y_f \end{pmatrix} = RQ^T \tag{E-12}$$

, where $Q$is an orthonormal matrix i.e. $Q^TQ = QQ^T = I_N$; R is a lower triangle matrix. The zeroes in R and the corresponding rows in Q^T can be omitted since $(r+l)i < N$.

$$H^{ref} = \begin{matrix} \\ ri \updownarrow \\ r \updownarrow \\ l-r \updownarrow \\ l(l-r) \updownarrow \end{matrix} \begin{matrix} ri & r & l-r & l(i-r) & N\to\infty \\ \leftrightarrow & \leftrightarrow & \leftrightarrow & \leftrightarrow & \leftrightarrow \end{matrix} \begin{pmatrix} R_{11} & 0 & 0 & 0 \\ R_{21} & R_{22} & 0 & 0 \\ R_{31} & R_{32} & R_{33} & 0 \\ R_{41} & R_{42} & R_{43} & R_{44} \end{pmatrix} \begin{pmatrix} Q_1^T \\ Q_2^T \\ Q_3^T \\ Q_4^T \end{pmatrix} \begin{matrix} \updownarrow ri \\ \updownarrow r \\ \updownarrow l-r \\ \updownarrow l(l-r) \end{matrix} \tag{E-13}$$

Because of their orthonormality the Qfactor will cancel out further in the algorithm. Thus, they are not needed. This results to an important data reduction of the technique. The next step is calculating the orthogonal projection, which is very important aspect of subspace identification. This is achieved by the projection of the row space of the future outputs into that of the past reference outputs:

$$\mathscr{P}_i^{ref} = Y_f / Y_p^{ref} \equiv Y_f Y_p^{ref^T} \left(Y_p^{ref} Y_p^{ref^T} \right)^{\dagger} Y_p^{ref} \tag{E-14}$$

The rationale behind the projection is that it preserves all the essential information in the past that is relevant to predict the future. Introducing equation (E-12); the QR-factorization of the Hankel matrix, into equation (E-13) results to the following expression for the projection:

$$\mathscr{P}_i^{ref} = \begin{pmatrix} R_{21} \\ R_{31} \\ R_{41} \end{pmatrix} Q_1^T \tag{E-15}$$

The main stochastic subspace identification theorem states that the orthogonal projection $\mathscr{P}_i^{ref}$ can be decomposed as the product of the observability matrix (7-17) and Kalman filter sequence (E-8) (Overschee and Moor, 1996):

$$\mathscr{P}_i^{ref} = \begin{pmatrix} C \\ CA \\ CA^2 \\ \cdots \\ CA^{I-1} \end{pmatrix} \begin{pmatrix} \hat{x}_i & \hat{x}_{i+1} & \cdots & \hat{x}_{i+N-1} \end{pmatrix} = O_i \hat{X}_i \tag{E-16}$$

The equation (E-16) holds asymptotically only for $N \to \infty$. The proof of this theorem where only the past reference outputs have been used (SSI/ref), is almost the same as the one where all the past outputs have been used, found in Overschee and Moor, 1996. The difference between both proofs is just the significance of the obtained Kalman filter state sequence$\hat{X}_i$. The obtained Kalman filter state sequence in the case of (SSI/ref), is the optimal prediction for the states using only observations of the reference outputs only instead of all outputs. Thus the Kalman filter state estimates in the case where all past outputs are used will be different from the one in the (SSI/ref). By applying SVD to the projection matrix, the observability matrix O_i and the state sequence $\hat{X}_i$ are obtained:

$$\mathscr{P}_i^{ref} = U_I S_1 V_1^T \tag{E-17}$$

The combination of equation (7-16) and (E-17) yields

$$O_i = U_1 S_1^{1/2}, \hat{X}_i = O_i^{\dagger} \mathscr{P}_i^{ref} \tag{E-18}$$

The order of the system n is the number of non-zero singular values in equation (E-17) while the observability matrix O_i and state sequence $\hat{X}_i$ can be calculated using equation (E-18). So as to calculate the system matrices A, C, Q, R, S another projection is obtained using the shifted past and future outputs of the data Hankel matrix (E-11):

$$\mathscr{P}_{i-1}^{ref} \equiv Y_f^- / Y_p^{ref+} = \begin{pmatrix} R_{41} & R_{42} \end{pmatrix} \begin{pmatrix} Q_1^T \\ Q_2^T \end{pmatrix} \tag{E-19}$$

The definition of the projection is given by the first equality while the second equality explains how it is computed from equation (E-13). Similar to equation (E-17), it can be proven that

$$\mathscr{P}_{i-1}^{ref} = O_{i-1}\hat{X}_{I+1} \tag{E-20}$$

, where O_{i-1} can be obtained from deleting the last rows of O_i computed in equation (E-18). The obtained shifted state sequence is:

$$\hat{X}_{I+1} = O_{i-1}^{\dagger}\mathscr{P}_{i-1}^{ref} \tag{E-21}$$

The Kalman state sequence $\hat{X}_{i,}\hat{X}_{i+1}$, at this moment are calculated using only the output data (E-18) and (E-20). By extending equation (E-7), the system matrices can be recovered from the following over determined set of linear equations:

$$A\begin{pmatrix}\hat{X}_{i+1}\\ Y_{i|i}\end{pmatrix} = \begin{pmatrix}A\\ C\end{pmatrix}\left(\hat{X}_i\right) + \begin{pmatrix}\rho_w\\ \rho_v\end{pmatrix} \tag{E-22}$$

, where $Y_{i|i}$ is a Hankel matrix with only one block row. So as to fit in the QR-scheme it is written as

$$Y_{i|i} = \begin{pmatrix}R_{21} & R_{22} & 0\\ R_{31} & R_{32} & R_{33}\end{pmatrix}\begin{pmatrix}Q_1^T\\ Q_2^T\\ Q_3^T\end{pmatrix} \tag{E-23}$$

Since the residuals $\left(\rho_w^T\ \rho_w^T\right)^T$ are uncorrelated with $\hat{X}_i$ and the Kalman state sequences as well as the outputs are known, the set of equations can be solved for $A,\ C$ in a least square sense:

$$\begin{pmatrix}A\\ C\end{pmatrix} = \begin{pmatrix}\hat{X}_{i+1}\\ Y_{i|i}\end{pmatrix}\hat{X}_i^{\dagger} \tag{E-24}$$

It is clear that the Q-factors cancel out when introducing equations (E-15), (E-18), (E-20), (E-21) into (E-24). The noise covariances Q, R and S are recovered as the covariance's of the residuals in equation (E-23). By solving the Lyapunov equation for Σ (7-15), A, C, Q, R, S matrices can be transformed into A, G, C, Λ_0

$$\Sigma = A\Sigma A^T + Q \tag{E-25}$$

, G and Λ_0 can then be computed from (7-15) as

$$G = C\Sigma C^T + S, \Lambda_0 = C\Sigma C^T + R \tag{E-26}$$

Theoretically at this point the identification problem has been solved: the system order n and the system matrices A, G, C, Λ_0 have been found based on the outputs. The modal parameters can be estimated since the dynamic behaviour of the system is completely characterised by its eigenvalues.

Covariance-Driven SSI Technique

In the covariance-driven SSI technique the covariance between the outputs instead of the raw sampled data are used for modal identification. The output covariance is defined in equation (7-13) as $R_i = E\left[y_{k+i} \quad y_k^T \right] = \lim_{N\to\infty} \frac{1}{N} \sum_{k=0}^{N-1} y_{k+i} \quad y_k^T$ where the second equality introduced here follows from the ergodicity assumption. The covariance can be computed by either direct or Fourier transform method. The direct method estimates covariance by multiplication and summation of time samples. The Fourier transform method computes the covariance by applying FFT to the time signals and cross multiplying the resulting Fourier transforms. Then inverse FFT is applied to the cross-products which results in a periodic covariance function estimate. The original signal is zero-padded to avoid bias error due to circular convolution. A major drawback of using the covariance as primary data in identification is that it squares up the data, thereby affecting the numerical accuracy of identified modal parameters. Due to its high-speed of implementation, this method it is adopted in this work instead of the direct method. The covariance-driven SSI technique outlined in this work uses the covariance between the outputs and a limited set of references instead of that between all outputs. Hence it is termed reference-based covariance-driven SSI technique. The output covariance functions are gathered in block Toeplitz matrix (a matrix where each diagonal consist of the repetition of the same element) computed from the data block Hankel matrix:

$$T_{1|i}^{ref} \equiv \begin{pmatrix} R_i^{ref} & R_{i-1}^{ref} & \cdots & R_1^{ref} \\ R_{i+1}^{ref} & R_i^{ref} & \cdots & R_2^{ref} \\ \cdots & \cdots & \cdots & \cdots \\ R_{2i-1}^{ref} & R_{2i-2}^{ref} & \cdots & R_i^{ref} \end{pmatrix} \tag{E-27}$$

Assuming ergodicity and for $N \to \infty$ the block Toeplitz matrix equals:

$$T_{1|i}^{ref} = Y_f \left(Y_p^{ref} \right)^T \tag{E-28}$$

In real life scenario a finite number of N data is available and by dropping the limits a covariance estimate $\widehat{R}_i$ is obtained as:

$$\widehat{R}_i = \frac{1}{N}\sum_{k=0}^{N-1} y_{k+1}\, y_k^T \tag{E-29}$$

If the factorization property (7-18) is applied to $T_{1|i}^{ref}$ the Toeplitz matrix would decompose as:

$$T_{1|i}^{ref} = \begin{pmatrix} C \\ CA \\ \cdots \\ CA^{i-1} \end{pmatrix} \begin{pmatrix} A^{i-1}G^{ref} & \cdots & AG^{ref} & G^{ref} \end{pmatrix} = O_i C_i^{ref} \tag{E-30}$$

By applying SVD to the block Toeplitz matrix, the referenced-reversed controllability and the observability matrix can be obtained:

$$T_{1|i}^{ref} = USV^T = \begin{pmatrix} U_1 & U_2 \end{pmatrix} \begin{pmatrix} S_1 & 0 \\ 0 & 0 \end{pmatrix} \begin{pmatrix} V_1^T \\ V_2^T \end{pmatrix} = U_1 S_1 V_1^T \tag{E-31}$$

, where S is a diagonal matrix which contains the singular values in descending order and while U and V are orthonormal matrices meaning $U^T U = UU^T$ and $V^T V = VV^T$. Since there is the assumption that $ri \geq n$ and the inner dimension of the product $O_i C_i^{ref}$ is equal to n, the rank of the product cannot exceed n. The number of non-zero singular values corresponds to the rank of a matrix. Hence, the zero singular values and corresponding singular vectors are omitted in the last equality of equation (E-31). From the equations (E-30) and (E-31), It can be stated that

$$\begin{aligned} O_i &= U_1 S_1^{1/2} \\ C_i^{ref} &= S_1^{1/2} V_1^T \end{aligned} \tag{E-32}$$

The solution to the identification problem becomes straightforward, once O_i, C_i^{ref} are known. From equation (7-17) and (7-18), its known that C equals the first l rows of O_i, while G^{ref} equals the last r columns of C_i^{ref}. By decomposing a shifted block Toeplitz matrix obtained as:

$$T_{2|i+1}^{ref} = O_i A C_i^{ref} \tag{E-33}$$

, the state matrix A can be obtained as:

$$A = O_i^{\dagger} T_{2|i+1}^{ref} C_i^{ref\,\dagger} = S_i^{-1/2} U_1^T T_{2|i+1}^{ref} V_1 S_1^{-1/2} \tag{E-34}$$

, where $(\bullet)^{\dagger}$ represents the pseudo-inverse of a matrix. Modal parameters such as damping ratio, modal frequency and mode shape can be extracted analytically using equations (5-47), (5-48) and (5-49).

Implementation and Stabilization

In reality, none of the singular values in equation (E-31) and (E-17) are exactly zero due to noise effect emanating from modelling inaccuracies, measurement and computational error. So classically, only by looking at a gap between two successive singular values can the model order n be determined. The model order is obtained from the singular values with the maximal gap. Though, in many practical cases there is no visible gap. Thus, in order to achieve a good model for modal identification, a stabilization diagram is constructed by identifying a complete set of models with different orders. To construct the stabilization diagram the model order is usually over-specified. Then there is a comparison between the poles corresponding to certain model order and that of one-order-lower. The pole is labelled as a stable one, if the differences between the damping ratio, eigenfrequency and the modal participation factor (or related mode shape) are within pre-set limits. For instance, if the following limits were chosen: 3% for damping ratio, 1.5% for eigenfrequencies, 1% for modal vectors, the stability requirements will be:

$$\begin{aligned} &100\%\frac{f^{(\mathrm{p})}-f^{(\mathrm{p}+1)}}{f^{(\mathrm{p})}}<1.5\% \\ &100\%\frac{\xi^{(\mathrm{p})}-\xi^{(\mathrm{p}+1)}}{\xi^{(\mathrm{p})}}<3\% \\ &100\%\left(1-MAC(\mathrm{p},\mathrm{p}+1)\right)<1\% \end{aligned} \tag{E-35}$$

, where p is the model order at which the modal properties (f eigenfrequency, ξ damping ratio and MAC Modal Assurance Criterion) are identified. The MAC is the squared correlation between two modal vectors defined as follows:

$$MAC(\mathrm{p},\mathrm{p}+1)=\frac{\left|v^{(\mathrm{p})^H}v^{p+1}\right|^2}{\left(v^{(\mathrm{p})^H}v^{(p)}\right)\left(v^{p+1^H}v^{p+1}\right)} \tag{E-36}$$

The spurious numerical poles can be sorted out of the modal parameter data set easily as they will not stabilize at all during this process.

Appendix F

Engine-dyno model

Based on the previous crank modelling presentation the single-body system of the crankshaft is modelled as shown in figure 0-1 (Brusa, et al., 1997). Where T_i represents the actual excitation torque, which is a combination of the both the gas and mass torque for the ith nodal point of the system. Whilst k, c and ca represents the torsional stiffness, relative damping coefficient and absolute damping coefficient of the elastic springs connecting inertia discs together J_i represent the inertia of individual disc. The crankshaft model for the four-cylinder diesel engine in chapter 4, considering the pulley wheel at the free end (left side) of the crankshaft, the flywheel inertia disc and dynamometer (right side) is shown in the Figure 0-2. As shown in the Figure 0-2, each crank slider mechanism of the JCB diesel engine is represented by separate inertia disc connected by torsional springs.

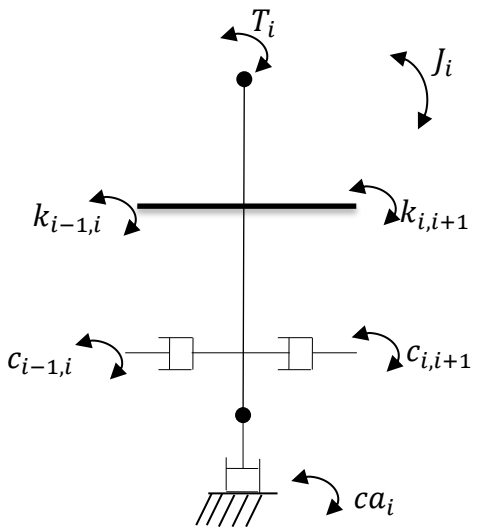

Figure 0-1 Single-body torsional vibration system of crankshaft assembly

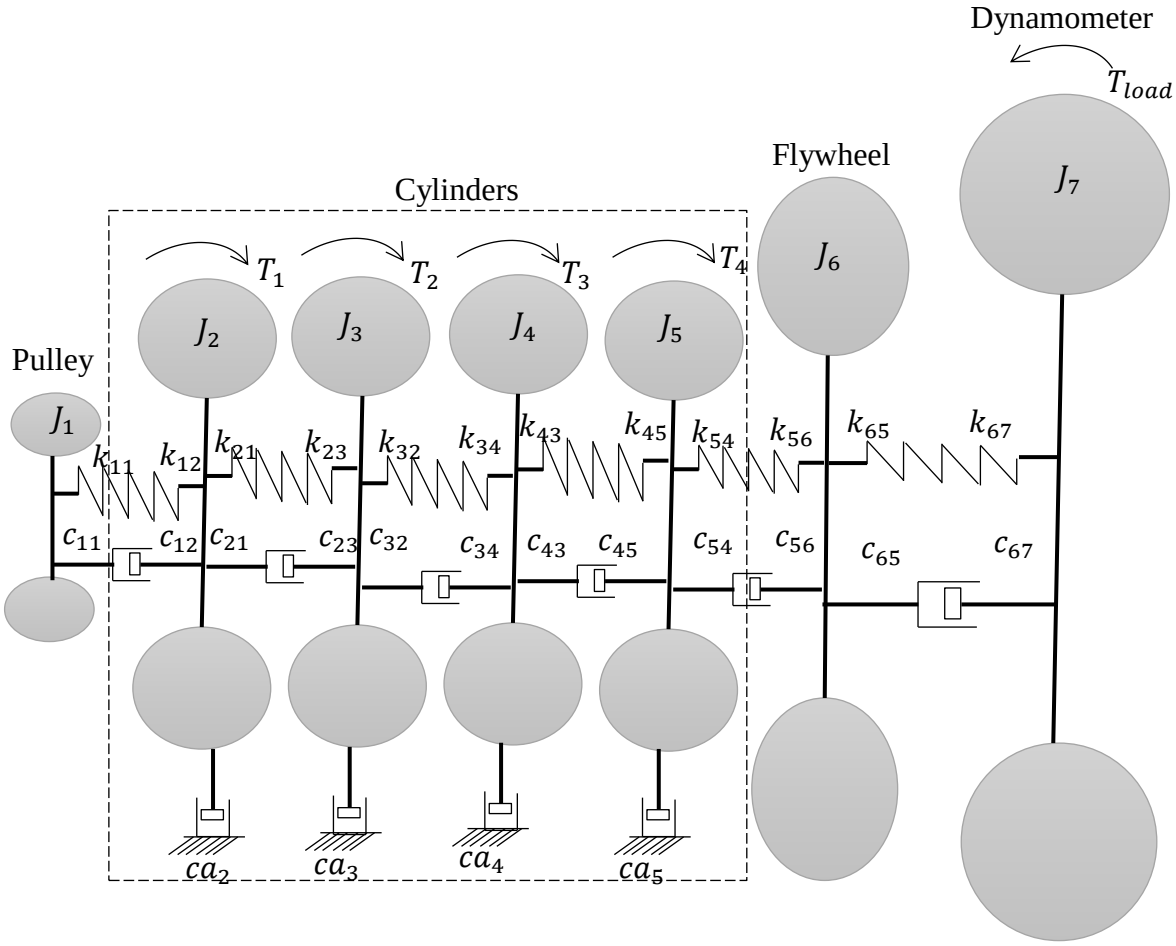

Figure 0-2 a lumped mass four cylinder engine-driveline

Numerical Model

The dynamic characteristics of a discrete mechanical system like the engine-driveline system, containing p inertias connected through torsional springs and dampers using Finite Element (FE) approximation is described by the following matrix differential equation:

$$[\mathrm{J}]\{\ddot{\theta}(t)\}+[C]\{\dot{\theta}(t)\}+[K]\theta(t)=T(t) \qquad \text{(F-1)}$$

, where $J, C, K \in \mathbb{R}^{p\times p}$ are the inertia damping and stiffness matrices; $\theta(t) \in \mathbb{R}^{p}$ is the angular displacement vector at continuous time t; $\dot{\theta}(t)$ is the angular speed vector and $\ddot{\theta}(t) \in \mathbb{R}^{p}$ is the angular acceleration vector. The vector $T(t) \in \mathbb{R}^{p}$ is the excitation toque acting on each inertia disc.

Although, the FE model (equation F-1) is a good representation of the torsional vibration of a typical engine-driveline structure, the main interest of this work cannot be obtained by the FE model. However, it is used as a starting point to derive the other model that is more suited in the context of experimental modelling. This is because the model is in continuous time while the measurement taken in real life experiments are mostly sampled at discrete time.

Reference

Aenlle, M. L., & Brincker, R. (2014). Modal Scaling in OMA Using the Mass matrix of a Finite Element Model. In *Dynamics of Civil Structures, Volume 4* (pp. 263–270). Springer, Cham. https://doi.org/10.1007/978-3-319-04546-7_30

Ahmed Yousef Ben Sasi. (2005). *The Exploitation of Instantaneous Angular Speed for Machinery Condition Monitoring*. University of Manchester.

Albarbar, A.S. (2006). *The Acoustic Condition Monitoring of Diesel Engine*. University of Manchester.

Al-Durra, A., Fiorentini, L., Canova, M., & Yurkovich, S. (2011). A Model-based estimator of engine cylinder pressure imbalance for combustion feedback control applications. In *Proceedings of the 2011 American Control Conference* (pp. 991–996). https://doi.org/10.1109/ACC.2011.5991196

Ali, S. A., & Saraswati, S. (2015). Reconstruction of cylinder pressure using crankshaft speed fluctuations. In *2015 International Conference on Industrial Instrumentation and Control (ICIC)* (pp. 456–461). https://doi.org/10.1109/IIC.2015.7150785

André, H., Girardin, F., Bourdon, A., Antoni, J., & Rémond, D. (2014). Precision of the IAS monitoring system based on the elapsed time method in the spectral domain. *Mechanical Systems and Signal Processing*, *44*(1–2), 14–30. https://doi.org/10.1016/j.ymssp.2013.06.020

A.S Rangwala. (2005). *Turbo-Machinery Dynamics*.

Azzoni, P. M., Minelli, G., Moro, D., Flora, R., & Serra, G. (1999). *Indicated and Load Torque Estimation using Crankshaft Angular Velocity Measurement* (SAE Technical Paper No. 1999-1–543). Warrendale, PA: SAE International. https://doi.org/10.4271/1999-01-0543

Badaoui, M. E., Danière, J., Guillet, F., & Servière, C. (2005). Separation of combustion noise and piston-slap in diesel engine—Part I: Separation of combustion noise and piston-slap in diesel engine by cyclic Wiener filtering. *Mechanical Systems and Signal Processing*, *19*(6), 1209–1217. https://doi.org/10.1016/j.ymssp.2005.08.010

Badawi, B. A., Shahin, M. A., Kolosy, M., Shedied, S. A., & Elmaihy, A. (2006). *Identification of Diesel Engine Cycle Events using Measured Surface Vibration* (SAE Technical Paper No. 2006-32-0097). Warrendale, PA: SAE International. https://doi.org/10.4271/2006-32-0097

Bart Peeters. (2000, December). *System Identification and Damage Detection in Civil Engineering*. katholieke universiteit leuven.

Basshuysen, R. V., & Schaefer, F. (Eds.). (2016). *Internal Combustion Engine Handbook: Basics, Components Systems, and Perspectives* (2 edition). Warrendale, PA: SAE International.

Bauer. H. (2004). *Dieselmotor-Management*. Stuttgart: Robert Bosch GmbH.

Blair, G. P. (1999). *Design and simulation of four-stroke engines*. Warrendale, PA: Society of Automotive Engineers.

Blair, G. P., & Drouin, F. M. M. (1996). *Relationship between discharge coefficients and accuracy of engine simulation*. SAE Technical Paper. Retrieved from http://papers.sae.org/962527/

Boashash, B. (1992). Estimating and interpreting the instantaneous frequency of a signal. II. Algorithms and applications. *Proceedings of the IEEE*, *80*(4), 540–568.

Brand, D., Onder, C. H., & Guzzella, L. (2005). *Estimation of the instantaneous in-cylinder pressure for control purposes using crankshaft angular velocity*. SAE Technical Paper. Retrieved from http://papers.sae.org/2005-01-0228/

Brandt, A. (2011). Noise and Vibration Analysis: Signal Analysis and Experimental Procedures. In *Noise and Vibration Analysis* (pp. 1–5). John Wiley & Sons, Ltd. https://doi.org/10.1002/9780470978160.ch1

Brincker, R. (2014). Some Elements of Operational Modal Analysis [Research article]. https://doi.org/10.1155/2014/325839

Brincker, R., & Ventura, C. (2015). *Introduction to Operational Modal Analysis* (1 edition). Chichester, West Sussex: Wiley-Blackwell.

Brincker, R., Zhang, L., & Andersen, P. (2001). Modal identification of output-only systems using frequency domain decomposition. *Smart Materials and Structures*, *10*(3), 441. https://doi.org/10.1088/0964-1726/10/3/303

Brown, T. S., & Neill, W. S. (1992). *Determination of Engine Cylinder Pressures from Crankshaft Speed Fluctuations* (SAE Technical Paper No. 920463). Warrendale, PA: SAE International. https://doi.org/10.4271/920463

Brusa, E., Delprete, C., & Genta, G. (1997). TORSIONAL VIBRATION OF CRANKSHAFTS: EFFECTS OF NON-CONSTANT MOMENTS OF INERTIA. *Journal of Sound and Vibration*, *205*(2), 135–150. https://doi.org/10.1006/jsvi.1997.0964

Bulatović, ž. M., Štavljanin, M. S., Tomić, M. V., Knežević, D. M., & Biočanin, S. L. (2011). Measurement and analysis of angular velocity variations of twelve-cylinder diesel engine crankshaft. *Mechanical Systems and Signal Processing*, *25*(8), 3043–3061. https://doi.org/10.1016/j.ymssp.2011.05.002

Caicedo, J. (2011). Practical Guidelines for the Natural Excitation Technique (NExT) and the Eigensystem Realization Algorithm (ERA) for Modal Identification Using Ambient Vibration. *Experimental Techniques*, *35*(4), 52–58. https://doi.org/10.1111/j.1747-1567.2010.00643.x

Charles, P. (2009). *Torsional Vibration-Based Monitoring of Medium-Speed Diesel Engines*. University of Manchester, Machester.

Citron, S. J., O'Higgins, J. E., & Chen, L. Y. (1989). *Cylinder by Cylinder Engine Pressure and Pressure Torque Waveform Determination Utilizing Speed Fluctuations* (SAE Technical Paper No. 890486). Warrendale, PA: SAE International. https://doi.org/10.4271/890486

Cohen, L. (1995). *Time-frequency analysis*. Englewood Cliffs, N.J: Prentice Hall PTR.

Connolly, F. T., & Yagle, A. E. (1993). Modeling and identification of the combustion pressure process in internal combustion engines. In *Proceedings of 36th Midwest Symposium on Circuits and Systems* (pp. 204–207 vol.1). https://doi.org/10.1109/MWSCAS.1993.343094

D. Vakman. (2000). New high precision frequency measurement, Measurement Science and Technology. Retrieved 19 June 2015, from http://hud.summon.serialssolutions.com.libaccess.hud.ac.uk/search?ho=t&l=en&q=D.+Vakman%2C+New+high+precision+frequency+measurement%2C+Measurement+Science+and+Technology+11+%282000%29+1493%E2%80%931497.#!/search?ho=t&l=en&q=D.%20Vakman,%20New%20high%20precision%20frequency%20measurement,%20Measurement%20Science%20and%20Technology%2011%20(2000)%201493%E2%80%931497.

Dalpiaz, G., & Rivola, A. (1997). Condition Monitoring and Diagnostic in Automatic Macchines: Comparison of Vibration Analysis Techniques. *Mechanical Systems and Signal Processing*, *11*(1), 53–73. https://doi.org/10.1006/mssp.1996.0067

David John Moore. (2013). *Condition Monitoring of Diesel Engines*. University of Manchester.

Desbazeille, M., Randall, R. B., Guillet, F., El Badaoui, M., & Hoisnard, C. (2010). Model-based diagnosis of large diesel engines based on angular speed variations of the crankshaft. *Mechanical Systems and Signal Processing*, *24*(5), 1529–1541. https://doi.org/10.1016/j.ymssp.2009.12.004

Di Leo, R. (2015). Methodologies for Air-Fuel ratio and trapped mass estimation in Diesel engines using the in-cylinder pressure measurement. *Energy Procedia*, *82*, 957–964. https://doi.org/10.1016/j.egypro.2015.11.850

D.J. Ewins. (1984). *Moal Testing: Theory and practice*.

Epaarachchi, J. A., & Kahandawa, G. C. (2016). *Structural Health Monitoring Technologies and Next-Generation Smart Composite Structures*. CRC Press.

Eriksson, L., & Andersson, I. (2002). *An Analytic Model for Cylinder Pressure in a Four Stroke SI Engine* (SAE Technical Paper No. 2002-1–371). Warrendale, PA: SAE International. https://doi.org/10.4271/2002-01-0371

Fang, C., Cao, Z., Ektesabi, M. M., Kapoor, A., & Sayem, A. H. M. (2013). Driveline modelling analysis for active driveability control. In *2013 IEEE Conference on Systems, Process Control (ICSPC)* (pp. 125–128). https://doi.org/10.1109/SPC.2013.6735117

Ftoutou, E., Chouchane, M., & Besbès, N. (2012). Internal combustion engine valve clearance fault classification using multivariate analysis of variance and discriminant analysis.

Transactions of the Institute of Measurement and Control, *34*(5), 566–577. https://doi.org/10.1177/0142331211408492

Gabor, D. (1947). Theory of communication. *Journal of the Institution of Electrical Engineers - Part I: General*, *94*(73), 58-. https://doi.org/10.1049/ji-1.1947.0015

Gawande, S. H., Navale, L. G., & Nandgaonkar, M. R. (2015). Power Balancing of Inline Multicylinder Diesel Engine. *Advances in Mechanical Engineering*, *4*(0), 937917–937917. https://doi.org/10.1155/2012/937917

Ghojel, J., & Honnery, D. (2005). Heat release model for the combustion of diesel oil emulsions in DI diesel engines. *Applied Thermal Engineering*, *25*(14–15), 2072–2085. https://doi.org/10.1016/j.applthermaleng.2005.01.016

Ghojel, J. I. (2010). Review of the development and applications of the Wiebe function: a tribute to the contribution of Ivan Wiebe to engine research. *International Journal of Engine Research*, *11*(4), 297–312. https://doi.org/10.1243/14680874JER06510

Gilkey, J. C., & Powell, J. D. (1985). Fuel-Air Ratio Determination From Cylinder Pressure Time Histories. *Journal of Dynamic Systems, Measurement, and Control*, *107*(4), 252–257. https://doi.org/10.1115/1.3140731

Girolami, G., & Vakman, D. (2002). Instantaneous frequency estimation and measurement: a quasi-local method. *Measurement Science and Technology*, *13*(6), 909.

Global Diesel Engine Market. (2016, July). Global Diesel Engine Market 2016-2020 - Research and Markets. Retrieved from https://www.researchandmarkets.com/reports/3802189/global-diesel-engine-market-2016-2020

Goyal, D., & Pabla, B. S. (2016). The Vibration Monitoring Methods and Signal Processing Techniques for Structural Health Monitoring: A Review. *Archives of Computational Methods in Engineering*, *23*(4), 585–594. https://doi.org/10.1007/s11831-015-9145-0

Groover, C. L., Trethewey, M. W., Maynard, K. P., & Lebold, M. S. (2005). Removal of order domain content in rotating equipment signals by double resampling. *Mechanical Systems and Signal Processing*, *19*(3), 483–500.

Gu, F., & Ball, A. (1996). Diesel injector dynamic modelling and estimation of injection parameters from impact response Part 1: modelling and analysis of injector impacts. *Proceedings of the Institution of Mechanical Engineers Part D Journal of Automobile Engineering*, *210*(44), 293–302.

Gu, F., Ball, A., & Li, W. (2000). The Condition Monitoring of Diesel Engines Using Acoustic Measurements-Part 1: Acoustic Characteristics of the Engine and Representation of the Acoustic Signals. *SAE Technical Papers*. Retrieved from http://www.sae.org/technical/papers/2000-01-0730

Gu, F., Jacob, P. J., & Ball, A. D. (1999). Non-parametric models in the monitoring of engine performance and condition: Part 2: Non-intrusive estimation of diesel engine cylinder pressure and its use in fault detection. *Proceedings of the Institution of Mechanical Engineers, Part D: Journal of Automobile Engineering*, *213*(2), 135–143. https://doi.org/10.1243/0954407991526757

Gu, F., Yesilyurt, I., Li, Y., Harris, G., & Ball, A. (2006). An investigation of the effects of measurement noise in the use of instantaneous angular speed for machine diagnosis. *Mechanical Systems and Signal Processing*, *20*(6), 1444–1460. https://doi.org/10.1016/j.ymssp.2005.02.001

Guangming, Z., & Zhengfeng, J. (2009). Study on Torsional Stiffness of Engine Crankshaft. In *2009 International Forum on Computer Science-Technology and Applications* (Vol. 3, pp. 431–435). https://doi.org/10.1109/IFCSTA.2009.345

Gubran, A. A., & Sinha, J. K. (2014). Shaft instantaneous angular speed for blade vibration in rotating machine. *Mechanical Systems and Signal Processing*, *44*(1–2), 47–59. https://doi.org/10.1016/j.ymssp.2013.02.005

Hamedovic, H., Raichle, F., & Bohme, J. F. (2005). In-cylinder pressure reconstruction for multicylinder SI-engine by combined processing of engine speed and one cylinder pressure. In *Proceedings. (ICASSP '05). IEEE International Conference on Acoustics, Speech, and Signal Processing, 2005.* (Vol. 5, p. v/677-v/680 Vol. 5). https://doi.org/10.1109/ICASSP.2005.1416394

Hamming, R. (2012). *Introduction to Applied Numerical Analysis* (Reprint edition). Mineola, N.Y: Dover Publications Inc.

Hardenberg, H. O., & Hase, F. W. (1979). *An empirical formula for computing the pressure rise delay of a fuel from its cetane number and from the relevant parameters of direct-injection diesel engines*. SAE Technical Paper. Retrieved from http://papers.sae.org/790493/

Hatch, M. R. (2000). *Vibration Simulation Using MATLAB and ANSYS* (1 edition). Boca Raton: Chapman and Hall/CRC.

Heywood, J. B. (1988). *Internal combustion engine fundamentals*. New York: McGraw-Hill.

Honda, Y., Saito, T., Wakabayashi, K., Kodama, T., & Iwamoto, S. (1989). *A Simulation Method for Crankshaft Torsional Vibration by Considering Dynamic Characteristics of Rubber Dampers*. SAE Technical Paper. Retrieved from http://papers.sae.org/891172/

Ibrahim, S. R., & Mikulcik, E. C. (1977). A method for the direct identification of vibration parameters from the free response. Retrieved from https://ntrs.nasa.gov/search.jsp?R=19800070016

Jacob, P. J., Gu, F., & Ball, A. D. (1999). Non-parametric models in the monitoring of engine performance and condition: Part 1: Modelling of non-linear engine processes. *Proceedings of the Institution of Mechanical Engineers, Part D: Journal of Automobile Engineering*, *213*(1), 73–81. https://doi.org/10.1243/0954407991526694

James, G. H., III, Carne, T. G., & Lauffer, J. P. (1993). The natural excitation technique (NExT) for modal parameter extraction from operating wind turbines. *NASA STI/Recon Technical Report N*, *93*. Retrieved from http://adsabs.harvard.edu/abs/1993STIN...9328603J

J.C. Wachel, & Fred R. Szenasi. (1993). Analysis of Torsional Vibrations in Rotating Machinery.

Jia-Dong, Z., Guang-Yao, O., & Hong-Bin, G. (2009). Demodulation of instantaneous rotational speed of diesel engine based on Hilbert transform. In *Electronic Measurement & Instruments, 2009. ICEMI'09. 9th International Conference on* (pp. 2–753). IEEE. Retrieved from http://ieeexplore.ieee.org/xpls/abs_all.jsp?arnumber=5274460

Jiang, J., Gu, F., Gennish, R., Moore, D. J., Harris, G., & Ball, A. D. (2008). Monitoring of diesel engine combustions based on the acoustic source characterisation of the exhaust system. *Mechanical Systems and Signal Processing*, *22*(6), 1465–1480. https://doi.org/10.1016/j.ymssp.2007.12.003

Jones, N. B., & Li, Y.-H. (2000). A review of condition monitoring and fault diagnosis for diesel engines. *Tribotest*, *6*(3), 267–291. https://doi.org/10.1002/tt.3020060305

Juang, J. (1993). *Applied System Identification* (Facsimile edition). Englewood Cliffs, N.J: Prentice Hall.

JUANG, J.-N., & PAPPA, R. S. (1985). An eigensystem realization algorithm for modal parameter identification and model reduction. *Journal of Guidance, Control, and Dynamics*, *8*(5), 620–627. https://doi.org/10.2514/3.20031

Kallenberger, C., Hamedović, H., Raichle, F., Breuninger, J., Fischer, W., Benninger, K., … Zoubir, A. M. (2008). Estimation of Cylinder-Wise Combustion Features from Engine Speed and Cylinder Pressure. *SAE International Journal of Engines*, *1*(1), 198–207. https://doi.org/10.4271/2008-01-0290

Kay, S. (1999). *Modern Spectral Estimation: Theory and Application* (1 edition). Upper Saddle River, N.J: Prentice Hall.

Kiencke, U., & Nielsen, L. (2005). *Automotive Control Systems: For Engine, Driveline, and Vehicle* (2 edition). Berlin: Springer.

Kiernicki, Z. (2004). Engine transient test technique. *Measurement*, *5*, 1.

Lakshminarayanan, P. A., & Aghav, Y. V. (2010). *Modelling Diesel Combustion*. Dordrecht: Springer Netherlands. Retrieved from http://link.springer.com/10.1007/978-90-481-3885-2

Lardies, J. (2015). Modal Parameter Identification from Output Data Only: Equivalent Approaches [Research article]. https://doi.org/10.1155/2015/124932

Leonhardt, S., Gao, H., & Kecman, V. (1995). Real time supervision of diesel engine injection with RBF-based neural networks. In *American Control Conference, Proceedings of the 1995* (Vol. 3, pp. 2128–2132 vol.3). https://doi.org/10.1109/ACC.1995.531274

Li .W. (2000). *A Study of Diesel Engine Acoustic Characteristics*. University of Manchester.

Li, Y., Gu, F., Harris, G., Ball, A., Bennett, N., & Travis, K. (2005). The measurement of instantaneous angular speed. *Mechanical Systems and Signal Processing*, *19*(4), 786–805. https://doi.org/10.1016/j.ymssp.2004.04.003

Lida, K., Akishino, K., & Kido, K. (1990). *IMEP Estimation from Instantaneous Crankshaft Torque Variation* (SAE Technical Paper No. 900617). Warrendale, PA: SAE International. https://doi.org/10.4271/900617

Lim, B., Lim, I., Park, J., Son, Y., & Kim, E. (1994). *Estimation of the Cylinder Pressure in a SI Engine Using the Variation of Crankshaft Speed* (SAE Technical Paper No. 940145). Warrendale, PA: SAE International. https://doi.org/10.4271/940145

Lingmi Zhang, Rune Brincker, & Palle Andersen. (2005). An Overview of Operational Modal Analysis Major Development and Issues. Retrieved from https://www.scribd.com/document/42166945/2005-10-an-Overview-of-Operational-Modal-Analysis-Major-Development-and-Issues

Liu, S., Gu, F., & Ball, A. (2002). The on-line detection of engine misfire at low speed using multiple feature fusion with fuzzy pattern recognition. *Proceedings of the Institution of Mechanical Engineers Part D Journal of Automobile Engineering*, *216*(5), 391–402.

Machinery Condition Monitoring: Principles and Practices. (2017, August 1). Retrieved from https://www.crcpress.com/Machinery-Condition-Monitoring-Principles-and-Practices/Mohanty/p/book/9781138748255

Mahon, L. L. J. (1992). *Diesel Generator Handbook*. Oxford ; Boston: Newnes.

Martyr, A. J., & Plint, M. A. (2007). *Engine testing: theory and practice* (3. ed). Amsterdam: Elsevier.

Mauer, G. F. (1992). On-line performance diagnostics for internal combustion engines. In *and Automation Proceedings of the 1992 International Conference on Industrial Electronics, Control, Instrumentation* (pp. 1460–1465 vol.3). https://doi.org/10.1109/IECON.1992.254386

Mauer, G. F., & Watts, R. J. (1989). *On-Line Cylinder Diagnostics on Combustion Engines by Noncontact Torque and Speed Measurements* (SAE Technical Paper No. 890485). Warrendale, PA: SAE International. https://doi.org/10.4271/890485

Mendes, A. S., Meirelles, P. S., & Zampieri, D. E. (2008). Analysis of torsional vibration in internal combustion engines: modelling and experimental validation. *Proceedings of the Institution of Mechanical Engineers, Part K: Journal of Multi-Body Dynamics, 222*(2), 155–178. https://doi.org/10.1243/14644193JMBD126

Merker, G. P. (Ed.). (2006). *Simulating combustion: simulation of combustion and pollutant formation for engine-development*. Berlin ; New York: Springer.

Merkisz, Boguś, P., & Grzeszczyk, R. (2001). Overview of engine misfire detection methods used in on board diagnostics. *Journal of KONES, Vol. 8, No. 1-2*, 326–341.

Mocanu, F. (2012). *Multi-fuel operation of modern engines; on board fuel identification*. Wayne State University.

Mocanu, F., & Taraza, D. (2013). Estimation of Main Combustion Parameters from the Measured Instantaneous Crankshaft Speed. https://doi.org/10.4271/2013-01-0326

Mollenhauer, K., & Tschöke, H. (Eds.). (2010). *Handbook of Diesel Engines*. Berlin, Heidelberg: Springer Berlin Heidelberg. Retrieved from http://link.springer.com/10.1007/978-3-540-89083-6

Mucheroni, M. F., & Cardoso, A. (2006). Output-only structural identification of random vibrating systems. *Journal of the Brazilian Society of Mechanical Sciences and Engineering*, *28*(1), 99–104. https://doi.org/10.1590/S1678-58782006000100011

Neda Nickmehr. (2015). *System Identification of an Engine-load Setup Using Grey-box Model*. Linköping University.

O'Shea, P., Sadik, A. Z., & Hussain, Z. M. (2011). *Digital Signal Processing*. Berlin, Heidelberg: Springer Berlin Heidelberg. Retrieved from http://link.springer.com/10.1007/978-3-642-15591-8

Oskam, G. (2014). *Optimizing diesel engine condition monitoring: Research on diagnostic representation techniques based on in-cylinder pressure measurement*. Delft University of Technology.

Peeters, B., & DE Roeck, G. (1999). Reference-Based Stochastic Subspace Identification for Output-Only Modal Analysis. *Mechanical Systems and Signal Processing*, *13*(6), 855–878. https://doi.org/10.1006/mssp.1999.1249

Peeters, B., & De Roeck, G. (2001). Stochastic System Identification for Operational Modal Analysis: A Review. *Journal of Dynamic Systems, Measurement, and Control*, *123*(4), 659–667. https://doi.org/10.1115/1.1410370

Piersol, A. G., & Paez, T. L. (2009). *Harris' Shock and Vibration Handbook* (6 edition). New York: McGraw-Hill Education.

Pineda-Sanchez, M., Riera-Guasp, M., Antonino-Daviu, J. A., Roger-Folch, J., Perez-Cruz, J., & Puche-Panadero, R. (2009). Instantaneous Frequency of the Left Sideband Harmonic During the Start-Up Transient: A New Method for Diagnosis of Broken Bars. *IEEE*

Transactions on Industrial Electronics, *56*(11), 4557–4570. https://doi.org/10.1109/TIE.2009.2026211

Pioldi, F., & Rizzi, E. (2017). A refined Frequency Domain Decomposition tool for structural modal monitoring in earthquake engineering. *Earthquake Engineering and Engineering Vibration*, *16*(3), 627–648. https://doi.org/10.1007/s11803-017-0394-9

Proulx, T. (2011). *Modal Analysis Topics, Volume 3: Proceedings of the 29th IMAC, A Conference on Structural Dynamics, 2011*. Springer Science & Business Media.

Rainieri, C., & Fabbrocino, G. (Eds.). (2014). *Operational Modal Analysis of Civil Engineering Structures* (2014 edition). New York: Springer.

Rakopoulos, C. D., & Giakoumis, E. G. (2006). *Review of thermodynamic diesel engine simulations under transient operating conditions*. SAE Technical Paper. Retrieved from http://papers.sae.org/2006-01-0884/

Rakopoulos, C. D., & Giakoumis, E. G. (2010). *Diesel Engine Transient Operation: Principles of Operation and Simulation Analysis* (2009 edition). London: Springer.

Randall. (2011). *Vibration-based Condition Monitoring* (1 edition). Chichester, West Sussex, U.K. ; Hoboken, N.J: John Wiley & Sons.

Randall, R. B. (2009). The use of simulation models to generate data corresponding to faults in machines. In *2009 8th International Conference on Reliability, Maintainability and Safety* (pp. 934–939). https://doi.org/10.1109/ICRMS.2009.5269971

Randall, R. B. (2011). *Vibration-based condition monitoring: industrial, aerospace, and automotive applications*. Chichester, West Sussex, U.K. ; Hoboken, N.J: Wiley.

Randall, R. B., & Luo, D. (1990). Hilbert Transform Techniques for Torsional Vibration Analysis. *Australian Vibration and Noise Conference 1990: Vibration and Noise-Measurement Prediction and Control; Preprints of Papers*, 122.

Rao, B. K. N. (1996). *Handbook of Condition Monitoring*. Oxford, UK: Elsevier Advanced Technology.

Remond, D. (1998). Practical performances of high-speed measurement of gear transmission error or torsional vibrations with optical encoders. *Measurement Science and Technology*, *9*(3), 347. https://doi.org/10.1088/0957-0233/9/3/006

Rizzoni, G. (1989a). A stochastic model for the indicated pressure process and the dynamics of the internal combustion engine. *IEEE Transactions on Vehicular Technology, 38*(3), 180–192. https://doi.org/10.1109/25.45471

Rizzoni, G. (1989b). Estimate of indicated torque from crankshaft speed fluctuations: a model for the dynamics of the IC engine. *IEEE Transactions on Vehicular Technology*, *38*(3), 168–179. https://doi.org/10.1109/25.45470

Roger Lewis. (2000, July). *Wear of Diesel Engine Inlet Valves and Seats*. University of Sheffield.

Schagerberg, S., & McKelvey, T. (2003). *Instantaneous Crankshaft Torque Measurements - Modeling and Validation* (SAE Technical Paper No. 2003-1–713). Warrendale, PA: SAE International. https://doi.org/10.4271/2003-01-0713

Shiao, Y., & Moskwa, J. J. (1994). *Misfire Detection and Cylinder Pressure Reconstruction for SI Engines* (SAE Technical Paper No. 940144). Warrendale, PA: SAE International. https://doi.org/10.4271/940144

Sinha, J. K. (2014). *Vibration Analysis, Instruments, and Signal Processing* (1 edition). Boca Raton: CRC Press.

Sood, A. K., Friedlander, C. B., & Fahs, A. A. (1985). Engine Fault Analysis: Part I-Statistical Methods. *IEEE Transactions on Industrial Electronics, IE-32*(4), 294–300. https://doi.org/10.1109/TIE.1985.350100

Spagnol, M., & Bregant, L. (2015). Instantaneous Angular Speed Analysis, Measurement Errors and Signal Filtering. In *Proceedings of the 9th IFToMM International Conference on Rotor Dynamics* (pp. 521–531). Springer, Cham. https://doi.org/10.1007/978-3-319-06590-8_42

Strang, G. (2009). *Introduction to Linear Algebra* (4 edition). Wellesley, Mass: Wellesley-Cambridge Press.

Sweeney, P. J., & Randall, R. B. (1996). Gear Transmission Error Measurement Using Phase Demodulation. *Proceedings of the Institution of Mechanical Engineers, Part C: Journal of Mechanical Engineering Science*, *210*(3), 201–213. https://doi.org/10.1243/PIME_PROC_1996_210_190_02

Taraza, D. (1993). *Estimation of the Mean Indicated Pressure from Measurements of the Crankshafts Angular Speed Variation* (SAE Technical Paper No. 932413). Warrendale, PA: SAE International. https://doi.org/10.4271/932413

Taraza, D., Henein, N. A., & Bryzik, W. (2000). The Frequency Analysis of the Crankshaft's Speed Variation: A Reliable Tool for Diesel Engine Diagnosis. *Journal of Engineering for Gas Turbines and Power*, *123*(2), 428–432. https://doi.org/10.1115/1.1359479

Taraza, D., Henein, N. A., Gade, M. J., & Bryzik, W. (2005). Cylinder Pressure Reconstruction From Crankshaft Speed Measurement in a Four-Stroke Single Cylinder Diesel Engine, 387–395. https://doi.org/10.1115/ICES2005-1023

Thomas Edwin Slaughter Kriel. (2000). *Assessment of Frequency Domain Force Identification Procedures*.

Trimby, S. (2016, May 13). *Engine cylinder pressure reconstruction using crank kinematics, block vibrations, and time-delay neural networks* (doctoral). University of Sussex. Retrieved from http://sro.sussex.ac.uk/61201/

Vakman, D. (1994). Computer measuring of frequency stability and the analytic signal. *IEEE Transactions on Instrumentation and Measurement*, *43*(4), 668–671. https://doi.org/10.1109/19.310187

Wharton, A. J. (1991). *Diesel Engines* (3 edition). Jordan Hill, Oxford: Butterworth-Heinemann.

Williams, J. (1996). *An Overview of Misfiring Cylinder Engine Diagnostic Techniques Based on Crankshaft Angular Velocity Measurements* (SAE Technical Paper No. 960039). Warrendale, PA: SAE International. https://doi.org/10.4271/960039

Yang, J., Pu, L., Wang, Z., Zhou, Y., & Yan, X. (2001). Fault Detection in a Diesel Engine by Analysing the Instantaneous Angular Speed. *Mechanical Systems and Signal Processing*, *15*(3), 549–564. https://doi.org/10.1006/mssp.2000.1344

Yousef Ben Sasi, A., Gu, F., Payne, B., & Ball, A. (2004). Instantaneous angular speed monitoring of electric motors. *Journal of Quality in Maintenance Engineering*, *10*(2), 123–135. https://doi.org/10.1108/13552510410539196

Zhao, M., Lin, J., & Xu, J. (2011). The measurement and error analysis of instantaneous angular speed using optical incremental encoder (Vol. 8201, p. 82010Y–82010Y–8). https://doi.org/10.1117/12.902978